

CR 151441

JSC-10975

ADVANCED SENSORS AND APPLICATIONS STUDY (ASAS)

Job Order 75-225

(NASA-CR-151441) ADVANCED SENSORS AND  
APPLICATIONS STUDY (ASAS) (Lockheed  
Electronics Co.) 353 p HC A16/MF A01

N77-26590

CSSL 14B

Unclas

G3/43

37056

Prepared By

Lockheed Electronics Company, Inc.

Aerospace Systems Division

Houston, Texas

Contract NAS 9-12200

For

EARTH OBSERVATIONS DIVISION

EXPLORATORY STUDIES DEPARTMENT



*National Aeronautics and Space Administration*  
**LYNDON B. JOHNSON SPACE CENTER**

*Houston, Texas*

November 1976

REPRODUCED BY  
**NATIONAL TECHNICAL  
INFORMATION SERVICE**  
U. S. DEPARTMENT OF COMMERCE  
SPRINGFIELD, VA. 22161

LEC-7790  
Revision A

**TECHNICAL REPORT INDEX/ABSTRACT**  
(See instructions on reverse side.)

1. TITLE AND SUBTITLE OF DOCUMENT  <p style="text-align: center;">Advanced Sensors and Applications Study (ASAS)</p>		2. JSC NO.  <p style="text-align: center;">JSC-10975</p>
3. CONTRACTOR/ORGANIZATION NAME  <p style="text-align: center;">Lockheed Electronics Co., Inc.</p>	4. CONTRACT OR GRANT NO.  <p style="text-align: center;">NAS 9-12200</p>	
5. CONTRACTOR/ORIGINATOR DOCUMENT NO.  <p style="text-align: center;">LEC-7790 Rev. A</p>	6. PUBLICATION DATE (THIS ISSUE)  <p style="text-align: center;">November 1976</p>	
7. SECURITY CLASSIFICATION  <p style="text-align: center;">Unclassified</p>	8. OPR (OFFICE OF PRIMARY RESPONSIBILITY)	
9. LIMITATIONS GOVERNMENT HAS UNLIMITED RIGHTS <input type="checkbox"/> YES <input type="checkbox"/> NO  IF NO, STATE LIMITATIONS AND AUTHORITY  <p style="text-align: center;">N/A</p>	10. AUTHOR(S)  <p style="text-align: center;">S. B. Chism C. L. Hughes</p>	
11. DOCUMENT CONTRACT REFERENCES  WORK BREAKDOWN STRUCTURE NO. <p style="text-align: center;">Earth Observations Division</p>	12. HARDWARE CONFIGURATION  SYSTEM <p style="text-align: center;">N/A</p>	
CONTRACT EXHIBIT NO.  <p style="text-align: center;">N/A</p>	SUBSYSTEM  <p style="text-align: center;">N/A</p>	
DRL NO. AND REVISION  <p style="text-align: center;">N/A</p>	MAJOR EQUIPMENT GROUP  <p style="text-align: center;">N/A</p>	
DRL LINE ITEM NO.  <p style="text-align: center;">N/A</p>	MAJOR EQUIPMENT GROUP  <p style="text-align: center;">N/A</p>	
13. ABSTRACT <p>A study has been completed summarizing the present EOD requirements for sensors in the Space Shuttle era. These sensor requirements are reported with emphasis on those applications which were deemed important enough to warrant separate sections. The application areas developed are (1) agriculture, (2) atmospheric corrections, (3) cartography, (4) coastal studies, (5) forestry, (6) geology, (7) hydrology, (8) land use, (9) oceanography, and (10) soil moisture. For each application area, the following aspects were covered (1) specific goals and techniques, (2) individual sensor requirements including types, bands, resolution, etc., (3) definition of mission requirements, type orbits, coverages, etc., and (4) discussion of anticipated problem areas and solutions.</p> <p>The remote sensors required for these application areas included (1) camera systems, (2) multispectral scanners, (3) microwave scatterometers, (4) synthetic aperture radars, (5) microwave radiometers, and (6) vidicons. The emphasis in the remote sensor area was on the evaluation of present technology implications about future systems. From these implications, recommendations for future remote sensors were developed.</p>		
14. SUBJECT TERMS  <hr/> <hr/> <hr/> <hr/> <hr/> <hr/>		

ADVANCED SENSORS AND APPLICATIONS STUDY (ASAS)

Job Order 75-225

EDITED AND PREPARED BY

*A. B. Chism Jr.*

---

S. B. Chism Jr., Principal Engineer  
Exploratory Investigations Section

*C. L. Hughes*

---

C. L. Hughes, Principal Scientist  
Exploratory Investigations Section

APPROVED BY

*J. J. Carney*

---

J. J. Carney, Supervisor  
Exploratory Investigations Section

*J. E. Davis*

---

J. E. Davis, Manager  
Exploratory Studies Department

Prepared By

Lockheed Electronics Company, Inc.

For

Earth Observations Division

NATIONAL AERONAUTICS AND SPACE ADMINISTRATION  
LYNDON B. JOHNSON SPACE CENTER  
HOUSTON, TEXAS

November 1976

## Note on the Revised ASAS Report

This report is a revision of the Advanced Sensors and Applications Study (ASAS) report, LEC-7790, April 1976. Most of the original sections have been revised and expanded to include new information. In addition, there are two new sections. These are the sensor sections on microwave radiometers and vidicons. Finally, an appendix is included on remote sensor systems.

## CONTRIBUTORS

The following authors contributed the indicated applications and sensor subsections of this report.

### Applications :

Agriculture	W. W. Hildreth
Atmospheric Corrections	C. L. Hughes (thermal) and J. F. Potter (visible & near infrared)
Cartography	R. G. Davis
Coastal Studies	E. A. Weisblatt
Forestry and Range	R. D. Dillman
Geology	V. R. Frierson
Hydrology	W. H. Scoggins
Land Use	F. R. Brumbaugh
Oceanography	W. H. Scoggins
Soil Moisture	D. E. Phinney (visible & thermal) J. R. Wang (microwave) H. V. Soule (polarization)

### Sensors

Camera Systems	R. A. Mendlowitz
Multispectral Scanners	S. B. Chism, Jr.
Microwave Scatterometer	W. A. Rosenkranz
Synthetic Aperture Radar	S. B. Chism and C. L. Hughes
Microwave Radiometers	D. J. Pounds
Vidicons	J. J. Dishler

## CONTENTS

Section	Page
1. INTRODUCTION . . . . .	1-1
2. APPLICATIONS REQUIREMENTS . . . . .	2-1
2.1 <u>AGRICULTURE</u> . . . . .	2.1-1
2.1.1 DETERMINING FUTURE REQUIREMENTS. . . . .	2.1-2
2.1.2 CROP IDENTIFICATION AND ACREAGE ESTIMATION . . . . .	2.1-3
2.1.3 YIELD ESTIMATION . . . . .	2.1-5
2.1.3.1 <u>Yield Estimates from Environmental Data</u> . . . . .	2.1-6
2.1.3.2 <u>Yield Estimation from Vegetation                   Conditions</u> . . . . .	2.1-7
2.1.3.3 <u>Modeling and Satellite Data</u> . . . . .	2.1-10
2.1.3.4 <u>Summary</u> . . . . .	2.1-10
2.2 <u>ATMOSPHERIC CORRECTIONS</u> . . . . .	2.2-1
2.2.1 <u>ATMOSPHERIC CORRECTIONS IN THE VISIBLE                   AND NEAR IR.</u> . . . . .	2.2.1-1
2.2.1.1 <u>Introduction</u> . . . . .	2.2.1-1
2.2.1.2 <u>Methods Involving the Determination of                   Haze Levels</u> . . . . .	2.2.1-1
2.2.1.3 <u>Methods Not Involving the Determination                   of Haze Levels</u> . . . . .	2.2.1-3
2.2.2 <u>INFRARED ATMOSPHERIC CORRECTIONS</u> . . . . .	2.2.2-1
2.2.2.1 <u>Correction Techniques for Sea Surface                   Temperature Determination</u> . . . . .	2.2.2-2
2.2.2.2 <u>Correction Techniques for Land Surface                   Data</u> . . . . .	2.2.2-24
2.3 <u>CARTOGRAPHY</u> . . . . .	2.3-1
2.3.1 INTRODUCTION . . . . .	2.3-1

Section	Page
2.3.2 BACKGROUND . . . . .	2.3-3
2.3.3 AREAL COVERAGE . . . . .	2.3-5
2.3.4 RESOLUTION . . . . .	2.3-7
2.3.4.1 <u>Cartographic Accuracy</u> . . . . .	2.3-9
2.3.4.2 <u>Spatial Resolution and Map Scale</u> . . . . .	2.3-10
2.3.5 GEOMETRIC FIDELITY . . . . .	2.3-11
2.3.6 BASE-HEIGHT RATIO. . . . .	2.3-14
2.3.7 SENSOR CONFIGURATION AND MISSION PROFILE . . . . .	2.3-15
2.3.8 SIDE-LOOKING RADAR (SLAR). . . . .	2.3-16
2.4 <u>COASTAL STUDIES</u> . . . . .	2.4-1
2.4.1 SPECIFIC GOALS AND TECHNIQUES. . . . .	2.4-1
2.4.1.1 <u>Environment Detection and Identification</u> . . . . .	2.4-1
2.4.2 SENSOR AND MISSION REQUIREMENTS. . . . .	2.4-3
2.4.3 PROBLEMS . . . . .	2.4-4
2.5 <u>FORESTRY</u> . . . . .	2.5-1
2.5.1 INTRODUCTION . . . . .	2.5-1
2.5.2 BACKGROUND . . . . .	2.5-1
2.5.3 RESOURCE PARAMETERS FROM SATELLITE SENSORS . . . . .	2.5-2
2.5.3.1 <u>The Living Leaf</u> . . . . .	2.5-4
2.5.3.2 <u>Camera Systems</u> . . . . .	2.5-4
2.5.3.3 <u>Scanner Systems - Visible and Near Infrared Bands</u> . . . . .	2.5-7
2.5.3.4 <u>Thermal Region - 8.0 <math>\mu</math>m to 14.0 <math>\mu</math>m</u> . . . . .	2.5-11
2.5.3.5 <u>Resolution in Visible and Infrared</u> . . . . .	2.5-12
2.5.3.6 <u>Microwave</u> . . . . .	2.5-12

Section	Page
2.5.4 FOREST MANAGEMENT SYSTEMS. . . . .	2.5-14
2.5.5 SUMMARY. . . . .	2.5-17
2.5.5.1 <u>Recommendations</u> . . . . .	2.5-18
2.6 <u>GEOLOGY</u> . . . . .	2.6-1
2.7 <u>HYDROLOGY</u> . . . . .	2.7-1
2.7.1 BACKGROUND . . . . .	2.7-1
2.7.2 SATELLITE MAPPING. . . . .	2.7-2
2.7.3 RECOMMENDATION FOR CONTINUATION OF STUDY . . . . .	2.7-3
2.8 <u>LAND USE</u> . . . . .	2.8-1
2.8.1 INTRODUCTION . . . . .	2.8-1
2.8.2 CAMERA SYSTEMS . . . . .	2.8-2
2.8.3 MULTISPECTRAL SCANNERS . . . . .	2.8-5
2.8.4 MICROWAVE SENSORS. . . . .	2.8-8
2.8.5 THERMAL INFRARED (IR) SCANNERS . . . . .	2.8-8
2.9 <u>OCEANOGRAPHY</u> . . . . .	2.9-1
2.9.1 PHYSICAL OCEANOGRAPHY. . . . .	2.9-1
2.9.2 BIOLOGICAL OCEANOGRAPHY. . . . .	2.9-1
2.9.3 GEOLOGICAL OCEANOGRAPHY. . . . .	2.9-2
2.9.4 REMOTE MEASUREMENT OF OCEANOGRAPHIC PARAMETERS . . . . .	2.9-2
2.9.5 SENSOR TECHNIQUES INVESTIGATED FOR SEASAT-A. . . . .	2.9-7
2.9.6 GENERAL OCEANOGRAPHIC SENSOR REQUIREMENTS. . . . .	2.9-7
2.10 <u>SOIL MOISTURE</u> . . . . .	2.10-1
2.10.1 USE OF VISIBLE, NEAR INFRARED, AND THERMAL INFRARED REMOTE SENSING OF STUDY SOIL MOISTURE. . . . .	2.10-1

Section	Page
2.10.1.1 <u>Reflectance Method</u> . . . . .	2.10-2
2.10.1.2 <u>Visible Polarization</u> . . . . .	2.10-3
2.10.1.3 <u>Temperature Method</u> . . . . .	2.10-7
2.10.1.4 <u>Discussion</u> . . . . .	2.10-9
2.10.2 REMOTE SENSING OF SOIL MOISTURE AT MICROWAVE FREQUENCIES . . . . .	2.10-14
2.10.2.1 <u>Introduction</u> . . . . .	2.10-14
2.10.2.2 <u>Dielectric Properties of Soil at Microwave Frequencies</u> . . . . .	2.10-15
2.10.2.3 <u>Soil Moisture Measurements by the Active Microwave Sensors</u> . . . . .	2.10-19
2.10.2.4 <u>Radiometric Measurements of Soil Moisture</u> . . . . .	2.10-22
2.10.2.5 <u>Summary</u> . . . . .	2.10-28
3. SHUTTLE ERA SENSORS . . . . .	3.1-1
3.1 <u>CAMERA SYSTEMS</u> . . . . .	3.1-1
3.1.1 INTRODUCTION . . . . .	3.1-1
3.1.2 MULTISPECTRAL CAMERA SYSTEMS . . . . .	3.1-1
3.1.2.1 <u>Skylab S-190A</u> . . . . .	3.1-3
3.1.2.2 <u>Single-Lens Multiband Camera</u> . . . . .	3.1-7
3.1.2.3 <u>Other Multispectral Cameras</u> . . . . .	3.1-7
3.1.2.4 <u>Films For Multispectral Applications</u> . . . . .	3.1-7
3.1.3 HIGH RESOLUTION CAMERAS . . . . .	3.1-11
3.1.3.1 <u>Frame Cameras</u> . . . . .	3.1-11
3.1.3.2 <u>Panoramic Cameras</u> . . . . .	3.1-11
3.1.3.3 <u>Strip Cameras</u> . . . . .	3.1-14
3.1.4 RECOMMENDATIONS . . . . .	3.1-16

Section	Page
3.2 <u>MULTISPECTRAL SCANNERS</u> . . . . .	3.2-1
3.2.1 MSS INTRODUCTION AND BACKGROUND. . . . .	3.2-1
3.2.1.1 <u>Aircraft Multispectral Scanners</u> . . . . .	3.2-1
3.2.1.2 <u>SO-65 Experiment</u> . . . . .	3.2-2
3.2.1.3 <u>ERTS-1 to Landsat-2</u> . . . . .	3.2-5
3.2.1.4 <u>Skylab S-192</u> . . . . .	3.2-6
3.2.2 FUTURE MULTISPECTRAL SCANNERS. . . . .	3.2-10
3.2.2.1 <u>Landsat-C</u> . . . . .	3.2-10
3.2.2.2 <u>Landsat-D</u> . . . . .	3.2-11
3.2.2.3 <u>Synchronous Earth Observatory Satellite (SEOS)</u> . . . . .	3.2-17
3.2.3 MULTISPECTRAL SCANNER DESIGN CHARACTERISTICS. . . . .	3.2-23
3.2.3.1 <u>Spectral Bands</u> . . . . .	3.2-23
3.2.3.2 <u>Pixel Size and Sampling</u> . . . . .	3.2-31
3.2.3.3 <u>Dynamic Range and Sensitivity</u> . . . . .	3.2-32
3.2.3.4 <u>Relief Displacement and Scan Geometry</u> . . . . .	3.2-35
3.3 <u>MICROWAVE SCATTEROMETERS</u> . . . . .	3.3-1
3.3.1 USES OF FUTURE SCATTEROMETERS. . . . .	3.3-1
3.3.1.1 <u>Sea State Studies</u> . . . . .	3.3-3
3.3.1.2 <u>Ice Studies</u> . . . . .	3.3-5
3.3.1.3 <u>Soil Moisture Studies</u> . . . . .	3.3-7
3.3.1.4 <u>Vegetation Studies</u> . . . . .	3.3-13
3.3.2 MEASUREMENT REQUIREMENTS OF FUTURE SCATTEROMETERS . . . . .	3.3-27
3.3.3 TENTATIVELY ESTABLISHED SCATTEROMETER DESIGN GOALS FOR ONE PARTICULAR APPLICATION . . . . .	3.3-42

Section	Page
3.3.4 SUMMARY . . . . .	3.3-45
3.4 <u>SYNTHETIC APERTURE RADAR (SAR)</u> . . . . .	3.4-1
3.4.1 SEASAT-A SAR . . . . .	3.4-1
3.4.2 SHUTTLE IMAGING RADAR (SIR) . . . . .	3.4-6
3.4.3 SARSAT . . . . .	3.4-10
3.5 <u>MICROWAVE RADIOMETERS</u> . . . . .	3.5-1
3.5.1 INTRODUCTION . . . . .	3.5-1
3.5.2 INSTRUMENT CHARACTERISTICS, ADVANTAGES, DISADVANTAGES, AND APPLICATIONS . . . . .	3.5-1
3.5.3 GROUND BASED RADIOMETER SYSTEMS . . . . .	3.5-4
3.5.4 FUTURE SENSORS AND FUTURE WORK . . . . .	3.5-5
3.5.4.1 <u>Background and Current Trends</u> . . . . .	3.5-5
3.5.4.2 <u>Anticipated Trends</u> . . . . .	3.5-6
3.5.4.3 <u>Potential Problems</u> . . . . .	3.5-9
3.5.4.4 <u>Recommendations for Future Work</u> . . . . .	3.5-11
3.6 <u>VIDICONS</u> . . . . .	3.6-1
3.6.1 LANDSAT-C RETURN BEAM VIDICON (RBV) . . . . .	3.6-1

## Appendix

A. REMOTE SENSING SYSTEMS RECENT, CURRENT AND FUTURE . .	A-1
--	-----

## TABLES

Table		Page
2-1	GENERAL EARTH RESOURCES APPLICATIONS AREAS AND SENSORS MEETING THEIR REQUIREMENTS . . . . .	2-2
2.2.2-1	NIMBUS 4 IRIS WINDOW BRIGHTNESS TEMPERATURE AND THE SST FROM IRIS AND SHIPS. . . . .	2.2.2-19
2.2.2-2	RELATIVE ABSORPTION COEFFICIENT $K(\nu)$ in $(g^{-1} cm^{-2})$ FOR THE THREE WINDOW CHANNELS . . . . .	2.2.2-19
2.3-1	AREA OF COVERAGE AND FIELD-OF-VIEW (FOV) FOR 9 IN. $\times$ 9 IN. FORMAT FRAME CAMERA FOR FOUR ORBITAL ALTITUDES AND SIX FOCAL LENGTHS. . . . .	2.3-8
2.3-2	MAP ACCURACY AND GROUND RESOLUTION REQUIREMENTS FOR COMMONLY-USED MAP SCALES . . . . .	2.3-11
2.5-1	INFORMATION REQUIRED AND PARAMETERS TO MEASURE FOR FOREST MANAGEMENT (REF. 2) . . . . .	2.5-3
2.5-2	FOREST AND GRASSLAND PARAMETERS DERIVED FROM PHOTOINTERPRETATION COMPARED WITH INFORMATION FROM AUTOMATIC ANALYSIS OF MULTISPECTRAL SCANNER DATA . . . . .	2.5-8
2.5-3	OPTIMUM CHANNELS SELECTED FOR AUTOMATIC CLASSIFICATION OF FOREST FEATURES FROM SEVERAL REFERENCES . . . . .	2.5-9
2.9-1	SEASAT SENSOR TECHNIQUES . . . . .	2.9-8
2.9-2	GENERAL OCEANOGRAPHIC SENSOR REQUIREMENTS. . . . .	2.9-9
2.10.2-1	A BRIEF SUMMARY OF SOIL MOISTURE MEASUREMENTS WITH MICROWAVE SENSORS . . . . .	2.10-31
3-1	FUTURE EARTH RESOURCES SATELLITES AND SENSOR SYSTEMS. . . . .	3.1-2
3.1-1	CHARACTERISTICS OF S-190A MULTISPECTRAL CAMERA SYSTEM. . . . .	3.1-4
3.1-2	MULTISPECTRAL CAMERA SYSTEMS . . . . .	3.1-9
3.1-3	FILM FOR AERIAL AND SATELLITE APPLICATIONS . . . . .	3.1-10
3.1-4	FRAME CAMERAS FOR SHUTTLE EVALUATION . . . . .	3.1-13

Table		Page
3.1-5	PANORAMIC CAMERAS FOR EVALUATION. . . . .	3.1-15
3.2-1	AIRCRAFT AND SPACEBORNE MSS DATA COMPARISON . .	3.2-7
3.2-2	LANDSAT-C MSS PERFORMANCE CHARACTERISTICS BANDS 4, 5, 6, AND 7. . . . .	3.2-12
3.2-3	TOP 20 SEOS APPLICATIONS (FROM REF. 3.2.2-4). .	3.2-19
3.2-4	SEOS BANDS AND GENERAL APPLICATIONS AREAS (FROM TABLE 3, REF. 3.2.2-4). . . . .	3.2-21
3.2-5	APPLICATIONS PERFORMANCE RANKINGS OF S-192 BANDS . . . . .	3.2-27
3.2-6	EARTH RESOURCES APPLICATIONS AND VISIBLE-IR MSS REQUIREMENTS - GENERAL SUMMARY. . . . .	3.2-30
3.3-1	PAST AND PRESENT SCATTEROMETERS . . . . .	3.3-2
3.3-2	SENSOR MEASUREMENT REQUIREMENTS FOR REMOTE SENSING OF SURFACE WINDS AND WAVES (REF. 3.3-2). . . . .	3.3-29
3.3-3	SCATTEROMETER PARAMETERS AND CONSTANTS FOR GEOS-C (REF. 3.3-2) . . . . .	3.3-44
3.4-1	FUTURE SPACEBORNE EARTH RESOURCES IMAGING RADARS. . . . .	3.4-3
3.4-2	CAPABILITY OF SEASAT-A SAR IN MEETING USER REQUIREMENTS. . . . .	3.4-4
3.6-1	LANDSAT-C RBV: FUNCTIONAL CONSTANTS SUMMARY . . . . .	3.6-3

## FIGURES

Figure		Page
2.1-1	Remote sensing simulation system . . . . .	2.1-4
2.1-2	The relationship between ERIM growth model, vegetation reflectance model, and yield model. (From Coldwell and Suits) (ref. 2.1-1) . . . .	2.1-8
2.1-3	Physiological yield model. . . . .	2.1-11
2.2.2-1	Comparison of the near infrared solar spectrum with laboratory spectra of various atmospheric gases. . . . .	2.2.2-3
2.2.2-2	Sample histograms of corrected Nimbus HRIR data showing their relation to sea-surface temperature. . . . .	2.2.2-4
2.2.2-3	Normalized reflectance measurements (0.2 $\mu\text{m}$ - 4.0 $\mu\text{m}$ ) for four days over the Atlantic (30-50N, 30-80W) between 15 June and 15 July, 1966 . . . . .	2.2.2-6
2.2.2-4	A plot showing the relative contribution from various heights to the radiance observed in the Nimbus 2 MRIR 6.4 to 6.9 $\mu\text{m}$ channel for a U.S. Standard Atmosphere containing 2.0 cm of precipitable water . . . . .	2.2.2-7
2.2.2-5	Spectral emittance of liquid water and opaque water-drop cloud . . . . .	2.2.2-9
2.2.2-6	Temperature error introduced by clouds in the field of view as a function of the percent of the subsatellite resolution element filled with clouds at 1 km. . . . .	2.2.2-10
2.2.2-7	Departure of Nimbus HRIR brightness temperature from ground and cloud radiating temperature as a function of observed brightness temperature. . . . .	2.2.2-14
2.2.2-8	Spectral radiance in band 1 versus that in band 2 as a function of atmospheric state. . .	2.2.2-17

Figure		Page
2.2.2-9	The deficit as a function of integrated water vapor content. $T_S - T_B = D = 0.066 M + 0.086 M^2$ , for $k_1, k_2 = 0.10, 5.0 \text{ g}^{-1} \text{ cm}^2$ . . .	2.2.2-23
2.2.2-10	Thermal inertia ( $\text{cal/cm}^2/\text{s}^{1/2}$ ) versus density ( $\text{g/cm}^3$ ) for a variety of rock-forming minerals, rocks, and soils . . . . .	2.2.2-26
2.3-1	Area of coverage of Skylab S-190A and S-190B imagery relative to that of conventional aircraft photography (6-in. focal length; 9 in. x 9 in. format; 30,000 ft flying height) . . . .	2.3-6
2.5-1	Spectral differences due to (a) species (ref. 2.5-11) and (b) loss of moisture (ref. 2.5-10). . . . .	2.5-5
2.5-2	Changes in spectral reflectance throughout growing season in <i>Quercus alba</i> : (a) April - May, and (b) June - November from ref. 2.5-11. . . . .	2.5-6
2.5-3	Classification accuracy versus resolution for three classes; softwood, hardwood, and other from three studies: Sadowski, ref. 2.5-26; Kan, ref. 2.5-14, and Thomson, ref. 2.5-19 . . .	2.5-13
2.5-4	Forest/Range Management System, using remote sensing data as an input . . . . .	2.5-16
2.8-1	Optimum resolution requirements for environmental planning surveys (from ref. 2.8-10) . .	2.8-3
2.9-1	Seasat ocean information system. . . . .	2.9-4
2.9-2	Interrelationships between Seasat-A sensors and geophysical variables to be derived. (After John R. Apel). . . . .	2.9-5
2.9-3	Ground track of Seasat-A for 24-hour period. .	2.9-6
2.10-1	Normalized albedo versus average volumetric water content of nine different soil layers having the surface as their upper boundary (IDSO, et al., ref. 2.10-8). . . . .	2.10-4
2.10-2	Red clay soil directional reflectance and polarization for two angles of incidence when wet and dry. (Source incidence $45^\circ$ and $80^\circ$ at a wavelength of $0.52 \mu\text{m}$ ). . . . .	2.10-6

Figure		Page
2.10-3	Polarization versus moisture for six soil types. . . . .	2.10-8
2.10-4	The amplitude of the diurnal surface soil temperature wave on clear day-night periods versus mean daylight volumetric soil water content of four different depth intervals. . .	2.10-10
2.10-5	The maximum value of the surface soil-air temperature differential versus the mean daylight volumetric soil water content of the 0- to 2-cm depth increment (IDSO, et. al., ref. 2.10-11) . . . . .	2.10-11
2.10.2-1	The dielectric relaxation spectrums of water at two temperatures. . . . .	2.10-16
2.10.2-2	The complex dielectric constant of soils as a function of volumetric water content at 10°C . . . . .	2.10-17
2.10.2-3	Plots of 1.55 cm dielectric constants and calculated emissivities for a silty clay loam soil. . . . .	2.10-18
2.10.2-4	Scattering coefficient response as a function of soil moisture for the combination of all three surface roughness profiles . . . . .	2.10-21
2.10.2-5	L-band relative HH return as a function of effective moisture content . . . . .	2.10-23
2.10.2-6	L-band relative HH return as a function of effective moisture content for bare fields in angular ranges: a) 42.8°-47.1°, b) 47.1°-50.7°, c) 50.7°-53.8°, and d) 53.8°-56.8°. . .	2.10-24
2.10.2-7	Plot of 21 cm brightness temperature versus soil moisture for bare fields. . . . .	2.10-27
2.10.2-8	Predictions of P and Q by a radiative transfer model for 2.8-cm emissions at various look angles $\theta_0$ . . . . .	2.10-29
3.1-1	Relative distortion of 6 inch focal length lens in Perkin Elmer Single Lens Multiband Camera . . . . .	3.1-8
3.1-2	Spectral sensitivity of EK SO-289 compared to EK 2424 . . . . .	3.1-12

Figure		Page
3.1-3	Dynamic resolution of S-190A camera system, high contrast target 6.3:1 . . . . .	3.1-17
3.2-1	Earth Resources MSS development, 1965-1980 . . . . .	3.2-3
3.2-2	Spaceborne MSS spectral bands and atmospheric transmission . . . . .	3.2-8
3.2-3	SEOS first priority applications versus spectral bands (derived from table 4, ref. D). . . . .	3.2-22
3.2-4	Landsat-D bands and Michigan study results . . . . .	3.2-24
3.2-5	Pixel size determination . . . . .	3.2-33
3.2-6	Pixel size as a function of field size and number of non-boundary pixels. . . . .	3.2-34
3.2-7	Relief displacement geometry . . . . .	3.2-36
3.2-8	Relief displacement plots. . . . .	3.2-37
3.2-9	Scan geometry effects for rectilinear scanner. . . . .	3.2-39
3.2-10	Conical scanner scan geometry effects. . . . .	3.2-40
3.3-1	Representation of approximate magnitude of backscatter cross sections from ocean at 2-cm to 3-cm radar wavelengths (ref. 3.3-3). . . . .	3.3-4
3.3-2	AAFE Radscat Scatterometer wind direction sensitivity (ref. 3.3-2) . . . . .	3.3-6
3.3-3	Experimental $\sigma^{\circ}$ compared to ice thickness for different incident angles (frequency of 13.3 GHz vertical transmit/vertical receive polarization) (ref. 3.3-6) . . . . .	3.3-8
3.3-4	Average of all the wet and dry fields in the entire test site, Ku-band, Mission 130 . . . . .	3.3-11
3.3-5	Temporal variations of $\sigma^{\circ}$ measured at 8.6 GHz for angles of incidence of (a) 0°, (b) 10°, (c) 40°, and (d) 70° (ref. 3.3-12) . . . . .	3.3-19

Figure		Page
3.3-6	Scattering coefficient $\sigma^\circ$ as a function of incidence angle at (a) 2.75 GHz, (b) 5.25 GHz, and (c) 7.25 GHz. Data set #1, July 16, 1974, (ref. 3.3-15). . . . .	3.3-23
3.3-7	Spectral response of $\sigma^\circ$ at incidence angles of (a) 20° and (b) 50° for data set #1, July 16, 1974, (ref. 3.3-15). . . . .	3.3-24
3.3-8	Simplified block diagram of a microwave scatterometer that uses a narrow-beam antenna (ref. 3.3-2) . . . . .	3.3-33
3.3-9	Plot of $\Delta\sigma^\circ/\sigma$ as a function of $(S/N)_{in}$ for integration times indicated; $\tau_{s-n}$ is assumed equal to $\tau_n$ ; the intermediate frequency bandwidth $B_{if}$ equals 11 kHz and is assumed to be approximately the Doppler spread (ref. 3.3-6) . . . . .	3.3-36
3.3-10	Simplified block diagram of a fan-beam microwave scatterometer (ref. 3.3-2). . . . .	3.3-38
3.3-11	Scatterometer fan beam geometry for GEOS-C . . . . .	3.3-43
3.4-1	Seasat-A sensor coverages. . . . .	3.4-2 <sup>17</sup>
3.4-2	Seasat SAR data management considerations. . .	3.4-5
3.4-3	Basic data flow diagram for the Shuttle Imaging Radar (SIR). . . . .	3.4-7
3.6-1	Landsat return beam vidicon. . . . .	3.6-2
3.6-2	Landsat RBV spectral sensitivity . . . . .	3.6-5
3.6-3	Picture coverage at the Equator with all parameters at nominal values. . . . .	3.6-6

## ABBREVIATIONS AND ACRONYMS

AASIR	Advanced Atmospheric Sounding and Imaging Radiometer (SEOS and SOS)
AMPS	Atmospheric, Magnetospheric and Plasmas in Space (Shuttle Payload)
ASAS	Advanced Sensors and Applications Study
CIR	Coherent Imaging Radar (on SEASAT-A)
CZCS	Coastal Zone Color Scanner (on Numbus-G)
DMAT	Daily Mean Air Temperature
EIFOV	Effective Instantaneous Field-of-View
EOPAP	Earth and Ocean Physics Application Program
EOS	Earth Observational Satellite
EREP	Earth Resources Experiment Package (Skylab)
ERPO	Earth Resources Program Office
ERSS	Earth Resources Survey System
ERTS	Earth Resources Technology Satellite
ESRO	European Space Research Organization
ESSA	Environmental Science Services Administration
GARP	Global Atmospheric Research Program
GESS	Geostationary Environmental Satellite System
GMS	Geostationary Meteorological Satellite
GOES	Geostationary Operational Environmental Satellite
GPS	Ground Processing System
GRD	Ground Resolvable Distance
GSFC	Goddard Space Flight Center
HCMR	Heat Capacity Mapping Radiometer

HDA	High Daily Average
HRIR	High Resolution Infrared Radiometer
HRPI	High Resolution Pointable Imager (on EOS)
Hydrosat	Hydrology Satellite
IGFOV	Instantaneous Geometric Field-of-View
IMC	Image Motion Compensation
IRIS	Infrared Interferometer Spectrometer
IR	Infrared
km	Kilometer
Landsat	Land Satellite
LARS	Laboratory for the Application of Remote Sensing
LEST	Large Earth Survey Telescope (on SEOS)
m	Meter
MASC	Multiplication Plus Additive Signature Correction
mm	Millimeter
METEOSAT	Meteorological Satellite
MRIR	Medium Resolution Infrared Radiometer
MSAS	Microwave Signature Acquisition System
MSS	Multispectral Scanner
NESS	National Environmental Satellite Service
nm	Nanometer ( $10^{-9}$ meter)
NMAS	National Map Accuracy Standards
NOAA	National Oceanographic and Atmospheric Administration
n.mi.	Nautical Mile
PAMIRASAT	Passive Microwave Radar Satellite
RBV	Return Beam Vidicon

ROOSTER	Rank order Optimal Signature Transformation Estimation Routine
SAR	Synthetic Aperture Radar
SARSAT	Synthetic Aperture Radar Satellite
SCARP	Skylab Concentrated Atmospheric Radiation Project
SCAT	Scatterometer
SEASAT	Sea Satellite
SEOPS	Standard Earth Observations Package for Shuttle
SEOS	Synchronous Earth Observatory Satellite
SIR	Shuttle Imaging Radar
SLAR	Side-Looking Airborne Radar
SMMR	Scanning Multifrequency Microwave Radiometer
SMS	Synchronous Meteorological Satellite
SPIR	Space Program Imaging Radar
SR	Scanning Radiometer
SSOS	Severe Storm Observing Satellite
TERSSE	Total Earth Resources System for the Shuttle Era
THIR	Temperature Humidity Infrared Radiometer
TM	Thematic Mapper (on Landsat-D)
TMTWG	Thematic Mapper Technical Working Group (Landsat-D)
TOSS	TERSSE Operational Systems Study
$\mu\text{m}$	Micrometer
VHRR	Very High Resolution Radiometer
VISSR	Visible-Infrared Spin Scan Radiometer (on SMS, GMS)
VTPR	Vertical Temperature Profile Radiometer

## 1. INTRODUCTION

The field of remote sensing from space is entering a whole new era which will see a proliferation of satellite sensor systems tailored to different applications, with more spectral bands, greater resolution and better temporal coverage. Multispectral scanners will continue to advance in development and microwave sensors of all types will find increasing use on future earth resources satellites, along with other new and advanced sensors.

The objective of this report is to discuss and summarize sensor characteristics and requirements for earth resources applications in the Space Shuttle era (1978 on). Accordingly, the report is divided into two main parts. The first discusses the status and anticipated sensor requirements, spectral bands, resolution, etc., for each of the major earth resources application areas. Wherever possible, these different fields of study were assigned to investigators either directly involved in or closely associated with them. The second part discusses the applications-related technical characteristics of sensor systems planned for the Space Shuttle era. These are discussed by sensor type, (e.g., cameras, multispectral scanners, etc.) and not by satellite systems, since the latter often have two or more different sensor types. Someone interested in geology, for example, can first read the geology section and then refer to the appropriate sensor sections without having to know all of the specific future satellite systems for which such sensors are planned. Background information is provided whenever it is felt necessary for the understanding of a sensor's current and anticipated states of development. References and/or bibliographies are given at the end of each section or subsection.

## 2. APPLICATIONS REQUIREMENTS

The major application areas are addressed in this section in alphabetical order (agriculture to soil moisture). Table 2-1 gives the satellite systems by sensor type which can be of use in each of the major application areas. This table shows mostly the primary application-sensor relationships. Some of the applications-sensors requirements are not met by any current or planned satellite sensor. Note that this is particularly true for photographic systems.

TABLE 2-1. — GENERAL EARTH RESOURCES APPLICATIONS AREAS AND SENSORS  
MEETING THEIR REQUIREMENTS

Application Area	Multispectral Scanners			Microwave			Photographic Systems
	Visible	Reflective IR	Thermal IR	Radiometers	Scatterometers	SAR	
Agriculture	Landsat-1, 2, C&D SEOS	Landsat-1, 2, C&D SEOS	Landsat C&D SEOS	Seasat-A	Seasat-A*		
Cartography						Seasat-A Shuttle SAR	S-190B equiv. or better
Wetlands or Coastal Studies	Landsat-1, 2, C&D SMS/GOES		Landsat C&D SMS/GOES		Seasat-A*	Seasat-A Sarsat Shuttle SAR	
Damage Assess.	SEOS	SEOS	SEOS		Sarsat	Seasat-A Sarsat Shuttle SAR	S-190B equiv. or better
Forestry	Landsat C&D	Landsat C&D	Landsat C&D		Seasat-A*	Seasat-A Sarsat Shuttle SAR	S-190B equiv. or better
Geology	Landsat-1, 2, C&D	Landsat C&D SEOS		Seasat-A		Seasat-A Sarsat Shuttle SAR	S-190B equiv. or better
Land-Use	Landsat-1, 2, C&D	Landsat-1, 2, C&D					S-190B equiv. or better
Oceanography & Hydrology	Landsat C&D Seasat-A SMS/GOES		Landsat C&D Seasat-A SMS/GOES	Seasat-A	Seasat-A	Seasat-A Sarsat Shuttle SAR	
Soil Moisture			Landsat C&D	Seasat-A*			

\*Potential or limited utility.

## 2.1 AGRICULTURE

Knowledge of the distribution and amount of agricultural production has taken on a new significance in the world during the last few years. The rapidly increasing population in the under-developed countries and the evidences of climate change have put a new urgency on increasing the world food supply. It is also most important that a more accurate and timely knowledge of the world-wide crop production be known to all involved in order that the transfer of food crops from the exporting nations to the importing nations can be efficiently and profitably managed.

Crop production is determined by two basic factors: crop acreage and crop yield. A crop type and its acreage amount is generally influenced by the local climate, soil, cultural tradition, government policy and economic considerations. The crop yield for a given variety is basically determined by the soil fertility, the weather sequence, cropping practices, and technology level. These factors determine for each crop and variety a certain yield per acre for optimum conditions. This optimum yield, however, is normally reduced because of unfavorable weather, infestations of insects, or diseases such as rusts or viruses. Unfavorable weather may be the lack of adequate rainfall, too much rainfall, unseasonable cold or warmth, strong desiccating winds and hail.

In general, both acreage and yield can be determined, in principle, by remote sensing techniques that involve analysis of the emission or reflection of radiation from the vegetation biomass. The character of this radiation depends on crop characteristics such as the amount of canopy cover, leaf angle or projected area, and the crop attributes such as color and vigor. These characteristics, in turn, are the result of agricultural practices, plant physiological processes and environmental inputs. The radiation received at the sensor, however, is modified by its passage through the atmosphere. This modification varies

depending principally on the aerosol, water vapor and ozone content of the atmosphere, as well as the solar and viewing angles. These aspects of remote sensing along with others related to the theory, principles and technology of remote sensing have been reviewed recently in depth by Reeves, et al., in the manual of Remote Sensing (ref. 2.1-15). This manual covers the state of the art into 1974. Additional information on the application, techniques and results of using earth resources survey data can be found in recent NASA technical memoranda (ref. 2.1-12, 2.1-13).

A survey or summary of some of the more recent developments can be found in this report. In particular, this section on agriculture discusses primarily the yield aspects of crops.

#### 2.1.1 DETERMINING FUTURE REQUIREMENTS

One approach to determining requirements for new sensors and observation systems is the modified Delphi approach based on user needs. An example of such an approach is summarized in Section 3.2. Another approach is to perform a systematic top-down analysis. This approach starts with general objectives and determines needed information and supporting research from which data and sensor requirements can be formulated. A third approach involves a system analysis and simulation. Such an approach has been suggested recently by Landgrebe (ref. 2.1-9) in discussing the requirements for future developments of remote sensing technology.

Landgrebe emphasizes that a generalized systems perspective is needed and discusses needed improvements related to (1) the scene, (2) the sensor system, and (3) the data processing system. In particular, he discusses among other aspects, the following: 1) significantly increasing knowledge of the variability of the scene, (2) more sophisticated sensor systems which consider incorporating improvements balancing spectral, spatial and temporal aspects of the scene, (3) more complex data processing

algorithms incorporating spatial and temporal as well as other features, (4) increased use of ancillary data, (5) more knowledgeable use of man in the analyses process, and (6) a more suitable array of output products to match the user needs.

This systems approach can be implemented in a manner that will allow a specific or desired requirement to be determined. One technique is to develop a system simulation model similar to that outlined in figure 2.1-1. Inspection of the schematic information flow diagram in figure 2.1-1 indicates that the overall relationship between the crop and field characteristics and the user outputs can be represented by a series of mathematical submodels. Each submodel represents a key function of the subsystem and uses the output of another submodel along with data on the model parameters to determine characteristic values for the system. The overall objective of the system model is to be able to simulate realistically the sensitivity or accuracy of the output of the subsystems or the overall system (i.e., crop production) to changing input data. As an example, such a simulation system can be used to determine the pacing technology, desired trade-offs and necessary ancillary data.

The following subsections discuss aspects of the scene that are pertinent to the overall system performance.

### 2.1.2 CROP IDENTIFICATION AND ACREAGE ESTIMATION

The standard method for acreage estimation of a crop type uses multispectral scanner (MSS) data and involves examining the spectral character of each picture element (pixel) and classifying the crop, as to type. The pixels of the different crops are then summed to give the acreage. The accuracy depends on the ability of the algorithm to correctly classify each pixel; the precision depends on the pixel size relative to the average field size.

2.1-4

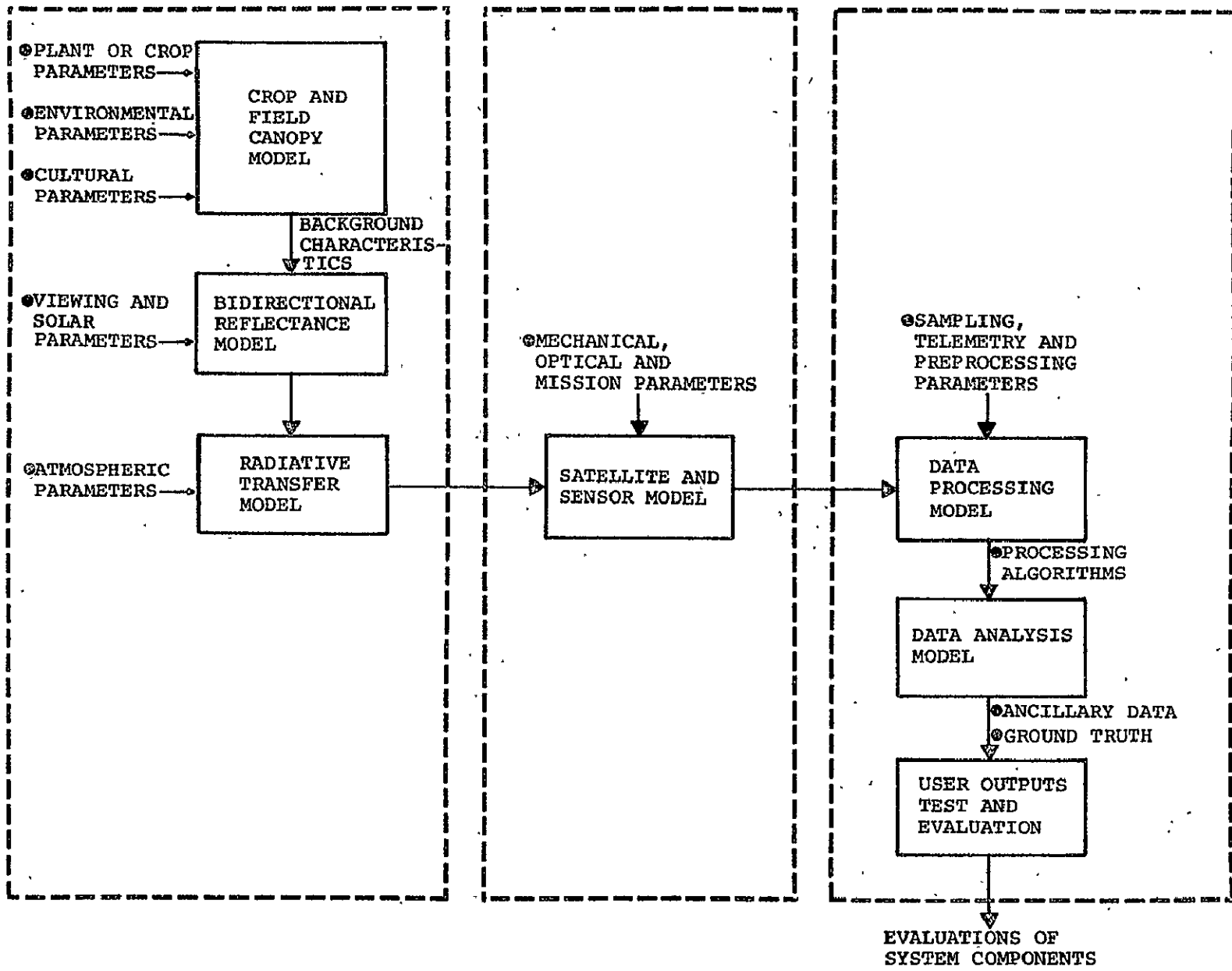


Figure 2.1-1 - Remote sensing simulation system.

In practice, the crop type and acreage determination utilizes spatial, spectral, and temporal features of the imagery, but with varying emphasis, depending on the cropping practice of the region under investigation. Fundamentally, the spectral aspect of the imagery holds the key position in determining the crop type. However, since the spectral characteristics of the scene change with the maturity or stage of the crop, temporal aspects can be important in determining or separating the crop types. The spatial aspects are particularly important in separating agricultural from non-agricultural land use. The stages of the crops are determined from so-called "crop calendars" which give the date when a certain percentage (for example, 50%) of the fields of a specific crop are expected to attain a certain stage.

Improved acreage estimates involve two aspects: (1) better discrimination of the crop type, and (2) better resolution to detect the smaller fields and discriminate field boundaries. The former problem could be improved by implementing the systems approach shown in figure 2.1-1. In particular, models need to be developed that consider the reflectance from an incomplete crop cover which involves varying percentages of vegetation cover over varying soil characteristics. The crop may be suffering from stress and the soil from varying degrees of moisture. Developments along these lines have been reported by Richardson, et al., (ref. 2.1-16), Kristof and Baumgardner (ref. 2.1-8), and Kanemasu (ref. 2.1-7). The other problem of better resolution involves improved optics, improved detectors and lower flight altitudes.

### 2.1.3 YIELD ESTIMATION

Yield estimates can be determined by three approaches: (1) using meteorological data, (2) using the condition of the vegetation, and (3) a combination of both. These estimates, which are based on models, are then combined with the acreage estimates to get the total production. At present, yield estimates are primarily

made from surface meteorological data, although some use is made of meteorological satellite data. A desirable goal is to be able to determine the yield primarily from satellite data. The three yield estimation approaches are discussed below.

#### 2.1.3.1 Yield Estimates from Environmental Data

Yield estimates of crops have traditionally been determined from regression analysis of field data relating yield to environmental parameters. These studies have resulted in a variety of mathematical expressions including linear, curvilinear, factorial, and exponential types. More recently there is a trend to functions that represent the plant growth.

The general problem of yield estimation and a summary of many of these studies are presented by McQuig (ref. 2.1-11). A more recent discussion of the yield problem for cereal crops is provided by Rickman et al., (ref. 2.1-17) and Grafius and Barnard (ref. 2.1-4). The use of meteorological satellite data for estimating spring wheat yields has been discussed in a report by Earth Satellite Corporation (ref. 2.1-3). This latter report has analyzed the sensitivity of the yield estimates to variations in the accuracy of the meteorological input as well as some of the inadequacy of these data.

Current operational meteorological satellites generally determine cloud cover and surface temperatures. However, techniques are being developed to estimate areal precipitation amounts and distribution on a daily basis. Evapotranspiration and soil moisture can be estimated from a combination of satellite and surface data such as maximum and minimum air and soil temperatures. Air temperature, particularly the daily maximum and minimum, are best determined at present from standard surface data. Surface soil temperatures can be estimated from thermal

infrared measurements. Passive microwave measurements have the potential to assist in determining soil moisture changes. The potential of satellite measurements for determining soil moisture has been summarized by Idso, Jackson and Reginato (ref. 2.1-6). The characteristics and potential of the current meteorological satellites in general have been summarized by Hildreth (ref. 2.1-5).

#### 2.1.3.2 Yield Estimation from Vegetation Conditions

This approach to yield estimation has been developed in order to use remote sensing from spacecraft to determine the yield. Such an approach is desirable in order to reduce reliance on surface meteorological data which requires extensive processing and calculation or may not be present in enough detail to provide accurate or precise estimates.

The need to reduce reliance on surface meteorological data has stimulated models that relate spectral and temporal reflectance values from a vegetation cover to yield. The details of such an approach have been reported by Coldwell and Suits (ref. 2.1-1). A schematic outline of their approach is depicted in figure 2.1-2. The basic scheme is to correlate a grain yield parameter with a parameter representing the bidirectional spectral reflectance from the vegetation canopy. In particular, their studies indicate that a possible parameter is the green projected leaf area index. The peak value or the temporal character of this value after heading was found to correlate well with yield. To determine the value of this parameter, they found that a ratio of intensities of Landsat channels 6 or 7 to 5 (i.e., near IR to red) to be most useful. The success of their approach depends on the timing and frequency of the images. In addition, much further work needs to be done to make the models more useful. A basic question concerns the relationship of the plant yield

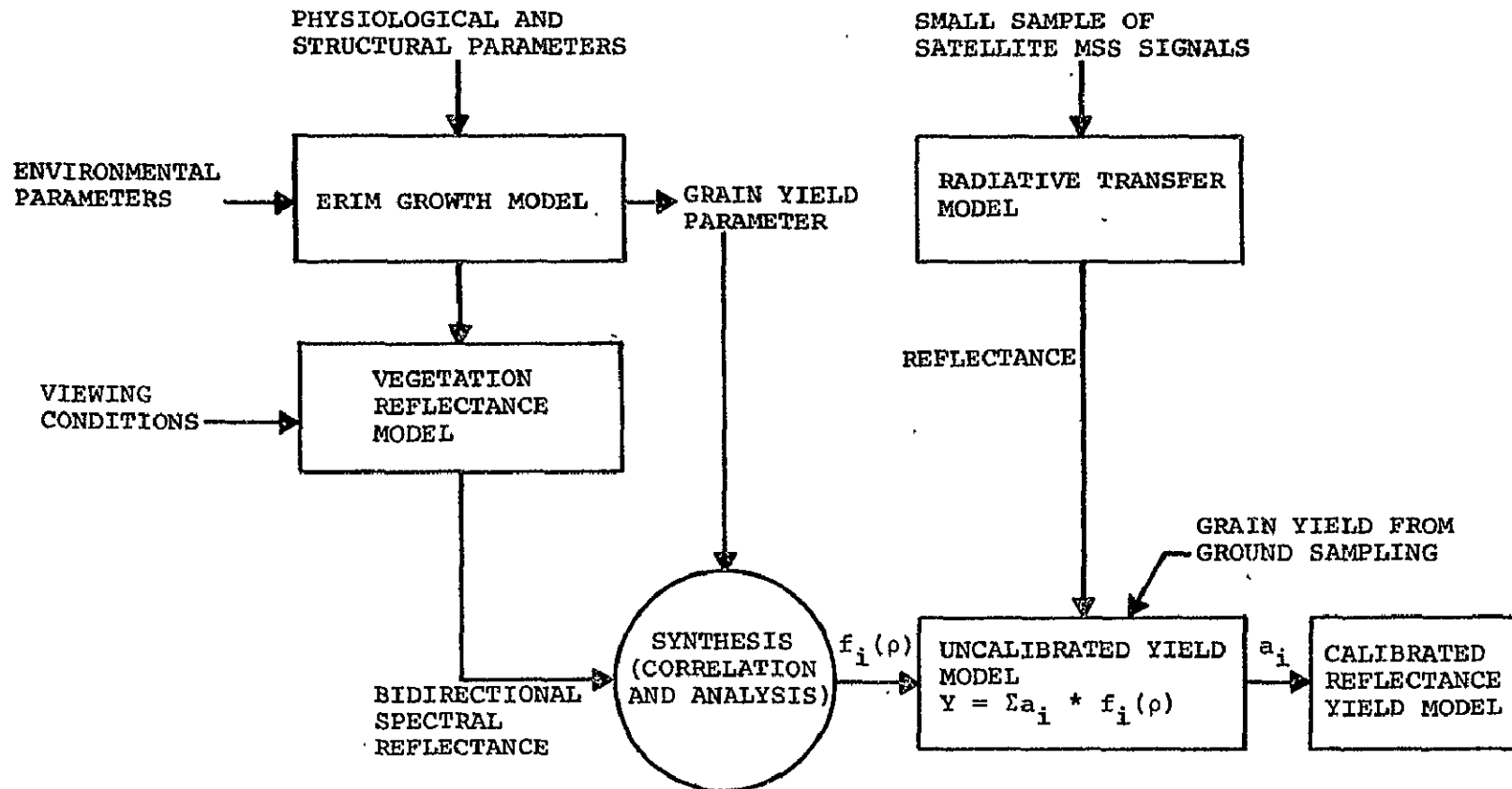


Figure 2.1-2 - The relationship between ERIM growth model, vegetation reflectance model, and yield model.  
(From Coldwell and Suits (ref. 2.1-1):

to the overall plant characteristics and growth patterns. This problem has been discussed by Grafius and Barnard (2.1-4).

A similar method using the ratio of the intensities of channels was suggested by Kanemasu (ref. 2.1-7). He showed that the ratio of channels 4 to 5 (i.e., green to red) provides information about the viewed surfaces regardless of the crop. Kanemasu found that the ratio closely followed crop growth and development and that the ratio may be an indicator of soils and soil moisture early in the season and of crop maturity late in the season. He found the ratio to be better than the near infrared reflectance because solar elevation variation causes the latter reflectance values to change. The ratio appears to eliminate this effect. He also suggested that the ratio may follow percentage cover more closely than leaf area index. This conclusion has also been supported by Grafius and Barnard (ref. 2.1-4). Kanemasu (ref. 2.1-7) also found that the ratio may serve as an indicator of physiological stress. Although the biomass production has been shown to be proportional to actual plant transpiration or evapotranspiration of plant-ground system, the yield is more complicated and is primarily related to the plant water stress in the different development stages.

Neghassi et. al., (ref. 2.1-14) have proposed a linear function that relates yield to fall dry matter production (tillers/m<sup>2</sup>), final dry matter weight and the number of days that certain weather values are exceeded. The essential feature is the temporal aspect of the vegetation amount, i.e., leaf area index (L.A.I.) or leaf area duration (L.A.D.). This corresponds to the approach of Coldwell and Suits (ref. 2.1-1).

The above relationships have been supported by Kristof and Baumgardner (ref. 2.1-8), using 13-channel multispectral scanner data taken by aircraft. They found that the ratio of a visible

band (0.58  $\mu\text{m}$  to 0.62  $\mu\text{m}$ ) to an infrared band (0.86  $\mu\text{m}$  to 1.00  $\mu\text{m}$ ) most useful for the study of the seasonal variation of vegetation cover.

#### 2.1.3.3 Modeling and Satellite Data

Another approach to determining yields from satellite data is to use a combination of multispectral (e.g., Landsat) and meteorological satellite data as inputs to physiological yield models. The difference between this approach and the previous approach is the use of the satellite data. In the earlier approach of section 2.1.3.2, the satellite multispectral data is correlated directly with yield. In this alternate approach, the satellite data are used as inputs to a physiological yield model (fig. 2.1-3). At present, such physiological yield models are not available although they are in the process of being developed. The approach to this type of modeling is typified by Splinter (ref. 2.1-18), McKinion et. al., (ref. 2.1-10) and Curry et. al., (ref. 2.1-2).

#### 2.1.3.4 Summary

In summary, improvements in remote sensing systems for agriculture production involve, in general, three aspects: (1) improvements in understanding and modeling the scene, (2) more sophisticated sensor systems, and (3) more elaborate data processing and analysis techniques and algorithms.

New, sophisticated sensor systems imply better optical systems, better detectors, additional and narrower spectral bands, and more frequent repetition. Improved models include better understanding of vegetation physiological processes, better overall models of the scene variability, field experimentation, and extensive simulation and verification. Improvements in the algorithms should take into account the spatial and temporal features of the scene, ratio values from different spectral bands, more use of ancillary data, and more informal human participation.

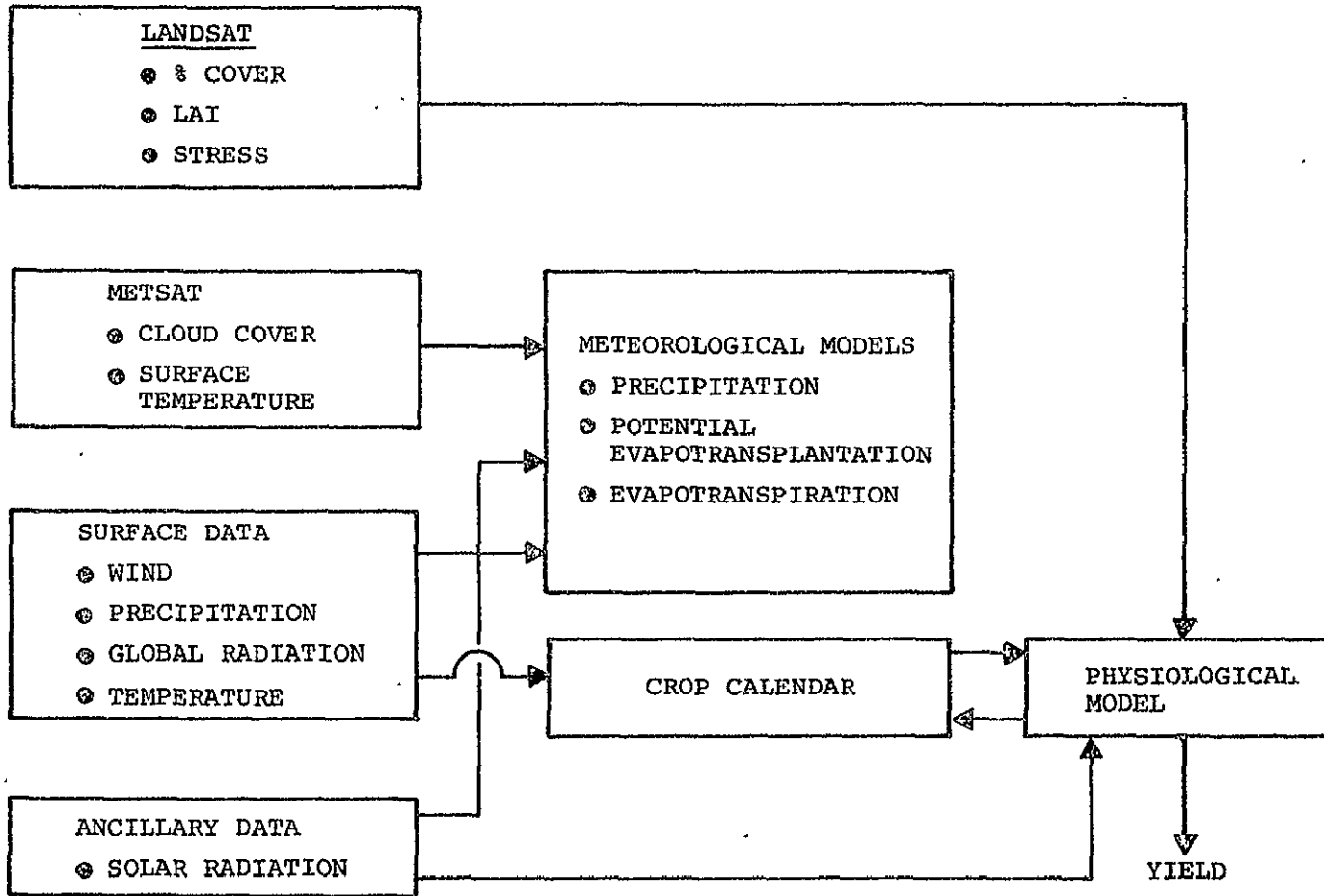


Figure 2.1-3. - Physiological yield model.

The optimum combination of the desired improvements in the sub-systems can be evaluated by developing an overall simulation systems model and determining the effects on the output of various possible changes.

## REFERENCES

- 2.1-1 Coldwell, J. E.; and Suits, G. H.: Yield Prediction by Analysis of Multispectral Scanner Data, Final Report. NASA CR-ERIM 109600-17-F, May 1975.
- 2.1-2 Curry, B. R.; Baker, C. H.; and Streeter, J. G.: SOYMOD1: A Dynamic Simulator of Soybean Growth and Development. Trans. ASAE, 963-974, 1975.
- 2.1.3 Earth Satellite Corporation: Earthsat Spring Wheat Yield System Test 1975, Final Report. E/S No. 1052, April 1976.
- 2.1.4 Grafius, J. E.; and Barnard, J.: Leaf Canopy as Related to Yield in Barley. Agron. J. 68, 398-402, 1976.
- 2.1.5 Hildreth, W. W.: Meteorological Satellite Data and LACIE. Tech. Memo. LEC-7159, Dec. 1975.
- 2.1-6 Idso, S. B.; Jackson, R. D.; and Reginato, R. J.: Detection of Soil Moisture by Remote Surveillance, American Scientist, 63, 549-557, 1975.
- 2.1-7 Kanemasu, E. T.: Seasonal Canopy Reflectance Patterns of Wheat, Sorghum and Soybean. Remote Sensing of Environment 3, 43-47, 1974.
- 2.1-8 Kristof, S. J.; and Baumgardner, M. F.: Changes of Multispectral Soil Patterns with Increasing Crop Canopy. Agron. J., 67, 317-321, 1975.
- 2.1-9 Langrebe, D.: Remote Sensing Technology - A Look to the Future. In LARS Symposium, (PA7 - PA18). Proceedings, Machine Processing of Remotely Sensed Data, IEEE Catalog No. 76CH 1103-1 MPRSD, June 29 - July, 1976.
- 2.1-10 McKinion, J. M.; Jones, J. W.; and Hesketh, J. D.: A System of Growth Equations for the Continuous Simulation of Plant Growth. Trans. ASAE, 975-979, 1975.
- 2.1-11 McQuigg, J. D.: Economic Impacts of Weather Variability. Atmospheric Science Dept., U. of Missouri - Columbia, Aug. 1975.
- 2.1.12 The ERTS-1 Investigation, V. 1, NASA TMX-58117, Nov. 1974.
- 2.1-13 Proceedings of the NASA Earth Resources Survey Symposium, Houston, Texas, NASA TMX-58168, June 1975.

- 2.1-14 Neghassi, H. M.; Heermann, D. F.; and Smika, D. E.:  
Wheat Yield Models with Limited Soil Water. Trans. ASAE,  
549-553, 1975.
- 2.1-15 Reeves, R. G.; Anson, A.; and Landen, D.; Editors:  
Manual of Remote Sensing, Volumes I and II. Am. Soc.  
of Photogrammetry, Falls Church, Virginia, 1975.
- 2.1-16 Richardson, A. J.; Wiegand, C. L.; Gausman, H. W.;  
Cuellar, J. A.; and Gerbermann, A. H.: Plant, Soil and  
Shadow Reflectance Components of Row Crops, Photogram-  
metric Eng. & Remote Sensing, 1401-1407, 1975.
- 2.1-17 Rickman, R. W.; Ramig, R. E.; and Allmaras, R. R.:  
Modeling Dry Matter Accumulation in Dryland Winter  
Wheat. Agron. J., 67, 283-289, 1975.
- 2.1-18 Splinter, W. E.: Modelling of Plant Growth for Yield  
Prediction. Ag. Meteor. 14, 243-253, 1974.

## 2.2 ATMOSPHERIC CORRECTIONS

The atmosphere presents a radiation variable in the measurement path of visible and infrared satellite borne instruments utilized in earth resource applications. For limited area sampling and classification of earth resource subjects in the visible and near infrared wavelengths, where ground truth information is available, the atmosphere can be simply "normalized" out to a first approximation. However, for classification of unknown subjects further along satellite track, signature extension becomes difficult if information about the atmosphere is not available. As an example, the effects of atmospheric water vapor were computer simulated during automatic classification of Landsat-1 data in a study by D. E. Pitts, et al. (ref. 2.2-1). It was found that water vapor primarily affects band 7 (.8 to 1.1 $\mu$ m) and significantly reduces classification accuracies if medium or high level horizontal gradients exist between training fields and the rest of the scene. J. Potter and M. Shelton (ref. 2.2-2) have studied the effects of sun angle and atmospheric haze on automatic classification of ERTS-1 data. It was determined that relatively small changes in sun angle and haze level can substantially reduce classification accuracies.

The ability to detect and monitor streams, lakes, and coastal pollution, including thermal pollution and oil spills, is a desirable feature of future visible and infrared earth resource satellites. Instruments aboard present weather satellites measure ocean surface temperatures and perform atmospheric soundings for prediction of temperature and water vapor profiles. Surface temperature measurements by these weather satellites are generally made on a large synoptic basis and are primarily concerned with ocean and atmospheric physics. Their resolutions would not be compatible with those desirable for studying smaller water bodies adjacent to or surrounded by land. However, the techniques developed in the data reduction from these satellites are of great

interest since they are applicable to any satellite borne temperature measuring and/or sounding devices.

Atmospheric corrections are a necessity for improving the ability of satellite borne visible and infrared instruments to perform earth resource measurements, e.g., signature extension. In some past experiments, including those on Skylab, these atmospheric measurements have been made by ground-based instruments which have not always been taken at the same time and at the same location as those from the satellite instrument. This has limited the accuracy of the experiments and has severely limited the amount of data which could be atmospherically corrected.

All this background information points to the need for simultaneous collection along the same optical path of both atmospheric and earth resource data. Then near real time atmospheric correction would be a possibility. With these desired features in mind, a study of applicable satellite techniques in the visible-near IR and thermal spectral regions will be presented.

## REFERENCES

- 2.2-1 Pitts, D. E.; McAllum, W. E.; Dillinger, A. E.: The Effect of Atmospheric Water Vapor and Automatic Classification of ERTS Data. Proceedings of the Ninth International Symposium on Remote Sensing of Environment, April 15-19, 1974, pp. 483-497.
- 2.2-2 Potter, J.; Shelton, M.: Effect of Atmospheric Haze and Sun Angle on Automatic Classification of ERTS-1 Data. Proceedings of the Ninth International Symposium on Remote Sensing of Environment, April 15-19, 1974, pp. 865-874.

## 2.2.1 ATMOSPHERIC CORRECTIONS IN THE VISIBLE AND NEAR IR

### 2.2.1.1 Introduction

This section discusses the correction of visible and near infrared data for atmospheric effects. The main effect to correct for is that produced by haze in the atmosphere. Thin clouds produce a similar effect and most correction methods can correct for either thin clouds or haze. However, haze is usually more uniform and therefore easier to treat. In the following, both cases are referred to as "haze."

The methods that can be used to correct for haze are of two general types; those that involve the determination of the haze levels present in the scene, and those that do not. These are treated separately below.

### 2.2.1.2 Methods Involving the Determination of Haze Levels

The determination of haze levels involves two steps. The first step consists of determining the haze level present; the second consists of correcting the data.

#### 1. Determination of Haze Levels:

The following paragraph describes four methods for determining haze levels.

- a. Solar Radiometer - The solar radiometer provides a direct method of measuring haze levels from the ground. The Earth Observations Division of JSC has produced about 30 of these instruments and has used them to determine haze levels for given areas at the time of Landsat passes for the purpose of checking haze correction methods. Also, a commercially available instrument, the "Eppley Photometer", is used to determine haze levels by various investigators around the country. The problem with

solar radiometer measurements is that it is very difficult to get the large amount of data necessary to correct a significant amount of satellite data.

Recently, Potter and Mendlowitz (ref: 2.2.1-1) have suggested two methods which show promise of being able to do this. These are the "Minimum Value Method" and the "Channel Correlation Method."

- b. The Minimum Value Method -- This method is based on the observation that for a given Landsat data set, the minimum values in channel 1 (MSS 4) for each line are generally very similar. These minimum values correspond to dark targets which appear to be wooded areas. A haze layer over such a target will increase its brightness, so these minimum values should contain information about the haze level. The study described in reference 2.2.1-1 found a substantial correlation between the minimum values and the haze level measured with a solar radiometer.
- c. The Channel Correlation Method -- This method is based on the well known fact that the data from the first two Landsat channels (MSS 3 and MSS 5) are highly correlated. The method consists of making a scatter plot of the data in the MSS 4-MSS 5 plane and fitting a regression line to it. Since haze affects MSS 4 more than MSS 5, one expects the slope and intercept of this line to be an indicator of the haze level present. In the study described in reference 2.2.1-1, it was indeed found that there was a high correlation between the measured haze levels and the y-intercept of the regression line. Thus, in principle one can determine the haze level (approximately) by making such a scatter plot and determining the intercept.

d. Future Method - The LIDAR scanner is probably the best solution to this problem of haze determination. In principle, a LIDAR scanner on a satellite could determine the haze level at every point in a scene. At present, there are several aircraft-mounted LIDAR scanners, but it will probably be several years before the state of the art is sufficiently advanced to mount these instruments in space satellites.

2. Correcting the Data After the Haze Level Has Been Determined:

Once the haze level has been determined, the data can be corrected. To do this, one uses an atmospheric model which relates the observed radiance to target reflectance and haze level (ref. 2.2.1-2). There are several ways the corrections can be applied. In one way, the data can be transformed so that it represents target reflectance rather than observed radiance, i.e., such that it is independent of haze level. Another method is to transform various data sets so that they each correspond to some "standard" haze level. When the application involves automatic classification of the data, one often prefers to correct the "signatures" used in classification rather than the data itself. This is discussed in references 2.2.1-3 and 2.2.1-4.

2.2.1.3 Methods Not Involving the Determination of Haze Levels

Several methods have been developed and used for classifying agricultural scenes. These utilize three general types of algorithms: (1) data transformations, (2) maximum likelihood methods, and (3) cluster transformations.

1. Data Transformations:

These methods involve transforming the data by taking linear combinations (or other functions) of the various channels of

data. For example one can form a new channel  $R^{(ij)}$  which is ratio of the data in channels  $i$  and  $j$ , i.e.,

$$R^{(ij)} = \frac{R^{(i)}}{R^{(j)}}$$

where  $R^{(i)}$  is the data for channel  $i$  and  $R^{(j)}$  is the data for channel  $j$ . This transformation is discussed in reference 2.2.1-5. The usefulness of these transformations is attributed to the fact that the transformed data is less sensitive to changes in the haze level than the original data.

The ideal transformation would provide data that was invariant with respect to the haze level. The disadvantage of these transformations is that the transformed data generally contains less information than the original channels. A good discussion of this approach is contained in reference 2.2.1-5. A new transformation which is based on an accurate atmospheric model and which shows considerable promise is being developed by Dr. J. Potter (ref. 2.2.1-6).

## 2. Maximum Likelihood Methods:

These methods have been developed for signature extension in agricultural scenes. It is assumed that there is a uniform haze difference between the training and test areas, and the training and test areas have the same classes present. The general method is described in reference 2.2.1-7 and a specific application is described in reference 2.2.1-8.

## 3. Cluster Transformations:

These methods involve clustering the data from the training and recognition areas and then finding the transformation which best takes the one set of clusters into the other. This transformation is caused by the difference in haze level between the two areas. However, in principle this method and

the maximum likelihood method described above also corrects for changes caused by other factors (such as a change in sun angle). Algorithms of this type include Multiplicative and Additive Signature Correction (MASC) (ref. 2.2.1-5) and Rank Order Optimal Signature Transformation Estimation Routine (ROOSTER) (ref. 2.2.1-9).

## REFERENCES

- 2.2.1-1 Potter, J. F.; and Mendlowitz, M: On the Determination of Haze Levels from Landsat Data. Proceedings of the Tenth International Symposium on Remote Sensing of Environment, 1975.
- 2.2.1-2 Potter, J. F.: The PREPS-ROTAR Atmospheric Correction Program - LEC Tech Memorandum. In Preparation.
- 2.2.1-3 Potter, J. F.; and Shelton, M.: Effect of Atmospheric Haze and Sun Angle on Automatic Classification of ERTS-1 Data. Proceedings of the Ninth International Symposium on Remote Sensing of Environment, 1974, p. 865.
- 2.2.1-4 Potter, J. F.: Haze and Sun Angle Effects on Automatic Classification of Satellite Data-Simulation and Correction. Proceedings of the Society of Photo-Optical Instrumentation Engineers, Vol 51, 1974, p. 73.
- 2.2.1-5 Henderson, R. G.; Thomas, G. S.; and Nalepka, R. F.: Methods of Extending Signatures and Training Without Ground Information. Environmental Research Institute of Michigan report, NASA CR-ERIM 109600-16-F, May 1975.
- 2.2.1-6 Potter, J. F. In preparation.
- 2.2.1-7 Duda, R. O.; and Hart, P. E.: Pattern Classification and Scene Analysis. Wiley, 1973.
- 2.2.1-8 Levy, S. A.; Minter, T. C.; and Thadani, S. G.: Maximum Likelihood Estimation of Signature Transformation. LEC Tech Memo LEC-4357, 1975.
- 2.2.1-9 Finley, D.: A New Algorithm to Correct MSS Signatures For Atmospheric Effects. LEC 6246, June 1975.

## 2.2.2 INFRARED ATMOSPHERIC CORRECTIONS

In the earth resources community, the requirements for infrared atmospheric corrections and soundings have not been as well defined as those in the visible regions. This is primarily because the major portion of satellite-received data has been from Landsat I and Landsat II and has been confined to the visible and near IR. Both S-191 and S-192 on Skylab had infrared bands and spectrums. However, those principal investigators reporting on atmospheric corrections utilized ground based radiosondes and measurements in reduction of Skylab data.

The primary contributor to atmospheric correction in the mid and far infrared, for purposes of application, has been reports and research on weather instruments flown by NOAA and the Goddard Space Flight Center (GSFC). This work has been aimed at ocean surface temperature measurements and atmospheric temperature and water vapor profile measurements. Both of these areas are interesting with regard to future aims of earth resources work. Water vapor profiles could be used in atmospheric corrections from the near IR through the thermal regions, and water temperature monitoring could be an important capability in the monitoring and study of streams, lakes, and coastal zones.

Additional work at JSC has utilized the Very High Resolution Radiometer (VHRR) flown on NOAA-2, 3, 4 to thermally map areas of Texas and Mexico for study of screwworm infestation. In the area of geology, thermal inertia mapping of the Arabian Peninsula has been accomplished utilizing the Nimbus satellite. This mapping has demonstrated the feasibility of discriminating a variety of geologic materials. Thermal inertia mapping may also be important for soil moisture determination as discussed in section 2.10.1.3. Researchers at Colorado State University have also reported on the comparison of atmospheric models in predicting land surface temperatures.

### 2.2.2.1 Correction Techniques for Sea Surface Temperature Determination

The major discussions in the literature about the infrared area have covered the thermal windows at 3.5  $\mu\text{m}$  to 4.0  $\mu\text{m}$ , 8  $\mu\text{m}$  to 9  $\mu\text{m}$ , and 10  $\mu\text{m}$  to 12  $\mu\text{m}$ . Constituents of the atmosphere which create these windows and surrounding absorption bands are shown in figure 2.2.2-1 (ref. 2.2.2-1). Additionally, the 6.7  $\mu\text{m}$  centered water absorption band has been utilized for identifying high altitude cirrus clouds and ice crystals. The 3.5  $\mu\text{m}$  to 4.0  $\mu\text{m}$  region was used in several early Nimbus satellite instruments for sea surface temperature measurements, but has generally been abandoned as a primary thermal channel because of susceptibility to reflected sunlight. The primary corrections required in surface temperature measurements are:

- A correction for eliminating pixels containing visible cloud cover and the relatively "invisible" high altitude cirrus.
- A final correction for water vapor absorption and emissivity in the 10  $\mu\text{m}$  to 12  $\mu\text{m}$  atmospheric window which sometimes utilizes other more absorptive windows through ratioing techniques.

These corrections will be discussed in the following sections.

#### 2.2.2.1.1 Cloud Discrimination

On several of the early Nimbus spacecraft, the instantaneous field-of-view (IFOV) of the scanning infrared instruments was so great\* that pixels containing cloud cover were the rule rather than the exception. For this reason, several statistical techniques were developed to pick only those pixels containing no cloud cover. La Violette and Chabot (ref. 2.2.2-2) proposed

---

\*The Medium Resolution Infrared Radiometer (MRIR) on Nimbus 2 and 3 had an instantaneous spot size at nadir of 55 kilometers.

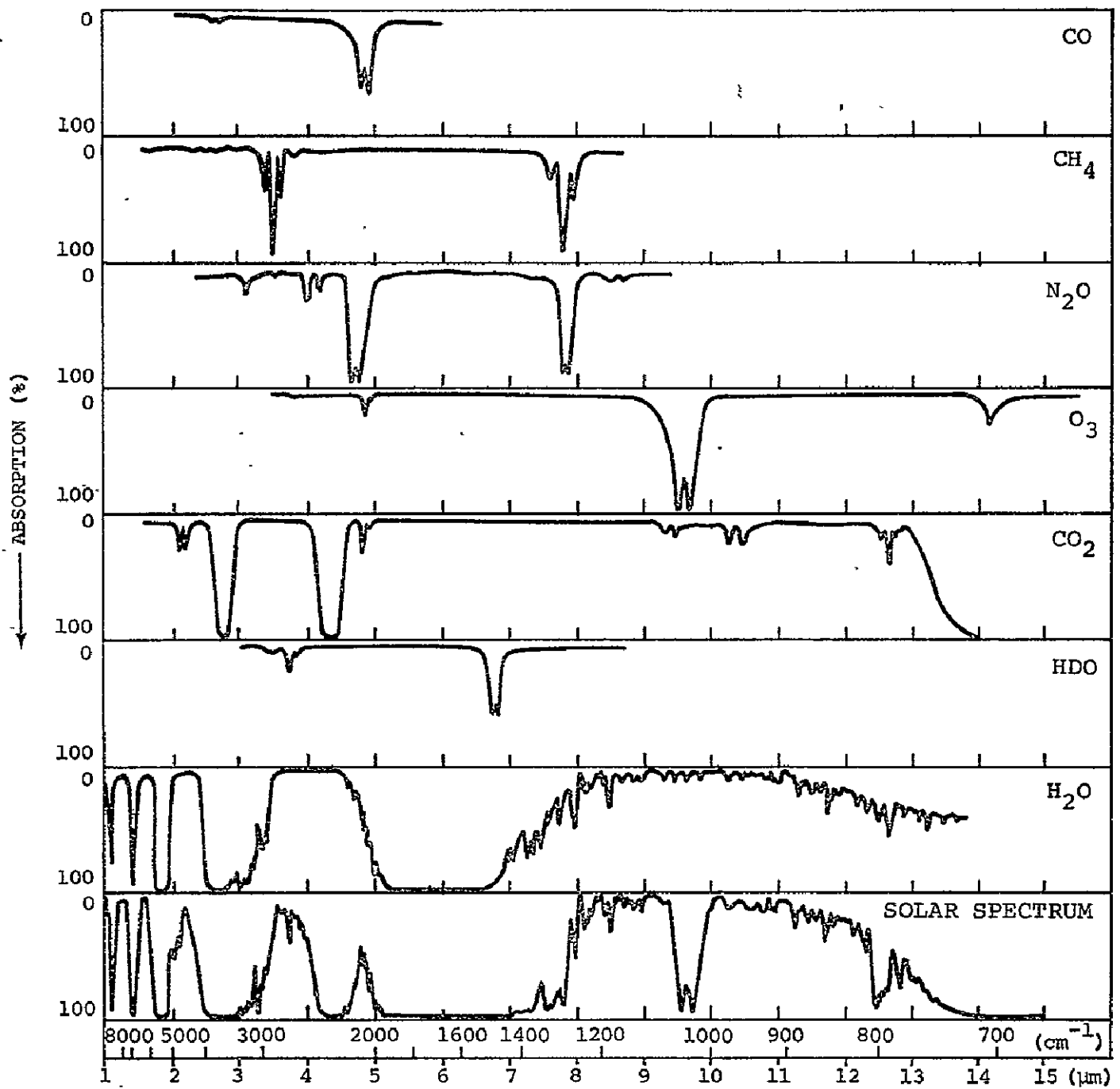


Figure 2.2.2-1. — Comparison of the near infrared solar spectrum with laboratory spectra of various atmospheric gases.

a method, called High Daily Average (HDA), for eliminating clouds from the measurements by compositing five days of overflights of an ocean area and selecting only the highest values in their measurements (cloud temperatures were generally cooler than water temperatures).

Smith, et al., (ref. 2.2.2-3) developed more objective statistical techniques to determine clear areas from cloudy ones. The reliability of this technique depended upon the number of composite cloud-free observations. Radiation data were obtained from the 3.8  $\mu\text{m}$  centered band on the High Resolution Infrared Radiometer (HRIR) flown on Nimbus 2 and 3. Typical temperature histograms of pixels containing cloudy and clear ocean areas within a  $2.5^\circ \times 2.5^\circ$  longitude/latitude grid pattern (approximately 1000 measurements) are shown in figure 2.2.2-2. The standard error,  $\sigma$ , for the MRIR is  $1.5^\circ\text{K}$  and the dispersion is

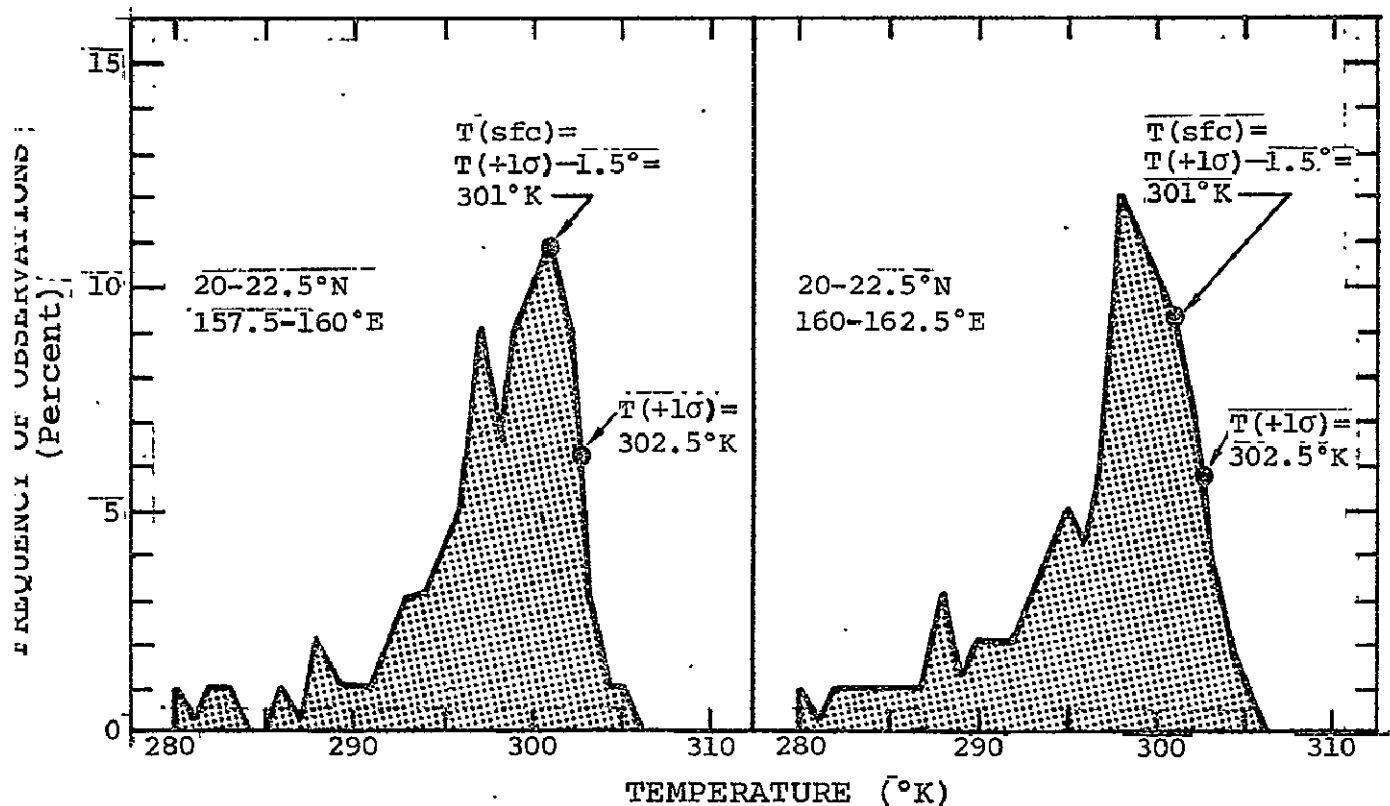


Figure 2.2.2-2.— Sample histograms of corrected Nimbus HRIR data showing their relation to sea-surface temperature.

Gaussian in nature when viewing a constant source. Smith theorized that the low temperature side of the curve was contaminated with clouds and that the high temperature or down side of the curve, because of its sharpness, was part of the Gaussian instrument response curve viewing a constant, clear sea surface target. By selecting the position of maximum slope on the downside, the  $+1 \sigma$  position was determined on the instrument Gaussian curve. In subtracting  $1.5^\circ\text{K}$  from the corresponding temperature position, Smith et al., was able to recalculate the sea surface temperature mean. This method, after atmospheric correction, showed rms differences of only  $1.7^\circ\text{K}$  from ship observations. A computer procedure was developed by Leese, et al., (ref. 2.2.2-4) which incorporated the objective techniques of Smith to process scanning radiometer (SR) data obtained from the NOAA-2 and 3 satellites.

Shenk and Salmonson (ref. 2.2.2-5) developed a multispectral technique utilizing two channels from the Medium Resolution Infrared Radiometer (MRIR) on Nimbus-2 to discriminate against cloud cover. The approach basically consisted of establishing thresholds for the  $.2 \mu\text{m}$  to  $.4 \mu\text{m}$  reflectance channel and the  $6.4 \mu\text{m}$  to  $6.9 \mu\text{m}$  water vapor channel which indicated whether a concurrent observation in the  $11 \mu\text{m}$  to  $12 \mu\text{m}$  region was cloud free.

In the  $.2 \mu\text{m}$  to  $.4 \mu\text{m}$  reflectance band, the reflectance from a cloud-no cloud ocean surface was normalized by the expression:

$$\bar{r} = \frac{\pi \bar{N}}{\bar{H}^* \cos \phi} \quad (1)$$

where

$\bar{r}$  = normalized reflectance

$\bar{N}$  = effective radiance

$\bar{H}^*$  = effective solar constant

$\phi$  = solar zenith angle

A histogram of the measurements taken from four days in a one-month period over an area encompassed by latitudes 30°N-50°N and longitudes 30°W-80°W are shown in figure 2.2.2-3.

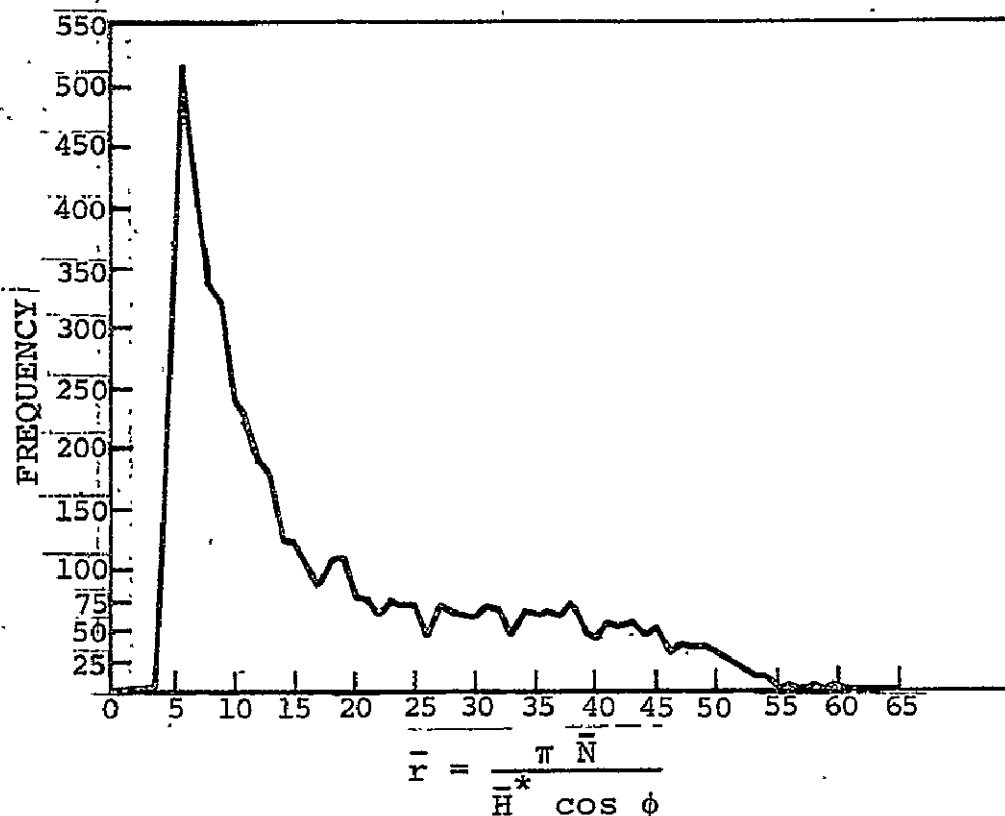


Figure 2.2.2-3.— Normalized reflectance measurements (0.2 $\mu$ m-4.0 $\mu$ m) for four days over the Atlantic. (30-50N, 30-80W) between 15 June and 15 July 1966.

A similar technique as utilized by Smith et al., (ref. 2.2.2-3) was applied to the data to determine cloud-no cloud thresholds. This was positioned at a distance  $\Delta \bar{r}$  on the high reflectance side of the frequency peak. The magnitude of  $\Delta \bar{r}$  was empirically set equal to the difference between the lowest observed reflectance and the reflectance corresponding to the frequency peak. Since there are no reliable  $\bar{r}$  values below 3 and the frequency peak is at  $\bar{r} = 6$ , then reflectance cutoff was placed at  $\bar{r} = 9$ .  $\Delta \bar{r}$  on the low side of the frequency peak is assumed to be instrument noise, sea surface glitter, and other minor factors.

Emission in the 6.4  $\mu\text{m}$  to 6.9  $\mu\text{m}$  band for an atmosphere containing 2.0 cm of precipitable water vapor is shown in figure 2.2.2-4.

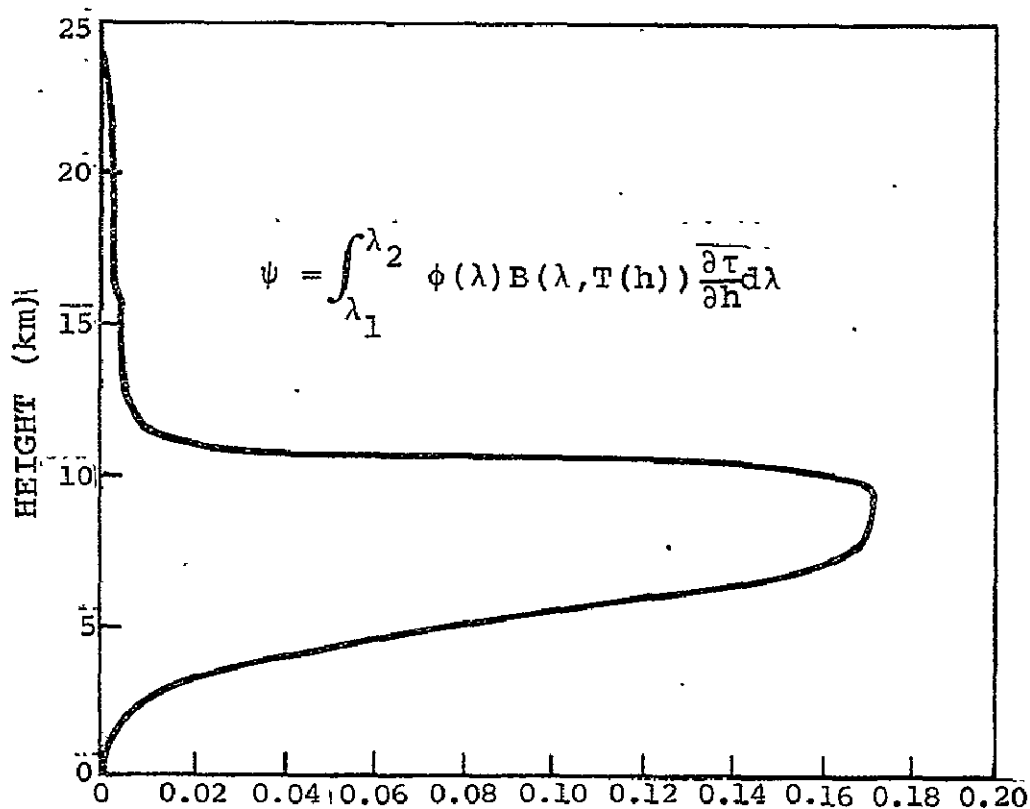


Figure 2.2.2-4.— A plot showing the relative contribution from various heights to the radiance observed in the Nimbus 2 MRIR 6.4 to 6.9  $\mu\text{m}$  channel for a U.S. Standard Atmosphere containing 2.0 cm of precipitable water.

A weighting function of the form

$$\psi = \int_{\lambda_1}^{\lambda_2} \phi(\lambda) \beta[\lambda, T(h)] \frac{\partial \tau(\lambda, h)}{\partial h} d\lambda \quad (2)$$

was utilized to determine the level at which radiation was emanating. The terms are defined as follows:

$\phi(\lambda)$  = spectral response

$\beta[\lambda, T(h)]$  = Planck radiance

$\partial \tau(\lambda, h) / \partial h$  = derivative of transmittance with height

$\lambda$  = wavelength

$T(h)$  = vertical temperature profile.

From figure 2.2.2-4, which shows 2.0 cm of precipitable water vapor, the major portion of water vapor emitted radiation comes from below 11 km, which is slightly below the level of cirrus clouds. In general, the less upper level water vapor, the lower level the sensed energy, and hence, the warmer temperature measured at the sensor.

A frequency distribution was also developed for the 6.4  $\mu\text{m}$  to 6.9  $\mu\text{m}$  thermal data and thresholds were established by two separate criteria. One was developed by setting the threshold at 1 $\sigma$  on the warm side of the mean and another consisted of establishing the threshold at the 70 percent point of the cumulative frequency distribution of the temperature observations.

Anding, et al., (ref. 2.2.2-6) noticed that differences existed in certain spectral intervals between the emissivity of opaque water-drop clouds and water surfaces. The maximum difference occurs at 5.0  $\mu\text{m}$  as shown in figure 2.2.2-5, which suggests that in the absence of an intervening atmosphere, a two-band measurement (5.0  $\mu\text{m}$  and 11.0  $\mu\text{m}$ ) would provide all the

information necessary to estimate fractional cloud cover. Unfortunately, due to the effects of the atmosphere, a third band is necessary in this analysis. From theoretical considerations, the centers of the bands chosen for discriminating against cloud cover and detecting sea surface temperatures were 4.9  $\mu\text{m}$ , 9.1  $\mu\text{m}$ , and 11.0  $\mu\text{m}$ .

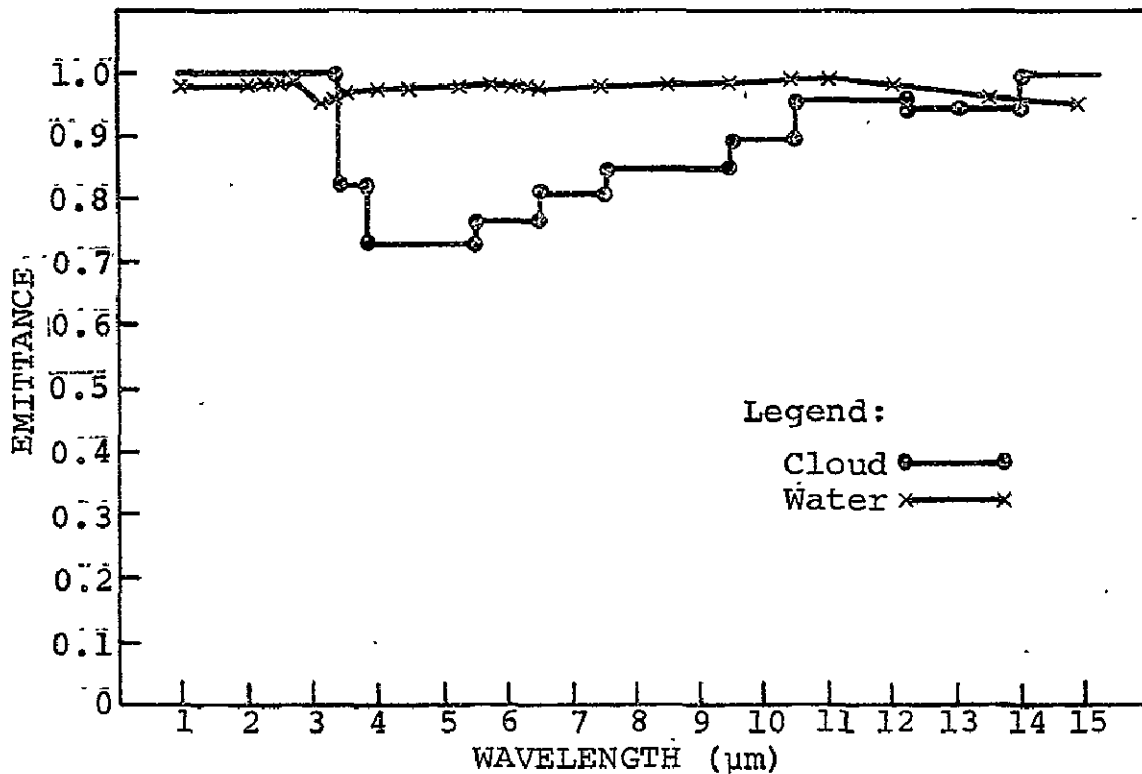


Figure 2.2.2-5.— Spectral emittance of liquid water and opaque water-drop cloud.

In attempting to make radiometric measurements of land or sea surface, the effects of cloud cover including that of the "nearly invisible" cirrus ice clouds should be taken into account. In a theoretical study by Maul and Sidran (ref. 2.2.2-7), the effects of fractional cloud cover in ocean surface temperature measurements are demonstrated and are shown in figure 2.2.2-6.

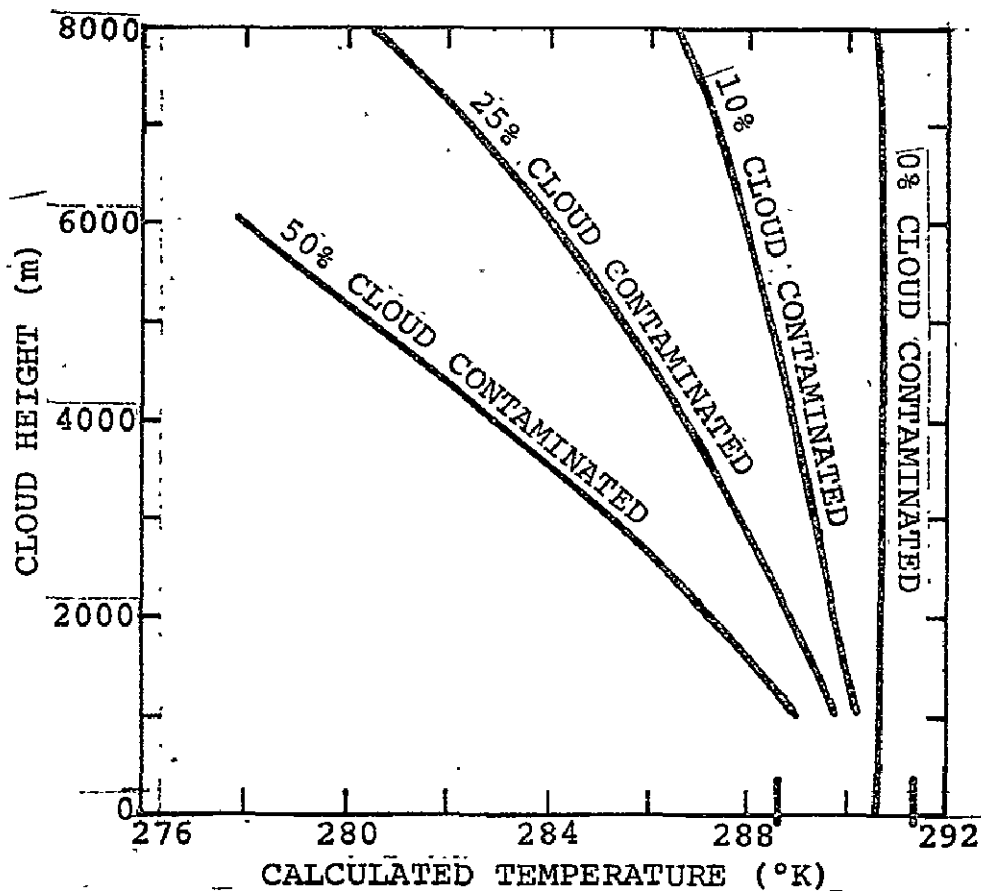


Figure 2.2.2-6.- Temperature error introduced by clouds in the field-of-view as a function of the percent of the subsatellite resolution element filled with clouds at 1 km. (Results are those obtained by averaging several calculations from an atmospheric model whose inputs were five hypothetical sea surface temperatures equally spaced in 2° K increments from 295.2° K to 303.2° K. The bounds of the *calculated* sea surface temperatures are indicated by the dark tic marks along the abscissa.)

This study concerned the NOAA 1 and 2 scanning radiometer (SR) with bands at 0.5  $\mu\text{m}$  to 0.7  $\mu\text{m}$  and 10.5  $\mu\text{m}$  to 12.5  $\mu\text{m}$ . The 0.5  $\mu\text{m}$  to 0.7  $\mu\text{m}$  band is adequate for detecting tropospheric clouds, but may not be adequate for detecting high cirrus.

A band at 6.4  $\mu\text{m}$  to 6.9  $\mu\text{m}$  would be the most desirable for this function and should be seriously considered for all future scanners, performing surface temperature measurements where extended area and time compositing is not possible. Failing to detect and correct for high cirrus can cause errors as great as 2°K to 3°K according to G. Maul (ref. 2.2.2-8).

D. E. Pitts (ref. 2.2.2-9), in a final report on severe storm environments developed from Skylab data, measured several Oklahoma lake and reservoir surface temperatures for calibration purposes. Differences between S-191 measured temperatures and lake/reservoir bucket temperatures were around 5°K to 12°K. Only 4.5°K of this difference could be accounted for through atmospheric absorption and emission data. However, it appeared from S-190 photography that overhead high cirrus were prevalent throughout the measurement area and were causing the considerable discrepancy between spacecraft and ground measurements.

All the foregoing surveys of cloud correction techniques have important implications for future spaceborne scanners designed for earth resources. Some of these implications are as follows:

- Cloud discrimination is a necessity in surface temperature determination in the infrared.
- Automated techniques are available for cloud discrimination.
- A visible channel will discriminate against most tropospheric clouds and should be utilized in all surface temperature determinations.
- Where large area and time compositing is not possible (as with most earth resources subjects), a channel centered at 6.7  $\mu\text{m}$  is highly desirable to further discriminate against high altitude cirrus and water vapor.

### 2.2.2.1.2 Final Corrections in the Atmospheric Window(s)

Even for cloud-free ocean surfaces, deficits exist between satellite measured temperature in the 10.5  $\mu\text{m}$  to 12.5  $\mu\text{m}$  region and the actual sea surface temperatures. According to Cogan and Willand (ref. 2.2.2-10), this is caused by water vapor continuum, carbon dioxide, aerosols, and ozone. Calculations taken from McClatchey, et al., (ref. 2.2.2-11) give deficits of  $< 1^\circ\text{K}$  for ozone and  $0.1^\circ\text{K}$  to  $0.2^\circ\text{K}$  for carbon dioxide. Both of these deficits are relatively small when compared to the water vapor continuum. Aerosols may not be as small where hazy conditions exist as those close to industrial sites. McClatchey (ref. 2.2.2-11) and Shelby (ref. 2.2.2-12) suggested that aerosol extinction contributes  $0.1^\circ\text{K}$  to  $0.2^\circ\text{K}$  for a very clear atmosphere and about  $0.5^\circ\text{K}$  for a hazy atmosphere with values as high as  $1.0^\circ\text{K}$  possible under extremely hazy conditions. Generally, over the ocean, aerosol conditions are not bothersome and are ignored along with ozone and carbon dioxide in the 10.5  $\mu\text{m}$  to 12.5  $\mu\text{m}$  band. This is usually valid in view of the inaccuracies in developing ground truth such as that from ship measurements, radiosonde data, and atmospheric profile data.

There are two general methods by which the water vapor continuum in the 10.5  $\mu\text{m}$  to 12.5  $\mu\text{m}$  region are corrected for in sea surface temperature determinations:

1. Linear or non-linear regression techniques where sea surface temperature predictions are based (1) upon best statistical fits to actual surface temperature measurements or (2) on inputs from tables developed from atmospheric models.
2. Direct atmospheric model correction calculations whose inputs are one of the following: (1) best guess atmosphere, (2) ground released radiosonde data or (3) atmospheric sounder measurements.

Calculations of atmospheric corrections based on models solve the radiative transfer equation. This general equation describing radiance at the top of the atmosphere can be written for a non-scattering atmosphere as follows:

$$\begin{aligned}
 I_{\nu} = & e_{\nu} B_{\nu}(T_0) \tau_{\nu}(0, P_0) \\
 & - \int_0^{P_0} B_{\nu}(T_p) \frac{d\tau_{\nu}(0, P)}{dp} dp \\
 & + (1 - e_{\nu}) \int_{P_0}^0 B_{\nu}(T_p) \tau_{\nu}(0, P_0) \frac{d\tau_{\nu}(P_0, P)}{dp} dp
 \end{aligned} \tag{3}$$

where

$I_{\nu}$  = measured radiance at wave-number  $\nu$

$e_{\nu}$  = emissivity of surface of earth at  $\nu$

$B_{\nu}(T)$  = Planck blackbody radiance at  $\nu$

$T_p$  = temperature of air at level where pressure is  $P$

$T_0$  = temperature of surface of earth

$\tau_{\nu}(a, b)$  = transmission of atmosphere between pressure levels  $a$  and  $b$ .

There are several numerical integration methods by which this equation can be handled in atmospheric correction. These are discussed by La Rocca (ref. 2.2.2-14) in an excellent summary article written in 1975. The methods discussed involve either exact line structure or use band models from artificially created line structure. Techniques discussed include (1) line-by-line method, (2) band model calculations, (3) empirical methods using band model considerations, and (4) multiparameter analytical methods. In addition, a discussion is made on the effects of scattering in a real atmosphere.

Earlier studies by Smith, et al., (ref. 2.2.2-3) developed a linear regression technique on Nimbus High Resolution Infrared Radiometer (HRIR) data where the thermal band was centered at 3.8  $\mu\text{m}$ . The departure of measured versus actual sea surface temperature was plotted for different model atmospheres which are shown in figure 2.2.2-7.

It was found that the best fit for zenith angles less than  $\pm 60^\circ$  could be expressed as follows:

$$\Delta T = \left[ \alpha_0 + \alpha_1 \left( \frac{\theta}{60^\circ} \right) \alpha_2 \right] \ln \left( \frac{100^\circ}{310^\circ - T_B} \right) \quad (4)$$

( $210^\circ\text{K} \leq T_B \leq 300^\circ\text{K}$  and  $\theta \leq 60^\circ$ )

where  $\alpha_0 = 1.13$ ,  $\alpha_1 = 0.82$ ,  $\alpha_2 = 2.48$ ,  $T_B$  is the observed brightness temperature in degrees absolute, and  $\theta$  is the local zenith angle of measurement.

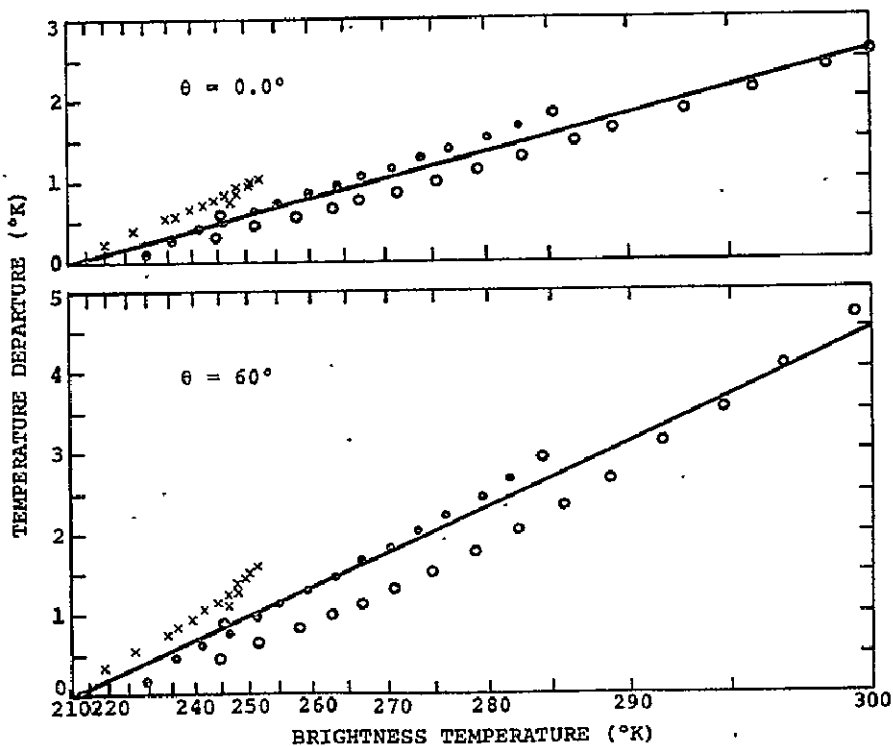


Figure 2.2.2-7.- Departure of Nimbus HRIR brightness temperature from ground and cloud radiating temperature as a function of "observed" brightness temperature. (The crosses, dots, and open circles pertain to the polar, midlatitude, and tropical model atmospheres, respectively.)

In comparing a large number of MRIR measurements to shipboard sea surface measurements, it was estimated that relative accuracies of this technique were better than 1°K.

Shenk and Salmonson (ref. 2.2.2-5) utilized three bands of the MRIR on Nimbus 2 in developing a linear regression technique to determine sea surface temperatures. The bands utilized were 0.2  $\mu\text{m}$  to .4  $\mu\text{m}$ , 6.4  $\mu\text{m}$  to 6.9  $\mu\text{m}$ , and 10  $\mu\text{m}$  to 11  $\mu\text{m}$ . A statistical summary was made of many satellite observations and the corresponding shipboard surface temperature measurements. A step-wise multiple regression technique was empirically applied to correct the observed window equivalent blackbody temperatures for the effects of the atmosphere. The best fits for different latitudes were determined by the following equations:

$$\begin{aligned} T_{ss} = & -75.48538 + 1.23200T_2 + 0.04416\gamma T_1 \\ & + 0.48997\gamma \bar{r} [31-43N] \end{aligned} \quad (5)$$

$$\begin{aligned} T_{ss} = & 44.00232 + 0.83610T_2 + 0.03208\gamma T_1 \\ & + 0.35678\bar{r} [31-37N] \end{aligned} \quad (6)$$

$$\begin{aligned} T_{ss} = & 55.79179 + 1.17053T_2 + 0.03261\gamma T_1 \\ & + 0.58844\gamma \bar{r} [37-43N] \end{aligned} \quad (7)$$

where

$T_{ss}$  = actual sea surface temperature

$T_1$  = apparent blackbody temperature of sea surface as measured from the 6.4  $\mu\text{m}$  to 6.9  $\mu\text{m}$  channel

$T_2$  = same as  $T_1$  except for 10  $\mu\text{m}$  to 11  $\mu\text{m}$  channel

$\gamma = \sec \theta$ , where  $\theta$  is the zenith angle

$\bar{r}$  = normalized reflectance in the 0.2  $\mu\text{m}$  to 0.4  $\mu\text{m}$  channel as defined in equation (1).

Accuracies are claimed by this technique to be in the order of 1°K to 1.5°K.

A multispectral approach utilizing band ratioing was developed by Anding and Kauth (ref. 2.2.2-15). This method has been further developed by McMillin (ref. 2.2.2-16) and Prabhakara, et al., (ref. 2.2.2-17)\*. The Anding and Kauth technique as developed requires no direct information about the atmosphere (except that the field-of-view of the sampling instrument is cloud free). This technique involves ratioing two or more water vapor bands of differing absorptive characteristics within infrared window(s). A linear regression technique is then applied to determine the relationship of measurements of the two or more wavelengths and sea surface temperatures. An example of these relationships from several model atmospheres are shown in figure 2.2.2-8.

---

\*A similar band ratioing technique is possible in determining precipitable water vapor in the optical path of a scanning instrument, if the temperature of the water target is known. D. E. Pitts of JSC has investigated a method which consists of determining the total precipitable water vapor along the S-192 optical path. This technique involves ratioing of either band 7 (.78  $\mu\text{m}$ -.88  $\mu\text{m}$ ) or band 8 (.98  $\mu\text{m}$ -1.08  $\mu\text{m}$ ), which are atmospheric windows, to band 9 (1.09  $\mu\text{m}$ -1.19  $\mu\text{m}$ ), a water vapor absorption band. According to D. E. Pitts, preliminary results of this technique have not been encouraging.

A similar technique was also recommended by C. L. Korb (ref. 2.2.2-18) in 1969 on the JSC 24-band multispectral aircraft scanner. The bands picked for ratioing were band 24 (1.06  $\mu\text{m}$ -1.10  $\mu\text{m}$ ) and band 23 (1.12  $\mu\text{m}$ -1.16  $\mu\text{m}$ ). Unfortunately, no further work on this recommendation has been reported. In retrospect, if this technique had been attempted, there may have been some instrument sensitivity difficulty in band 24. This band utilizes a silicon detector and is located at the edge of the silicon response curve. S-191 used a silicon detector and a large amount of scatter was noted in its output data in the 1.05  $\mu\text{m}$ -1.10  $\mu\text{m}$  band as compared to other wavelengths (ref. 2.2.2-19).

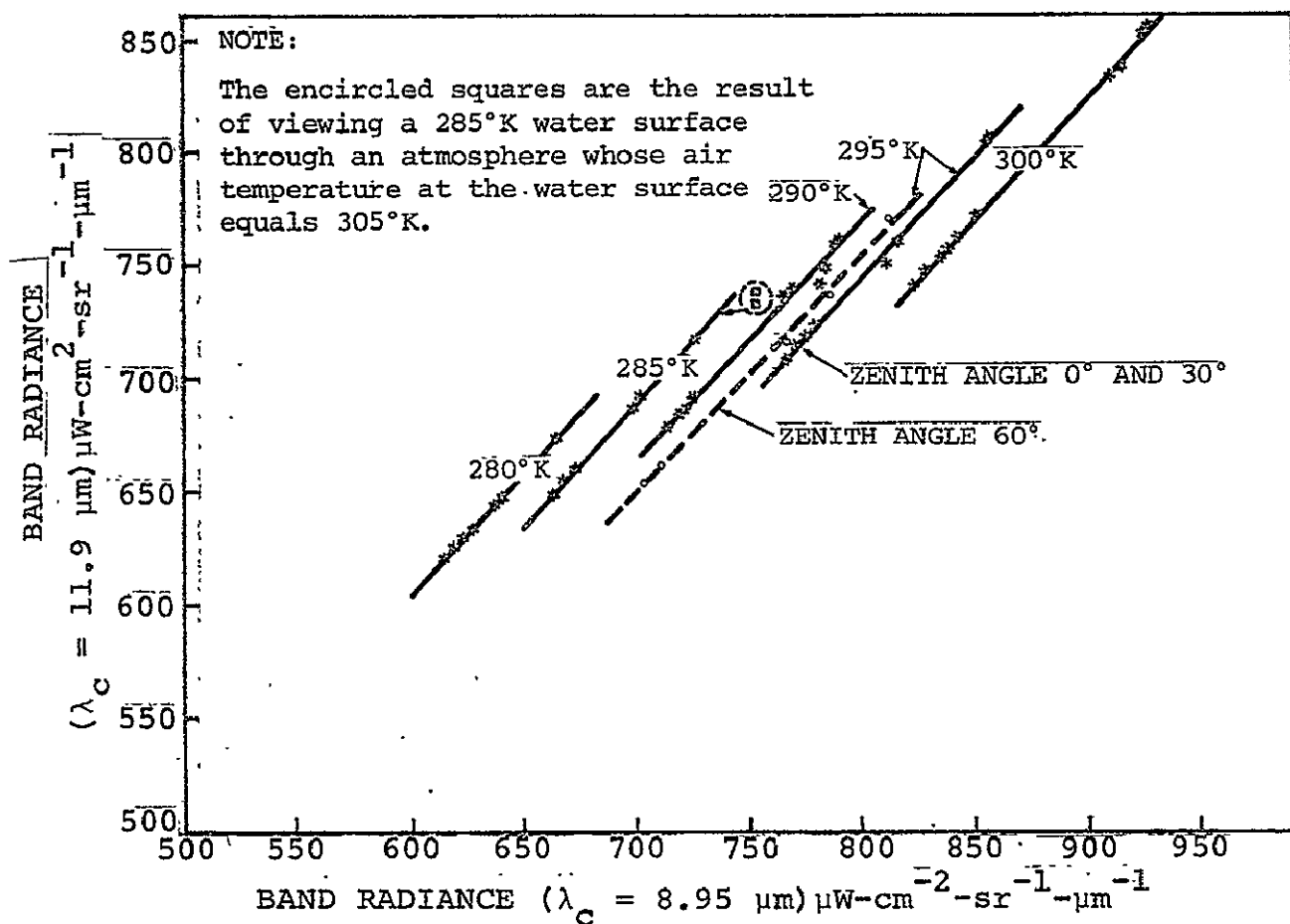


Figure 2.2.2-8.— Spectral radiance in band 1 versus that in band 2 as a function of atmospheric state.

A similar technique was developed by Saunders (ref. 2.2.2-20) utilizing two look angles with airborne scanner data. Two things are important to the accuracy of the two spectral band method: (1) the proper choice of bands for ratioing within the infrared window(s) and (2) an accurate model of the atmosphere. The accuracy of Anding and Kauth's earlier work (ref. 2.2.2-15) suffered from the use of simulated atmospheric measurements to select wavelengths. They found wavelengths 10.96  $\mu\text{m}$  and 9.19  $\mu\text{m}$  as the best ratio combination. Maul and Sidran (ref. 2.2.2-21) repeated Anding and Kauth's calculations utilizing a different model and found 10.96  $\mu\text{m}$  and 8.60  $\mu\text{m}$  to be the best wavelengths. In addition, the original Anding and Kauth model did not account for the added absorption of water

vapor in tropical atmospheres. A component proportional to the partial pressure of water vapor (ref. 2.2.2-22 and ref. 2.2.2-23) is necessary to develop a proper correction. Anding and Kauth (ref. 2.2.2-24) developed a revised absorption model which contained this component. However, because of the added water vapor, their standard error increased from 0.15°K to 1.59°K.

Prabhakara, et al., (ref. 2.2.2-25) further investigated the two or more band technique utilizing the Infrared Interferometer Spectrometer (IRIS) on Nimbus 3 and 4 in the 11  $\mu\text{m}$  to 13  $\mu\text{m}$  region. The IRIS is a non-imaging device capable of high spectral resolution and longer dwell times (for improved signal-to-noise ratios) than scanners. Three windows from 775 to 960  $\text{cm}^{-1}$  (12.9  $\mu\text{m}$  to 10.5  $\mu\text{m}$ ) were utilized in the analysis.

By several assumptions made on the radiation transfer equation, Prabhakara, et al., developed the following approximation:

$$T(\nu) \cong T_s - \beta K(\nu) \quad (8)$$

where

$T(\nu)$  = the apparent temperature at frequency  $\nu$

$T_s$  = sea surface temperature

$K(\nu)$  = absorption coefficient at frequency  $\nu$

$\beta$  = constant for a given atmosphere

A sample of eight clear sky spectra were selected where shipboard sea surface temperatures (SST's) and the IRIS on Nimbus 4 data were available. By comparing these data as in table 2.2.2-1 (where  $T_1$ ,  $T_2$ ,  $T_3$  are the apparent temperatures at frequencies 775 to 831  $\text{cm}^{-1}$ , 831 to 887  $\text{cm}^{-1}$ , and 887 to 960  $\text{cm}^{-1}$ , respectively) to shipboard data, a set of absorptive coefficients,  $K(\nu)$ , were developed. These are shown in table 2.2.2-2.

TABLE 2.2.2-1. -- NIMBUS 4 IRIS WINDOW BRIGHTNESS TEMPERATURE  
AND THE SST FROM IRIS AND SHIPS

Spectrum	Lat.	Long.	T <sub>1</sub>	T <sub>2</sub>	T <sub>3</sub>	T <sub>IRIS</sub>	T <sub>ship</sub>
1	41.0°N	62.5°W	272.9	275.2	276.8	281.2	281.0
2	36.6°N	60.9°W	284.5	286.9	287.9	292.0	290.5
3	11.0°N	53.5°W	287.8	291.7	293.4	300.1	300.5
4	35.6°N	33.8°W	281.2	283.8	285.0	289.6	291.0
5	44.6°N	37.1°W	280.9	283.1	284.0	287.7	287.0
6	19.7°N	82.6°W	291.2	294.2	295.6	300.7	301.5
7	15.1°N	144.7°W	292.7	294.9	296.1	300.1	301.2
8	39.4°N	69.1°W	286.9	290.6	291.8	298.0	296.2

TABLE 2.2.2-2. -- RELATIVE ABSORPTION COEFFICIENT K( $\nu$ ) IN  
(g<sup>-1</sup> cm<sup>2</sup>) FOR THE THREE WINDOW CHANNELS

	Channel 1	Channel 2	Channel 3
$\Delta\nu$ (in)	775 to 831	831 to 887	887 to 960
K( $\nu$ )	0.191	0.131	0.104

These absorptive coefficients were tested for linearity as well as against other data sets. One data set was from Nimbus 4 and was an IRIS sequence over the Arabian Sea from 8°N to 14°N

latitude. This showed deviations of only 1°C, whereas the best fit atmospheric models would have predicted a 3°C deviation. Another data set was available from the IRIS aboard Nimbus 3 where corresponding shipboard sea surface data were available. By utilizing the previously calculated absorption coefficients,  $K(\nu)$ , from the Nimbus 4 IRIS, comparison was made between the Nimbus 3 IRIS sea surface temperature predictions and those measured from ships. An rms difference of only 1.3° was noted. It appeared that the derived  $K(\nu)$  tended to slightly underestimate the SST's over cold water in high altitudes and overestimate the SST's in the tropics. A further refinement of  $K(\nu)$  improved accuracies to 1°C.

In anticipation of the NOAA-2 launch, McMillin (ref. 2.2.2-26) developed several variations to a technique for atmospheric correction in sea surface temperature determination. Both the scanning radiometer (SR) and the Vertical Temperature Profile Radiometer (VTPR), an atmospheric sounder, have a common band-pass at  $835 \text{ cm}^{-1}$ . This theoretical treatment utilized 106 atmospheres developed in appendix A of Wark, et al., (ref. 2.2.2-27). McMillin ratioed the calculated radiances for the look angles ( $0^\circ$ ,  $60^\circ$ ) received in space for 32 of the 106 Wark atmospheres. The derived formula used to calculate sea surface temperature was as follows:

$$B(\nu_r, T_s) = I_1(\nu_r) + \gamma[I_1(\nu_r) - I_2(\nu_r)] \quad (9)$$

where

$B(\nu_r, T_s)$  = Planck radiance of the sea surface at reference frequency  $\nu_r$  ( $835 \text{ cm}^{-1}$ ) and surface temperature  $T_s$

$I_1(\nu_r)$  = radiance at top of atmosphere for look direction 1 ( $0^\circ$ ) and reference frequency  $\nu_r$ .

$I_2(\nu_r)$  = radiance at top of atmosphere for look direction 2 ( $60^\circ$ ) and reference for reference frequency  $\nu_r$ .

$\gamma$  is derived by the formula:

$$\gamma = [1 - \tau(\nu_1, P_0, \theta)] / [\tau(\nu_1, P_0, \theta) - \tau(\nu_2, P_0, \theta)] \quad (10)$$

where

$\tau(\nu_1, P_0, \theta_1)$  = atmospheric transmission a frequency  $\nu_1$ , surface pressure  $P_0$ , and look angle  $\theta$

$\tau(\nu_2, P_0, \theta_1)$  = same as previous definition except at frequency  $\nu_2$ .

The value of  $B$  ( $835 \text{ cm}^{-1}$ ,  $T_s$ ) was obtained by three techniques (1) by taking an average value of  $\nu$ , (2) the weighted average value of  $\nu$ , and (3) the value of  $\nu$  given by several iterations on the function,  $[I_1(\nu_r) - I_2(\nu_r)]$ , resulting in:

$$\gamma = \gamma_0 + \gamma_1 [I_1(\nu_r) - I_2(\nu_r)] \quad (11)$$

A comparison of errors from the three methods were  $0.85^\circ\text{K}$ ,  $0.55^\circ\text{K}$ , and  $0.35^\circ\text{K}$ , respectively. The third technique of non-linear regression gave improved accuracies relative to the first two methods which used linear extrapolation.

A forecast approach to improvement of the error in  $B$  ( $835 \text{ cm}^{-1}$ ,  $T_s$ ) was studied. It was concluded that improvement over the non-linear technique would only be possible in very moist atmospheres.

Cogan and Willand (ref. 2.2.2-10) have derived a very interesting parametric formula which can greatly simplify data reduction as compared to the use of the radiation transfer equation. By making several assumptions in the derivation of the radiation transfer equation, the following approximation of the sea surface temperature deficit,  $D$ , centered at  $11.5 \mu\text{m}$  was obtained:

$$D = \alpha(\lambda, n, \ell, T)k_1M + \beta(\lambda, n, \ell, T)k_2M^2 \quad (12)$$

where

$\alpha(\lambda, n, \ell, T)$  = a function  $\alpha$  of wavelength  $\lambda$ , number of assumed layers  $n$ ,  $\ell \approx .7$  for radiation near  $11.5 \mu\text{m}$ , and  $T$  the temperature

$\beta(\lambda, n, \ell, T)$  = a function of  $\beta$  similarly defined as  $\alpha(\lambda, n, \ell, T)$

$k_1$  = first part of the mass absorption coefficient

$k_2$  = second part of the mass absorption coefficient

$M$  = the integrated water vapor content in  $\text{g}\cdot\text{cm}^2$

When  $T = T_0$  is the surface temperature and commonly observed values of  $\alpha$  and  $\beta$  are substituted into the equation as well as values of  $k_1 = 0.10 \text{ g}^{-1}\text{cm}^2$  and  $k_2 = 5 \text{ g}^{-1}\text{cm}^2$ , then a further approximation can be made:

$$D \approx 0.66M + 0.86M^2, \quad (13)$$

Fourteen cases were compared by this approximation to the deficits obtained by integration of the radiative transfer equation. The deficit,  $D$ , from the parametric formula (13) was within  $\pm 0.3^\circ\text{K}$  of the radiation equation in 11 of the 14 cases and  $< 0.6^\circ\text{K}$  in the remaining 3 cases. A plot of the deficit,  $D$ , versus  $M$  (integrated water vapor content) is shown in figure 2.2.2-9.

It is estimated that this technique can give accuracies of  $\pm 0.5^\circ\text{K}$  in the  $10.5 \mu\text{m}$  to  $12.5 \mu\text{m}$  channel of the scanning radiometer (SR) on NOAA-2.

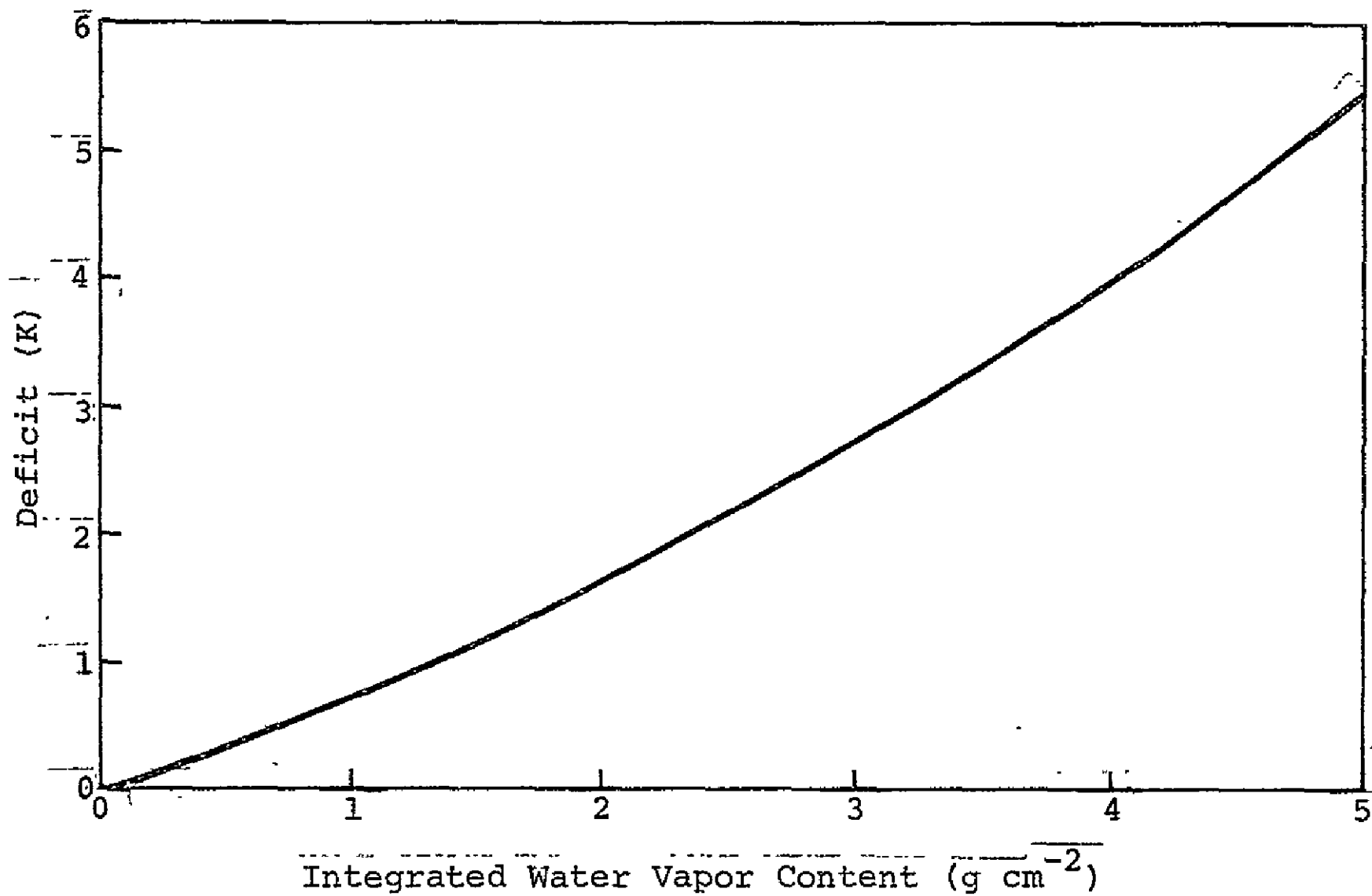


Figure 2.2.2-9.— The deficit as a function of integrated water vapor content.  $T_S - T_B = D = 0.066 M + 0.086 M^2$ , for  $k_1, k_2 = 0.10, 5.0 \text{ g}^{-1} \text{ cm}^2$ .

## 2.2.2.2 Correction Techniques for Land Surface Data

### 2.2.2.2.1 Introduction

Land surface data have been given considerably less attention than sea surface data because the emissivities of land surfaces are not as well known. Most data reported on have concerned the thermal bands.

A field technique has been developed at JSC for measuring emissivities of land surfaces and their vegetative cover. This technique has been utilized along with infrared data from the Very High Resolution Radiometer (VHRR) on board NOAA-2, 3, and 4 to predict areas subject to screwworm infestation.

The Temperature Humidity Infrared Radiometer (THIR) on board Nimbus-6 has been utilized to develop a thermal inertia map of the Arabian Peninsula. A study has also been performed by Colorado State University during the Skylab program in which several atmospheric models were compared in predicting temperatures of land surfaces within the southern United States.

### 2.2.2.2.2 Thermal Data

An earth resources use of land surface thermal data has been reported on by D. Phinney (ref. 2.2.2-28). The infrared data from the VHRR on board the NOAA satellites has been utilized to estimate the daily mean air temperature (DMAT) throughout parts of Mexico and Texas. This DMAT has been used to identify areas susceptible to screwworm infestation.

A field technique for measuring the emissivity of soils and vegetative cover was developed for the DMAT program input by D. Phinney and G. Arp (ref. 2.2.2-29). This field technique utilized an emissivity box as discussed by Buettner and Kern (ref. 2.2.2-30). Atmospheric correction was performed by linear

regression techniques similar to those of Smith, et al., (ref. 2.2.2-3). The DMAT standard error under closely controlled conditions was estimated to be 2.5°C.

A very excellent summary article is available by K. Watson (ref. 2.2.2-31) on geologic applications of thermal infrared images. Obviously, not all of these applications require atmospheric correction. One area which does require correction is thermal inertia mapping. A relationship between thermal inertia mapping and the density of certain geologic materials is shown in figure 2.2.2-10).

Thermal inertia is the ratio of thermal conductivity to the square root of the thermal diffusivity, and for dry materials it correlates almost linearly with density as shown in figure 2.2.2-10. Thermal inertia mapping is presently only applicable to rock discrimination in areas where the geology is well exposed. Oxidation, stain, lichen covering, soil covering, vegetation covering, etc., all give false signatures in the thermal inertia mapping technique.

The Nimbus Temperature Humidity Infrared Radiometer was utilized (ref. 2.2.2-31) for thermal inertia mapping of Oman on the Arabian Peninsula. The resulting map showed gross agreement with major units on a reconnaissance map. Some anomalies which did not correspond to the reconnaissance map were found to match features on a more detailed geologic map or in more detailed ERTS images (ref. 2.2.2-32). Further increases in the capability of thermal inertia mapping will come from increased resolutions of future instruments.

It may also be possible to detect soil moisture by thermal inertia mapping as discussed in section 2.10.1.3. The measurement of geothermal flux is also possible by infrared mapping,

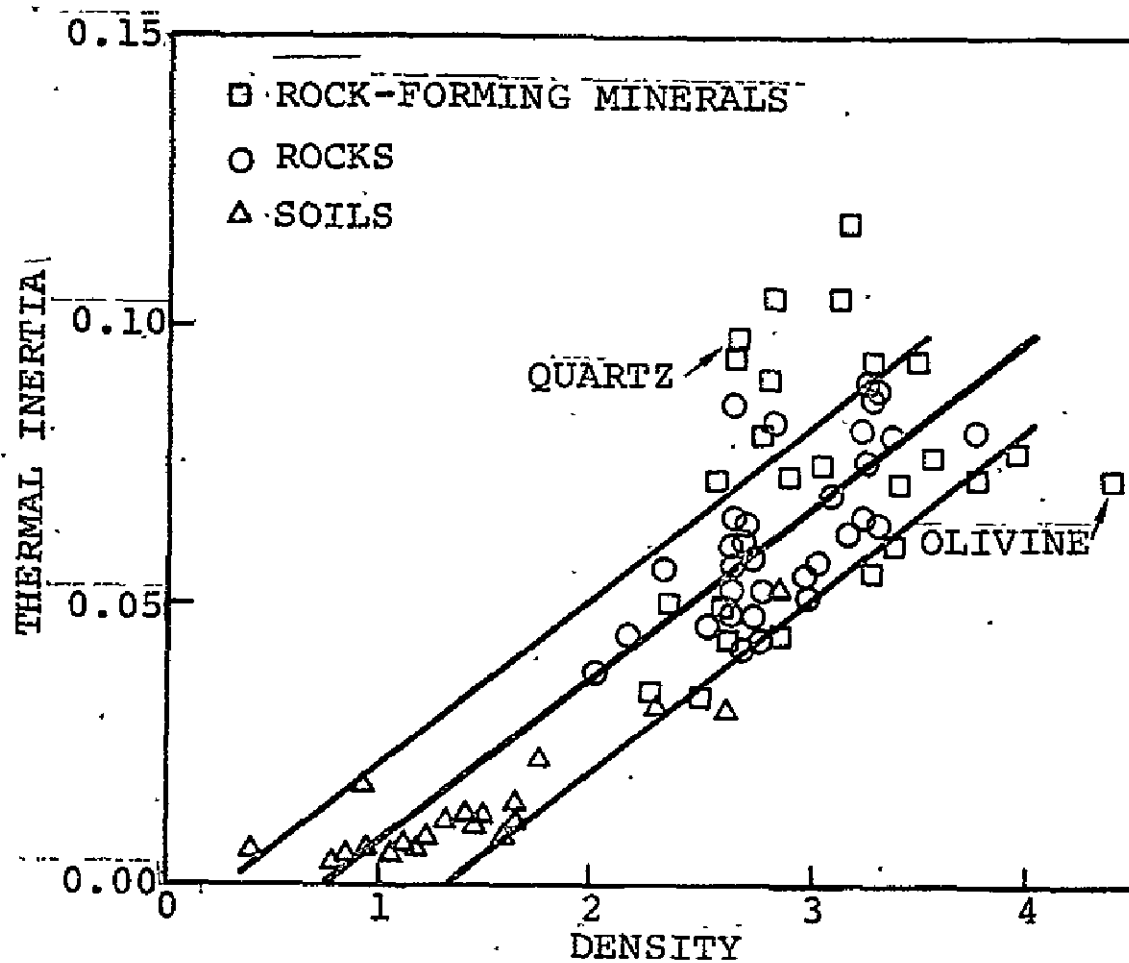


Figure 2.2.2-10.— Thermal inertia ( $\text{cal}/\text{cm}^2/\text{s}^{1/2}$ ) versus density ( $\text{g}/\text{cm}^3$ ) for a variety of rock-forming minerals, rocks, and soils. (The linear correlation line, bracketed by lines showing the standard deviation, shows the increase of thermal inertia with increasing density. Rocks and rock-forming minerals which are high in silica tend to fall above the line (see quartz). Those which are low in silica and high in iron oxide tend to fall below the line (see olivine).)

but techniques utilizing atmospheric corrections are not too well defined at this time.

A recent research effort, Skylab Concentrated Atmospheric Radiation Project (SCARP), was conducted during the Skylab mission in 1973-1974. As part of these experiments conducted over the southern United States, Renne, et al., of Colorado State University (ref. 2.2.2-33) compared predictions of several infrared radiative transfer models to observed apparent surface temperatures as measured by airborne radiometers and by the S-191 spectrometers. The models compared were called (1) the Boudreau model, (2) RADIAN C, (3) RADIAN V, and (4) EXTCOEAF Aerosol Thermal Transmissivity model. The models differed in the manner in which transmissivities were calculated. In addition, RADIAN V contained the additional option of calculating ozone and aerosol transmissivities. All models calculated water vapor and carbon dioxide transmissivities. It was found that the models were capable of computing atmospheric absorption and emission effects for prediction of thermal radiance emitted from the earth's surface to within a 5 percent accuracy.

## REFERENCES

- 2.2.2-1 Valley, S. L., editor: Handbook of Geophysics and Space Environment. A.F.C.R.L., U. S. Air Force, 1965, pp. 10-3.
- 2.2.2-2 La Violette, P. E.; and Chabot, P. L.: A Method of Eliminating Cloud Interference in Satellite Studies of Sea Surface Temperatures. Deep Sea Research, 1969, Vol. 16, pp. 539-547.
- 2.2.2-3 Smith, W. L.; Rao, R. K.; Koffler, R.; Curtis, W. R.: The Determination of Sea-Surface Temperature from Satellite High Resolution Infrared Window Radiation Measurements. Monthly Weather Review, Vol. 98, No. 8, 1970, pp. 604-611.
- 2.2.2-4 Leese, J.; Pichel, W.; Goddard, B.; and Brower, R.: An Experimental Model for Automated Detection, Measurement and Quality Control of Sea Surface Temperatures from ITOS-IR Data. Proc. of the Seventh International Symposium in Remote Sensing, 1971, pp. 625-646.
- 2.2.2-5 Shenk, W. E.; and Salomonson, V. V.: A Multispectral Technique to Determine Sea Surface Temperature Using Nimbus 2 Data. J. of Physical Oceanography, Vol. 2, April 1972, pp. 157-167.
- 2-2-2.6 Anding, D.; Kauth, R.; Turner, R: Atmospheric Effects on Infrared Multispectral Sensing of Sea-Surface Temperature from Space. NASA CR-1858, July 1971.
- 2.2.2-7 Maul, G. A.; Sidran, M.: Atmospheric Effects on Ocean Surface Temperature Sensing from the NOAA Satellite Scanning Radiometer. J. Geophys. Res., Vol. 78, No. 2, April 20, 1973, pp. 1909-1916.
- 2.2.2-8 Maul, G. A.: Infrared Sensing of Ocean Surface Temperature. Advances in the Astronautical Sciences, Vol. 30, June 19-20, 1973, pp. 461-464.
- 2.2.2-9 Pitts, D. E.: Severe Storm Environments. NASA CR 147486, Final Report on EPN-582, Jan. 16, 1976.
- 2.2.2-10 Cogan, J. L.; Willand, J. H.: Measurement of Sea Surface Temperature by the NOAA-2 Satellite. J. of Applied Meteorology, Vol. 15, Feb. 1976, pp. 173-180.

- 2.2.2-11 McClatchey, R. A.; Fenn, R. W.; Selby, J. E. E.; Volz, F. E.; and Garring, J. S.: Optical Properties of the Atmosphere, 3rd ed. A.F.C.R.L. 72-0497, Environ. Res. Papers, No. 411, Air Force Cambridge Research Laboratories, L. G. Hanscom Field, Bedford, Mass., 1972, 108 pp.
- 2.2.2-12 Selby, J. E. E.; and McClatchey, R. M.: Atmospheric Transmittance from 0.25 to 28.5  $\mu\text{m}$ : Computer Code LOWTRAN-2. A.F.C.R.L. 3572-0745, Environ. Res. Papers, No. 427, Air Force Cambridge Research Laboratories, L. G. Hanscom Field, Bedford, Mass., 1972, 77 pp.
- 2.2.2-13 Yates, H. W.: Limitations and Prospects for Atmospheric Sounding. Proc. of the Society of Photo-Optical Instrumentation Engineers, Vol. 51, Aug. 19-20, 1974, pp. 1-14.
- 2.2.2-14 La Rocca, A. J.: Methods of Calculating Atmospheric Transmittance and Radiance in the Infrared. Proc. IEEE, Vol. 63, No. 1, Jan. 1975, pp. 75-94.
- 2.2.2-15 Anding, D.; Kauth, R.: Estimation of Sea Surface Temperature from Space. Remote Sensing of Environment, 1, 1970, pp. 217-220.
- 2.2.2-16 McMillin, L. M.: A Method of Determining Surface Temperatures from Measurements of Spectral Radiance at Two Wavelengths. Ph.D. dissertation, Iowa State Univ., Iowa City, 1971.
- 2.2.2-17 Prabhakara, C.; Conrath, B. J.; and Kunde, V. G.: Estimation of Sea Surface Temperature from Remote Measurements in the 11-13  $\mu\text{m}$  Window Region. NASA/GSFC X Doc. 651-72-358, 1972, 15 pp.
- 2.2.2-18 Korb, C. L.: Physical Considerations in the Channel Selection and Design Specifications of an Airborne Multispectral Scanner. Proceedings of the Purdue Centennial Symposium on Information Processing, Purdue University, Apr. 28, 1969.
- 2.2.2-19 Hughes, C. L.: S-191 Sensor Performance Evaluation Final Report. Lockheed Electronics Company, Report No. 5778, June 1975, pp. 2-21.
- 2.2.2-20 Saunders, P. M.: Aerial Measurement of Sea Surface Temperature in the Infrared. J. Geophys. Res., 72 (16), 1967, pp. 4109-4117.

- 2.2.2-21 Maul, G. A.; and Sidran, M.: Comment on Anding and Kauth, Remote Sensing Environ., 2, 1972, pp. 165-169.
- 2.2.2-22 Bignell, K.: The Water-Vapour Infrared Continuum. J. Roy. Meteorol. Soc., 96, 1970, pp. 390-403.
- 2.2.2-23 Burch, D. E.: Investigation of the Absorption of Infrared Radiation by Atmospheric Gases. Publ. U-4784, Aeronutronic Div., Philco-Ford Corp., Newport Beach, Calif., 1970, pp. 2-5.
- 2.2.2-24 Anding, D.; and Kauth, R.: Reply to the Comment by G. A. Maul and M. Sidran, Remote Sensing Environ., 2, 1972, pp. 171-173.
- 2.2.2-25 Prabhakara, C.; Dalu, G.; Kunde, V. G.: Estimation of Sea Surface Temperature From Remote Sensing in the 11- to 13- $\mu$ m Window Region. J. of Geophys. Res., Vol. 79, No. 33, Nov. 20, 1974, pp. 5039-5044.
- 2.2.2-26 McMillin, L. M.: Estimation of Sea Surface Temperatures from Two Infrared Window Measurements With Different Absorption. J. of Geophys. Res., Vol. 80, No. 36, Dec. 20, 1975, pp. 5113-5117.
- 2.2.2-27 Wark, D. Q; Yamamoto, G.; and Lienesch, J. H.: Infrared Flux and Surface Temperature Determinations from TIROS Radiometer Measurements. Tech. Rep. 10, U. S. Weather Bur., Washington, D. C., 1962.
- 2.2.2-28 Phinney, D.: Estimation of Daily Mean Air Temperature from Satellite Derived Radiometric Data. LEC-7852, Jan. 1976.
- 2.2.2-29 Phinney, D. E.; Arp, G. K.: The Measurement and Interpretation of Thermal Infrared Emissivities. LEC-5621, Feb. 1975.
- 2.2.2-30 Buettner, K. J. K.; Kern, C. D.: The Determination of Infrared Emissivities of Terrestrial Surfaces. J. of Geophys. Res., Vol. 70, No. 6, March 15, 1965, pp. 1329-1337.
- 2.2.2-31 Watson, K.: Geologic Applications of Thermal Infrared Images. Proc. IEEE, Vol. 63, No. 1, Jan. 1975, pp. 128-137.
- 2.2.2-32 Pohn, H. A.: A Comparison of ERTS Images and Nimbus Thermal Inertia Mapping of Oman. Unpublished (in review by U. S. Geological Survey).

2.2.2-33

Renne, D. S.; Marlatt, W. E.: A Comparison of Models for Computing Atmospheric Infrared Transmission. Submitted to Colorado State University for fulfillment of Ph.D. requirements, 1975.

## 2.3 CARTOGRAPHY

### 2.3.1 INTRODUCTION

As the population of the world continues to increase and the need for inventorying, managing, and monitoring the environment becomes increasingly important, the need and demand for accurate, up-to-date maps and other cartographic products continues to grow. Despite the importance of maps and the obvious need for more and better maps, the overall status of mapping is deplorable. This was emphasized in a recent United Nations study (ref. 2.3-1) which estimated the worldwide availability of topographic map data as follows:

<u>Map Scale</u>	<u>Percent of the World</u>	<u>Percent of the U.S.</u>
1:1,250 - 1:31,680	6.0	40.5
1:40,000 - 1:75,000	24.5	44.7
1:100,000 - 1:126,720	30.2	20.8
1:140,000 - 1:253,440	92.0	100.0

The rate of obsolescence of maps is of even more concern, particularly in urban and other rapidly developing areas. Using present day methods, the production cycle for a topographic map is typically 3 to 4 years. Consequently, a map may be as much as 4 years out of date on the day it is published. The rate of obsolescence is increasing and may soon equal the production rate. Therefore, with current techniques and capacities, the world mapping task will never be completed.

Before the advent of practical aerial photography, maps were made in the field by teams of cartographers who painstakingly measured their way over the landscape. During the 1920's and 1930's, advances in the development of aircraft, photography,

and photogrammetric plotting instruments enabled photogrammetry (the art and science of deriving reliable measurements from photography) to assume an increasingly important role in the production of maps. Through the use of specialized cameras, customized photographic flights and complex stereoscopic plotting equipment, a major portion of the mapmaking process was shifted from the field to the offices. The rate of map production was accelerated and the geometric accuracy and content of these cartographic products were greatly improved. During recent years, cartographers and photogrammetrists have turned to large-scale, high-speed electronic computers and improved mathematical techniques in an effort to enhance the speed and accuracy of map production. Today, photogrammetrists and cartographers consider photography from orbiting spacecraft as the next logical major step that will enable the preparation and revision of many types of maps and map products more rapidly and more inexpensively than the present methods.

The feasibility of mapping from space was demonstrated by several cartographic principal investigations using S-190A and S-190B photographic data acquired during the recent Skylab mission. Prior to Skylab, limited mapping efforts were attempted using photographic imagery acquired during Gemini and Apollo. Although these investigations and studies were generally impressive, they were handicapped by the fact that none of the various cameras used on Gemini, Apollo, or Skylab were designed for photogrammetric use and none of them met conventional standards for metric quality.

The forthcoming Space Shuttle provides a potential for rectifying this inadequacy and enabling an evaluation of the true cartographic potential of photography from earth-orbital altitudes. The first logical step in preparing for a Shuttle cartographic mission or experiment is to define the camera system or systems

that would best serve the mapping community. In this section, various influencing factors will be discussed, and ultimately, a cartographic camera system for Shuttle will be proposed.

### 2.3.2 BACKGROUND

Besides charts, which are special-purpose maps used for air or water navigation, the most commonly-used cartographic products are planimetric maps, topographic maps, and controlled photo-mosaics. Planimetric maps reveal only the horizontal locations of features, whereas topographic maps show both horizontal and vertical locations of various features. A controlled photo-mosaic is a mounted assemblage of a number of individual photographs that have been rendered "tilt free" by a process termed rectification, and the edges of which have been cut or torn and matched in order to form a continuous photographic representation of a portion of the Earth's surface.

Planimetric and topographic maps and photomosaics are produced at almost all conceivable scales; however, a number of somewhat standard scales have evolved. In the United States, the standard national map series are produced at scales of 1:24,000, 1:62,500, and 1:250,000. In those parts of the world using the metric system, the more commonly-used scales are 1:25,000, 1:50,000, 1:100,000, 1:250,000 and 1:500,000. Most uses or applications generally seek the smallest scale map capable of depicting the minimum degree of detail required to support the particular use or application.

In most photogrammetric mapping, the position and the spatial orientation of the camera must be determined to a high degree of accuracy at the instant in which each photograph is exposed. This is generally accomplished through a network of photoidentifiable points (control points), the horizontal and/or vertical locations of which have been established by ground surveying or

other means. Because of the nature of the propagation of various dimensional imperfections in the photographs, errors in photogrammetric instruments and shortcomings in mathematical procedures, a minimum of one or two preestablished ground control points must appear about every seventh photograph to achieve and maintain required accuracy standards. After a basic network of ground control has been created, photogrammetric triangulation methods are usually used to densify or extend this basic control network. This typically involves establishing six to nine points, well-distributed over the format, for each photograph being used in photogrammetric mapping or in the preparation of controlled photomosaics. The establishment of a basic ground control network and the densification of this network is generally the costliest and most time consuming portion of the overall photogrammetric mapping process, especially in remote regions.

From the foregoing, it logically follows that a space cartographic system must be analyzed from its ability to support five distinct mapping activities, namely:

1. Construction of planimetric maps
2. Construction of topographic maps
3. Construction of photomosaics
4. Map revision and updating
5. Photogrammetric establishment and densification of ground control

The most critical characteristic of a system, regarding the above mapping activities, are the area of coverage, resolution, geometric fidelity, and base-height ratio. Since the success of the system depends on these factors, each characteristic will be considered in the following sections.

### 2.3.3 AREAL COVERAGE

If camera parameters of focal length and film format remain constant, the higher the altitude from which a photograph is taken, the greater the area which appears on the photograph. An increase in altitude reduces the number of photographs required to cover a given ground area, which in turn reduces the number of photographs that must be handled in the mapping process, and, most importantly, increases the distance between required surveyed ground control points. This reduces the number of both mandatory and supplemental control points. The major attribute of space photography, for considerations of photogrammetric mapping, is the increased area of coverage over conventional aircraft photography.

Most mapping cameras possess a 9 in. x 9 in. usable format and a focal length of 3 in., 6 in., 9 in., or 12 in., with 6 in. being by far the most widely-used. The S-190A cameras aboard Skylab had 2 1/4 in. x 2 1/4 in. formats and a 6-in. focal length; the S-190B camera had a 4 1/2 in. x 4 1/2 in. format and an 18-in. focal length. Despite the smaller formats, the increase in ground coverage by these systems is impressive when compared to that of conventional (6-in. focal length, 30,000 ft altitude) aircraft photography. As illustrated in figure 2.3-1, an S-190A frame covers 10,201 sq. mi. and an S-190B frame covers 4,624 sq. mi. whereas the conventional aerial frame contains an area of only 81 sq. mi. If the traditional 60 percent forward overlap between photos and 20 percent sidelap between strips of photos are assumed, it requires about 153 conventional aircraft photos to cover an area equivalent to that of the S-190B and 338 such photos to cover the area of a single S-190A frame. With aircraft photography from 60,000 ft, 28 photos equate to an S-190B frame and 72 photos are required to cover the area photographed on an S-190A frame. As a result of this increased area of coverage with Skylab S-190A and S-190B photographs,

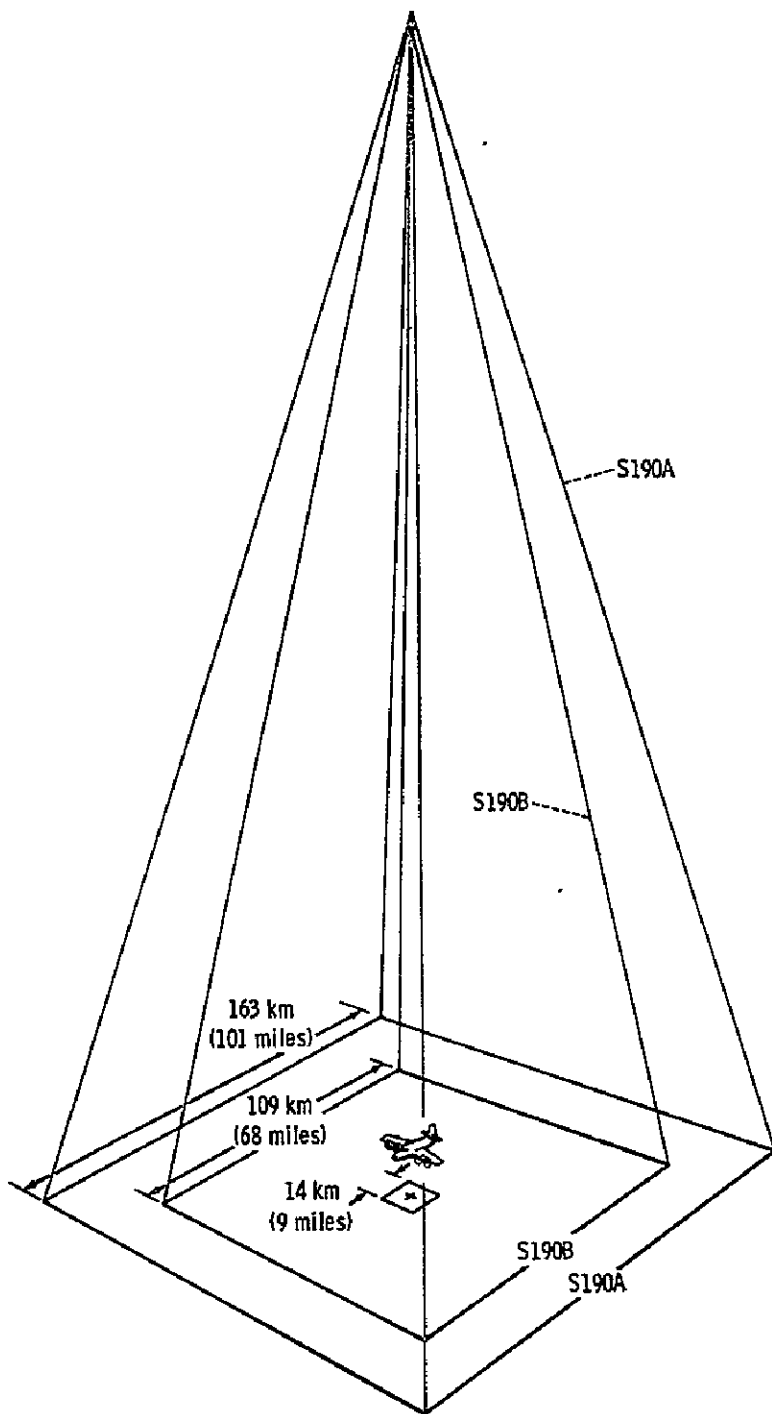


Figure 2.3-1.— Area of coverage of Skylab S-190A and S-190B imagery relative to that of conventional aircraft photography (6-in. focal length; 9 in. × 9 in. format; 30,000 ft flying height).

several Latin American Skylab principal investigators (Staples, et al., ref. 2.3-2) found that various original mapping and map revision activities could be accomplished in about one-sixth the time and manpower required using aircraft photography from 60,000 ft.

The area of coverage of a frame photograph is a function of three parameters, namely, format, focal length, and altitude above the terrain (flying height). These parameters in turn interrelate with resolution and base-height ratio, two of the previously mentioned factors of concern. Table 2.3-1 lists the area of coverage in nautical miles (assuming a spherical earth) of two formats, 9 in. x 9 in. and 9 in. x 18 in., for six focal lengths between 3 in. and 24 in. for four orbital altitudes. A discussion of the trade-offs between area of coverage, resolution and base-height ratio will be deferred until these factors are discussed.

#### 2.3.4 RESOLUTION

Excluding geometric fidelity, the most critical property of cartographic photographic imagery is resolution. The degree of detail on a map is obtained from photographic resolution or, more directly, from ground resolution. For a variety of reasons, it is difficult, if not impossible, to establish a direct relation between map scale and required ground resolution, because some major cultural features like roads and railroads must generally be shown on a map regardless of its scale. Further complication exists because lineal features whose lateral dimensions are well below the resolution limit can be detected and interpreted on imagery. In order to establish resolution requirements, therefore, it is useful to consider certain fundamentals that apply to the mapmaking process and to maps of all types.

TABLE 2.3-1. — AREA OF COVERAGE AND FIELD-OF-VIEW (FOV) FOR 9 IN. × 9 IN. FORMAT FRAME  
CAMERA FOR FOUR ORBITAL ALTITUDES AND SIX FOCAL LENGTHS

Camera Focal Length	Spacecraft Altitude (Nautical Miles)							
	100		150		200		250	
	Area (nautical miles) <sup>2</sup>	FOV (nautical miles)						
8 in.	139,942	374.1	344,410	586.9	681,014	825.2	1,215,162	1,102.3
6 in.	31,260	176.8	71,515	267.4	129,583	360.0	206,289	454.2
9 in.	13,634	116.8	30,870	175.7	55,313	235.2	87,161	295.2
12 in.	7,620	87.3	17,200	131.2	30,724	175.3	48,204	219.6
18 in.	3,360	58.0	7,596	87.2	13,537	116.3	21,182	145.5
24 in.	1,887	43.4	4,264	65.3	7,572	87.0	11,854	108.9

2.3-8

#### 2.3.4.1 Cartographic Accuracy

In the United States, accuracy of cartographic presentation is specified by National Map Accuracy Standards (NMAS). These standards require:

1. Horizontal accuracy -- For maps at publication scales larger than 1:20,000, not more than 10 percent of the points tested shall be in error by more than 0.85 mm (1/30 inch); for maps on publication scales of 1:20,000 or smaller 0.5 mm (1/50 inch).
2. Elevation accuracy -- For contour maps at all publication scales, not more than 10 percent of elevations tested shall be in error more than one-half the contour interval. The apparent vertical error may be decreased by assuming a horizontal displacement within the permissible horizontal error for a map of that scale.

Extensive testing by the U.S. Geological Survey shows that map errors are not normally distributed and do not have zero mean. To account for these facts, the Survey has adopted the following standards:

1. Horizontal accuracy

$$\begin{aligned} \text{RMS}_p &= 5.7 \times 10^{-4} S_m \text{ for scales } 1:20,000 \text{ and larger} \\ &= 3.4 \times 10^{-4} S_m \text{ for scales smaller than } 1:20,000 \end{aligned}$$

where

$\text{RMS}_p$  is the root mean square planimetric error at test points (meters)

$S_m$  is the map publication scale number.

## 2. Vertical accuracy

$$\text{RMS}_h = 0.34 \text{ contour interval}$$

where

$\text{RMS}_h$  is the root mean square elevation error at test points in the same units as contour interval.

For military mapping Class A standards are the same as NMAS, and Class B standards permit the allowable errors to be doubled.

NMAS were originally established for conventional line-drawn maps. They are compatible with standard cartographic techniques, with the dimensional limitations of photographic and lithographic technology, and with the dimensional stability of paper. Although established for line maps, the standards are a useful criterion to apply to image base maps produced from remote sensor data. It will frequently be found, however, that spatial resolution of image data has more to do with the scale of its cartographic presentation than does planimetric accuracy. Indeed the preferred approach is to present the data at a scale compatible with its spatial resolution, and then determine the extent to which the resultant product meets NMAS.

### 2.3.4.2 Spatial Resolution and Map Scale

Map content is obtained from photographic resolution and scale. Under normal conditions, the unaided human eye can resolve about five to six line pairs per millimeter. In order to retain this resolution in the final map product and to allow for some inevitable losses in processing, imagery should contain a minimum of about ten line pairs per millimeter. The ground resolution which can be presented on any photographic image product is then 0.1 mm times the map scale number. Thus a

1:50,000 scale map should have about 5 m ground resolution, while a 1:250,000 scale product would require about 25 m.

The same visual criteria leads to a useful relationship that can be employed to determine the enlargement limit of high resolution space photos. This relation is simply the resolution of the photo divided by ten. Further enlargement merely takes up more paper or film without presenting any more useful information to the observer.

Table 2.3-2 summarizes the ground resolution and accuracy requirements for various planimetric and topographic map publication scales, which should be considered as basic minimal requirements for any space sensor to be used in mapping applications.

TABLE 2.3-2. — MAP ACCURACY AND GROUND RESOLUTION REQUIREMENTS FOR COMMONLY-USED MAP SCALES

Map Scale	Standard Error of Position (m)	Ground Resolution (m)	Nominal Contour Interval (m)	Standard Error of Elevation (m)
1:1,000,000	300	100	500	150
1:250,000	75	25	100	30
1:100,000	30	10	50	15
1:50,000	15	5	25	8
1:25,000	7.5	2.5	10	3

### 2.3.5 GEOMETRIC FIDELITY

The imagery produced by a space camera system represents the mapping, in the topological sense, of three-dimensional object space to the two-dimensional space of the camera film plane. Producing a map from such a film record basically requires

reversing the mapping (the inverse transformation). If a relatively distortion-free and error-free map product is to result, the imaging camera must either be sufficiently free of geometric distortions or the distortions introduced must be known, stable, and determinable. A detailed analysis of the metric distortions of a camera system is beyond the current scope of this section. However, the combined geometric distortions in an earth-orbital mapping camera should not exceed 2  $\mu\text{m}$  over the useful format. Based on experience gained with a variety of non-metric cameras carried by Gemini, Apollo, and Skylab, the following geometric factors should be considered in a satellite-borne mapping camera to obtain the necessary geometric fidelity:

1. Calibrated focal length and principal point
2. Radial and decentering lens distortion
3. Film flatness
4. Internal reseau system

The focal length and location of the intersection of the optical axis with the film plane (principal point) must be both stable and determinable. The focal length and principal point must be calibrated prior to flight, and a reliable means of determining the principal point on each frame of photography must be provided. This is generally accomplished by a system of "fiducial marks" contained within the film plane of the camera body as projected from within the rigid body of the camera.

Radial distortion is a true optical aberration, whereas decentering distortion is the result of tilt and alignment imperfections introduced during the fabrication of a lens assembly. With proper care during assembly, decentering errors can be held down to the point where tangential distortion does not amount to more

than 2  $\mu\text{m}$  at any point on the format. Techniques for measuring radial and decentering distortions, although difficult and time-consuming, have been perfected to a degree where these distortions can be modeled to a fraction of a micrometer.

The lens assembly of any space mapping camera should be designed for stability, assembled to exacting standards, and thoroughly calibrated by the most accurate and precise means available.

In order to minimize errors introduced by tendencies of the film to buckle, warp, or otherwise fail to lie flat in the film plane of the camera, an effective film flattening mechanism must be incorporated into the camera design. Flattening systems employing vacuum backs on the camera and glass pressure plates in front of the film have both been successfully employed to minimize lack of flatness problems. Since lack of film flatness is probably one of the major overall contributors to uncompensatable metric errors in mapping cameras, an effort should be made to obtain the best system that the state-of-the-art is capable of providing.

Although external to the camera system itself, various metric errors of serious magnitude are often introduced by stretch, warping and other dimensional changes in the film base during photoprocessing of the exposed film. If an adequate internal reseau system is incorporated into the camera, these errors can be removed or minimized to acceptably low levels during subsequent processing of the data. Reseau systems superimposed on glass pressure plates, projected from behind the film plane, or projected from the lens cone have all proven successful. The particular system chosen and the density of the reseau marks should be consistent with the dimensional properties of the film base and the photoprocessing techniques employed. Again, the goal should be to suppress these errors to below the 2  $\mu\text{m}$  level.

In addition to the four items just discussed, a space mapping camera should ideally possess a between-the lens shutter (as opposed to a focal plane shutter) and should contain a high-performance image motion compensation (IMC) system. Although the IMC system primarily influences resolution rather than the metric properties of a system, a near flawless system is essential to a quality space mapping camera if mapping from orbit is to be fully exploited. Ideally, such a system would contain a real-time VH sensor and a continuously-variable range of VH compensation.

### 2.3.6 BASE-HEIGHT RATIO

If elevation data is to be derived from photography for the purpose of producing vertical ground control or topographic maps, sufficient image parallax must be present in the basic imagery. Image parallax depends upon the camera configuration (focal length and format), the image scale (as influenced by focal length and flying height), and the measuring accuracy. A statistical interpretation of U.S. Map Accuracy Standards requires that

$$\sigma_h = 0.3 \text{ c.i.}$$

where

$\sigma_h$  = standard error of elevation

c.i. = contour interval

In terms of camera configuration, scale and measuring accuracy,

$$\sigma_h = S_p \frac{H}{B} \sigma_p$$

where

$S_p$  = photograph scale number

$\frac{H}{B}$  = the reciprocal of the base/height ratio

$\sigma_p$  = residual measuring error

The critical requirements ( $\sigma_n$ ) for maps at various scales have been previously listed in table 2.3-1. These values are based on the requirement that  $\sigma_p$ , the error in point positions, does not exceed 0.3 mm at map scale. Ideally, a B/H ratio of 1.0 or greater is desirable, however, a value of 0.6 is more realistically achievable with vertical aircraft photography.

#### 2.3.7 SENSOR CONFIGURATION AND MISSION PROFILE.

Based on the foregoing, the "best compromise" space mapping system to support original planimetric and topographic mapping, the revision of existing maps, and the construction of controlled photomosaics at scales of between 1:24,000 and 1:1,000,000, would consist of:

1. A 12-in. or 18-in. focal length and 9 in.  $\times$  18 in. format metric frame camera
2. A 24-in. focal length panoramic camera with a 4.5 in.  $\times$  45.25 in. format.

From a 110-n. mi. orbital altitude, the 12-in. focal length frame camera would provide a favorable B/H ratio of 0.6 with 60 percent forward overlap in the in-flight direction. This system would not provide contiguous coverage between orbital tracks. However, through orbital decoy or maneuvering, such coverage could be achieved over a period of time.

The panoramic camera should be operated in a 25° convergent mode to achieve stereoscopic coverage and with a 70° scan angle to achieve contiguous coverage (from 24°N latitude). Both systems should possess a timing system capable of recording exposure time to an accuracy of 0.001 second. This together with orbital parameters from ground-based tracking will enable the position of each exposure station to be located to within a few meters.

#### 2.3.8 SIDE-LOOKING RADAR (SLAR)

Recently, considerable attention has been devoted to the development of mapping techniques using side-looking radar (SLAR). The primary attraction of SLAR is the all-weather capability which allows imagery to be acquired through clouds, rain, haze and at night. Since radar ground resolution depends primarily upon pulse length rather than upon distance from the antenna to the ground, imaging radar appears as a logical candidate for an earth-orbital mapping sensor. Consideration of this is outside the scope of the present effort, however, serious consideration and study of SLAR as an orbital mapping tool should be made in the near future.

## REFERENCES

- 2.3-1 United Nations: The Status of World Topographic Mapping. World Cartography, Vol. X, 1970.
- 2.3-2 Staples, J. E., et al.: Overall Evaluation of Skylab Imagery for Mapping of Latin America. Final Report EREP Investigation Number 496B, Sept. 1975.

## 2.4 COASTAL STUDIES

### 2.4.1 SPECIFIC GOALS AND TECHNIQUES

Contemporary thought in ecology considers three levels in an integrated hierarchal structure. At the base is the physiology of individual plant and animal organisms. These combine to form the second level, populations, which in turn comprise the fundamental constituents of the third level, communities or natural environments. Typically, satellite remote sensing views ecology at the third level, (i.e., natural environments) and without the aid of low altitude aircraft or ground observations, investigation must infer the two lower ecological levels. Inference is achieved through direct observation occasionally and through modelling in several rare cases. Recent work in satellite remote sensing focuses almost exclusively on environment detection and identification utilizing automatic digital pattern recognition techniques.

#### 2.4.1.1 Environment Detection and Identification

As a physiographic unit on earth, the coastal zone is the most varied, spanning virtually all biotic and abiotic conditions. Natural assemblages of the physical, chemical, and biological components cover the widest ranges encountered in nature. To optimize environment discrimination using automatic pattern recognition techniques, in general, a remote sensing device limited essentially to reflected and emitted energy must incrementally cover the broadest possible spectral bands. Landsat I and II coastal zone studies covering visible and near infrared bands have demonstrated acceptable environment detection and marginally acceptable identification capabilities. Satellite instruments designed to sense emitted infrared energy have yielded only gross thermometric information, but satellite data has not been extensively studied in integrated systems with visible and near infrared sensors. In low altitude aircraft studies, thermometric information has proven useful in environment detection and

identification. Because of the large "footprint" size, passive microwave radiometry must still be considered experimental in coastal area applications. However, aircraft studies utilizing active microwave (radars) sensors in X and L bands have proven potential in environment discrimination.

In rare cases, specific ecological populations, if densely distributed and spectrally distinct from ambient environments, may be observed directly. However, the primary spectral constituents within satellite detected natural environments corresponds to specific zones along transitions from one environment to another. For example, grasses at one end of an imaginary spectrum blend gradually with shrubs and trees until trees become ecologically dominant in the scene. Automatic classification techniques typically discriminate various levels of mixtures along the gradient between pure grass and pure trees. Although explored in only a cursory way on single data sets, recent studies suggest the potential of correlating environmental gradients with reflectance spectra, then employing these correlations as prediction devices to quantitatively estimate reflectance-controlling factors such as tree density. Assuming that the sun angle and atmospheric effects can be systematically accounted for, it is reasonable to assume that regression techniques could be used on an operational basis with multiple data sets as predictive devices. Some automatic classification results would then depict types of isarithmic maps.

Regression techniques can be enhanced by including ground observed or low altitude aircraft data in the prediction equations. For example, satellite reflectance data represents a single prediction parameter. Assuming that soil moisture and the height of trees could be measured and included in the regression, a more accurate measure of tree density in the previous example would be feasible. In this case, regression techniques become multidimensional.

Periodic observation is essential to coastal zone studies because of the broad dynamic range of many environments. Short term changes, such as turbidity levels within a plume at the mouth of a river, or temperature fluctuation in an open bay are sensed from orbital altitudes only from a geosynchronous platform. Current platforms can not be used for short term measurements. Long term changes such as shoreline regressions or transgressions, and annual reflectance variations in natural vegetation are currently measureable. Because dynamic factors such as tide level so strongly influence environment discrimination, it is desirable to include this information to maximize classification accuracies.

#### 2.4.2 SENSOR AND MISSION REQUIREMENTS

Based on previous studies of Landsat I and II primarily, and Skylab (EREP) and Nimbus satellites secondarily, a satellite remote sensing system dedicated to coastal zone studies requires visible, near infrared, and thermal infrared bands. A minimum of three visible bands are desirable; (1) .525-.600 $\mu\text{m}$  to discriminate water turbidity, (2) .450-.525 $\mu\text{m}$  for benthic conditions and beach vegetation densities, and (3) .600-.650 $\mu\text{m}$  for chlorophyll absorption.

At least four near infrared bands are recommended. Wetland mapping in the .770-.800 $\mu\text{m}$ , .800-1.1 $\mu\text{m}$ \* bands and 1.1-1.5 $\mu\text{m}$  have proven useful. Skylab S-192 studies indicate that several bands in the .800-2.25 $\mu\text{m}$  region are useful for coastal zone discriminations and soil moisture measurements, and a band in the .900-1.10 $\mu\text{m}$  region permits accurate oil-spill discrimination. Thus, at a minimum, the near infrared band should be segmented into .70-.80 $\mu\text{m}$ , .80-1.10 $\mu\text{m}$ , 1.10-1.60 $\mu\text{m}$  and 1.60-2.25 $\mu\text{m}$ .

\*This band could be further segmented into .800-.875 $\mu\text{m}$  and .875-1.1 $\mu\text{m}$ .

Virtually all significant thermal infrared work in the coastal zone has focused on 8.00-14.0 $\mu$ m band. This band, although not significantly tested from satellite altitudes, is most familiar to the user committee and is therefore recommended.

In general, most coastal zone applications require resolution on the order of three to ten meters with an absolute maximum of approximately 25 meters. Beyond the 25 meter resolution level, the instantaneous field-of-view most likely contains a broad range of environmental conditions and dilutes identification capabilities. This is particularly true in wetland and beach conditions when ecological gradients are extremely steep, i.e., highly variable over short distances.

Two types of orbits may prove useful. These include off polar orbits (e.g., Skylab) which tend to pass most coastlines of the Western hemisphere, Europe and Africa at oblique or normal angles and geosynchronous orbits to be utilized in sensing short term hydrologic changes. Primary sensing should occur under daylight conditions and variable sun zenith angles.

Ideally, some ground to satellite communication from an in situ data collection station indicating water levels and temperature and wind conditions would be desirable. In addition, simultaneous aerial photography over ground sampled controlled areas should ultimately be integrated with satellite data for detailed modeling of natural environments.

#### 2.4.3 PROBLEMS

Outside of problems associated with atmospheric interference and sun angle adjustments, problems associated with registration, pixel size, ground data integration, and short term change measurements need consideration.

Registration of multiple data sets acquired from low flying aircraft and the ground need control points to insure accurate results. Ideally, this should be achieved through a network of telemetered information to the orbiting platform and the low flying aircraft from in situ data collection stations. Information concerning ecological conditions could simultaneously be transferred and integrated with spectral information.

The higher the resolution of the system, the higher the potential registration accuracy. In a scanning system this implies that the resolution element (i.e., picture element) would be smaller, which in turn provides considerably more ecological information at the population level. In addition, better correlations between ground observed data and satellite data can be expected with high resolution (small instantaneous field-of-view) systems.

Of course the primary trade-off between low and high resolution digital scanning systems lies in quantities of data. Doubling resolution of a Landsat type system would increase data levels by a factor of four and increasing the number of channels to eight would double that. Special computer systems capable of handling data loads on the order of  $6 \times 10^7$  per image would be required to handle an image. Decisions are therefore required to determine the point at which the need for increased resolution from satellite scanners is traded for high resolution aerial photography.

In conclusion, some compromise between resolution and data bands is wanting. In coastal zone environments, the potential for modeling low resolution systems in order to infer information at the lower ecological levels seems resolvable but demands considerable future research and development.

## 2.5 FORESTRY

### 2.5.1 INTRODUCTION

This section will briefly present the background and information required for forest management decisions, the capabilities and requirements for satellite forest/range remote sensing systems, and how remote sensing can be part of a system of data analysis and information management.

### 2.5.2 BACKGROUND

The Forest Service (ref. 2.5-1) in assessing the nation's renewable resources indicates that 69 percent of the nation's area, 3.95 billion hectares (1.6 billion acres) is in forest and rangeland. However, only 31 percent of the area (1.24 billion hectares = .5 billion acres) is in commercial timberland, i.e., land capable of producing in excess of .268 cubic meters (20 cubic feet) of industrial wood per year per hectare.

The productivity of these forests and rangelands is generally low even though they have the capacity to produce larger volumes of forest and range products through the use of management programs and physical facilities. As the demand for timber and range forage products increases, the use of more intensive management of forest and range resources will be a necessity in the future. However, in addition there will be an equally high demand on these lands for outdoor recreational activities, wilderness areas, wildlife management, and improved water supplies. All these activities must be considered and a plan developed for the best use of these timber and range resources.

More intensive management, which makes use of the best combination of multiple uses of the resources, can increase productivity to meet the projected demands. The intensive management and planning functions, however, will require the analysis of large

amounts of information from many sources. Satellite remote sensing systems could provide some of the information needs for inputs to computer information systems.

Table 2.5-1 (ref. 2.5-2) lists the types of information required to make management decisions in forest and rangelands and the physical parameters which must be measured in order to derive the desired information.

The parameters of interest are traditionally measured on the ground using some statistical sampling strategy and expanded to represent the entire management area. Black and white aerial photography (ref. 2.5-3), and more recently, color infrared (CIR) photography (ref. 2.5-4) have been used to decrease the time necessary to stratify and classify an area while reducing the amount of field work necessary for determination of physical parameters.

### 2.5.3 RESOURCE PARAMETERS FROM SATELLITE SENSORS

This section will discuss the types of forest information currently available from satellite sensors in the visible and near infrared, the thermal, and microwave portions of the spectrum, and the expected sensor requirements needed for optimal performance in future systems.

Most of the past work with satellite systems has involved mainly an analysis of the significance of the spectral signatures in terms of species, vigor, etc. and how they can best be analyzed, i.e., manually or automatically (ref. 2.5-5, 2.5-6, 2.5-7, 2.5-8, 2.5-9). Satellite remote sensing systems to be most useful, however, should be part of a system which analyzes satellite data in relation to other information sources, i.e., geology, soil, weather, and provides information which has a more direct value.

TABLE 2.5-1. -- INFORMATION REQUIRED AND PARAMETERS TO MEASURE FOR FOREST MANAGEMENT (ref. 2)

Information Required	Parameters	Information Required	Parameters
Forest inventory	Acreage of individual trees species (or species groups) Location Number of trees Tree size Phenological data	Forest fire assessment	Dynamics - Fire size - Fire temperature - Wind speed and direction - Rain - Topography
Timber yield	Tree sizes Tree density Growth rate Acreage of crop trees Tree mortality rate		Past fire assessment - Location of burn - Acreage of burn - Degree of damage
Forest stress	Disease Infestation Wildlife Drought index Air pollution Competitive species Flood, landslides Icing	Flammatory conditions	Fuel moisture Wind direction & intensity Air temperature Humidity Precipitation Abundance of dead fuels Density of brush/slash Moisture content of organic debris Topography Prevailing causative factors
Understory inventory	Species Distribution Plant density Plant vigor	Grasslands inventory	Species Acreage Location Plant vigor Phenological data
Soil capability	Mineral content Organic material content Moisture content Soil depth and horizon Mechanical properties Natural drainage	Grasslands stress	Plant diseases Infestation Soil moisture Drought index Humidity Insolation Wind Air pollution Animal grazing Fire
Precipitation	Form Amount Rate Extent Depth of snow fields Water equivalency of snow	Grasslands fire potential	Condition of live vegetation Abundance of dead grass Wind Humidity Precipitation Topography Prevailing causative factors
Surface relief and drainage patterns	Topography Vegetative cover Location of intermittent streams		

2.5-3

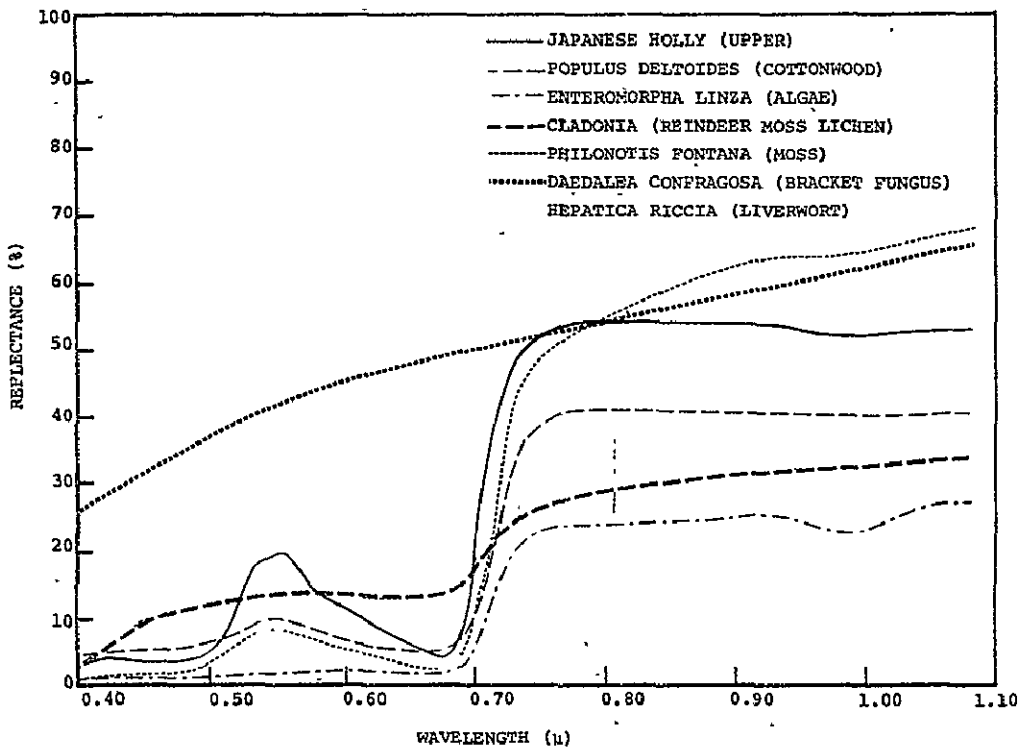
For example, instead of providing area of pine forest, a suitability rating for handling deer is calculated using scanner data. This aspect of remote sensing systems will be discussed in section 2.5.4.

#### 2.5.3.1 The Living Leaf

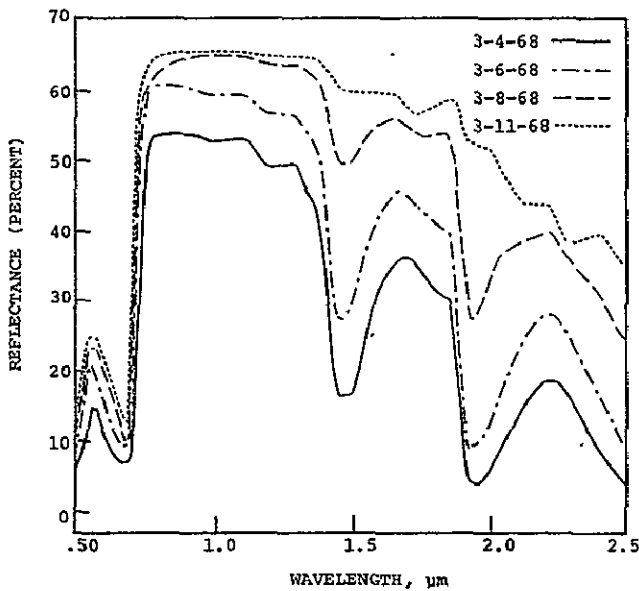
Spectral reflectance from living vegetation can be explained as follows for three spectral regions. The reflected energy from leaves in the visible (.50  $\mu\text{m}$  to .76  $\mu\text{m}$ ) is mainly a function of the pigments (primarily chlorophyllis). In the .75  $\mu\text{m}$  to 1.35  $\mu\text{m}$  region, high reflectance is governed by the internal leaf structure, i.e., reflectance increases with an increase in the number of leaf air spaces because the light passes from regions of high to low refractive index. The 1.35  $\mu\text{m}$  to 2.50  $\mu\text{m}$  region is influenced some by leaf structure, but mainly by water concentration in the tissues (ref. 2.5-10). The spectral reflectances of leaves can differ between species (fig. 2.5-1(a)) due to a stress condition (fig. 2.5-1(b)) and as they age (fig. 2.5-2). However, any one or a combination of these factors can lead to a change in cell structure and a reflectance change. The characteristic reflectance properties of different vegetation has been used as the basis for identifying and classifying forest and soil properties on color and CIR photography (refs. 2.5-3, 2.5-4, 2.5-12) and for automatic classification of multispectral scanner data (refs. 2.5-5 to 2.5-9, 2.5-13 to 2.5-15).

#### 2.5.3.2 Camera Systems

Cameras have been used for a long time as part of forest inventory systems. They provide high resolution data in an easily interpretable form at relatively low cost. These factors are at present unattainable with scanner systems. On the other hand, scanner systems are more compatible with computer systems, which can provide rapid, consistent feature classification for large



(a).- Spectral reflectance of seven species of plants representing diverse groups.



(b).- Effect of progressive leaf drying on spectrophotometrically measured reflectance of upper surfaces of cotton leaves at four dates over the .5- to 2.5 μm wavelength interval. Each spectrum is an average of five leaves.

Figure 2.5-1 - Spectral differences due to (a) species, (ref. 2.5-11), and (b) loss of moisture, (ref. 2.5-10).

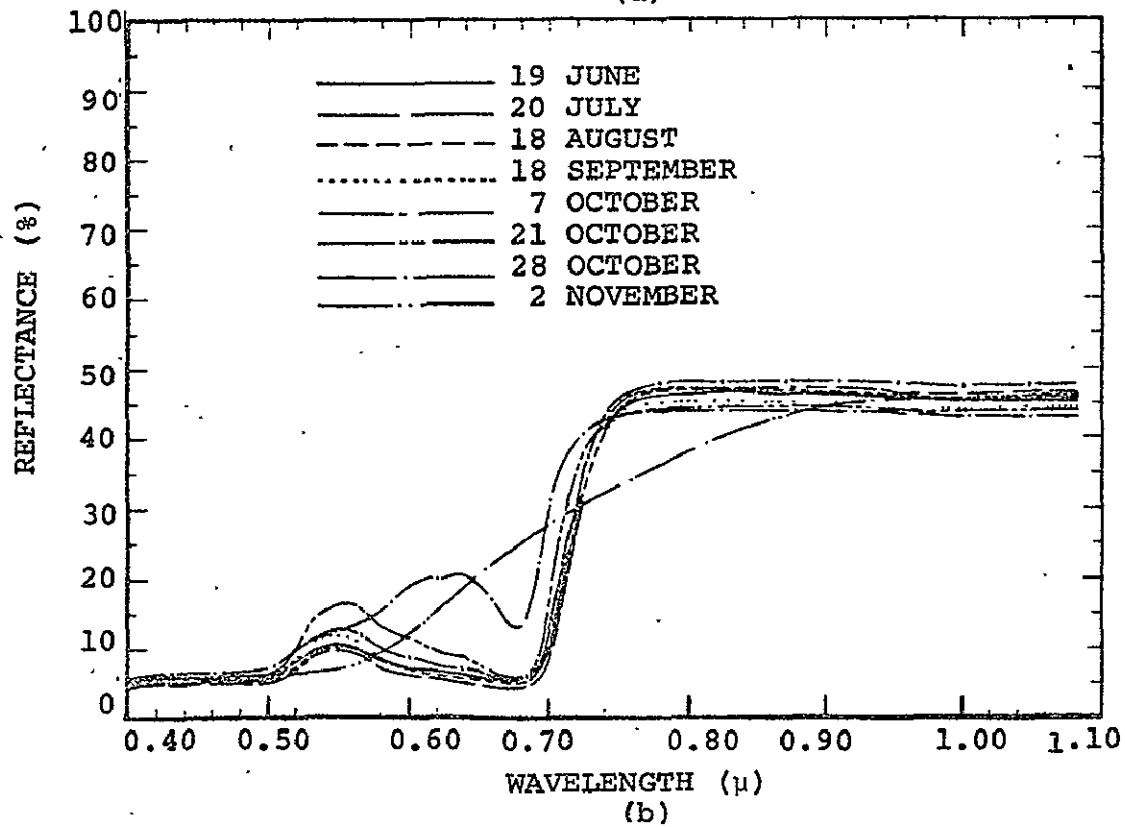
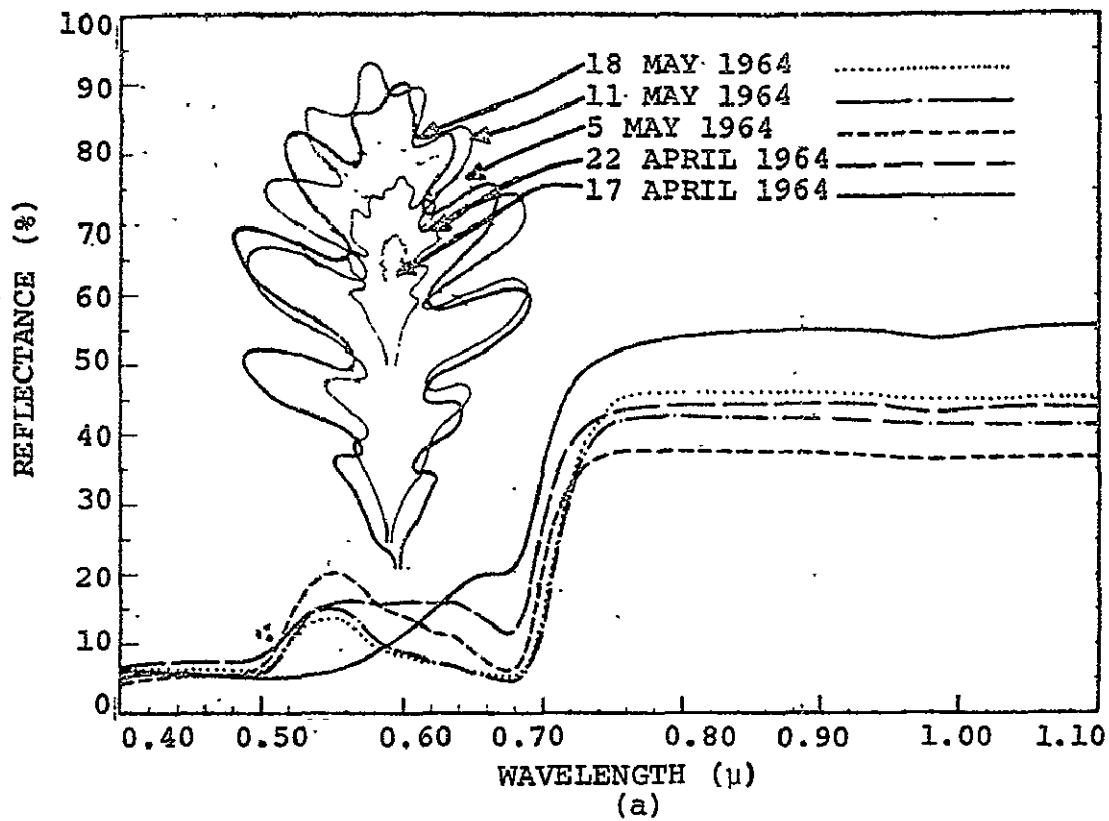


Figure 2.5-2 — Changes in spectral reflectance throughout growing season in *Quercus alba*: (a) April-May; and (b) June-November from ref. 2.5-11.

areas. In addition, the data is easily evaluated or corrected, i.e., for atmospheric corrections or compared with a previous date for detection changes, etc. Future forest managers will no doubt be making increasingly more use of computerized forest inventory data bases, forest models of growth and fire potential, etc., in making their decisions.

At present, the most efficient forest inventories which use satellite scanner data also use high resolution photography as part of a multistage sampling strategy (refs. 2.5-9, 2.5-16). This will probably continue to be the case for sometime in the future. Therefore, for selected areas of interest, high resolution (5m) CIR imagery in a 5 x 5 inch or 9 x 9 inch format will be required as part of statistical sampling plan for correlation of ground data with scanner derived data.

Those forest and grassland parameters of interest which are usually provided by photointerpretation are presented in table 2.5-2. Photointerpretation is able to identify these parameters by an analysis of size, shape, shadow, tone or color texture and pattern. Sometimes site, association, and resolution may also be included. The scanner system currently makes use of only two of these features; color in terms of spectral response and texture or pattern features (refs. 2.5-17, 2.5-18). Scanners can provide the same type of parameters, e.g., density, vigor, but usually not to the same level of detail available from photography or ground surveys.

#### 2.5.3.3 Scanner Systems - Visible and Near Infrared Bands

Several studies into optimal spectral bands (refs. 2.5-13 to 2.5-15, 2.5-19 to 2.5-23) for forest and rangeland features classification have identified a variety of bands as being useful (table 2.5-3). As indicated, the variability in spectral bands

TABLE 2.5-2 - FOREST AND GRASSLAND PARAMETERS DERIVED FROM PHOTO-INTERPRETATION COMPARED WITH INFORMATION FROM AUTOMATIC ANALYSIS OF MULTISPECTRAL SCANNER DATA

Forest Information from Photointerpretation	SCANNER INFORMATION (a)		
	Visible Near Infrared	Thermal	Microwave
Acreage of Tree Species (or Species Group)	+	o	o
Location	+	o	o
Number of Trees	o	/	?
Tree Size	o	/	?
Tree Density	o	/	?
Plant Vigor	o	+	?
Natural Drainage Patterns	+	+	+
Vegetation Cover	+	+	+
Post Fire Assessment			
Location of Burn	+	+	o
Acreage of Burn	+	+	o
Degree of Damage	o	o	o
Density of Brush	o	o	o
Grassland			
Species	o	/	o
Acreage	+	+	o
Location	+	+	o
Plant Vigor	+	+	o
Animal Grazing			

<sup>a</sup>Scanner data is usually not to the same level of detail.

EVALUATION BASED ON PAST STUDIES

- + Highly correlated with photointerpretation results
- o Correlated to some extent
- / Not very correlated

TABLE 2.5-3. - OPTIMUM CHANNELS SELECTED FOR AUTOMATIC CLASSIFICATION OF FOREST FEATURES FROM SEVERAL REFERENCES

REFERENCE	FOREST PARAMETER CLASSIFIED	OPTIMUM CHANNELS			
22	RANGE BIOMASS				
14	SPECIES				
21	RANGE				
19	FOREST/RANGE LAND USE				
20	RANGE				
	FOREST LAND USE				
	SPECIES				
13	FOREST LAND USE				
33	TREE VIGOR w/SNAG				
	w/o/SNAG				
	FOREST LAND USE				
	TREE SPECIES				
	RANGE				

2.5-9

depends on the individual study, i.e., the classes of interest and the geographic area of investigation.

However, from table 2.5-3 and the spectral curves of living vegetation (figs. 2.5-1 and 2.5-2), at least five spectral regions which are consistently selected for forest and range classification can be identified and related to physiological features of leaves:

1. .55  $\mu\text{m}$  to .60  $\mu\text{m}$ . This band covers the chlorophyll transmittance area and may reflect the species, maturity and/or health of the leaves.
2. .66  $\mu\text{m}$  to .70  $\mu\text{m}$  This band covers the region of maximum chlorophyll absorption and variation within the band is related to plant maturity and health. A band centered on the trough at about .68  $\mu\text{m}$  ratioed with a narrow band at .8  $\mu\text{m}$  has been found to be highly correlated with grassland biomass (refs. 2.5-22, 2.5-23).
3. .75  $\mu\text{m}$  to 1.00  $\mu\text{m}$  This band when ratioed with the .66  $\mu\text{m}$  to .70  $\mu\text{m}$  band is highly correlated with grassland biomass. This area also exhibits changes in reflectance due to species, maturity, and/or plant vigor.
4. 1.5  $\mu\text{m}$  to 1.8  $\mu\text{m}$  This band is in the region where reflectance is most influenced by cell moisture and therefore can be used as an indicator of plant health. This band may also help in separating species.

5. 2.1  $\mu\text{m}$  to 2.5  $\mu\text{m}$  This band is also influenced by leaf moisture and may help separate forest types.

#### 2.5.3.4 Thermal Region - 8.0 $\mu\text{m}$ to 14.0 $\mu\text{m}$

The thermal infrared region 8.0  $\mu\text{m}$  to 14.0  $\mu\text{m}$  is used to measure the scene radiance from a target, with respect to a blackbody reference; temperature is calculated using the Stefan-Boltzmann equation. It is generally assumed that plant leaves have emissivity in the range .95 to .98.

Theoretical and experimental studies of individual leaf temperatures (refs. 2.5-24, 2.5-25) have shown them to be dependent on a complex interaction of absorption of solar radiation, transpiration rate, convection forces, background reflectance, leaf size and shape. These all interact to cause differences in single leaf temperatures to range from 2° to 4°C at any one time during the diurnal cycle. Therefore, meaningful thermal scanner data must be measured to within at least 1°C. In general, the thermal band provides temperature data on vegetation which may be indicative of stress, species, moisture levels, or forest types.

In spectral band studies (table 2.5-3) the thermal band (9.3  $\mu\text{m}$  to 11.0  $\mu\text{m}$ ) was consistently selected (when available) as one of the most useful in separating forest features, especially in differentiating non-forest cover types. However, Coggeshall in his study (ref. 2.5-13) concluded that overall classification accuracies and accuracies of classifying deciduous and coniferous stands were not significantly affected when the thermal band was not used in classification.

### 2.5.3.5 Resolution in Visible and Infrared

The resolution of satellite multispectral scanner systems determines the amount of data to be transmitted from the satellite and later analyzed. If the resolution is too small, more information than is necessary is being supplied, which in turn increases the costs and equipment for data transmission and processing. If the resolution is too large, the full information potential of the satellite system can not be realized.

Three recent studies (refs. 2.5-14, 2.5-19, 2.5-26) have considered this question of optimal scanner resolution versus classification accuracy for selected forest features. Results of these studies indicate that the classification accuracies do not increase significantly for resolutions of greater than about 32 meters<sup>2</sup> (m<sup>2</sup>) (fig. 2.5-3).

This value, 32 m<sup>2</sup>, should not be accepted now as the absolute limit, as it is based on only three studies and is considered a limited number of classes and study sites. The data presented in figure 2.5-3 was based on classifying the general forest classes of hardwood, softwood, and others. The study by Sadowski (ref. 2.5-26), which was the most comprehensive, showed increased accuracies with resolutions less than 32 m<sup>2</sup> when five channels were used instead of all eleven possible channels.

### 2.5.3.6 Microwave

The microwave region of the spectrum covers wavelengths of .1 cm to 100 cm and can be divided into active systems such as radar which use an electromagnetic source for illumination and passive systems which record natural radiation from objects. The return from natural materials is a function of the surface roughness, incident angle, polarization, frequency and complex dielectric constant of the material (refs. 2.5-10, 2.5-11).

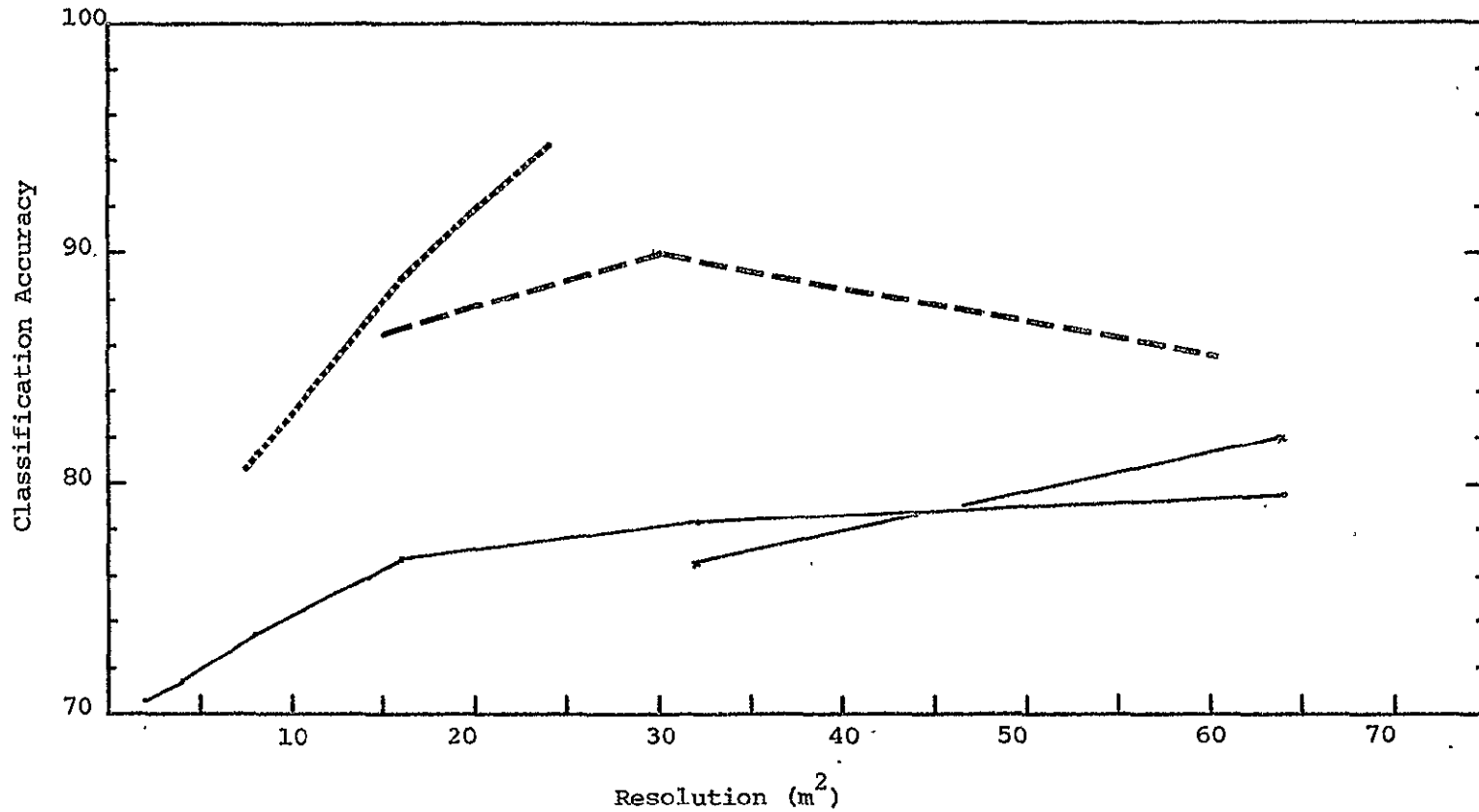


Figure 2.5-3. - Classification accuracy versus resolution for three classes; softwood, hardwood, and other, from three studies: Sadowski, ref. 2.5-26, (—); Kan, ref. 2.5-14, (.....); Thomson, ref. 2.5-19, (- - -).

Most of the studies in the uses of the microwave region have centered on manual interpretation of radar imagery for identification of agricultural features and soil moisture. Surveys on the uses of radar data for forest applications are few (refs. 2.5-27, 2.5-28), but they do indicate that imaging radar may be used for general forest mapping, broad classification of vegetation and site types, and damage assessment. Again, these have been concerned mainly with visual interpretation of radar imagery.

To accurately evaluate the usefulness of the microwave region for forest application, extensive laboratory and field measurements of forest species need to be made for later correlation with airborne data. These measurements would investigate a wide range of frequencies, polarization, view angles, etc., in order to define those parameters which are most useful in identifying forest features. This would be similar to the field data collected and signal modeling performed for agricultural crops and grassland areas (refs. 2.5-29, 2.5-30). Techniques for automatic classification of digital microwave data must be investigated.

In the meantime, satellite microwave systems are planned or are in existence which were designed to meet other discipline requirements. These may be studied to determine their usefulness, if any, in providing additional and unique forest information.

#### 2.5.4 FOREST MANAGEMENT SYSTEMS

Future remote sensing systems developed for forestry will have major significant meaning only if they are compatible and relate to a total forest management model. These management models should be designed to utilize inputs from all sources, including remote sensors, to develop forest management alternatives for evaluation by forest administrators. The parameter model outputs would input to the decision model, which would develop sets of

management alternatives, which would then be analyzed by the administrator.

Figure 2.5-4 presents a block diagram of this management model. The following is an example of how the forest manager might use it to evaluate fire danger within a large forested area such as the state of California. Spectral signatures in the visible, infrared and microwave region collected by satellite sensors over California are used to map the distribution and location of vegetation species, vegetation vigor, vegetation or soil moisture, and amount of dead vegetation. These parameters are input to the user model which uses other data, for example, weather, topography, location of logging operations, etc., in order to develop a rating of fire potential throughout the area. This fire potential would then be evaluated in light of other management decisions (such as costs to fight a fire if it developed in a given area, danger to cities, etc.); in order to develop criteria and contingency plans for reducing activity in forest areas or prepositioning fire fighting forces. It would then be the administrator's function to analyze and select the options presented, or develop his own in order to best handle the fire danger.

The remote sensing aspects of this system have been studied for some time, but the user models and decision models using remote sensing are only now beginning to be developed, tested, and implemented (ref. 2.5-31, 2.5-32).

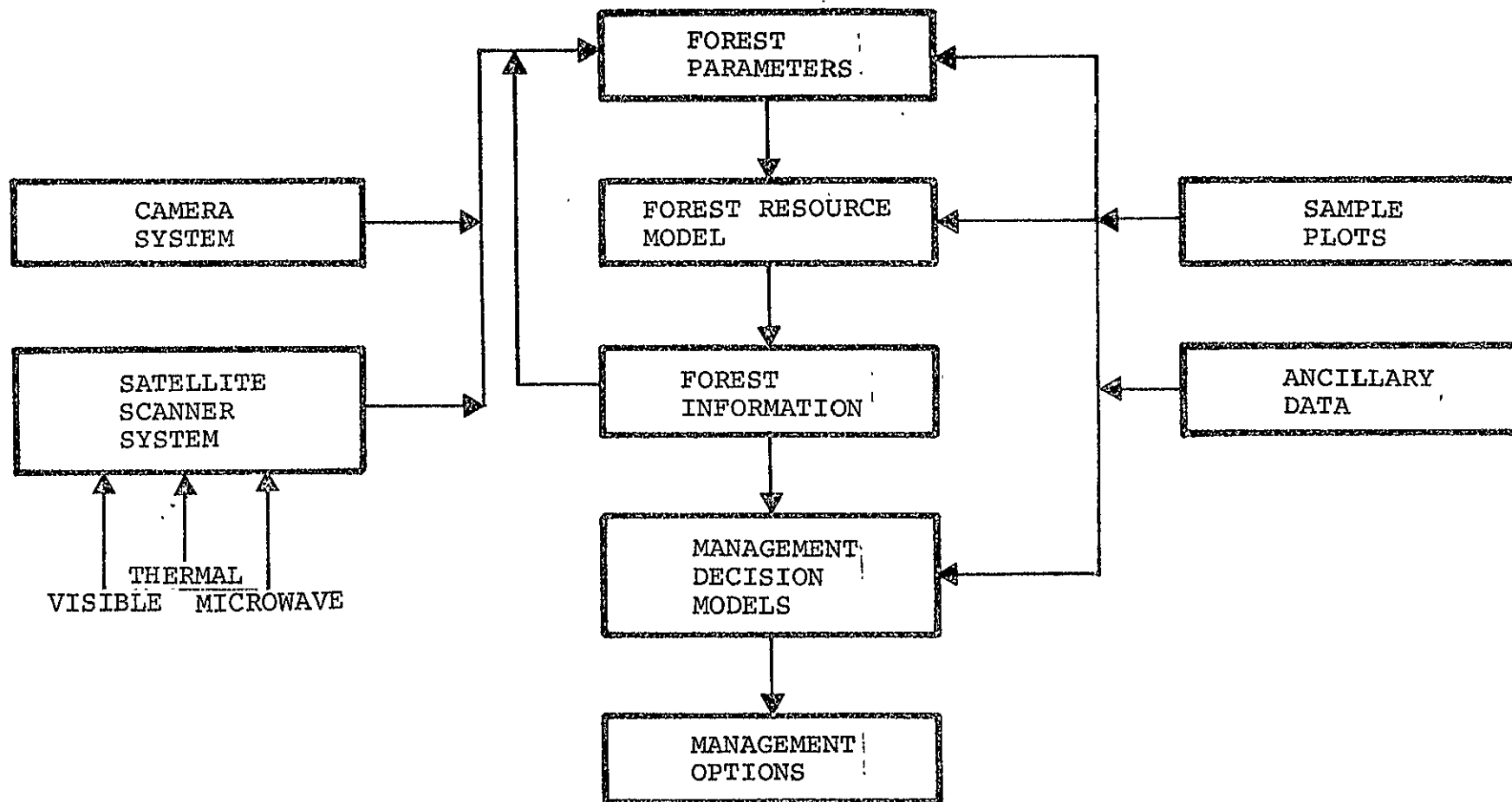


Figure 2.5-4.— Forest/Range Management System, using remote sensing data as an input.

### 2.5.5 SUMMARY

Studies into the use of multispectral scanner systems for forest applications have demonstrated their usefulness in rapidly providing certain general levels of vegetation classification for large areas, but with the expense of large computer systems and time in data acquisition and preparation.

Future forestry remote sensing systems should include some or all of the following components:

Camera:	Film - CIR
	Format - 9 x 9
	Resolution - 5 m
Multispectral Scanner:	Bands - .55 $\mu\text{m}$ to .60 $\mu\text{m}$
	.66 $\mu\text{m}$ to .70 $\mu\text{m}$
	.75 $\mu\text{m}$ to 1.00 $\mu\text{m}$
	1.50 $\mu\text{m}$ to 1.80 $\mu\text{m}$
	2.10 $\mu\text{m}$ to 2.50 $\mu\text{m}$
	9.30 $\mu\text{m}$ to 11.0 $\mu\text{m}$
	Resolution - 30 meters
Microwave:	Bands - unknown
	Polarization - unknown
	Resolution - unknown

Data collection would include total coverage every year, i.e., for the entire U. S., and more frequent coverage over selected study sites or areas of high activity. The remote sensing systems should be compatible with and provide useful forest information for inputs to larger forest data bases and management systems. These data bases would include information from not only remote sensing sources, but past inventories, soil survey, topographic information, and weather information, etc.

#### 2.5.5.1 Recommendations

1. Determine how the data from all sensors can be used together to derive the most useful forest information data. Decide from where the user and decision models will come.
2. Develop models for prediction of biomass, forest composition, fire potential, etc. which make use of visible, near infrared, and microwave data.
3. Conclude what the microwave region can do for forestry, and what are the optimal frequencies, resolution, and polarization.
4. Evaluate the information content of the thermal region by study of the smaller bandwidths, importance of thermal region for classification accuracy, and resolution versus accuracy.
5. Determine what resolutions are required for automatic classification of forest features in the visible, thermal, and microwave regions.

## REFERENCES

- 2.5-1 Forest Service: The Nation's Renewable Resources, 1975 (Draft). Forest Service, U.S.D.A., August 1975.
- 2.5-2 : Definition of the Total Earth Resources System for the Shuttle Era. General Electric, Report to NASA/JSC, Contract NAS9-13401, October 31, 1973.
- 2.5-3 Avery, T. E.: Forester's Guide to Aerial Photo-Interpretation. Agricultural Handbook #308. Forest Service, U.S.D.A., December 1969.
- 2.5-4 Forestry Application Project: Photo-Interpretation Guide for Forest Resource Inventories. Lockheed Electronics Co., Inc., NASA/JSC Contract NAS9-12200, JSC-09977, October 1975.
- 2.5-5 Erb, R. B.: A Compendium of Analysis Results of the Utility of ERTS-1 Data for Land Resources Management. NASA Tech. Memo, NASA TM X-58156, 1974.
- 2.5-6 Heller, R. C.; et al.: Evaluation of ERTS-1 Data for Inventory of Forest and Rangeland and Detection of Forest Stress. Pacific Southwest and Rocky Mountains Forest and Range Experimental Stations, Final Report, Contract S-70251-AD, sponsored by NASA Goddard Space Flight Center, Code 430 GSFC, Greenbelt, Md., December 1974.
- 2.5-7 Kan, E. P.; and Dillman, R. D.: Timer Type Separability in Southeastern United States on Landsat-1 MSS Data. Proc. of the NASA Earth Resources Survey Symposium, Houston, Tx., 1975.
- 2.5-8 Sattinger, I. J.; et al.: Analysis of Recreational Land and Open Space Using ERTS-1 Data. Environmental Res. Inst. of Mich., NASA CR ERIM 193300-60-F, Ann Arbor, Mich., April 1975.
- 2.5-9 Colwell, R. N.: An Integrated Study of Earth Resources in the State of California Based on ERTS-1 and Supporting Aircraft Data. Forestry Remote Sensing Lab., U. of Calif., Berkeley, Calif. NASA Contract NAS5-21827, Final Report, July 1973.
- 2.5-10 American Society of Photogrammetry: Manual of Remote Sensing, Falls Church, Va., 1975.

- 2.5-11 National Academy of Sciences: Remote Sensing with Special Reference to Agriculture and Forestry. Nat. Acad. of Sci., U.S., 1971.
- 2.5-12 Forestry Applications Project: Soil Resources Inventory, Lockheed Electronics Co., Inc. (To be published).
- 2.5-13 Coggelhall, M. E.; and Hoffer, R.M.: Basic Forest Cover Mapping Using Digitized Remote Sensor Data and ADP Techniques. The Lab. for Appl. of Remote Sensing, Purdue U., West Lafayette, Ind., LARS Note 030573, May 1973.
- 2.5-14 Kan, E. P.; Ball, D. B.; Basu, J. P.; and Smelser, R. L.: Data Resolution Versus Forestry Classification and Modeling. Proc. of the Second Symposium on Machine Processing of Remotely Sensed Data, held at Purdue U., West Lafayette, Ind., June 3-5, 1975.
- 2.5-15 Weber, F. P.; Aldrich, R. C.; Sadowski, F. G.; and Thomson, F. J.: Land Use Classification in the Southeastern Forest Region by Multispectral Scanner and Computerized Mapping in Monitoring Forest Land from High Altitude and from Space. Pacific Southwest Forest and Range Experiment Station, Forest Service, USDA, Berkeley, Calif., 1972.
- 2.5-16 Aldrich, R. C.: Space Photos for Land Use and Forestry. Photogrammetric Engineering, Vol. 37(3), 389-401, 1971.
- 2.5-17 Haralick, R.: Documentation of Procedures for Textural/Spatial Pattern Recognition Techniques. Final Report, RSL 278-1, U. of Kansas Space Tech. Center, April 1976.
- 2.5-18 Kervida, L.; and Johnson, G.: Automatic Interpretation of ERTS Data for Forest Management. Symposium on Remote Sensing of the Environment, NASA Goddard Symposium on Significant Results Obtained from ERTS 1, Vol. 1, 1973.
- 2.5-19 Thomson, F. J.; et al.: Multispectral Scanner Data Applications Evaluation; Vol. 1 User Applications Study. Envir. Res. Inst. of Mich., U. of Mich., Ann Arbor, Mich. Final Report to NASA/JSC Contract NAS9-13386-CCA2, NASA JSC 09241, ERIM 102800-40-F, December 1974.
- 2.5-20 Hoffer, R.; et al.: Computer-Aided Analysis of Skylab Multispectral Scanner Data in Mountainous Terrain for Land Use, Forestry Water Resources and Geologic Applications Laboratory for Application of Remote Sensing. LARS Note 121275, 1975.

- 2.5-21 Wagner, T.; and Coldwell, J.: An Investigation of Grassland Resources Using Multispectral Processing and Analysis Techniques. Willow Run Labs., Report 34795-1-F. U. of Mich., Ann Arbor, Mich.
- 2.5-22 Pearson, R.; et al.: Spectral Mapping of Shortgrass Prairie Biomass. Photogrammetric Eng. and Remote Sensing. Vol. 42, No. 3, March 1976.
- 2.5-23 Coldwell, J.; Grass Canopy Bidirectional Spectral Reflectance. Proc. of the 9th Int. Symposium on Remote Sensing of Environment, Environmental Res. Inst. of Mich., April 1974.
- 2.5-24 Gates, D.: Characteristics of Soil and Vegetated Surfaces to Reflected and Emitted Radiation. Proc. of 3rd Int. Symposium on Remote Sensing of the Environment, Willow Run Labs., November 1965.
- 2.5-25 Gates, D.; and Wirojana, T.: The Reflectivity of Deciduous Trees and Herbaceous Plants in the Infrared to 25 Microns. Science, Vol. 115, June, 6, 1952.
- 2.5-26 Sadowski, F.; and Sarno, J.: Forest Classification Accuracy as Influenced by Multispectral Scanner Spatial Resolution. Environmental Res. Inst. of Mich., ERIM Report 109600-71-F, May 1976.
- 2.5-27 Hughes, C.: A Survey of SLAR Investigations on Earth Resources with Applications to Forestry. Lockheed Electronics Co., Inc., Job Order 75-315, December 1975.
- 2.5-28 Hughes, J.: Potential Applications of SLR to the Remote Sensing of Earth Resources, Vol. 3, Forestry. ESTEC Contract 1537/71/EL.
- 2.5-29 Cosgriff, R.; et al.: Terrain Scattering Properties for Sensor System Design (Terrain Handbook II). Eng. Exper. Station, Ohio State U., Vol. XXIX, No. 3.
- 2.5-30 Ulaby, F.; et al.: On Microwave Remote Sensing of Vegetation. Eighth Int. Symposium on Remote Sensing of the Environment. Environmental Res. Inst. of Mich., October 1972.
- 2.5-31 Sattinger, I.; et al.: Analysis of Recreational Land and Open Space Using ERTS-1 Data. Environmental Res. Inst. of Mich., ERIM 193300-60-F, April 1975.

- 2.5-32 Tanner, C.: A System Verification Package for LUPAP (Land Use Planning Assistance Process). Forestry Applications Program, NASA/JSC, Job Order 75-315, December 1975.
- 2.5-33 Heller, R.: Monitoring Forest Land From High Altitude and From Space. Pacific Southwest Forest and Range Experiment Station, Forest Service, USDA, Final Report, September 1972.

## 2.6 GEOLOGY

The following discussions are based upon a consensus of Skylab investigator reports and the writer's experience formed over years of interpreting aerial photography and viewing and interpreting Skylab and Landsat data.

The application of remote sensing in geologic mapping began in the early 20's. Aerial photography has been used for many years and the use advanced rapidly after World War II. It was used extensively in certain domestic areas, especially the Rocky Mountain region and in foreign countries for regional geologic mapping and for petroleum and mineral exploration. The use of photogeology reached a peak in the United States by the mid fifties. The most recent flurry of activity in remote sensing for geological applications began with the distribution of Landsat (ERTS) and Skylab data although some studies were conducted using Gemini and Apollo handheld photography.

The most practical and useful space sensor for geological studies is the high resolution camera. The photography from this instrument will probably continue to be the data most in demand by geologists. The main characteristics or advantages of a camera system such as the Skylab S-190A or S-190B are synoptic view, stereoscopic viewing capability and resolution. These two camera systems provide the geologist with the synoptic view which is so important in understanding and interpreting the regional geology of an area. This view obtained with high resolution color or color infrared film gives the geologist an opportunity to look at his area of interest from a new altitude and at a different scale. Field geologists have always climbed the highest peak in their area to get that "best look." Space data provides this "best look" and enables the geologist to map and extend trends for hundreds of miles and to perceive anomalies which may be indicators of subsurface structures which can trap oil or gas

and can also indicate areas prospective for mineral deposits. Faulting and alteration zones are probably the two most useful indicators of mineralization. These often appear as tonal lineaments and color anomalies on the photography. Space photography does not provide direct indicators of oil, gas, or mineral deposits but can give clues on where to conduct other exploration surveys such as aerial photography, surface mapping, geophysical surveys and exploration drilling. Space photography can be useful in geothermal exploration for mapping major fault trends which can be conduits for magma and hot water to move upward to the near surface where the heat can be economically tapped.

The major benefit of using space data is the development of new geologic concepts provided by the synoptic view, high resolution, high quality color and stereoscopic capability. These new developments will probably result from the observation of obscure and subtle features that have not been mapped by conventional methods. The most obvious and exposed geologic features have been mapped.

The multispectral scanner of the Landsat system is useful for geologic mapping since it provides a synoptic view and continuous coverage. Temporal data is an asset for mapping geology in some areas. An example of such an area is the Great Plains where the best time of the year for acquiring data is in the early spring before the vegetation conceals the soil and surficial deposits. A light snow cover can be useful for enhancing linear features in some areas. Certain types of vegetation can be indicators of geologic lithology or formations. Data over these areas should be taken at the height of the growing season. Recent Skylab studies suggest that bands 8, 10 and 11 of the S-192 multispectral scanner provide the highest contrast for mapping rocks. This may prove to be the most important feature of the

multispectral scanner for geologic mapping. These spectral bands of the infrared region are not available on the film of the camera systems. The automatic discrimination and identification of rock types by computer analysis of multispectral scanner data does not look promising at the present time. A large number of variables including vegetation cover, weathering, soil cover, changing composition of the rock, topography, moisture, dip and strike, atmospheric conditions, sun angle, sun azimuth and temperature affect the spectral signature of exposed rocks and tend to inhibit the identification of unique signatures for rock types. The best discriminator of rocks which are well exposed in space data is the geologist trained in photogeology interpreting high resolution color film. Further research is required for using the near and middle infrared scanner bands in geologic mapping and for determining if these bands are practical for automatic discrimination by computer. These studies should be conducted with the S-192 data.

The thermal band of the scanner has not proven to be very useful for mapping regional geology or for locating geothermal areas. There were very few pre-dawn passes during Skylab and daytime thermal infrared data is degraded by solar heating. Higher resolution detectors and nighttime data takes are required for the thermal infrared scanner to be of use for geologic mapping. The resolution of the microwave radiometer, scatterometer and the K-band sensors which were on-board Skylab was too large to be of use in geologic mapping.

A radar type image of high resolution would be a useful tool over jungle and cloud covered areas of high topographic relief. The instrument will not be of particular benefit over low relief, plains type terrain and areas where the rocks are well exposed, such as arid regions. High resolution color is obviously the best data collector for these areas if lower cloud cover would permit its acquisition.

A recommended sensor package for future space missions for geologic mapping should consist of the following instruments, based upon a 250-mile polar drifting orbit:

- A multispectral camera system consisting of at least four cameras with S-190B resolution, (12 meters), 9 inch format, and loaded with color, color infrared, black and white panchromatic, and black and white infrared film. This system should be operated to obtain worldwide cloud-free stereoscopic coverage at least once and also on a demand basis.
- A high resolution multispectral scanner to obtain data in the near, middle, and thermal infrared region and to be operated only over specific areas of interest.
- An imaging radar system to be operated only over areas covered with dense vegetation or clouds. The areas which are constantly covered by clouds and have a vegetative cover should be imaged by a radar system at least once.

Astronaut Carr reported in one of the Skylab geology debriefing sessions that even the high quality S-190B imagery is a poor substitute for the view that can be seen with the human eye from space. The best method for regional geologic mapping from space may be an astronaut geologist conducting interpretations aboard a spacecraft and aided by remote sensing systems with developing and processing capability of the data onboard the spacecraft.

## BIBLIOGRAPHY

- Abdel-Gawad, M.; and Tubbesing, L.: Analysis of Tectonic Features in U.S. Southwest from Skylab Photographs. NASA CR-144464, 1975.
- Bannert, D.: Hydrogeological Investigation in the Pampas of Argentina. NASA CR-144488. 1976.
- Bechtold, I.C.; Reynolds, J.T.; Archer, R.L.; and Wagner, C.G.: An Evaluation of Skylab (EREP) Remote Sensing Techniques Applied to Investigations of Crustal Structure. NASA CR-144383, 1975.
- Cassinis, R.; Lechi, G.M.; and Tonelli, A.M.: Results of Skylab Investigation Over Italy. NASA CR-147396, 1975.
- Collins, R.J.; Petzel, G.J.; and Everett, J.R.: Evaluation of the Suitability of Skylab Data for the Purpose of Petroleum Exploration. NASA CR-147468, 1975.
- Colwell, R.; and Bowden L.W.: Use of Skylab Imagery to Assess and Monitor Change in the Southern California Environment. NASA CR-147561, 1976.
- Cooper, S.; Anderson, D.; et al.: Skylab Imagery: Application to Reservoir Management in New England. NASA CR-144514, 1975.
- Frierson, V.R.; and Amsbury, D.L.: Space-Acquired Imagery: Versatile Tool in Development of Energy Sources. 59th Annual Meeting of American Association of Petroleum Geologists, April 1974.
- Goetz, A.F.H.; Abrams, J.J.; et al.: Comparison of Skylab and Landsat Images for Geologic Mapping in Northern Arizona. NASA CR-147503, 1976.
- Goetz, A.F.H.; Rowan, L.C.; Wetlanfer, P.N.; Billingsley, F.C.; and Stewart, J.H.: Discrimination of Rock Types and Detection of Hydrothermally Altered Areas in South-Central Nevada by the Use of Computer-Enhanced ERTS Images. U.S.G.S. Prof. Paper 883, 1974.
- Guillemot, J.; and Rivereau, J.C.: Project Pyralp-Tectonic Relationship Between the Pyrenees and Alps (Southern France). NASA CR-140127, 1974.
- Gumerman, G.J.; Hanson, J.A.; Brew, D.; Tomoff, K.; and Weed, C.S.: The Hydrology of Prehistoric Farming Systems in a Central Arizona Ecotone. NASA CR-144492, 1975.

- Hoffer, R.M.: Computer-Aided Analysis of Skylab Multispectral Scanner Data in Mountainous Terrain for Land Use, Forestry, Water Resource, and Geologic Applications. NASA CR-147473, 1976.
- Hoppin, R.A.: Experiment to Evaluate the Feasibility of Utilizing Skylab/EREP Remote Sensing Data for Tectonic Analysis Through a Study of the Big Horn Mountain Region, Wyoming. NASA CR-147543, 1976.
- Houston, R.S.; Marrs, R.W.; and Borgman, L.E.: Final Report on Multidisciplinary Study on Wyoming Test Sites. NASA CR-147719, 1975.
- Lambert, B.P.: A study of the Usefulness of Skylab EREP Data for Earth Resources Studies in Australia. NASA CR-144488, 1975.
- Lee, K.; Prost, G.L.; Knepper, D.H.; Sawatzky, D.L.; Huntley, D.; and Weimer, R.J.: Geologic and Mineral and Water Resources Investigations in Western Colorado, Using Skylab EREP Data. NASA CR-144513, 1975.
- McMurtry, G.J.; and Peterson, G.W.: Interdisciplinary Applications and Interpretations of EREP Data Within the Susquehanna River Basin. NASA CR-147541, 1976.
- Merifield, P.E.; and Lamar, D.L.: Application of Skylab Imagery to Analysis of Fault Tectonics and Earthquake Hazards in the Peninsular Ranges, California. NASA CR-144447, 1976.
- Moore, G.K.: Hydrologic Significance of Skylab Lineaments in Central Tennessee. NASA CR-144490, 1976.
- Morrison, R.B.; Lineback, J.A.; Fuller, H.K.; and Rinkenberger, R.K.: Applications of Skylab EREP Photographs to Mapping Landforms and Environmental Geomorphology in the Great Plains and Midwest. NASA CR-144491, 1975.
- Olson, N.K.: Application of Multispectral Photography to Mineral and Land Use Resources in South Carolina. NASA CR-144109, 1975.
- Siegal, B.S.; et al.: Final Report on the Detection of Geothermal Areas From Skylab Thermal Data. Jet Propulsion Laboratory Tech. Memo 33-728, 1975.
- Stoiber, R.E.; and Rose, W.I.: An Investigation of Thermal Anomalies in the Central American Volcanic Chain and Evaluation of the Utility of Thermal Anomaly Monitoring in the Prediction of Volcanic Eruptions. NASA CR-144496, 1975.

- Thomson, F.: Machine Processing of S-192 and Supporting Aircraft Data Studies of Atmospheric Effects, Agricultural Classification, and Land Resource Mapping. NASA CR-144503, 1975.
- Van der Meer Mohr, H.E.C.: Evaluation of EREP Techniques for Geological Mapping. NASA CR-144494, 1975.
- Vincent, R.; Salmon, B.; Pillars, W.; and Bennett, C.: Assessment of Mapping Exposed Ferrous and Ferric Iron Compounds Using Skylab EREP Data. NASA CR-144504, 1975.
- Watson, K.; O'Leary, D.W.; and Pohn, H.A.: A Photography Comparison of Skylab and Landsat Images of Southwestern Nevada and Southeastern California. NASA CR-144642, 1975.
- Wier, C.E.; Amato, R.V.; Russell, O.R.; Martin, K.R.: Application of EREP Imagery to Fracture-Related Mine Safety Hazards in Coal Mining and Mining Environmental Problems in Indiana. NASA CR-144495, 1975.

## 2.7 HYDROLOGY

### 2.7.1 BACKGROUND

There are basically six types of hydrologic environments of interest which lend themselves directly or indirectly to being mapped or detected by remote sensors flown on aircraft or satellites. These six are: (1) surface water within the interior of land masses, i.e., lakes and streams; (2) ground water which cannot be directly detected but rather inferred from surface features and/or conditions; (3) coastal waters which include bays, estuaries, and marshes; (4) ocean water masses; (5) ice and snow masses; and (6) atmospheric water vapor.

Only three of these hydrologic environments will be covered in this section. They include surface water, subsurface water, and ice and snow. The other three types, i.e., coastal waters, ocean waters and atmospheric water, are covered under sections entitled coastal studies, oceanography, and atmospheric, respectively.

It goes without saying that many papers have been written regarding the applicability of remotely sensed data, acquired from both aircraft and satellites, to hydrologic problems. Most of these studies include the use of one or more of the following types of sensor data: photographic imagery, microwave imagery, infrared imagery, and multispectral spectrometry imagery.

Historically, surface hydrology and hydrologic features such as drainage patterns, flood basins, etc., were mapped from surface observations and from low to medium altitude aircraft imagery. However, in recent years it has become increasingly clear that high altitude aircraft and satellite imagery can provide much of the data required to map surface water bodies, surface features and conditions related to surface and subsurface hydrology

and for the detection and mapping of essentially all significant surface snow and ice masses. The synoptic view acquired from high altitudes provides the means for mapping very large areas, and has proven to be an asset in mapping features and trends valuable to ground water hydrology.

### 2.7.2 SATELLITE MAPPING

Nimbus I was the first satellite with a sufficiently high inclination orbit to provide daily photographic type imagery for most of the earth. This imagery has proven to be directly applicable to hydrologic type mapping. The acquisition of data from Nimbus I began in 1964 and has been followed by six additional Nimbus satellites. In 1971, Landsat-1 was launched with a multispectral imaging capability which provided a great deal of imagery directly applicable to many disciplinary mapping problems including that of hydrology. Landsat-2 has subsequently been launched and is equally applicable to this type mapping even though it is primarily dedicated to agricultural mapping.

Landsat imagery has been used not only to map surface water bodies and drainage patterns as related to hydrologic problems, but also to map such geologic features as faults, fractures and lineations which in many cases are indicative of areas where ground water accumulates. Fault and lineation mapping for possible sources of ground water using Landsat imagery has been demonstrated by numerous hydrologists and Landsat principal investigators.

Skylab photography and multispectral spectrometry data have also been used in mapping hydrologic features. Much of the Skylab data are of higher resolution than are either the Nimbus or Landsat data. However, because of the relatively low inclination orbit, it does not provide the extensive global coverage as does the higher inclination satellites. In addition, photography

acquired from satellites is somewhat limited when compared to scanner imagery in that there have been restrictions on the amount of film which could be transported to and from orbit in the manned spacecraft program.

### 2.7.3 RECOMMENDATION FOR CONTINUATION OF STUDY

Any continuation of this study should include the examination of advantages and disadvantages of the different types of imagery, resolution requirements, spectral bands, data accuracy requirements, etc., as required for hydrologic mapping. This should include an assessment of remotely sensed data acquired from both aircraft and satellite systems. Also a more extensive bibliography should be compiled on past work regarding the application and applicability of remotely sensed data to hydrological problems. This would facilitate a more complete assessment and understanding of the overall application and potential application of remote sensors to hydrology.

## BIBLIOGRAPHY

"An Analytical and Experimental Study of Stereo for Radar,"  
Photogrammetric Engineering, Vol. 29, 1963, pp. 294-300.

"An Evaluation of Radar Imagery As a Tool for Drainage Basin  
Analysis," ERTS Tech. Dept. 61-31, University of Kansas, 1967.

"Procedures of Applying Air Photointerpretation in the Location  
of Ground Water," Photogrammetric Engineering, Vol. 24, 1958,  
pp. 35-49.

McCoy, Rodger M.: "Rapid Measurement of Drainage Density,"  
Dept. of Geography, University of Kentucky, Society of American  
Bulletin, Vol. 82, March 1971, pp. 577-762.

## 2.8 LAND USE

### 2.8.1 INTRODUCTION

During the past decade, there has been a dramatic increase in land use studies. Along with this increased activity, attempts to exploit remote sensing systems to serve as a "tool" have also increased. These studies extend from a simple investigation of mapping the extent of a city by the analysis of a single frame of photography to the more complicated and sophisticated statewide inventories of all natural resources. The former study might find a planner using a direct method of overlaying a photograph with mylar to record and convey whatever information is deemed important. The latter situation is much more complex in terms of the interaction of the number of personnel, data sources, equipment requirements, storage and retrieval capabilities, etc. In terms of specific land use discipline applications, it has been reasonably demonstrated that Skylab S190B-type photography can provide valuable information for recreational planning (Sattinger, ref. 2.8-1); mapping and inventorying of coastal wetland features (Klemas, ref. 2.8-2); (Welby, ref. 2.8-3 and Anderson, ref. 2.8-4); wildlife habitat identification and mapping (Gilmer, ref. 2.8-5); surface mining and reclamation activities (Brooks, ref. 2.8-6); Baldrige, ref. 2.8-7; and Weir, ref. 2.8-8); and a wide variety of urban, country, regional, and statewide planning projects (Hardy, ref. 2.8-9; Baldrige, ref. 2.8-7; Simonett, ref. 2.8-10; Alexander, ref. 2.8-11; and Hanna, ref. 2.8-12).

Although the findings of the recently concluded Skylab land use investigations are not quantitative, sufficient evidence exists to make at least qualitative statements about recommended spatial and spectral requirements for future space sensor systems.

## 2.8.2 CAMERA SYSTEMS

To maximize the potential and practical applications of remote sensing data, as applied to general land use problems, the prime sensor should be a camera or preferably, a cluster of cameras. Specifically, an optimum camera system would include several (two to four) Skylab S190B-type cameras with (1) improved spatial resolution of 3 to 5 meters for low contrast scenes and (2) an enlarged film format (either 9 x 9 in. or 9 x 18 in.). Based on previous studies, namely Skylab S190B results, increased spatial resolution for the bulk of land use related activities is a prime requirement. The spatial resolution afforded by the S190B camera (and the three different film types used) was a positive step, but even that camera system did not provide adequate resolution to enable a comprehensive assessment for a wide range of discipline objectives. Non-Skylab surveys of actual user requirements which were conducted by the USGS and Cornell University verified that spatial resolution of 3 to 5 meters would dramatically increase the value of photography collected from a space platform. Figure 2.8-1 is a fairly typical, representative graphic that communicates the different spatial resolution requirements that are essential for the identification of a broad range of environmental features (Simonett, ref. 2.8-10).

In addition to the spatial aspect, the spectral qualities of spaceborne camera systems (film/filter combinations) must be considered. Again, sufficient evidence is now available to recommend that the first choice of film type for future systems would be a high resolution color infrared (CIR) film, e.g., S0-131. A high resolution natural color film would be a close second choice. Although panchromatic black and white film and black and white infrared films are also considered important for selected applications, their consideration for inclusion into a future photo-system module (PSM) is not as critical as the first two choices.



Flexibility in engineering design of a PSM should ensure a high degree of flexibility for ease of interchanging film magazines and also have the capability for rapid filter changes.

Another important factor to be considered for future land use remote sensing endeavors is the frequency of data collection. Naturally, the interval between data collection passes will be a function of the specific application or objective of the discipline area being studied. Despite the unique qualities for some studies, several general statements can be made regarding overall land use/planning data collection intervals. For most land use regional scale and relatively static inventorying efforts, three to five year intervals would be adequate. For smaller or more dynamic areas and most urban planning activities, data collection would only be required every one to two years.

For very unique and dynamic studies, i.e., monitoring strip mines, dam sites and highway construction, and fluctuating water impoundment studies, etc., data would be required as frequently as every six months.

In some geographical areas and for certain types of natural resource inventories, it would be desirable to collect data, at least initially, two times during the year to observe and assess the implications and impact of temporal data, e.g., leaf-on versus leaf-off scenes. In conjunction with the frequency interval, the appropriate type of film/filter combination(s) would be a vital consideration during the pre-mission phase of the planning cycle.

Perhaps the key ingredient for a successful mission is the development of a comprehensive and detailed pre-mission plan. In the past, sensors and mission parameters have been established prior to the selection of principal investigators or the

determination of how the collected data would be used. This constitutes a very harsh constraint in that (1) there is no input into designing the complete experiment, and (2) the eventual investigation is locked into a mode of performing with the data provided. Obviously, this type of "cart before the horse" philosophy is inefficient and does not provide the vast majority of remote sensing and earth science practitioners with an opportunity to make valuable inputs into that part of the investigation that would appreciably enhance their study and applications.

### 2.8.3 MULTISPECTRAL SCANNERS

Although a few applications systems have been developed, a sampling of aircraft, Skylab, and Landsat multispectral investigations and experiments indicates multispectral sensing systems have been utilized primarily in an experimental mode. In spite of the frequently heralded fact that Landsat 1 and 2 provides the advantage of repetitive coverage, this type of data has limited application to assist in the solution of land use problems. This is primarily because of the large resolution of 79 meters. Even though narrow spectral bands of Landsat 1 and 2 and even narrower spectral bands of Skylab coupled with the machine processing capability offer some potential benefits, most land use investigations are not afforded adequate spatial resolution to perform inventory and planning functions for making either policy-making or management decisions. Photographic systems, such as the S190B, offer much greater land use application utilization, and the Landsat D thematic mapper with a resolution of 30 meters will offer much greater detail for land use than the Landsat 1 and 2 multispectral scanners.

Surveys have been conducted where actual scanner products (imagery, printouts, etc.) have been furnished to assorted levels of planning agencies (from federal agencies down to small town planning agencies). The results of these surveys are almost unanimous: scanner products are of little practical value,

except for public relations efforts and graphic presentations. This response can partially be attributed to a viable means to transfer the existing technology to actual users, but it is also attributable to the fact that insufficient detail is available.

On a more positive note, a group of Skylab investigators: Sattinger, Klemas, Gilmer, Simonett, Alexander and Hannah, op cit.; Hoffer (ref. 2.8-13); Silvan (ref. 2.8-14); and Higer (ref. 2.8-15) provided a great deal of insight into the use of computer processing techniques for analyzing spacecraft multispectral scanner data for land use applications. Reasonably accurate (75-90%) overall classification accuracies were achieved for Level II land use maps using computer-aided analysis techniques (Anderson, ref. 2.8-16). Acreage estimates, based upon computer-aided analysis of Skylab S192 data, were highly correlated with acreage estimates obtained through standard photointerpretation techniques using aircraft photography.

The increased spectral range offered by the S192 scanner system was of particular significance since this was the first time that multispectral scanner data had been obtained from the visible through thermal infrared wavelengths of the electromagnetic spectrum from satellite altitudes. Several investigators found that at least one wavelength band from each of the four major portions of the electromagnetic spectrum (visible, near infrared, middle infrared, and thermal infrared) was necessary to achieve optimal computer classification of land use categories. The near infrared portion of the spectrum was found to be particularly important for accurate discrimination among various vegetative cover types. In other studies, a combination of six wavelength bands were cited as being optimal for land use mapping using computer-aided analysis techniques.

Considering all of the Skylab S192 users, it appears that two wavelength bands in the visible wavelengths, two bands in the near infrared, one in the middle infrared, and one in the thermal infrared band would provide the optimum number of bands for overall classification of land use categories.

Several of the Skylab S192 land use investigators (ref. 2.8-5, 2.8-10, 2.8-13, and 2.8-14) concluded that the improved spectral resolution and the increased spectral range available in scanner systems such as the Skylab S192 (as compared to the Landsat-1 MSS system) enabled significant improvement in classification performance for land use mapping. A few investigators (ref. 2.8-1, 2.8-13, and 2.8-14) even indicated that the improved spectral resolution obtained in the Skylab S192 scanner data was more important for mapping many cover-type features than was the spatial resolution obtained through use of the S190 photographic sensor systems.

In nearly every study in which S192 data was utilized in conjunction with computer-aided analysis techniques, the investigators concluded that traditional definitions of land use categories often will not produce spectrally separable informational classes of data output. To obtain maximum benefit from multispectral scanner data, it will be necessary in many cases to establish land use category definitions that are based upon spectrally discriminable classes of cover type.

The Skylab experiments enabled both photographic and multispectral scanner data to be applied to many land use mapping activities in a manner never before possible. Both the photographic and scanner data were shown to be of value for land use mapping purposes. Evaluation of Skylab data, as well as map and tabular products obtained from the Skylab data, by representatives of many user agencies brought positive responses concerning the

value of such data. The Skylab EREP experiment successfully demonstrated, beyond any doubt, the significant value of such photographic and multispectral scanner data obtained from satellite altitudes for a multitude of land use purposes.

#### 2.8.4 MICROWAVE SENSORS

Few attempts have been made to investigate the use of microwave sensors (including imaging radar systems) for land use purposes. Although attempts have been made by avid proponents of imaging radar capabilities to promote these sensors as an effective land use tool, more effective means are available, e.g., photography to accomplish the same objectives. Radar has only a limited capability, primarily in areas that are almost constantly cloud covered or in areas where the mapping is poor or nonexistent.

#### 2.8.5 THERMAL INFRARED (IR) SCANNERS

From a space platform, the same spatial resolution limitations exist for the thermal infrared scanners as for the multispectral scanners. Future space platforms with thermal IR scanners would offer some advantages if sufficient spatial resolution and spectral sensitivity were attained to permit monitoring of water pollution, forest fires, various oceanographic investigations, urban/rural temperature differentiations, etc. This is certainly an area where future experimentation should occur.

## REFERENCES

- 2.8-1 Sattinger, P.J.; Sadowski, F.G.; and Roller, N.E.G.: Analysis of Recreational Land Using Skylab Data. NASA CR-144471, January 1976.
- 2.8-2 Klemas, V.; Bartlett, D.S., et al.; Philpot, W.D.; Rogers, R.A. and Reed, L.E.: Skylab/EREP Application to Ecological, Geological, and Oceanographic Investigations of Delaware Bay. CMS-NASA-1-76, May 1976.
- 2.8-3 Welby, C.W.; Lammi, J.O.: Utilization of EREP Data in Geological Evaluation, Regional Planning, Forest Management and Water Management in North Carolina. NASA CR-144104, October 1975.
- 2.8-4 Anderson, R.R.; Carter, V.; Alsid, L.: Skylab-EREP Investigation of Wetlands Ecology. Draft - Final Report - to be published.
- 2.8-5 Gilmer, D.S.; Work, E.A., Jr.: Utilization of Skylab EREP System for Appraising Changes in Continental Migratory Bird Habitat. NASA CR-147452, December 1975.
- 2.8-6 Brooks, R.L.; Parra, C.G.: Applicability of Satellite Remote Sensing for Detection and Monitoring of Coal Strip Mining Activities. NASA CR-144474, September 1975.
- 2.8-7 Baldridge, P.E.; Goesling, P.H.; Martin, T.A.; Wukelic, G.E.; Stephan, J.G.; Smail, H.E.; and Ebbert, F.F.: Utilizing Skylab Data In On-Going Resources Management Programs in the State of Ohio. NASA CR-134938, November 1975.
- 2.8-8 Weir, C.F.; Powell, R.L.; Amato, R.V.; Russell, O.R.; and Martin, K.R.: Application of EREP Imagery to Fracture-Related Mine Safety Hazards in Coal Mining and Mining-Environmental Problems in Indiana. NASA CR-144495, October 1975.
- 2.8-9 Hardy, E.E.; Shaley, J.E.; Dawson, C.P.; Weiner, G.D.; Phillip, E.S.; and Fisher, R.A.: Enhancement and Evaluation of Skylab Photography for Potential Land Use Inventories. NASA CR-144473, July 1975.
- 2.8-10 Simonett, D.S.; Shotwell, R.; and Belknap, N.: Applications of Skylab EREP Data for Land Use Management. Final Report NASA CR-147457, January 1976.

- 2.8-11 Alexander, R.H.; et al.: Selected Applications of Skylab High-Resolution Photography to Urban Area Land Use Analysis, NASA CR-13997, August 1974.
- 2.8-12 Hanna, J.W.; Thomas, G.L.; and Esparza, F.: Planning Applications in East Central Florida, NASA CR-139189, August 1975.
- 2.8-13 Hoffer, R.M.: Computer-Aided Analysis of Skylab Multi-spectral Scanner Data in Mountainous Terrain for Land Use, Forestry, Water Resources and Geologic Applications. NASA CR-147473, December 1975.
- 2.8-14 Silva, L.F.: A Study of the Utilization of EREP Data from the Wabash River Basin. NASA CR-147412, December 1975.
- 2.8-15 Higer, A.L.; Coker, A.E.; Schmidt, N.F.; and Reed, L.E.: An Analysis and Comparison of Landsat-1, Skylab (S192) and Aircraft Data for Delineation of Land-Water Cover Types of the Green Swamp, Florida. Kennedy Space Center, CR 144855, November 1975.
- 2.8-16 Anderson, J.R.; Hardy, E.E.; and Roach, J.T.: A Land-Use Classification System for Use With Remote Sensor Data. U.S. Geol. Survey Circ. 671, 1972.

## 2.9 OCEANOGRAPHY

The three major categories comprising oceanography are: (1) physical, (2) biological, and (3) geological. These categories may be subdivided into more detailed categories. However, for the purpose of investigating oceanographic conditions with the use of remote sensors from aircraft and spacecraft this discussion is restricted to the three major categories, discussed briefly below with some examples of remote sensor applications to specific problems.

### 2.9.1 PHYSICAL OCEANOGRAPHY

Physical oceanography deals with the physical aspects of the ocean properties such as waves, currents, thermal properties and patterns, salinity concentration and distributions, and water depths and pressures. Of the many types of oceanographic parameters, the physical parameters lend themselves more readily to detection by remote sensors. For example, wave heights and patterns and surface temperatures can be measured and/or mapped by both imaging and point source remote sensors. Water salinity at the surface can be measured in relative concentrations by point source sensors, namely, by microwave radiometers. In addition, salinity can be inferred from mathematical models where several parameters are known, and with the use of such models salinity with depth can be estimated.

### 2.9.2 BIOLOGICAL OCEANOGRAPHY

Biological oceanography deals with the animal and plant life of the oceans and coastal zones as determined by their environmental conditions. Detection and mapping of biological parameters are primarily restricted to phenomena which can be used to infer conditions and properties of the local biology, e.g., oil slicks produced by schools of fish. Also, the water temperature, salinity, turbidity and depths can be used to isolate areas of

fish and plant life concentrations. Some plant life phenomena such as algae blooms (commonly termed red tides) can be detected and mapped directly by the use of certain spectral bands of photography and/or multispectral line scan imagery.

### 2.9.3 GEOLOGICAL OCEANOGRAPHY

Geological oceanography encompasses those aspects of the ocean that relate directly to their formation and modification, including marine sedimentation, deposition and formation of marine mineral deposits, coastline formation and destruction, and the recording of ocean dynamics and life forms in its sediments. Since geological aspects of oceanography are basically inferred, in most cases they cannot be mapped directly by remote sensors with the exception of coastal and shoreline features. However, in some cases where the water is clear and the turbidity is low, bottom features and relative depths can be seen in some parts of the visible spectrum. This data can be used to infer information about the local and regional geological conditions.

### 2.9.4 REMOTE MEASUREMENT OF OCEANOGRAPHIC PARAMETERS

The measurement of ocean properties by remote sensors has been an objective of both private and government groups for many years. However, a concerted effort to measure these ocean properties from remote sensors was only begun during the mid-1960's. This effort was initiated as a joint NASA-Naval Research Laboratory program. Oceanographic test sites were selected by the U. S. Navy to be flown over by NASA aircraft equipped with a variety of remote sensors in order to determine the possible applicability of sensors to oceanographic problems.

Since the mid-1960's much work has been done and many papers have been written regarding the applicability of a variety of data remotely acquired from both aircraft and satellites. The most

recent plan in measuring the ocean parameters by remote sensing is that of the earth orbiting Seasat-A system, the primary objective of which is the measurement of *physical* parameters, with very little emphasis on biological and geological parameters. As such, Seasat-A will measure and monitor the following data:

- 1) ocean wave statistics, heights, lengths, and energy spectra
- 2) ocean currents, tides, surges, and tsunamis
- 3) surface winds
- 4) ocean temperature, including the effects of polar ice
- 5) surface topography and surface roughness
- 6) general ocean geoid
- 7) ice extent, age, etc.

Understanding these oceanographic properties will improve the understanding of not only the physics of the ocean, but also of meteorology as related to ocean dynamics. An overall system concept of how the data will be acquired and processed for Seasat operations is illustrated in figure 2.9-1.

Figure 2.9-2 demonstrates the interrelationships of the data acquired from the sensors proposed for measurement of the physical parameters. Similar relationships could be diagrammed for biological and geological parameters, and then a composite made of the three basic categories of oceanographic disciplines.

As shown in figure 2.9-3, the planned orbital coverage of Seasat-A gives excellent coverage of the oceans and seas. Should additional satellites with a better cross section of sensors be launched in the future with a similar orbit, much information could be obtained on all types of oceanographic parameters.

2.9-4

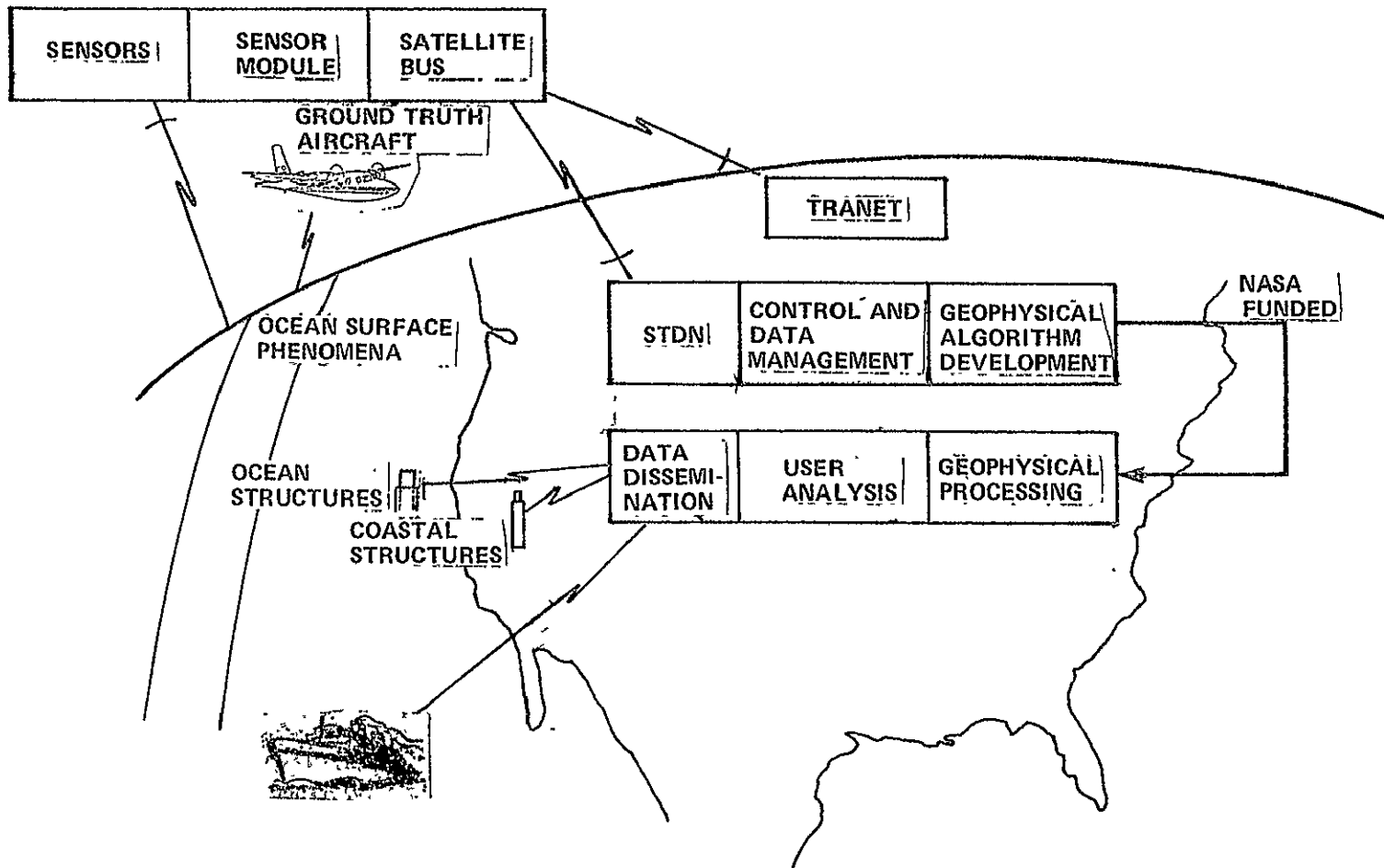


Figure 2.9-1. - Seasat ocean information system.

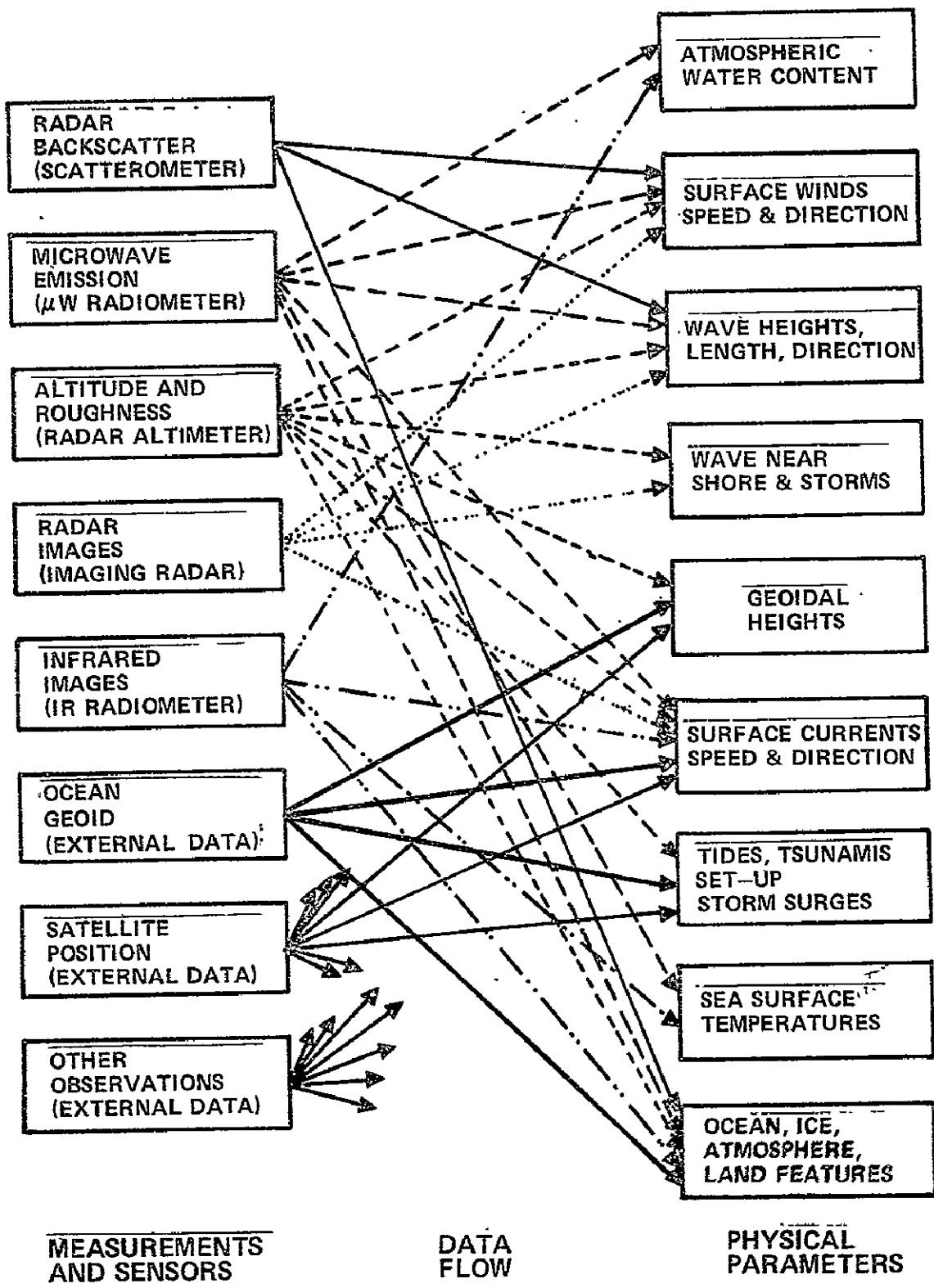


Figure 2.9.2. - Interrelationships between Seasat-A sensors and geophysical variables to be derived. (After John R. Apel)

2.9-6

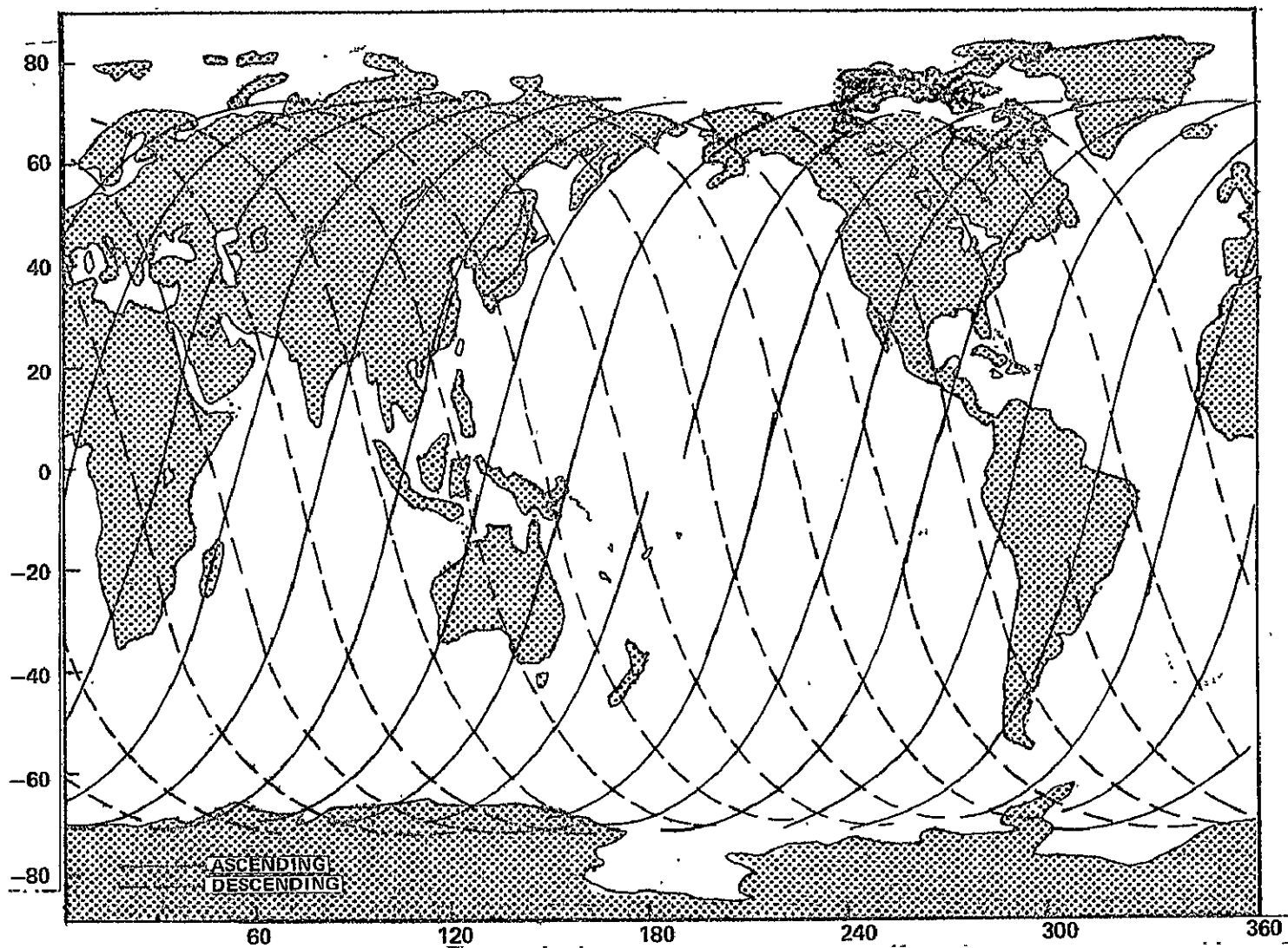


Figure 2.9.3. - Ground track of Seasat-A for 24-hour period.

#### 2.9.5 SENSOR TECHNIQUES INVESTIGATED FOR SEASAT-A

Sensor techniques which were investigated by NASA and the Jet Propulsion Laboratory for possible use aboard Seasat are shown in table 2.9-1.

#### 2.9.6 GENERAL OCEANOGRAPHIC SENSOR REQUIREMENTS

Table 2.9-2 gives the sensor type requirements for measuring various physical, biological, and geological parameters.

TABLE 2.9-1. - SEASAT SENSOR TECHNIQUES  
 (After J. R. Rose & S. Walter McCandless)

Frequency Range	Active or Passive	Differentiating Technique	Measurement Types	Seasat-A Payload
Visible and Infrared	Active	Range Processing	Altimetry Ocean Bottom Sounding	Radar Antenna
	Passive	Spatial Variation	Images Thermal Maps	Scanning Radiometer
		Multifrequency Spectrometry	Atmospheric Profiles (Water, Thermal) Atmospheric and Surface Constituents	None None
Microwave	Active	Range Processing	Altimetry Surface Roughness- Wave Height	Radar Altimeter
		Doppler Processing Range and Doppler	Backscatter (Winds, Surface Roughness) Images Wave Spectra Ice Maps	Far Beam Scatterometer Synthetic Aperture Radar
	Passive	Spatial Variation Multifrequency	Images Thermal Maps Atmosphere Path Corrections	SMMR SMMR

TABLE 2.9-2. — GENERAL OCEANOGRAPHIC SENSOR REQUIREMENTS

Sensor Type	Infrared	Laser	Micro-wave	Multi-spectral	Photographic	Radar
Physical Parameters:						
Sea state		X			X	X
Currents	X			X	X	
Surface temperature	X					
Sea ice	X			X	X	X
Salinity			X			
Tides	X			X	X	
Sea-air interface	X		X			
Biological Parameters:						
Coastal vegetation	X			X	X	X
Sea life areas	X		X	X	X	
Geological Parameters:						
Coastal changes				X	X	X
Coastal sedimentation				X	X	
Bottom mapping		X			X	
Geoid		X				X

2.9-9

## 2.10 SOIL MOISTURE

The measurement of soil moisture over sizable areas is a high priority need for several earth resources applications. Areas as diverse as agriculture, civil engineering, and meteorology have stated a requirement for information on the water content of the soil. Literature reviews by Idso, et. al., (ref. 2.10-1) and by Blanchard, et. al., (ref. 2.10-2) discuss the variety of measurement techniques and a number of direct and indirect applications of soil moisture.

### 2.10.1 USE OF VISIBLE, NEAR INFRARED, AND THERMAL INFRARED REMOTE SENSING TO STUDY SOIL MOISTURE

Measuring soil moisture remotely has been an objective of many experiments. Three general methods have evolved for estimating soil moisture, using radiometric data from the 0.4 micrometer ( $\mu\text{m}$ ) to 14.0  $\mu\text{m}$  spectral region. These methods are: (1) measurement of spectral reflectance or albedo, (2) measurement of visible polarization, and (3) measurement of surface radiometric temperature. The reflectance method is based on observation of a decrease in reflectance as soil moisture increases for a given soil. The polarization method is a result of the sensitivity of polarization of reflected light to soil moisture. The soil temperature method is dependent upon the observed decrease in temperature difference between day and night soil temperature with increasing soil moisture.

There are a number of factors which must be kept in mind when using remotely sensed data for the determination of soil moisture conditions. For instance, the moisture content of soils can vary greatly over a given area so that soil moisture determinations, even when made by ground methods, are valid only for limited areas and for limited periods of time. Soils which dry quickly even after extensive wetting are especially difficult to measure accurately. Vegetative cover severely restricts the utility of

most of these methods. However, to the extent that the vegetation responds to underlying soil conditions some information may be derived even in areas of total ground cover.

#### 2.10.1.1 Reflectance Method.

Qualitatively, it has long been known that the reflectance of bare soil is dependent upon the moisture content of the surface layer of the soil. A decrease in reflectance of bare soil with increasing soil moisture is well documented. Planet (ref. 2.10-3) noted that this decrease is the result of internal reflections within a thin film of surface water. However, the predictive value of this relationship was not evaluated until Bowers and Hanks (ref. 2.10-4) conducted a laboratory study of the spectral reflectance of several soils with different water contents. In all cases, the dry samples had the highest reflectivity with a maximum occurring in the near infrared. Their results indicated that there was a good potential for estimating surface soil moisture from reflectance measurements.

Condit (ref. 2.10-5) presented spectral reflectance data for 30 typical soils. Measurements were made of both wet and dry samples, which varied widely in color and reflectance. Based on an examination of 160 data sets, it was concluded that all of the data could be classified into three general types of curves. Linear regression equations were developed which allow the reconstruction of the spectral reflectance curve from five measurements made at specified wavelengths.

Sewell, et al., (ref. 10.2-6) conducted a laboratory study of the relation between moisture content and fallow soil reflectance of nine wavelengths in the visible. Quadratic equations were developed to describe the functional relationship. A corresponding field study favored color infrared film to enhance photointerpretation of soil moisture content. Favorable results were obtained for soil moisture contents up to 25 percent.

Weiner, et al., (ref. 10.2-7) obtained the best correlations between soil moisture and reflectance using imagery in the red portion of the visible spectrum. Their study included fallow fields and fields partially covered by grain sorghum.

Idso, et al., (ref. 10.2-8) found that simple albedo measurements when normalized to remove variations due to solar zenith angle were linear functions of soil moisture for the top layers of the soil. Figure 2.10-1 shows that as the depth of the surface layer increases, the relationship becomes more difficult to use at low moisture contents. The function must be rederived for each new soil type, but for at least the surface layer the relationship seems to be independent of season.

Data from the literature shows that reflectance can be related to soil moisture. Such a relationship is dependent on the soil type, but it is not strongly dependent on past or present environmental conditions. Therefore, with adequate ancillary soils information, there appears to be hope of calibrating a soil moisture model, and hence, quantifying surface soil moisture of bare soil.

#### 2.10.1.2 Visible Polarization

It has long been known that the polarization of light reflected from soils is very sensitive to surface moisture. Reflectance from natural soils is primarily diffuse, whereas reflectance from water is strongly specular. The specular component is strongest as the Brewster angle ( $53^\circ$ ) is approached. Hence, the geometry between the detector and the light source strongly affects the intensity of the reflected component of the radiation.

When the detector and the light source are in the principal reflecting plane, the combined reflectance from both the diffuse component from the soil and the specular component from the

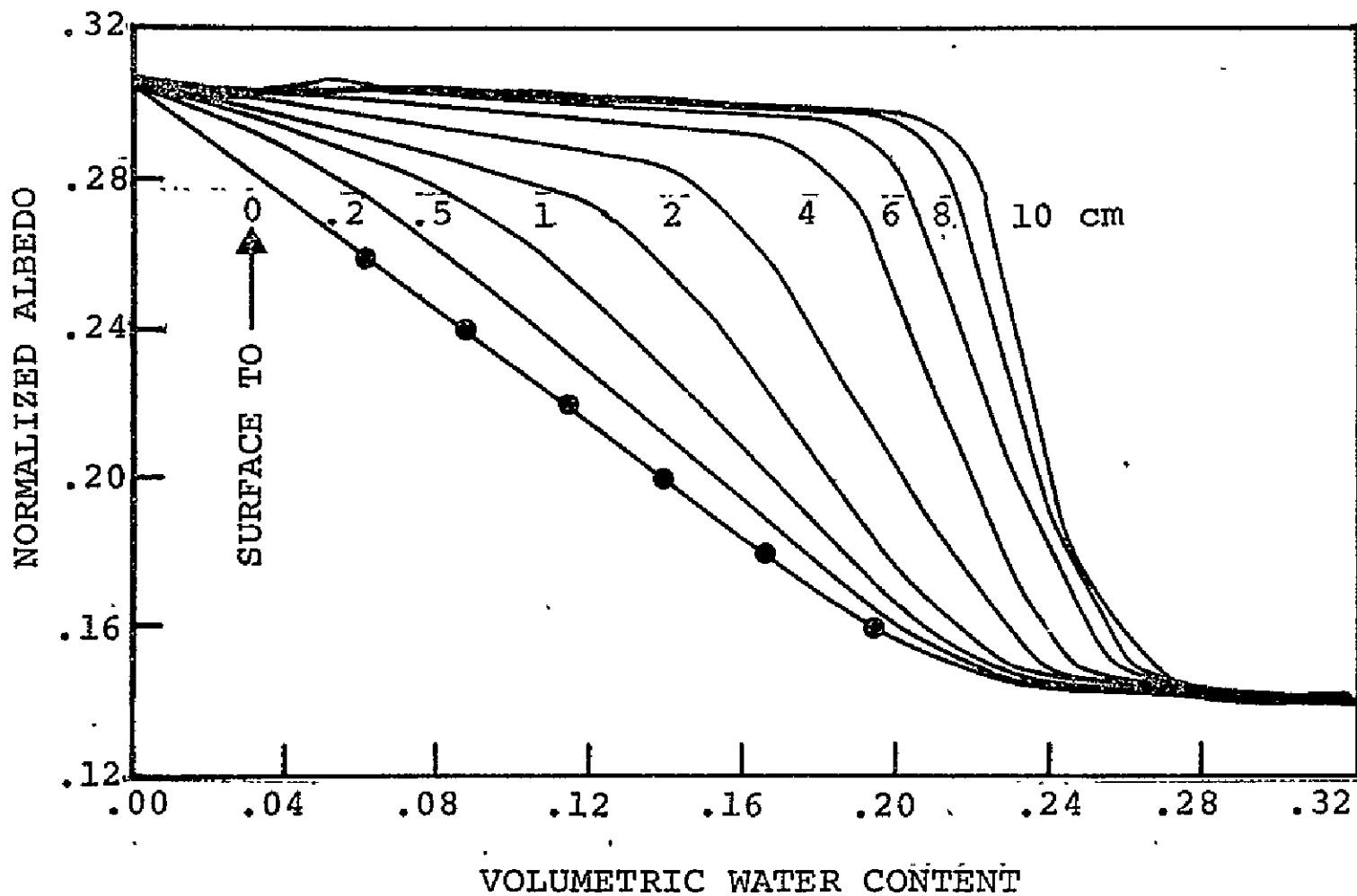


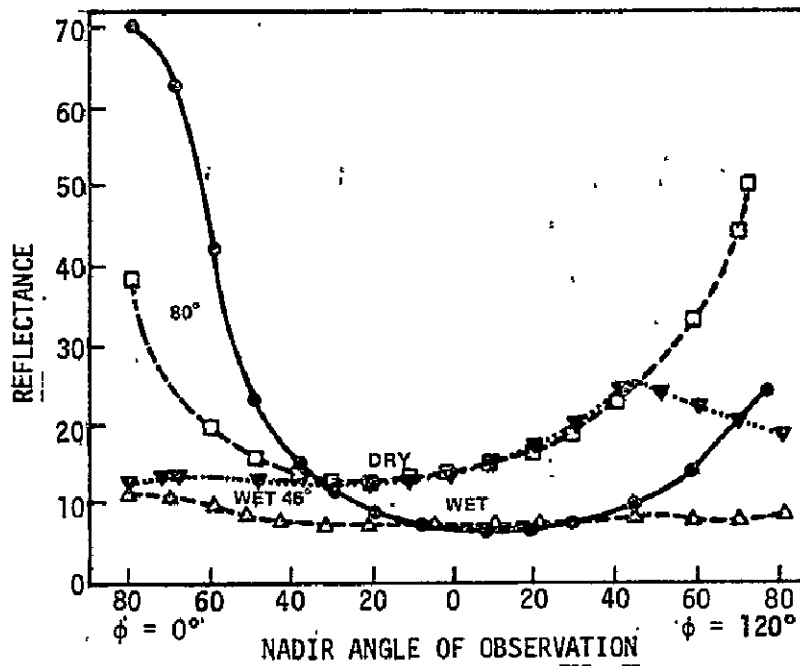
Figure 2.10-1.— Normalized albedo versus average volumetric water content of nine different soil layers having the surface as their upper boundary. (IDSO, et al., ref. 2.10-8).

water are measured. As a result, increased reflectances at high soil moistures are observed for all angles between the detector and light source. The maximum reflectance is observed when the detector is at  $53^\circ$  from the zenith.

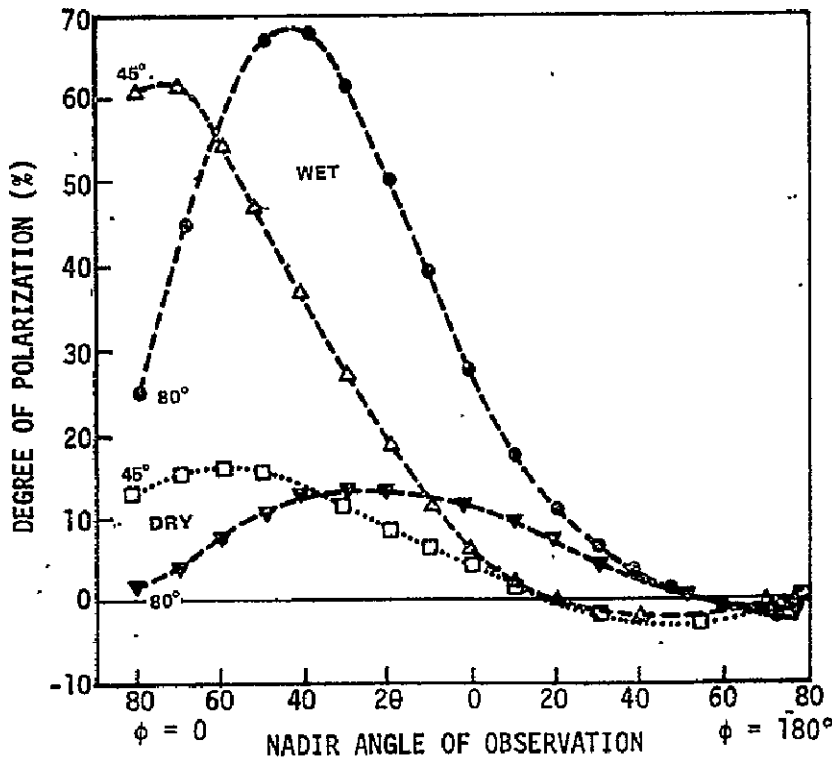
When the detector is not in the principal reflecting plane only the diffuse component from the surface is observed. In this case, the reflectance decreases with increasing soil moisture as discussed in section 2.10.1.1.

A principal advantage of the polarization signature is its reasonable degree of invariance to the illuminating and viewing angles. Frost and Steg (ref. 2.10-9) showed that the degree of polarization of reflected light is very nearly independent of illuminating angle, even for rough soils with the source at a  $69^\circ$  zenith angle such that a large fraction of the surface viewed is shadowed. This result is not unexpected since the illuminated areas contribute their characteristic polarization to the measured signal and the dark areas contribute in only a minor way because of reflected sky light. This circumstance is quite advantageous in that, to a very good approximation, it frees the measurements from the influence of unknown ground roughness parameters such as furrows in plowed fields and from a requirement for *a priori* knowledge of the average ground slope.

A typical comparison of the reflectance and polarization for red clay soil such as is found throughout the southeastern United States is given in figure 2.10-2. As will be noted in figure 2.10-2(b), the polarization of wet red clay soil is quite large compared to that of the dry clay. At observation points looking toward the source when it is either  $45^\circ$  or  $80^\circ$  from nadir, the percent polarization rises to between 60 and 70 percent of its dry value. These measurements were made at 0.53 micrometers.



(a) Directional reflectance for red clay soil in the principal plane.



(b) Polarization of radiation reflected from red clay soil in the principal plane.

Figure 2.10-2. — Red clay soil directional reflectance and polarization for two angles of incidence when wet and dry. (Source incidences 45° and 80° at a wavelength of 0.52  $\mu\text{m}$ .)

It will be noted in figure 2.10-2(b) that a remote sensor directly overhead and having the usual 10° to 20° field-of-view would not sense a large polarization effect unless the sun were quite low in the sky. Figure 2.10-3 gives a comparison of the present polarization for various soils containing various amounts of soil moisture. It will be noted that large and increasing polarization results from increasing the soil moisture content.

### 2.10.1.3 Temperature Method

Early attempts to develop a relationship between soil moisture and temperature were qualitative. Myers and Heilman (ref. 2.10-10) demonstrated the occurrence of temperature differences between wet and dry areas of the same soil. In general, wet soils were cooler than dry soils in the daytime. The reverse situation was observed during the night. Temperature differences of up to 9° were observed during the day. Myers and Heilman (ref. 2.10-10) found that the range of the diurnal oscillation was related to soil moisture conditions.

The difference between the daily maximum and minimum surface soil temperature decreases with increasing soil moisture. The relationship occurs because the heat transfer properties of the soil change with soil moisture content. The amount of water in the soil governs both the amount of energy absorbed as well as the rate of evaporative cooling, and hence, the soil temperature.

Blanchard (ref. 2.10-2) found that in sandy soils surface temperature differences reflected subsurface soil moisture differences. His data demonstrated that soil moisture differences occurring at depths greater than 10 cm could produce surface temperature differences of 2° to 3° C.

2.10-8

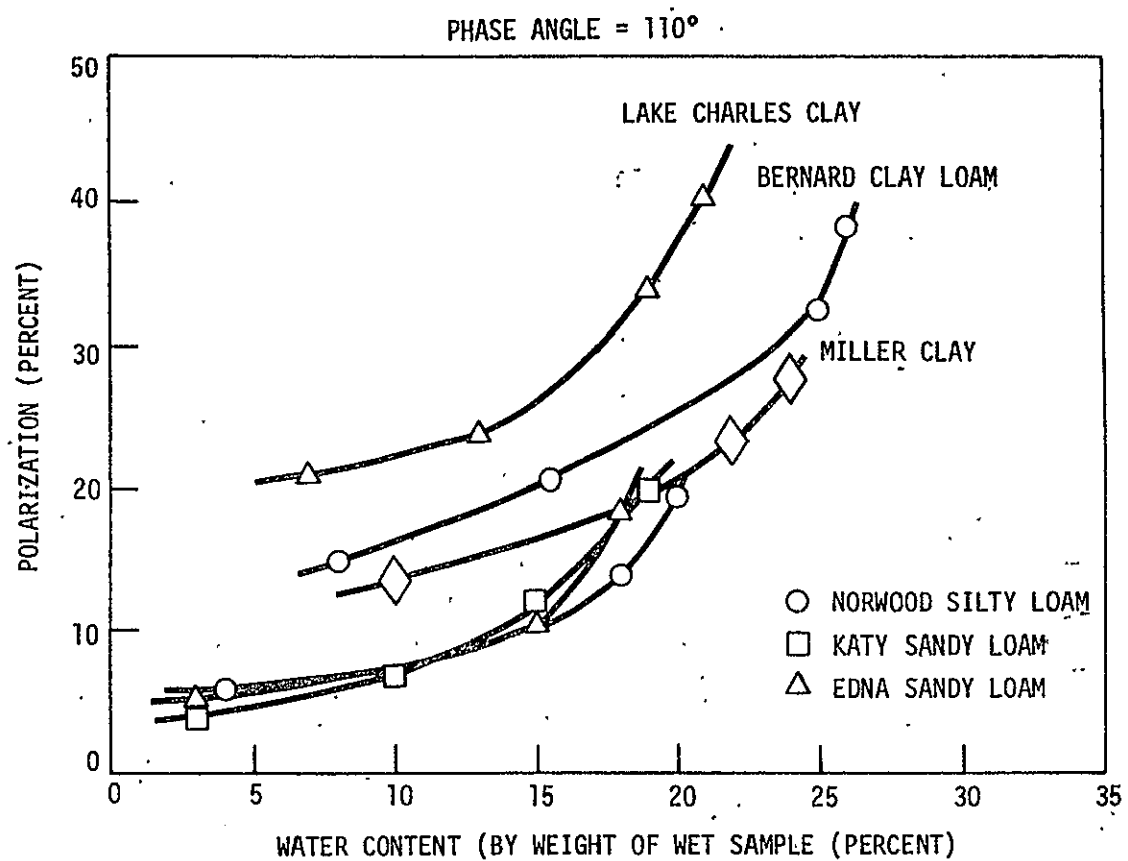


Figure 2.10-3.— Polarization versus moisture for six soil types.

Idso, et al., (ref. 2.10-11) carried out experiments which verified the utility of the temperature approach. The soil moisture of the surface layer to 4 cm was found to be a linear function of the range of soil surface temperatures. Figure 2.10-4 illustrates these results. The maximum difference between soil surface temperature and air temperature produced similar results as can be seen in figure 2.10-5. Tests on other soil types indicated that the derived functions were not universal and required knowledge of each soil for application. However, it was determined that the soil water pressure potential could be determined without prior knowledge of the soil type.

#### 2.10.1.4 Discussion

The reflectance and polarization methods share major drawbacks which restrict their general application. First, the wide variation of soil albedos increases the difficulty of developing a universal relation that does not require ground truth data on soil type. Secondly, reliable inferences about subsurface water will probably require water budget modeling using reflectances as input data.

The temperature method also requires ground truth soil information for estimation of soil moisture. However, the correlation with subsurface water is stronger over a wider range of soil moisture levels for this method, and this may justify developing the required ancillary data. In addition, soil water pressure potential may be estimated independently of soil type.

Further, experimental work is required to determine the worth of these approaches in the real world. To this end, NASA's Heat Capacity Mapping Mission, scheduled for a 1978 launch, will carry a high resolution two-channel radiometer (0.5  $\mu\text{m}$  - 1.1  $\mu\text{m}$  and 10.5  $\mu\text{m}$  - 12.5  $\mu\text{m}$ ) for measuring both reflectance and surface radiometric temperature.

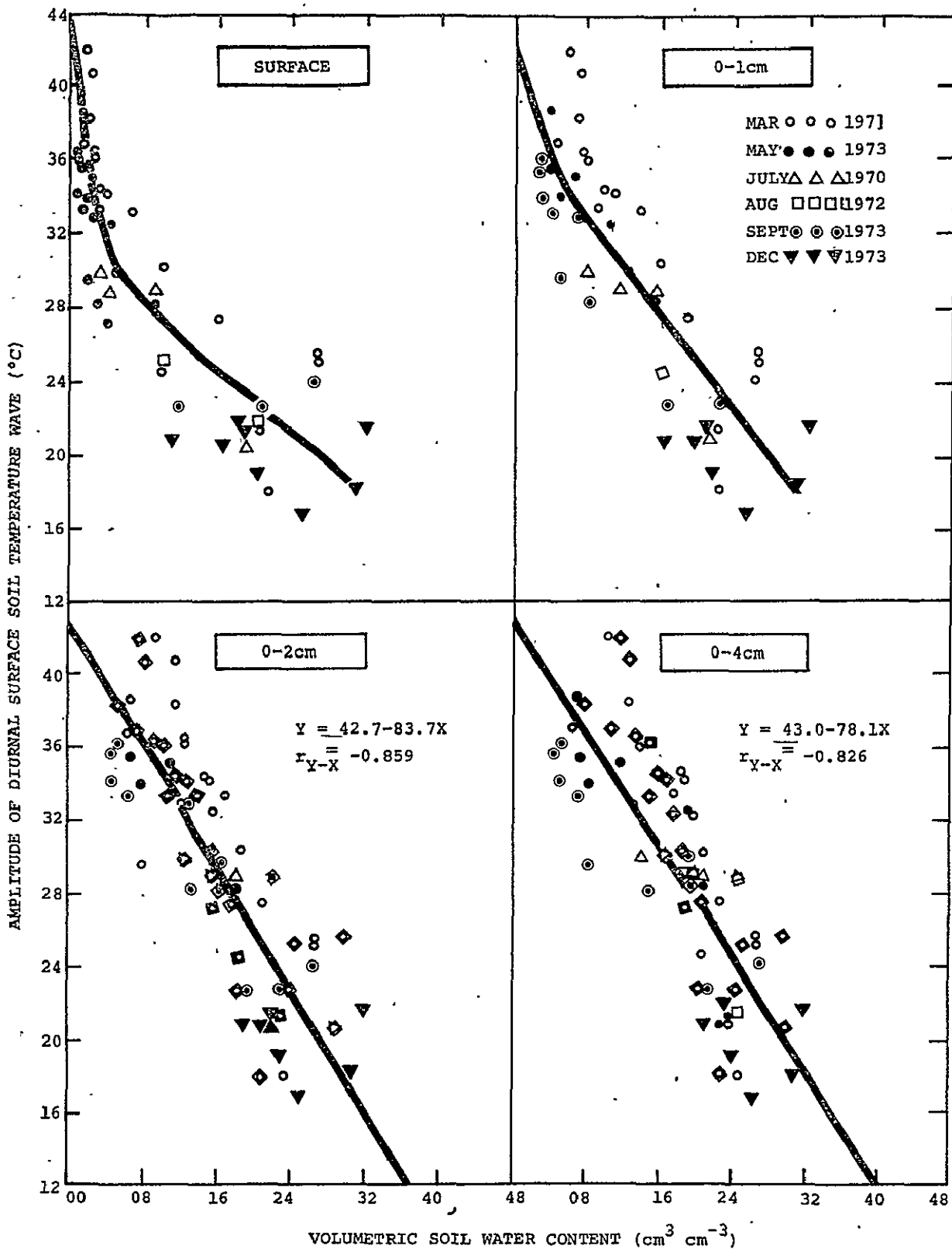


Figure 2.10-4 - The amplitude of the diurnal surface soil temperature wave on clear day-night periods versus the mean daylight volumetric soil water content of four different depth intervals. The points enclosed by diamonds represent volumetric water contents obtained by direct gravimetric sampling of the soil, while all remaining points represent volumetric water contents obtained by the albedo assessment technique of Idso, et al. (ref. 2.10-8).

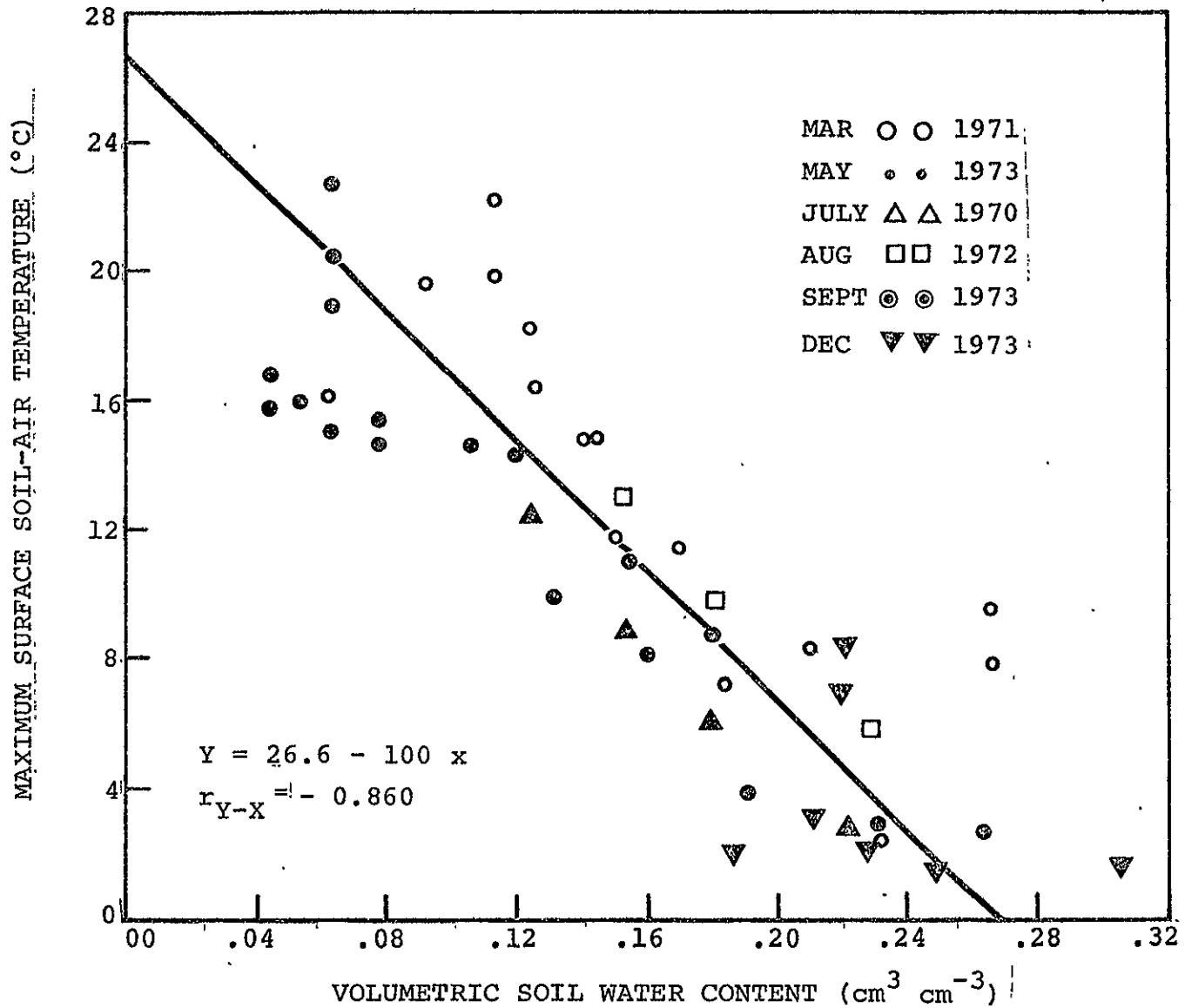


Figure 2.10-5.—The maximum value of the surface soil-air temperature differential versus the mean daylight volumetric soil water content of the 0- to 2-cm-depth increment. (Idso, et al., ref. 2.10-11).

## REFERENCES

- 2.10-1 Idso, S.B.; Jackson, R.D. and Reginato, R.J.: Detection of Soil Moisture by Remote Surveillance. *American Scientist*, 63(5), 549-557, 1975.
- 2.10-2 Blanchard, M.B.; Greenley, R.; and Goettelman, R.: Use of Visible, Near-Infrared, and Thermal Infrared Remote Sensing to Study Soil Moisture. *Proceedings of the Ninth International Symposium on Remote Sensing of Environment*. 1:693-700, April 15-19, 1974.
- 2.10-3 Planet, W. G.: Some Comments on Reflectance Measurements of Wet Soils. *Remote Sensing of Environment*, 1:127-129, 1970.
- 2.10-4 Bowers, S.A.; and Hanks, R.J.: Reflection of Radiant Energy from Soils. *Soil Scientist*, 100(2):130-138, 1965.
- 2.10-5 Condit, H.R.: The Spectral Reflectance of American Soils. *Photogrammetric Engineering*, 36(9):955-966, 1970.
- 2.10-6 Sewell, J.I.; and Allen, W.H.: Visible and Infrared Sensing in Soil Moisture Determination. *Proceedings of the 2nd Remote Sensing of Earth Resources*, 2:689-702, March 26-27, 1973.
- 2.10-7 Werner, H.D.; Schmer, F.A.; Horton, M.L.; and Waltz, F.A.: Application of Remote Sensing Techniques to Monitoring Soil Moisture. *Proceedings of the Seventh International Symposium on Remote Sensing*, 1245-1255, 1971.
- 2.10-8 Idso, S.B.; Jackson, R.D.; Reginato, R.J.; Kimball, B.A.; and Nakayama, F.S.: The Dependence of Bare Soil Albedo on Soil Water Content. *Journal of Applied Meteorology*, 14(1):109-113, 1975.
- 2.10-9 Frost, R.T.; and Steg, L.: Visible Polarization Signature for Remote Sensing of Soil Surface Moisture. A.3.4, COSPAR, 13th Plenary Meeting, Leningrad, USSR, May 1970.
- 2.10-10 Myers, V.J.; and Heilman, M.D.: Thermal Infrared for Soil Temperature Studies. *Photogrammetric Engineering*, 1024-1032, Oct. 1969.

2.10-11 Idso, S.B.; Schmugge, T.J.; Jackson, R.D.; and  
Reginato, R.J.: The Utility of Surface Temperature  
Measurements for the Remote Sensing of Surface Soil  
Water Status. Journal of Geophysical Research,  
80(21):3044-3049, 1975.

## 2.10.2 REMOTE SENSING OF SOIL MOISTURE AT MICROWAVE FREQUENCIES

### 2.10.2.1 Introduction

The importance of soil moisture remote sensing to the application areas of hydrology, meteorology, and agriculture has been stressed in the previous sections. In the microwave region, considerable interest and studies in the remote sensing of moisture content in soil were generated only in recent years (ref. 2.10.2-1 through ref. 2.10.2-7). The results obtained from these studies strongly suggest that microwave sensors in aircraft and satellites could provide large-scale mapping and estimates of soil moisture content to a reasonable degree of accuracy. Undoubtedly, there still exist many problems to be explored and solved before the full utilization of an operational soil moisture remote sensor can be realized. This promises a lot of research efforts and activities in this area for many years to come.

A microwave sensor detects the electromagnetic properties of a terrain surface by measuring either the backscattered portion of its transmitted radiation or the radiation emitted by the terrain surface. The electromagnetic properties of a terrain surface are strongly affected by: (1) the water content of soil, (2) the type of soil, (3) the vertical profile of water content, (4) the surface roughness and row direction (for furrowed fields), (5) the temperature at the surface and its variation with depth, (6) the state of vegetal cover, and (7) the frequency, polarization and the look angle of the electromagnetic radiation. Only the first and the last items will be emphasized in the following discussions. The remaining items will be briefly described when necessary.

### 2.10.2.2 Dielectric Properties of Soil at Microwave Frequencies

At microwave frequencies, a typical dry soil has a dielectric constant of  $\leq 5$  and a dielectric loss factor of  $\ll 1$ . The dielectric parameters of water, on the other hand, are quite large. It can be seen from figure 2.10.2-1 (fig. 1 of ref. 2.10.2-8) that the dielectric constant and loss factor for water can vary in the ranges of 20-80 and 2-40, respectively. This marked difference in the dielectric property between dry soil and water makes it possible to electromagnetically detect the moisture content in a soil-water mixture.

Laboratory measurements of dielectric constants and loss factors for soils at microwave frequencies have been performed by several groups (ref. 2.10.2-1, ref. 2.10.2-8, and ref. 2.10.2-9). Figure 2.10.2-2 (figure 11 of ref. 2.10.2-8) shows a typical result. It is clear from this figure that, at all frequencies shown here, both the dielectric constant and loss factor increase markedly with water content. The data also indicate that both of these dielectric parameters are relatively independent of soil type. Results from other measurements (ref. 2.10.2-14 and ref. 2.10.2-9) support the same conclusions. Additional measurements on the dielectric properties of soil are expected to be made at X and L bands in support of the 1976 Joint Soil Moisture experiment (ref. 2.10.2-17).

The relationship established between the dielectric constant as well as loss factor and the water content of soil is of fundamental importance in our understanding and interpretation of the data collected by a microwave sensor. As an example, figure 2.10.2-3 (fig. 7 of ref. 2.10.2-2) shows the calculated emissivity variation with soil moisture content for the silty clay loam at the wavelength of 1.55 cm. According to the figure, a radiometer operated at this wavelength is expected to observe decreasing brightness temperature with increasing soil moisture

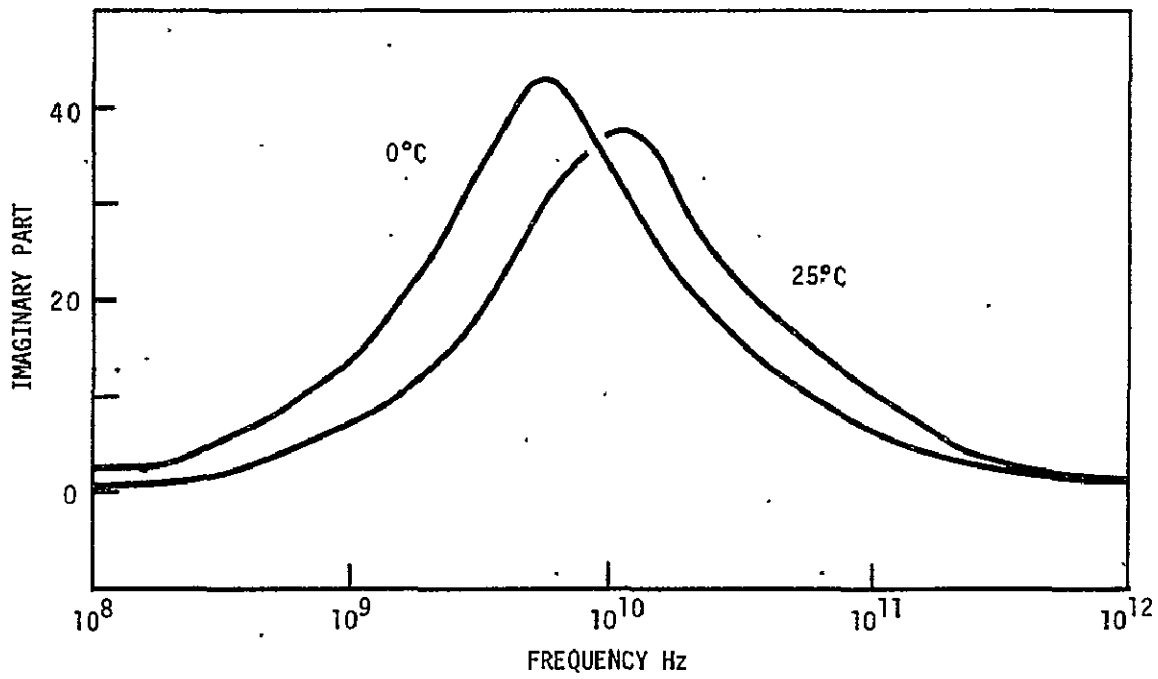
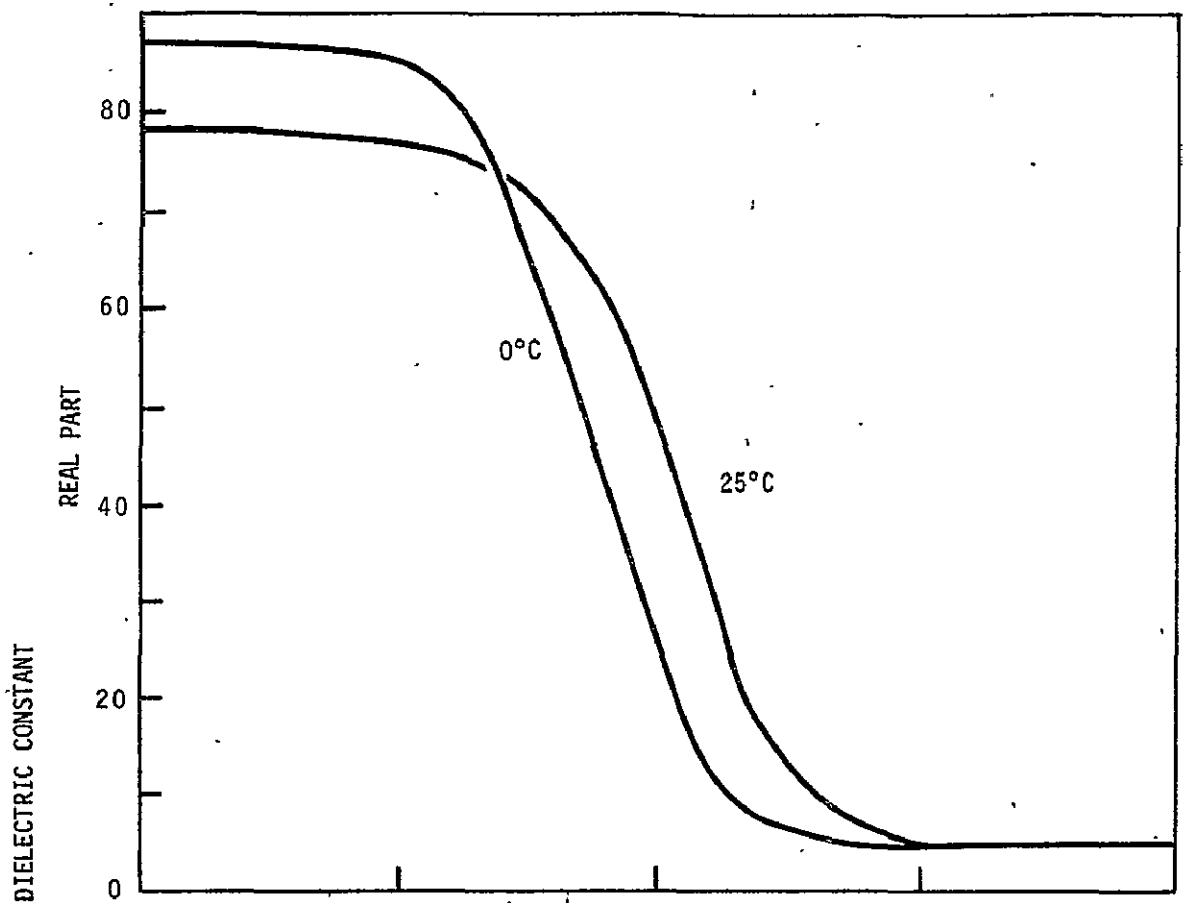
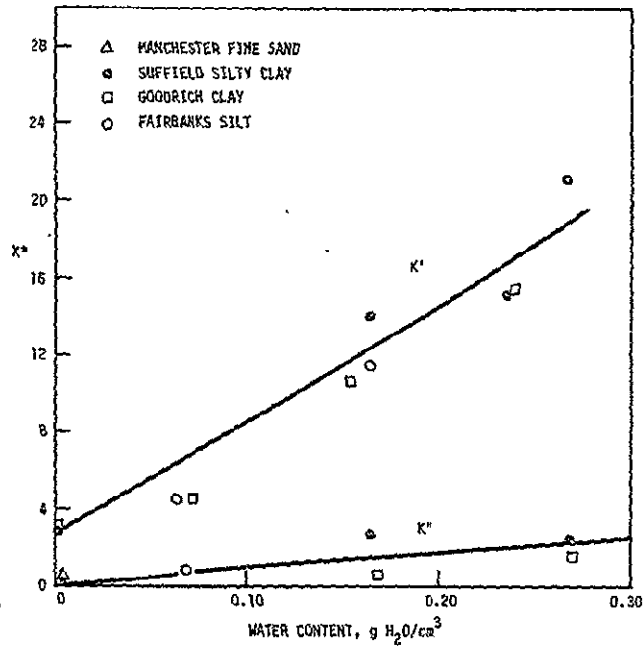
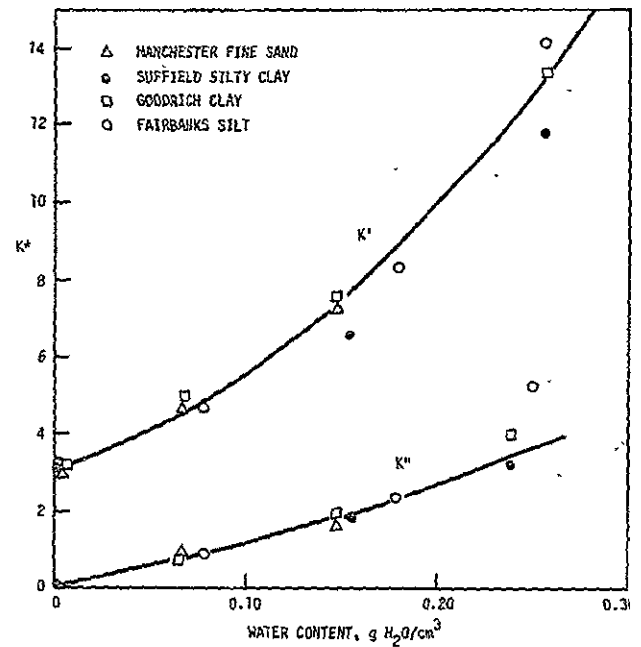


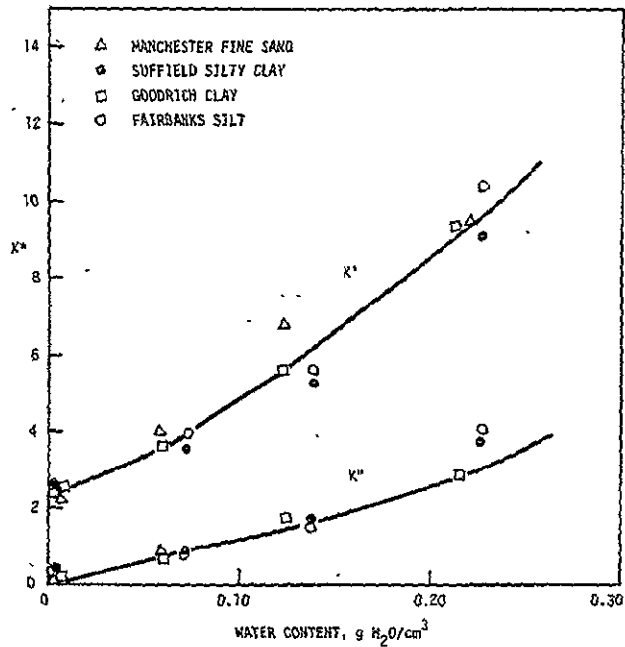
Figure 2.10.2-1.— The dielectric relaxation spectrums of water at two temperatures.



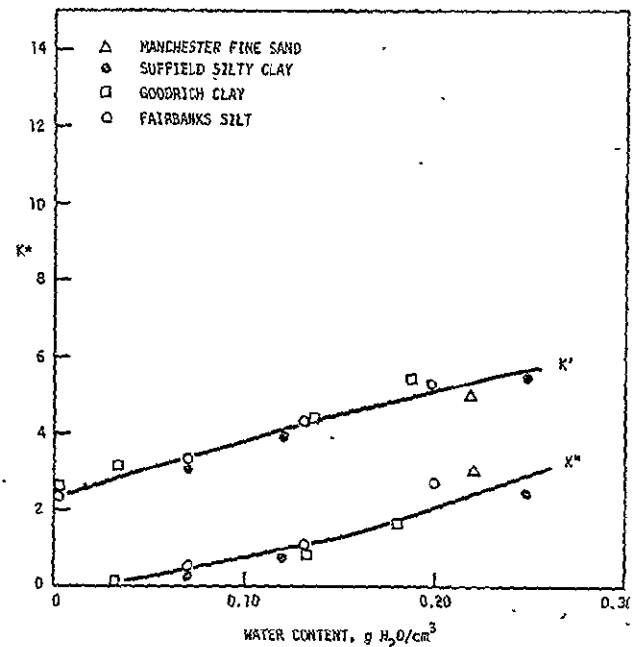
(a)  $5 \times 10^8$  Hz



(b)  $4 \times 10^9$  Hz



(c)  $10 \times 10^9$  Hz



(d)  $25 \times 10^9$  Hz

Figure 2.10.2-2.— The complex dielectric constant of soils as a function of volumetric water content at 10°C.

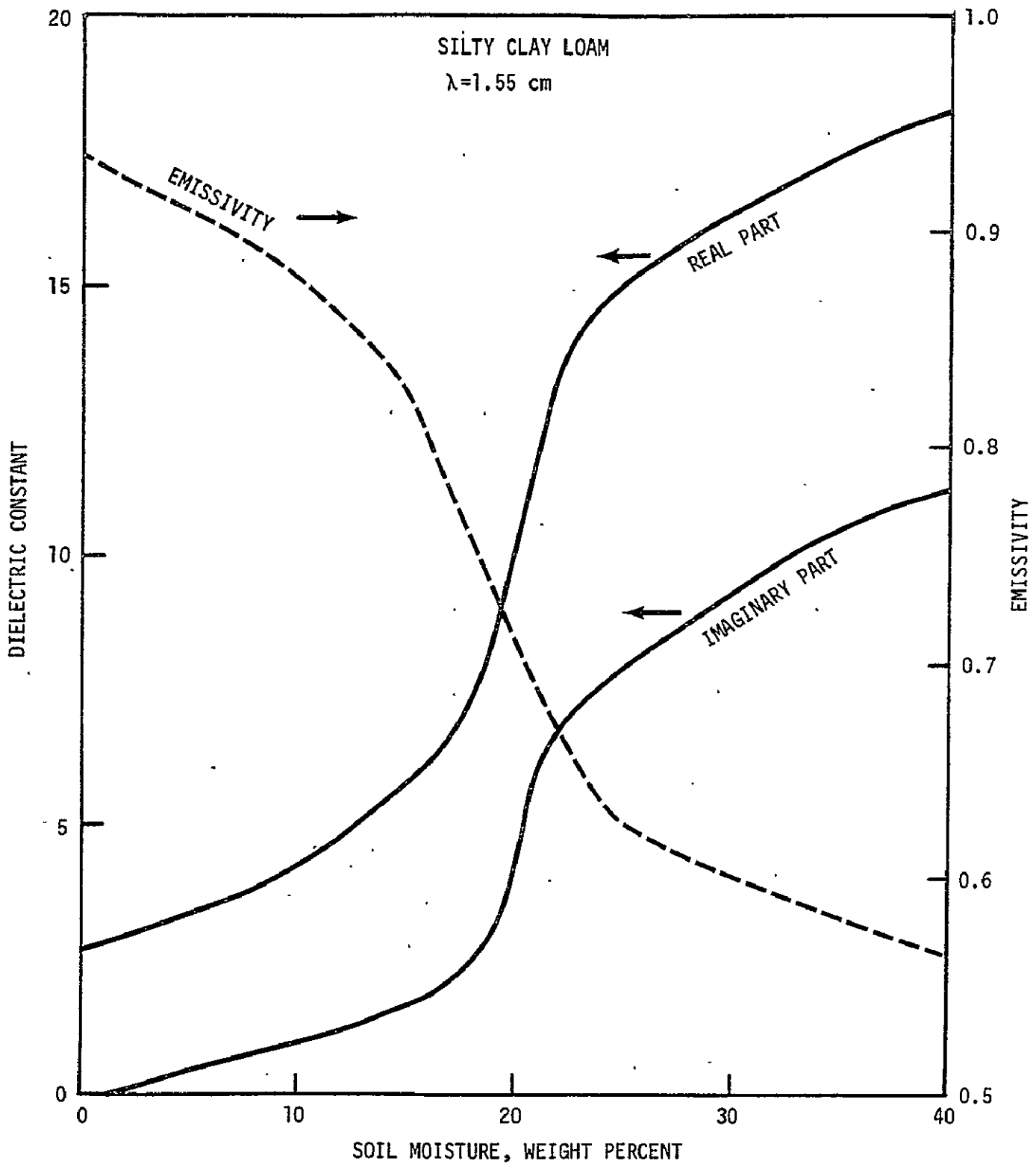


Figure 2.10.2-3.— Plots of 1.55 cm dielectric constants and calculated emissivities for a silty clay loam soil.

content. Both the dielectric constant and loss factor enter explicitly into the mathematical model calculations on the emission and scattering of electromagnetic radiation from a terrain surface (e.g., ref. 2.10.2-10 through ref. 2.10.2-13). These model calculations are ultimately needed in order to explain and understand the observations made at aircraft and satellite altitudes.

### 2.10.2.3 Soil Moisture Measurements by the Active Microwave Sensors

An active microwave sensor transmits electromagnetic radiation and receives a portion of it backscattered from a terrain surface. Knowing the powers transmitted and received, the angle of incidence, the two-way antenna pattern, and other sensor system parameters (i.e., noise, gain, etc.), the dielectric property of the terrain surface can be derived. The main advantages of an active microwave sensor over its passive counterpart are that it can provide good spatial resolution even at satellite altitudes and that the backscattered power it receives does not depend too strongly on the thermal temperature of the terrain surface. However, an active microwave sensor system is generally more expensive to build and the associated data processing system (both hardware and software) is more complicated.

The application of the active microwave sensors to the detection of soil moisture content is only at the investigative stage. The most extensive work in the area was performed by a scatterometer mounted on a moving track (ref. 2.10.2-1 and references therein). The scatterometer was operated in the frequency range of 2 to 8 GHz, both for HH and VV polarizations. The measurements were made on a 150' x 150' plot divided into three fields of smooth, medium rough and rough surfaces. The scattering coefficients were measured for eight frequency intervals (between 2 and 8 GHz) and five angles of incidence in increments of 10° from 0° to 40°.

The results from these measurements indicated that, at an operating frequency of  $\sim 4.75$  GHz and an incident angle of  $\sim 10^\circ$ , the scattering coefficients are almost independent of roughness and dependent only on soil moisture. Figure 2.10.2-4 (fig. 15 of ref. 2.10.2-1) shows the plot of the scattering coefficient against the soil moisture content for data taken at the frequency of 4.75 GHz, angle of incidence of  $10^\circ$ , and for VV polarization. Measurements from smooth, medium rough, and rough fields were all included. A correlation coefficient of 0.75 and a soil moisture sensitivity of 0.25 dB per  $0.01 \text{ g/cm}^3$  water content were obtained.

The soil moisture measurements by a scatterometer at aircraft or satellite altitudes are scarce. Three scatterometers at the frequencies of 400 MHz, 1.6 GHz, and 13.3 GHz mounted on a NASA/JSC aircraft were flown over the Finney County and Lawrence-Topeka, Kansas, test sites in April to May of 1976. Both the ground truth and the scatterometer data have not been completely analyzed as of October 1976. At satellite altitudes, measurements were made over a Texas test site in 1973 with the S193 13.9-GHz radiometer/scatterometer system aboard the Skylab (ref. 2.10.2-6). The correlation coefficient at a pitch angle of  $29.4^\circ$  and the soil moisture content in the top 2.5 cm layer was  $\sim 0.67$ . For those areas in the test site where the ground truth measurements were not made, the scattering coefficient was correlated with the composite rainfall in inches. The correlation coefficient in this case was found to be 0.62. Considering the footprint of the scatterometer of  $\sim 12 \text{ km} \times 16 \text{ km}$  (based on two-way antenna pattern) and only a few soil samples taken in each footprint, these correlation results are indeed encouraging.

An attempt was also made to measure the soil moisture content by an imaging radar system. In April of 1974, a synthetic aperture radar operating at both X and L bands and for both like and cross polarization was flown over about 80 agricultural fields

FREQUENCY (GHz): 4.75  
 ANGLE OF INCIDENCE: 10°  
 POLARIZATION: VV  
 ● SMOOTH SURFACE (RMS HEIGHT = 0.88 cm)  
 ▼ MEDIUM ROUGH SURFACE (RMS HEIGHT = 2.6 cm)  
 ■ ROUGH SURFACE (RMS HEIGHT = 4.3 cm)  
 S = SOIL MOISTURE SENSITIVITY (dB/0.01 g/cm<sup>3</sup>)  
 R = CORRELATION COEFFICIENT

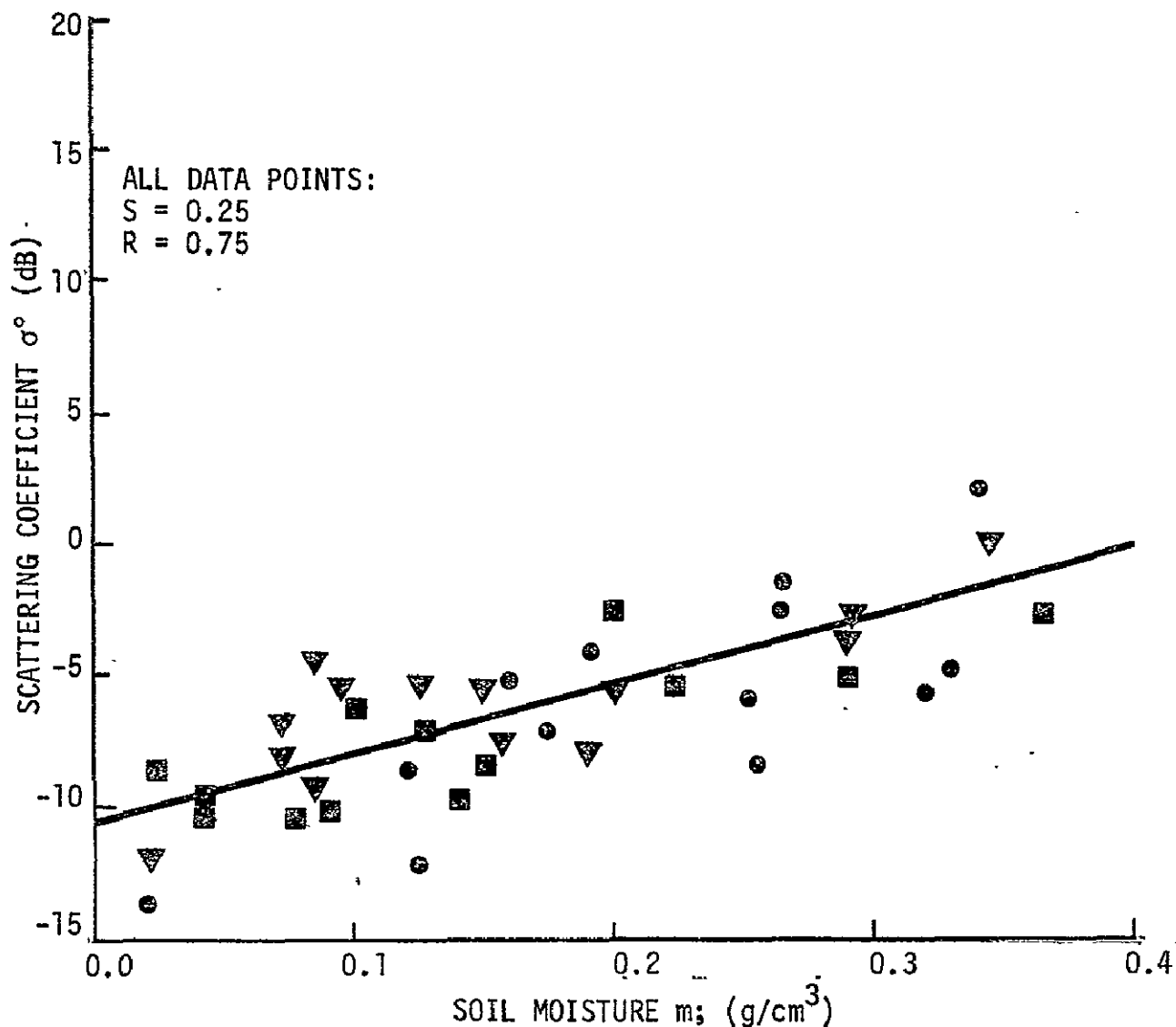


Figure 2.10.2-4.— Scattering coefficient response as a function of soil moisture for the combination of all three surface roughness profiles.

near Phoenix, Arizona (ref. 2.10.2-7). The backscattered electromagnetic radiation was processed and recorded on film so that the images of the measured agricultural fields would appear with different gray density levels according to their representative intensity returns. The relative intensities of those fields were derived from the films and correlated with the corresponding soil moisture contents. Figure 2.10.2-5 (fig. 12 of ref. 2.10.2-7 shows the results of these measurements. Clearly there is no apparent correlation between the relative intensity return and the soil moisture content. When the fields were separated in zones according to the angles of incidence, a good correlation was found between the intensity return and the moisture content for those fields falling in the 43° to 51° zone. Figure 2.10.2-6 (fig. 14 of ref. 2.10.2-7) shows such a correlation. Although a correlation coefficient of ~0.95 was obtained, only five data points were used in the study, the results of which do not appear convincing. Further measurements and studies are clearly needed before an imaging radar system can be used as an effective tool in the remote sensing of soil moisture.

#### 2.10.2.4 Radiometric Measurements of Soil Moisture

A radiometer measures the electromagnetic radiation emitted from a terrain surface (or an object). At microwave frequencies, the intensity of the radiation is proportional to the thermal temperature of the terrain surface, with emissivity as a constant of proportionality. (Hence the intensity of radiation and the brightness temperature are used interchangeably.) There are relatively more measurements on soil moisture made with radiometers than with either scatterometers or imaging radar systems. At aircraft and satellite altitudes, positive evidence has been accumulated for using radiometers to remotely detect soil moisture content (ref. 2.10.2-5). For example, the results from Skylab S194 radiometer measurements showed an excellent correlation between the brightness temperature and the soil moisture

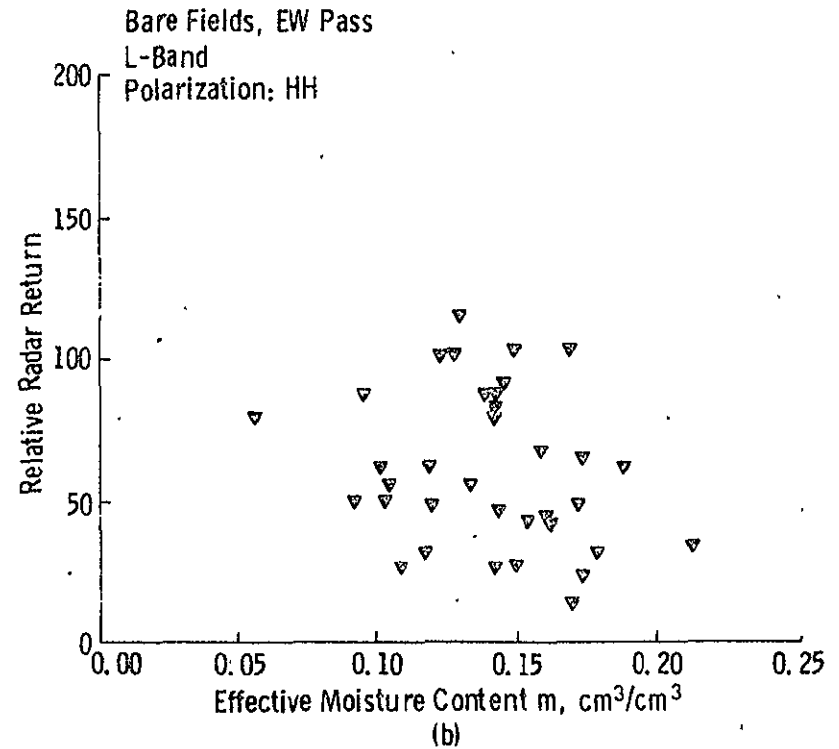
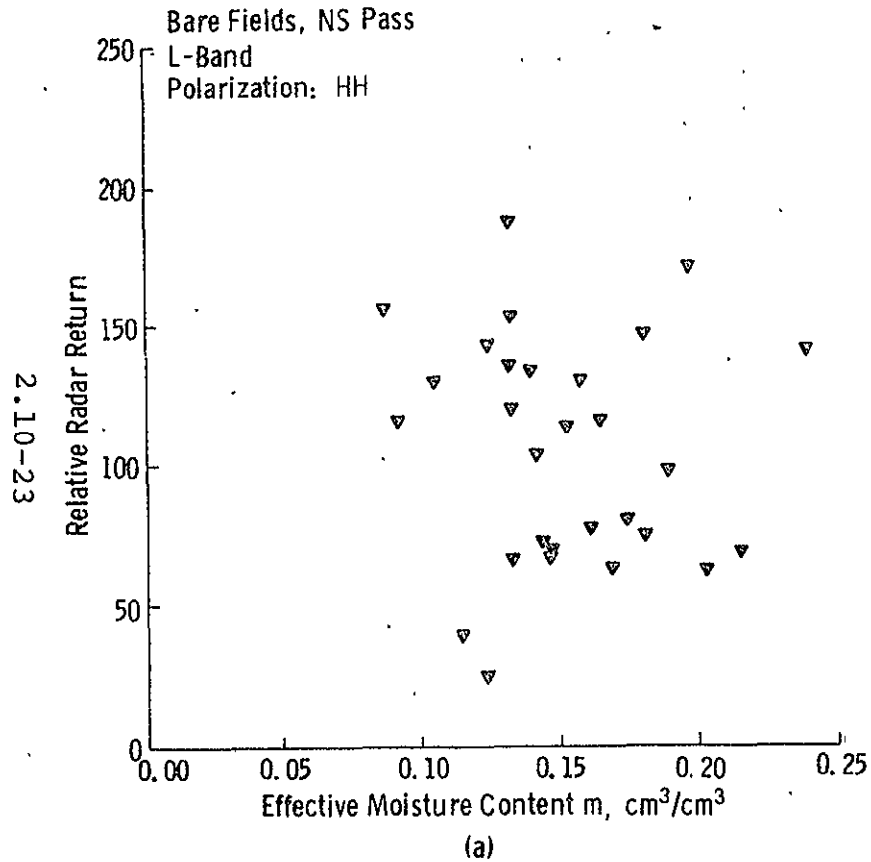


Figure 2.10.2-5.—|L-band relative HH return as a function of effective moisture content. a) NS pass, b) EW pass.

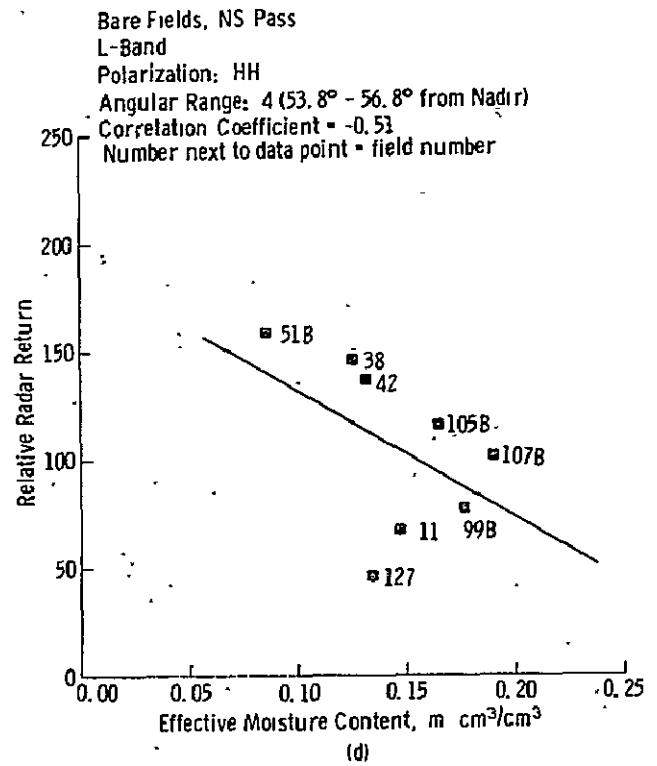
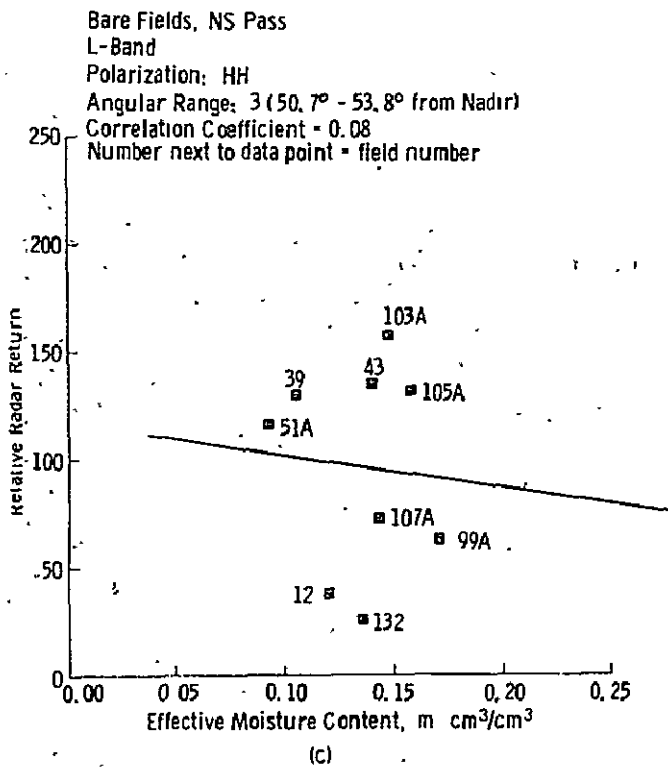
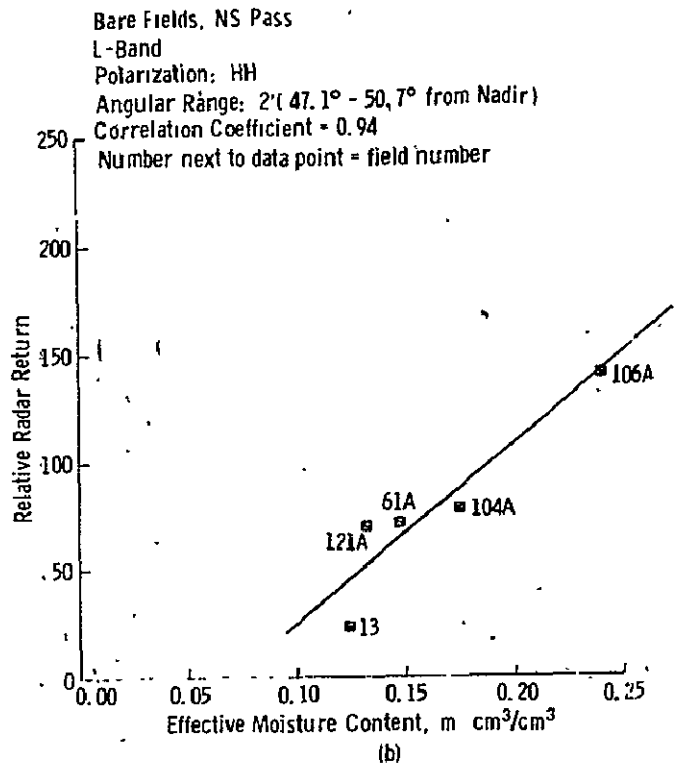
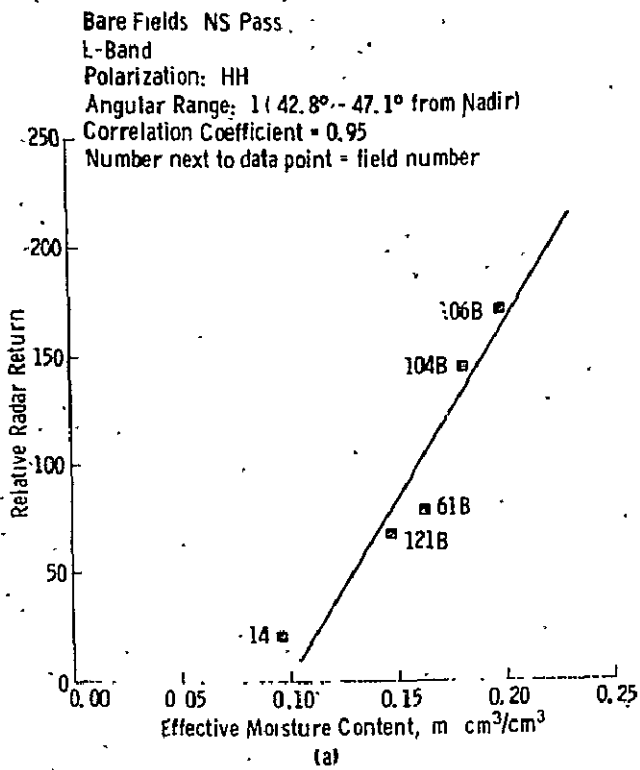


Figure 2.10.2-6.— L-band relative HH return as a function of effective moisture content for bare fields in angular ranges: a) 42.8°-47.1°, b) 47.1°-50.7°, c) 50.7°-53.8°, and d) 53.8°-56.8°.

content in the top 2.5 cm surface layer (ref. 2.10.2-5). The radiometer, operating at the wavelength of 21 cm and at the Skylab altitude, measured the brightness temperature over a circular surface area of ~110 km in diameter. The brightness temperature measurements were made at intervals corresponding to 6.5 km in surface distance of Skylab travel. The soil moisture samples were taken at intervals of ~6 km along two somewhat parallel routes through the test sites selected in both Texas and Kansas. Each of the soil moisture content measurements used in the correlation was derived from the average of the samples encircled in the 110 km diameter of the antenna footprint. The correlation coefficients between the brightness temperature and the soil moisture content for all cases in the Texas site were ~0.90 or better, whereas those for the Kansas site were >0.80. This strongly shows the capability of a high-altitude radiometer for the remote sensing of soil moisture over a large area.

Another example of soil moisture measurement with a radiometer at satellite altitudes was provided by the Nimbus 5 Electronically Scanning Microwave Radiometer (ESMR). This radiometer operated at the frequency of 19.3 GHz and scanned perpendicularly to the spacecraft suborbital track from 50° left to 50° right in 78 steps. It measured only the horizontally polarized radiation and had a spatial surface resolution of 25 km at nadir. There was no direct ground truth measurement on soil moisture like that in the case of Skylab S194 radiometer. However, a study over the central Illinois-Indiana region, Mississippi Valley, and the Great Salt Lake Desert showed that substantial drops in ESMR brightness temperature were generally observed after rainfall in these areas (ref. 2.10.2-3).

A pioneer experiment was performed at aircraft altitudes over some 200 selected agricultural fields near Phoenix, Arizona, in 1971 (ref. 2.10.2-2). The measurement was conducted with three

radiometers at the frequencies of 1.42 GHz, 19.35 GHz, and 37 GHz. The soil moisture data were obtained from field samples with soil types ranging from sandy soil to heavy clay. The results showed that at the frequency of 19.35 GHz, there was little variation in the radiometer brightness temperature for soil moisture values below ~10 to 15 percent moisture content by weight. Above ~15 percent moisture content, there was a steady decrease in the brightness temperature with moisture content. The slope of a linear regression was ~3°K for each percentage point increase in soil moisture. Furthermore, there was an observable difference in the brightness temperature values at a given moisture content for heavy clay and sandy soil. On the other hand, the brightness temperature at 1.42 GHz was observed to depend linearly on the soil moisture over the moisture range 0 to 35 percent. Figure 2.10.2-7 (fig. 5 of ref. 2.10.2-2) showed such a linear dependence with a slope of ~2.2°K/percent soil moisture. There was no apparent difference in the variation of the brightness temperature with moisture content between sandy loam and clay loam. Finally, it was concluded from the same report that the 37 GHz radiometer had poor sensitivity to the soil moisture.

After this pioneer experiment, it was recognized that a cooperative effort would be necessary to utilize manpower and resources more effectively. Consequently, a series of Joint Soil Moisture Experiments (JSME) were conducted by NASA and research institutions in 1974, 1975, and 1976. Both the 1975 and 1976 missions had four nonscanning radiometers at the wavelengths of 21, 1.67, 1.36, and 0.8 cm, and a scanning radiometer at 2.8 cm. The data obtained from the 1975 mission are not fully analyzed yet and the analysis effort for the 1976 mission has begun as of September 1976. The 1974 mission had only two radiometers. The three nonscanning radiometers at 1.67, 1.36, and 0.8 cm were not included.

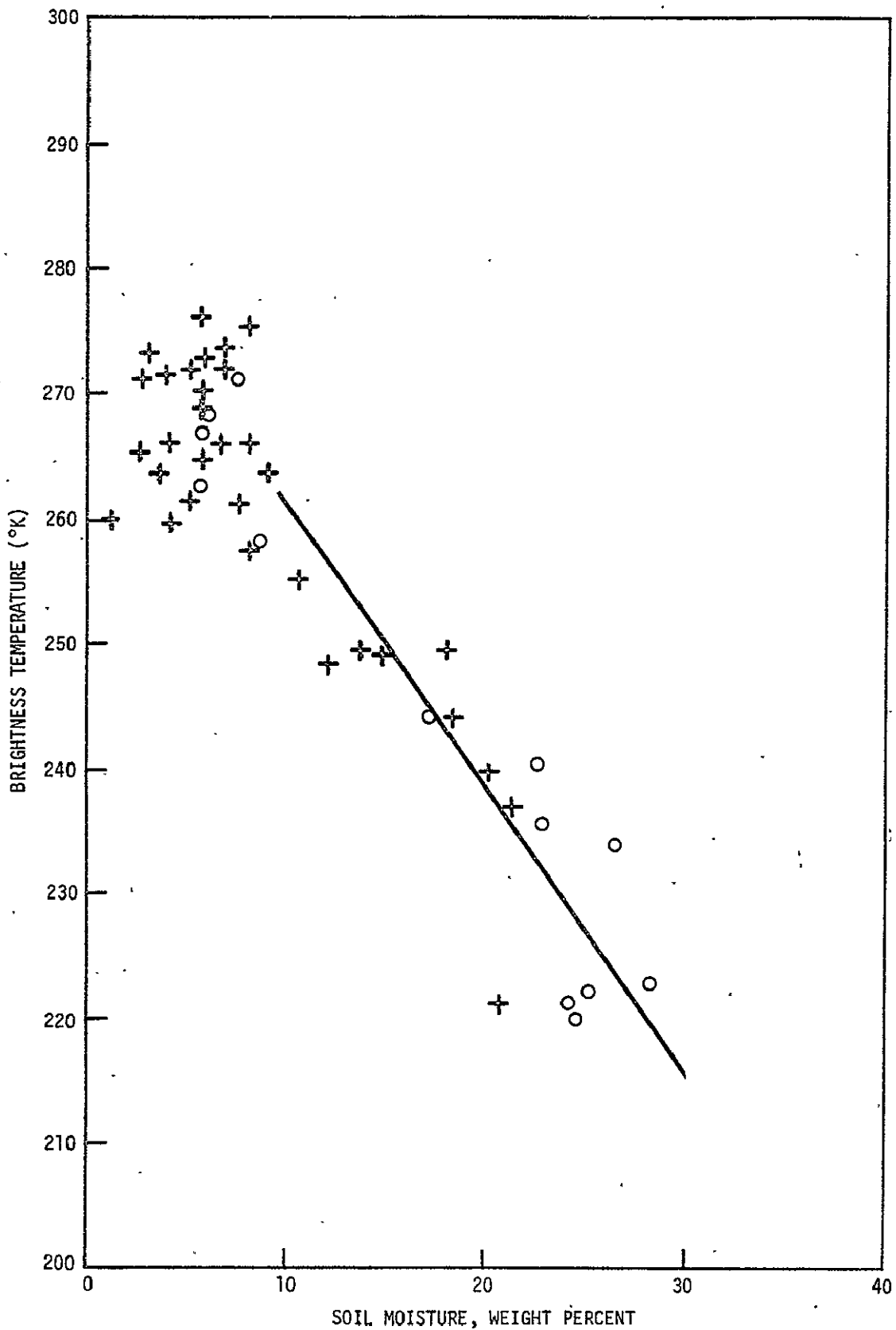


Figure 2.10.2-7.— Plot of 21 cm brightness temperature versus soil moisture for bare fields. Plus signs indicate sandy loam; open circles indicate clay loam.

Several new techniques were derived from the 1974 mission (ref. 2.10.2-4). First, by simultaneously observing the vertically and horizontally polarized brightness temperatures,  $T_V$  and  $T_H$ , the parameters  $P = 1/2(T_V + T_H)$  and  $Q = T_V - T_H$  could be formed. It was shown that the soil moisture content and the surface roughness effect might be separated by a comparison of these parameters. Figure 2.10.2-8 (fig. 5 of ref. 2.10.2-4) displays such a comparison. The  $Q$  versus soil moisture plot clearly shows the separation of the flat fields from the furrowed fields. Secondly, it was found that when soil moisture was expressed as a percent of field capacity ( $F$ ), the correlation between  $P$  and  $F$  was improved. This implies the capability of quantifying the effects of soil type. Finally, by comparing the values of  $Q$  as observed during the afternoon and dawn flights, it was found that the microwave signature of the surface rewetting effect is an increase in the polarization.

#### 2.10.2.5 Summary

From the results presented in the above subsections, it can be stated that both passive and active microwave sensors possess the potential of mapping and estimating the moisture content in soils effectively. Furthermore, because of their longer operating wavelengths, these sensors have certain advantages over their counterparts operated in the visible or infrared region. These advantages are: (1) that the electromagnetic radiation in the microwave region can penetrate through the non-raining clouds and, therefore, the sensors can be operated in nearly all weather conditions, (2) that the microwave sensors are time-of-day independent, (3) that microwaves can penetrate the lightly vegetated cover and provide information on the dielectric property of soils, and (4) that moisture content in deeper soil layers may be measured by sensors operated at longer wavelengths. In view of these advantageous properties, the microwave sensors

2.10-29

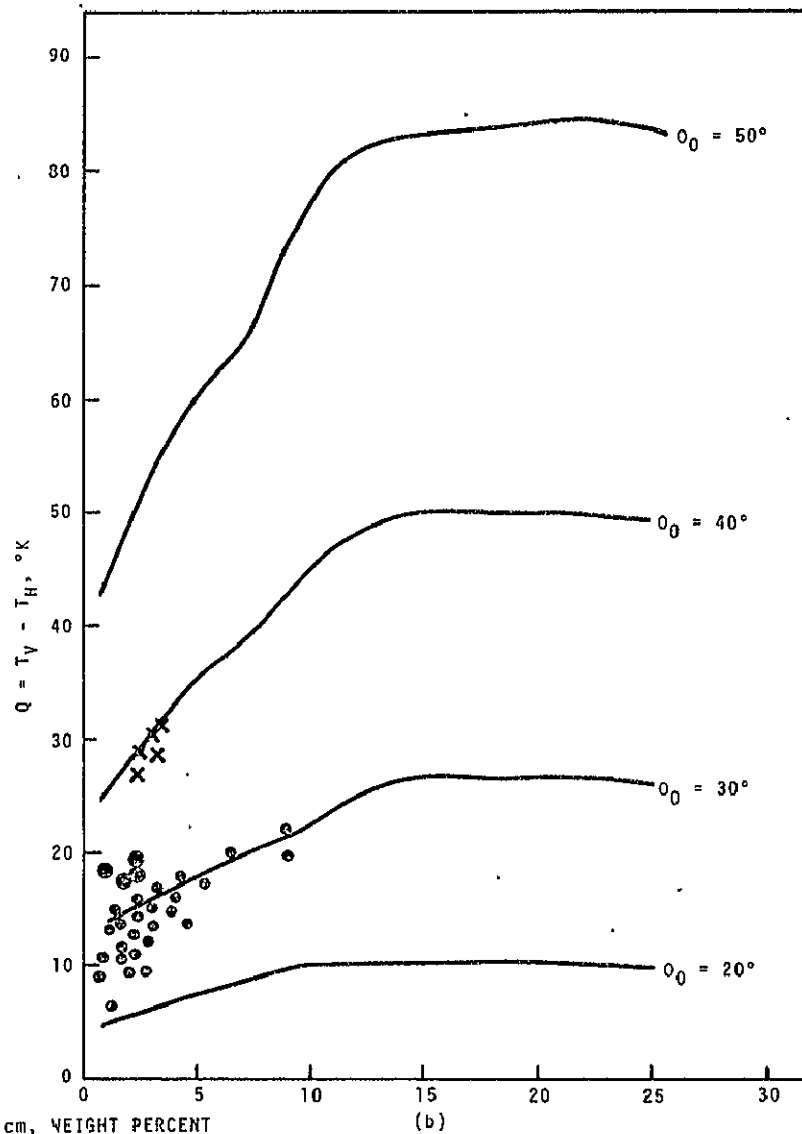
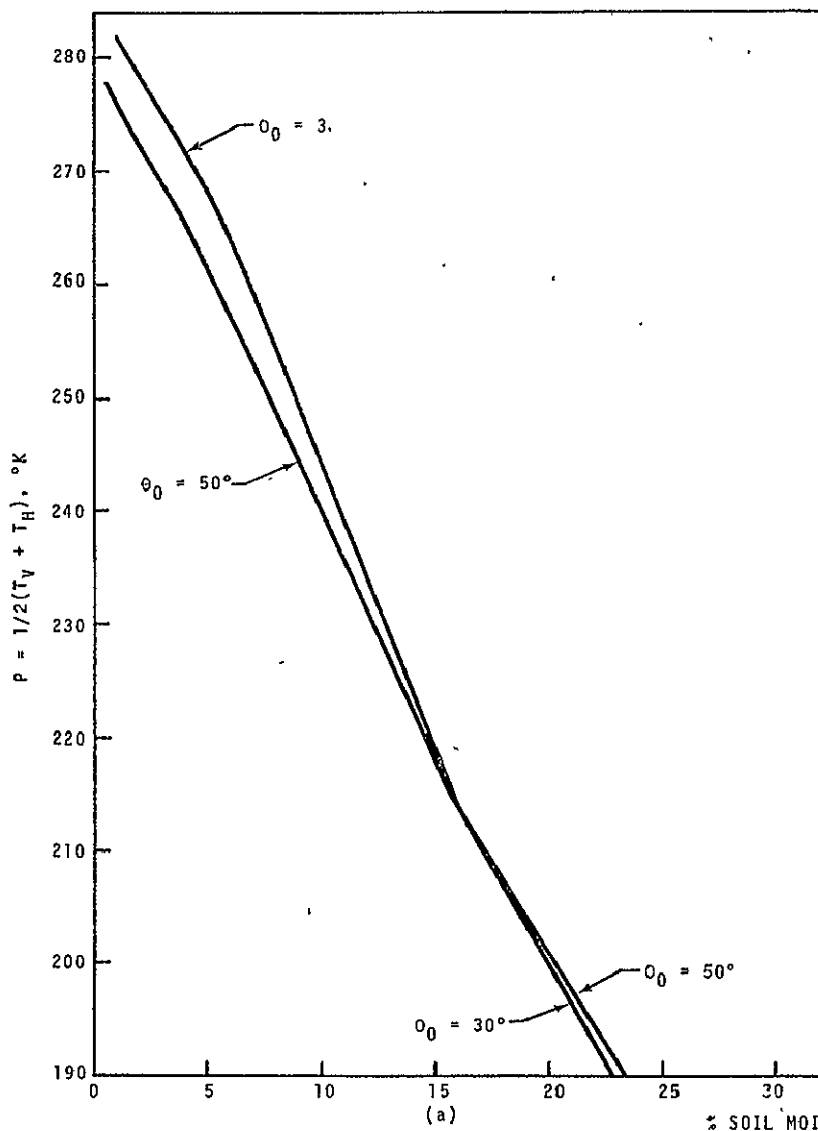


Figure 2.10.2-8.—Predictions of P and Q by a radiative transfer model for 2.8-cm emissions at various look angles  $\theta_0$ . Values of Q observed for the afternoon run are plotted in (b) with X - flat fields,  $\ominus$  - planted fields, and  $\bullet$  - furrowed fields.

are expected to play an important role in the future remote sensing of moisture content.

It is also clear from these results that many problems about soil moisture remote sensing remain to be attacked and resolved.

These problems can be conveniently grouped into two categories: (1) microwave sensor systems, and (2) microwave terrain surface interactions and mathematical modeling. To briefly discuss the questions yet to be answered in the first category, a summary on the performance of the microwave sensors described in the previous subsections is prepared in table 2.10.2-1. It is felt that further measurements and studies with both radiometers and active microwave sensors are needed in the following areas:

1. Simultaneous radiometric measurements with dual polarizations at wavelengths other than 2.8 cm. An optimal wavelength may be found so that the effects of surface roughness, vegetal cover and moisture content in the soil can be clearly separated.
2. Further study on the correlation between ground truth and spacecraft radiometric measurements at 19.3 GHz and 1.42 GHz as well as other frequencies.
3. Establishment of relation between sensor response at a given wavelength with the moisture and temperature profiles.
4. Measurements at both aircraft and satellite altitudes with scatterometers. Most of the scatterometer experiments were done on the ground with a truck-mounted system. Measurements at high altitudes are clearly necessary.
5. Measurements at both aircraft and satellite altitudes with imaging radar systems. So far, the measurements performed with an aircraft synthetic aperture radar system at both X and L bands have not given any positive and convincing results. Extensive work is needed in this area.

TABLE 2.10.2-1 - A BRIEF SUMMARY OF SOIL MOISTURE MEASUREMENTS WITH MICROWAVE SENSORS

Sensor System Frequency	3-dB Beamwidth	Pointing Rel. Nadir	Polarization	Results	Measurement Date & Vehicle	References
Radiometers: 1.42 GHz  19.35 GHz  37 GHz	15°  2.8°  5°	0°  Scans ±50° cross track  45°, Astern	N/A  Horizontal  Horizontal & Vertical	For 1.42 GHz, linear response over 0-35% moisture range, with sensitivity of ~2.2°K/% moisture.  For 19.35 GHz, little variation below ~10-20% with sensitivity of ~3°K/% moisture.  Poor sensitivity to soil moisture at 37 GHz.	Feb-March, 1971 Aircraft	2.10.3-2
1.42 GHz (MPMR)  10.7 GHz (PMIS)	15°  2.6° × 1.6°	0° and 40°  49°	Horizontal & Vertical  Horizontal & Vertical	Improved correlation when soil moisture field capacity was used instead of soil moisture content. Moisture and surface roughness effects are separable by a simultaneous observation with both vertically and horizontally polarized components. Soil types can be quantified. Increase in polarization was observed for surface rewetting effect.	April, 1974; Aircraft	2.10.3-4
19.35 GHz (ESMR)  1.42 GHz (S194)	1.4° at Nadir  Footprint at earth's surface ~110 km in diameter	Scans ±50° from Nadir  0°	Horizontal  N/A	~60°K difference in brightness temperature was observed between dry region and wet region after fair amount of rainfall (~7.5 cm for example). Presence of vegetal cover appears to raise the brightness temperature of a wet surface.  ~55° brightness temperature variation over the range of 0-35% soil moisture in top 2.5 cm layer. Correlation coefficient was ~0.97.	Jan. 1973; Nimbus 5  June-Sept. 1973 Skylab	2.10.3-3
Radiometer Scatterometer 13.9 GHz (S193 RAD/SCAT)	Radiometer footprint ~14 × 12 km and scatterometer 12 × 16 km at earth's surface	A pitch angle of 29.4°	Vertical	For radiometer, the correlation coefficients of 0.88 and 0.81 were obtained for correlations between emissivity and moisture content (top 2.5 cm) and between emissivity and composite rainfall in inches respectively. For scatterometer, the correlation coefficients of 0.67 and 0.62 were obtained for correlation between the scattering coefficient and the moisture content and between the scattering coefficient and composite rainfall in inches, respectively.	June 5, 1973; Skylab	2.10.3-6
Active Spectrometer: 2-8 GHz	5.4° at 2.75 GHz and 2.2° at 7.25 GHz (two-way)	0° - 40°	VV and HH	Recommended an operational radar system at frequency of ~4 GHz, angle of incidence of ~7°-15°, and polarization of either VV or HH. The surface roughness effect is expected to be small with this system and the estimated soil moisture sensitivity is ~0.25dB/0.01 g/cm <sup>3</sup> moisture content.	Truck	2.10.3-1
Synthetic Aperture Radar (SAR): 1.2 and 10 GHz	In the order of ~10m		VV, VH, HH, VV	Fair correlation between relative intensity return and moisture content for fields falling in the strip bounded by look angle of 47°-52°. Overall results are not conclusive.	April, 1974 Aircraft	2.10.3-7

2.10-31

The second category of problems includes the first six items mentioned in subsection 2.10.2.1. Within these items, the effects of both water content and temperature variations with depth on the response of a microwave sensor have not been explored in great detail. A small discrepancy also appears to exist in the measured microwave response on the soil type. The laboratory measurements suggest a very slight dependence of both dielectric constant and loss factor on soil type. (ref. 2.10.2-1, ref. 2.10.2-8, and ref. 2.10.2-9), whereas aircraft measurements indicate a substantial improvement in the correlation of radiometric brightness temperature with soil moisture field capacity (soil types are quantified in the process). The other two items which are not quantitatively understood are the effects of vegetal cover and surface roughness. The microwave response of vegetal cover has been observed and studied (ref. 2.10.2-4 and ref. 2.10.2-15). However, the problems of handling the vegetation-soil moisture mixture as well as the sensor frequency dependence on the mixture still remain to be explored. The effect of surface roughness has also been observed and studied with both passive and active microwave sensors (ref. 2.10.2-1 and ref. 2.10.2-4). However, the dependence of microwave response on the row directions of the furrowed fields has not been investigated. The row direction and surface roughness could very well be two of the dominant factors in determining the relative intensity of the fields in the SAR imagery described in subsection 2.10.2.3.

Finally, the mathematical models developed in the past (refs. 2.10.2-10 through 2.10.2-12) form the fundamental physical basis towards the understanding of the interaction between the electromagnetic radiation and the terrain surface. To help quantitatively interpret the observational data obtained with either passive or active microwave sensors, more sophisticated approaches are probably needed. For example, the functional

description to account for surface roughness developed in the past (e.g., ref. 2.10.2-16) may have to be incorporated in those mathematical models. Computer codes will then have to be developed and implemented to solve those models numerically.

## REFERENCES

- 2.10.2-1 Batlivala, P.P.; and Ulaby, F.T.: Effects of Roughness on the Radar Response to Soil Moisture of Bare Ground. Univ. Kansas RSL Technical Report 264-5, Sept. 1975.
- 2.10.2-2 Schmugge, T.; Gloersen, P.; Wilheit, T.; and Geiger, F.: Remote Sensing of Soil Moisture With Microwave Radiometers. J. Geophys. Res., Vol. 79, No. 2, p. 317, 1974.
- 2.10.2-3 Schmugge, T.; Rango, A.; and Neff, R.: Satellite Microwave Observations of Soil Moisture Variations. NASA/GSFC preprint X-193-75-304, Nov. 1975.
- 2.10.2-4 Schmugge, T.; Blanchard, B.; Burke, W.; Paris, J.; and Wang, J.: Results of Soil Moisture Flights During April 1974. NASA/GSFC TN D-8199, May 1976.
- 2.10.2-5 Eagleman, J.R.: Moisture Detection From Skylab. Proc. 9th Intern. Symposium. Remote Sensing of Environ., Vol. 1, p. 701, April 1974.
- 2.10.2-6 Ulaby, F.T.; Barr, J.; Sobti, A.; and Moore, R.: Soil Moisture Detection by Skylab Microwave Sensors. Univ. Kansas RSL Technical Report 243-9, Oct. 1974.
- 2.10.2-7 Cihlar, J.; Ulaby, F.; and Mueller, R.: Soil Moisture Detection From Radar Imagery of the Phoenix, Arizona Test Site. Univ. Kansas RSL Technical Report 264-4, June 1975.
- 2.10.2-8 Hoekstra, P.; and Delaney, A.: Dielectric Properties of Soils at UHF and Microwave Frequencies. J. Geophys. Res., Vol. 79, No. 11, p. 1699, April 1974.
- 2.10.2-9 Geiger, F.; and Williams, D.: Dielectric Constants of Soils at Microwave Frequencies. NASA/GSFC preprint X-652-72-238, 1972.
- 2.10.2-10 Stogryn, A.: The Brightness Temperature of a Vertically Structured Medium. Radio Science, Vol. 5, No. 12. p. 1397, Dec. 1970.
- 2.10.2-11 Burke, W.J.; and Paris J.F.: A Radiative Transfer Model for Microwave Emissions From Bare Agricultural Soils. NASA/JSC Technical Memorandum TM X-58166, Aug. 1975.

- 2.10.2-12 Wilheit, T.T.: Radiative Transfer in a Plane Stratified Dielectric. NASA/GSFC preprint X-911-75-66, March 1975.
- 2.10.2-13 Rouse, J.W.: The Effect of the Subsurface On the Depolarization of Rough-Surface Backscatter. Radio Science, Vol. 7, No. 10, p. 889, Oct. 1972.
- 2.10.2-14 Cihlar, J.; and Ulaby, F.T.: Dielectric Properties of Soils as a Function of Moisture Contents. Univ. Kansas RSL Technical Report 177-47, Nov. 1974.
- 2.10.2-15 Ulaby, F.T.: Radar Response to Vegetation. IEEE Transactions on Antennas and Propagation, Vol. AP-23, No. 1, Jan. 1975.
- 2.10.2-16 Barrick, D.E.: Rough Surfaces. Radar Cross Section Handbook, Chapter 9, Plenum Press, New York, 1970.
- 2.10.2-17 Krishen, K.: 1976 Joint Soil Moisture Experiment Plan. Johnson Space Center, RTOP No. 177-44-83, 1976.

### 3. SHUTTLE ERA SENSORS

This section discusses future earth resources sensors by sensor type, not by satellite system, since the latter often have two or more sensor types. Specific satellites and sensor systems are described in each sensor type subsection, along with the general characteristics and trade-offs involved. The latter are tied whenever possible to applications requirements. Table 3-1 gives specific satellite sensor systems by satellite and sensor type.

#### 3.1 CAMERA SYSTEMS

##### 3.1.1 INTRODUCTION

The camera systems to be considered in this section are primarily of two types: multiband and high resolution. Metric accuracy was also taken into consideration in both cases. The tightest restriction on the selection of camera systems for earth observations in the Shuttle era appears to be a minimum ground resolved distance (GRD) of 5 meters requested by several users. This GRD may prove impossible to obtain in both a multiband and high resolution camera system given restraints of cost, weight, size and power. Methods to arrive at a compromise need to be evaluated.

##### 3.1.2 MULTISPECTRAL CAMERA SYSTEMS

Because of problems in the retrieval of exposed film, the use of multispectral camera systems has been limited to manned satellites and aircraft programs. NASA is the only civilian government agency with past and future space programs incorporating multispectral photographic camera systems. These are the Skylab and Shuttle programs. The sensors to be flown on the Shuttle have not yet been determined; however, much can be learned from the evaluation of the Skylab sensors.

TABLE 3-1.- FUTURE EARTH RESOURCES SATELLITES AND SENSOR SYSTEMS

Satellite	Agency-Year	Multispectral Scanners	Photo-Graphic	Vidicons	Microwave Active	Radiometers Passive	Microwave Scatterometers	Synthetic Aperture Radar	Miscellaneous and Advanced Sensors	Comments
Landsat-C	NASA-1977	5 band MSS (2 visible 2 near IR 1 thermal IR)		RBV (2 vidicons)						Haze filters only, each RBV covers 50x50 n.mi. with improved resolution
Landsat-D	NASA-1980	7 band MSS (TM-Thematic Mapper)								Altitude 702.4 km 2 satellites; 9 days/coverage
SEOS Synchronous Earth Observatory Satellite	NASA-1981	LEST Large Earth Survey Telescope		Advanced <sup>a</sup> RBV Framing Camera	Microwave <sup>a</sup> Sounder	AASIR Advanced Atmos- pheric Sounder and Imaging Radiometer				LEST will have 1.5 m dia. aperture and cover continental and coastal U.S.
SARSAT Synthetic Aperture Radar SATellite								SAR (X-band)		
Seasat-A	NASA-early 1978	Scanning Radiometer (2 bands 1 visible, 1 IR)				SMR Scanning Multi- frequency Microwave Radio- meter (5 bands)	Fan Beam Scatterometer	CIR Coherent Imaging Radar (L-band)	Precision Altimeter (Ku-band)	
SMS/GOES Synchronous Meteorological SATellite	NASA SMS-1 May '74 SMS-2 Feb '75	VISSR Visible-Infrared Spin Scan Radiometer								International system with Russian, Japanese, and European satellites joining in near future
ERSS		'Chameleon' NSS (France) (Select 3 of 9 visible bands plus 2 thermal IR bands)	(USSR) 0.45- 0.9μ	(USSR) 0.5- 1.2μ	(Canada) L-band					

<sup>a</sup>Potential sensors.

3.1-2

### 3.1.2.1 Skylab S-190A

While approximately 5 years have elapsed since the initial planning and development stage, the Skylab multispectral photographic facility, S-190A, represents the most advanced operational multi-band photographic system to date. Table 3.1-1 presents a summary of the performance characteristics of the S-190A system.

Eighteen filters were provided with the S-190A camera system. Of these, only four (N,O,P,Q) were used in addition to the basic six filters (A,B,C,D,E,F). The following is a list of filters and corresponding bandwidths and peak transmission wavelengths.

<u>Filter</u>	<u>Bandwidth</u>	<u>Peak</u>
	NM	NM
A	450-650	540
B	550-800	(650 cut-on)
C	690-880	740
D	750-1000	(860 cut-on)
E	450-600	(560 cut-on)
F	400-700	(480 cut-on)
G	350-550	470
H	350-550	450
I	490-630	540
J	600-750	640
K	700-850	770
L	740-950	850
M	330-700	500
N	440-560	490
O	540-660	620
P	650-760	710
Q	720-870	820
R	800-1000	(930 cut-on)

TABLE 3.1-1. -- CHARACTERISTICS OF S-190A MULTISPECTRAL  
PHOTOGRAPHIC CAMERA SYSTEM

Focal Length, inches	6
Aperture	f/2.8 Manually adjustable from f/2.8 to f/16 in 1/2 stop increments.
Photographic Field, degrees	21.24 x 21.24
Format, inches	2 1/4 x 2 1/4
Exposure Time, milliseconds	2.5, 5, and 10
V/h Range, milliradians per second	10 to 35
Framing Rate, seconds per frame	2 to 32
Spectral Range, nanometers	500-600 600-700 700-800 800-900 500-880 400-700
Image Registration, micrometers	
Radially (100 nm bands)	5
(combined bands)	.10
Tangentially (100 nm bands)	20 tan $\beta$ ( $\beta$ = field angle)
(combined bands)	20 tan $\beta$
Film Capacity, feet	100
Image Distortion, micrometers	<10
Weight, kilograms	
Camera	109
Control electronics	34
Power, watts	
Average operating	120
Continuous thermal control	50

These filters could be used in combinations of up to two at a time; however, this capability was never utilized. The effective bandwidths of each S-190A camera station with the primary set of filters are listed as follows:

<u>Station</u>	<u>Film</u>	<u>Filter</u>	<u>Bandwidth</u>
1	2424	C	690-840
2	2424	D	780-900*
3	2443	E	510-800
4	SO-242	F	410-710*
5	SO-022	B	590-710*
6	SO-022	A	480-620

\*film cut off

The radiometric calibration accuracy of the S-190A camera system is limited by the sensitometric stability of the film. In most cases, the sensitometry change of the film resulted in an exposure inaccuracy of about a quarter to a half stop. The change of the 2424 IR film may be attributed to a degradation of spectral sensitivity with time; while the SO-022 change was caused by an increase in sensitivity with time.

S-190A photography was intended for use as registered imagery in multiband photographic viewers. It appears that few researchers took advantage of the registrational capability of the sensor. The most common method of data analysis was conventional macro- and microdensitometry with manual locating of target features. Although procedures were outlined by the NASA Johnson Space Center Photographic Technology Division (PTD) (ref. 3.1-1) for generating density values in terms of original Skylab densities, most researchers did not avail themselves of this capability.

In general, the technology for handling, processing and analyzing multispectral photographic data has lagged behind sensor

technology. Skylab proved the technical feasibility of using a satellite-borne multispectral system to gather remote sensing data.

With some exceptions, Skylab photographic data users were not taking full advantage of the registrational capability of the S-190A multispectral camera system. It has been noticed by Pilonero (ref. 3.1-2) and Yost (ref. 3.1-3) that by combining black and white imagery in a false color representation, better resolution and more information is obtained than with three-layer color film. Thematic extraction of data has been accomplished on a scale of 1:250,000 which is cartographically significant (Colvocoresses, ref. 3.1-4).

The transfer sensitometry was provided with each user's photo copies. With this sensitometry it is possible to generate density values in terms of the original Skylab imagery. By referring density values to the original, a check on the exposure of the original can be performed and it can be determined whether a particular frame was suitably exposed and processed for a given application. For example, it appears that data used for detecting patterns of suspended sediment are underexposed, Hargis (ref. 3.1-5), Yost (ref. 3.1-3), and Yarger (ref. 3.1-6). This cannot be substantiated or corrected unless the data is transferrable to the original Skylab image densities.

In one case, Yost (ref. 3.1-3), it was reported that there was too great a variability in the steps of the transfer sensitometry for it to be of any use. Variations do occur within the steps of the sensitometry. These have been measured on a first generation copy to be between .01 and .03 within the linear range. The problem seems to be in the reproduction process and should be investigated to avoid such problems in the future.

The limiting factor in the cartographic applications of S-190A was resolution. Because features such as railroads, secondary

roads, or urban boundaries cannot be identified, map revision is not possible with the S-190A imagery (Colvocoresses, ref. 3.1-4). Planimetric maps were compiled from a single image at 1:250,000 scale and a stereo pair at 1:50,000 scale with an accuracy fulfilling Class B NATO standards.

#### 3.1.2.2 Single-Lens Multiband Camera

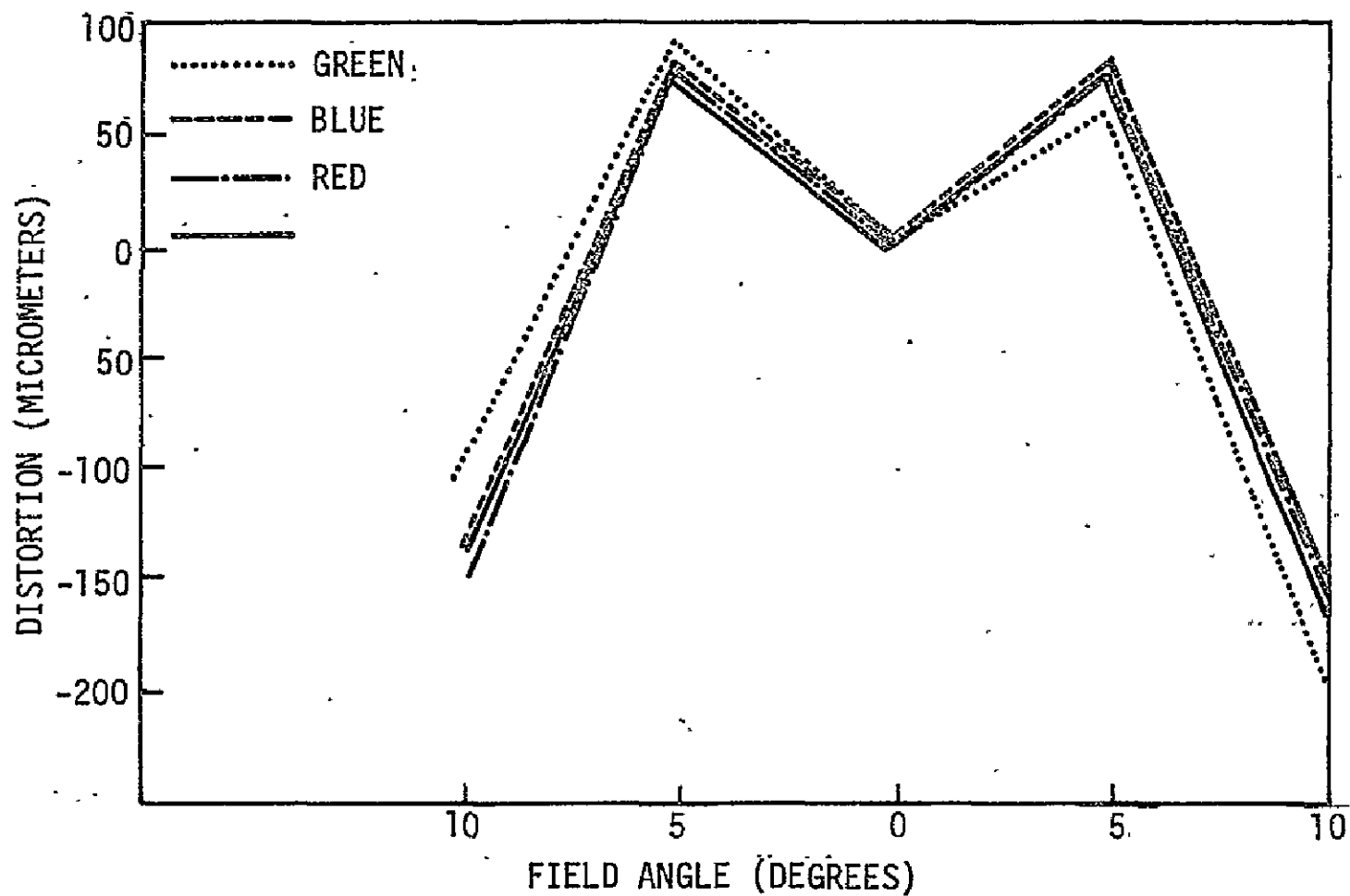
A single-lens multiband camera was developed by the Boller and Chivens Division of Perkin Elmer for the U.S. Army Engineering Topographic Laboratories, Brooke (ref. 3.1-7). This consists of a 6 in. or 4 in. focal length lens, an inverted telephoto system designed by Optical Research Associates, with prisms to split the beam into four channels. A 70 mm format is used to record images in the blue, green, red and infrared spectral regions. While the resolution is less than the S190A camera system, the relative distortion of the four images (figure 3.1-1) is within 10 microns, making it a promising design for future research.

#### 3.1.2.3 Other Multispectral Cameras

Table 3.1-2 is a list of available multiband cameras for aerial and satellite applications. With the exception of the Itek Multispectral Photographic Facility (MPF), multispectral cameras were not specifically designed for photogrammetric or radiometric purposes, because they incorporate focal plane shutters.

#### 3.1.2.4 Films for Multispectral Applications

The most important criterion of film selection for multispectral applications is that the spectral sensitivity of the film should be reasonably flat within the particular bandwidth of the camera channel. The resolving power and granularity of the film should be such that these factors do not limit the ultimate resolution of the photographic system. A tabulation of commonly used aerial photographic films is found in table 3.1-3.



NOTE: HEAVY, DARK BAND SHOWS EFFECT OF PRISM MISALIGNMENT

Figure 3.1-1.— Relative distortion of 6 inch focal length lens in Perkin Elmer. Single Lens Multiband Camera.

2-3

TABLE 3.1-2. - MULTISPECTRAL CAMERA SYSTEMS

Camera	Nine Lens	Model II	Mark I	Aero I	Multispectral Photographic Facility/S190A
Manufacturer	Itek	Spectral Data	I <sup>2</sup> S	Dot Products	Itek
Bands	9	4	4	4	6
Format (cm)	5.7 x 5.7	8.9 x 8.9	8.9 x 8.9	5.7 x 5.7	5.7 x 5.7
Film Length (m)	76	76	76	120	30
Base Thickness (µm)	100	100	100	100	100
Frames/Roll	325	188	300	470	115
Magazine	A9B (Mod)	A-5A or A-9	A-5A	A-9	cassette
Cycle time (sec)	1.25-1.75	2.0	2.0	2.0	2.0+
FMC Type	moving film	moving film	N/A	N/A	rocking mount
FMC Rate (mm/sec)	2.5-125	2.5-700	N/A	N/A	15.8 mrad/sec (variable)
FMC Error	N/A	N/A	N/A	N/A	<10%
Lens	Xenotar	Xenotar	Xenotar	Xenotar	MPF
Manufacturer(s)	Schneider Gheity	Schneider	Schneider	Schneider	Itek
Focal Length (mm)	152	150, 100	150, 100	150, 100	150
f/No Range	2.4-16	2.8-16	2.8-16	2.8-16	2.8-16
AWAR, 1,000, 1	N/A	451/mm	N/A	N/A	
Film	N/A	2424	N/A	N/A	
Filters	Wratten	40 available	Wratten	N/A	special
Shutter Speed (sec)	1/30 - 1/120	1/25 - 1/33 or 1/150 - 1/350	1/150 - 1/350(A) 1/350 - 1/800(B)	1/150 - 1/350(A) 1/350 - 1/800(B)	1/100, 1/200, 1/400
Shutter Type	focal plane	focal plane	focal plane	focal plane	rotary, intralens
Weight (kg) Without film	23	43	26	N/A	57
Data Annotation	band no. & flight detector	N/A	N/A	N/A	card, digital
Intervalometer	N/A	yes	external	external	yes
Exposure Control	N/A	N/A	N/A	N/A	N/A
Remarks	fiducials		modified K-22	modified K-22	grid reseau

TABLE 3.1-3. - FILM FOR AERIAL AND SATELLITE APPLICATIONS

Film	Film Number	Base Thickness (µm)	Aerial Film Speed (AFS)	Aerial Exposure Index (AEI)	Developer or Processes	Resolving Power Lines/mm Target/Object Contrast		Diffuse RMS Granularity*
						1000:1	1.6:1	
Plus X Aerographic	2402	100	200	80	D-19	100	50	19
Tri-X Aerographic	2403	100	650	250	D-19	80	20	33
Double-X Aerographic	2405	100	320	125	DK-50	80	40	26
Panatomic X Aerial	3400	60	64	20	D-19	160	63	16
Plus-X Aerial	3401	60	200	64	D-19	100	40	30
Hi-Definition Aerial	3414	60	8	2.5	D-19	630	250	9
	1414	40	8	2.5	D-19	630	250	9
IR Aerographic	2424	100	200	100	D-19	80	32	33
Multispectral IR Aerial	SO-289	100	100	-	-	200	80	12
Aerochrome IR	2443	100	40	10	EA-5	63	32	17
	3443	60	40	10	EA-5	63	32	17
Hi-Definition	SO-127	100	6	-	EA-5	160	50	9
Aerochrome IR	SO-131	60	6	-	EA-5	160	50	9
	SO-130	40	6	-	EA-5	160	50	9
Aerocolor Neg	2445	100	100	32	Aero-Neg	80	40	13
Ektachrome MS	2448	100	32	6	EA-4	80	40	12
Aerial Color	SO-242	60	6	2	ME-4	200	100	11
	SO-255	40	6	2	(Modified)	200	100	11
Ektachrome EF	SO-397	100	64	12	EA-4	63	32	13
	SO-154	60	64	12	EA-4	63	32	13
Water Penetration	SO-224	100	40	-	EA-5	125	50	24
Ansochrome	D/200	100	90	30	AR-IC	100	50	25
	D/500	100	230	75	AR-IC	80	40	45

3.1-10

Since the Skylab Mission there have been improvements in resolution for black and white infrared and color films. Multispectral infrared aerial film SO-289 has recently become available to replace the older 2424. SO-289 has about 2.5 times the resolving power of 2424 and a relatively flat spectral response from 0.4  $\mu\text{m}$  to 0.9  $\mu\text{m}$ . The weak response of 2424 in the green region is eliminated in this new film as seen in figure 3.1-2.

### 3.1.3 HIGH RESOLUTION CAMERAS

The cameras considered in this section are those designed to operate with high resolving power and low f-number. Since mapping camera requirements are considered elsewhere, highly corrected distortion is not a requirement. The high resolution cameras may be divided into three categories; frame, panoramic and strip.

#### 3.1.3.1 Frame Cameras

The criteria used in selecting frame cameras for consideration in Shuttle sensor evaluation are high resolution, capability of producing a photograph which can be enlarged to at least a 1:250,000 scale with a resolution of 5 lines per mm or better, the availability of forward motion compensation (FMC) to correct a forward image motion on the order of 10 mr/sec, and automatic exposure control. There are not many cameras which satisfy all these conditions. As a result, only four are listed in table 3.1-4.

#### 3.1.3.2 Panoramic Cameras

One advantage of the panoramic camera is that it has a high resolution over a larger angular field-of-view. This type of camera records the ground from horizon-to-horizon in the cross track direction across the width of the picture format with a slit equal in length to the width of the picture format. The width of the slit is variable to control exposure time. The instantaneous field-of-view is small because the image falls onto a

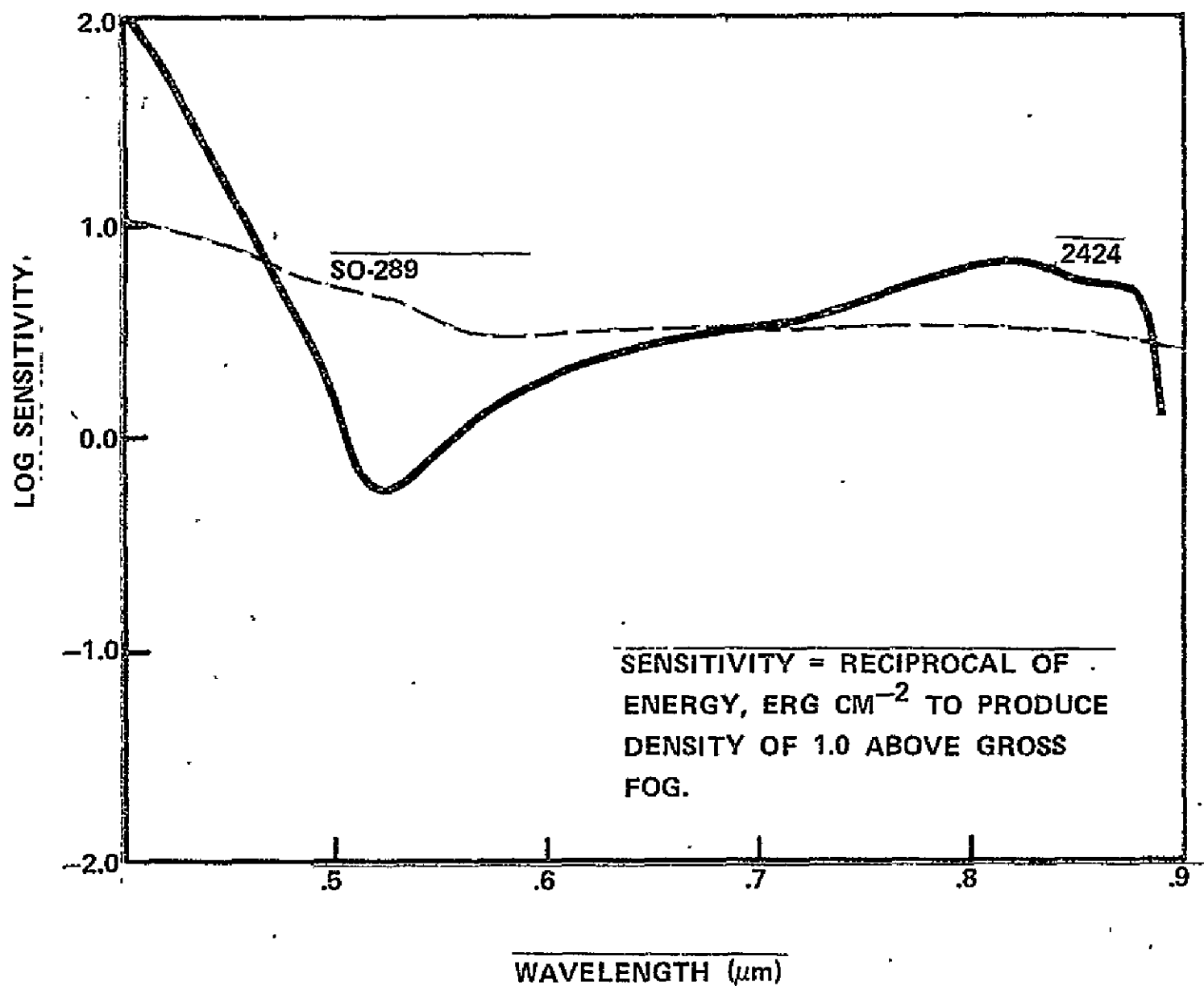


Figure 3.1-2.— Spectral sensitivity of EK SO-289 compared to EK 2424.

TABLE 3.1-4. - FRAME CAMERAS FOR SHUTTLE EVALUATION

Camera	KRb/824C	KS-87B	HLT-548	KA-61
Manufacturer	Carl Zeiss (3 lenses)	Chicago Aerial	Hycon	Itek
Format (cm)	7.2 x 7.2	11.5 x 11.5	11.4 x 11.4	5.7 x 5.7
Film Length (m)	15	150	60	15
Base Thickness (µm)	160	60, 100, 130	64	100
Frames/Roll	185	1,200	456	225
Magazine	cassette	cassette	N/A	integral
Cycle Time (sec)	.17	.17	.8	.3
FMC Type	angle correct	moving film	rocking	moving film
FMC Rate mm/sec	(max) 1.4	2.5-305	1.7-175mmrad/sec	0.0-38.1
FMC Error	N/A	2%	N/A	< 10%
AWAR <sup>a</sup> (1:1000)	60	40-60	150	54
Film	Pan-X	Pan-X	3414	Pan-X
Focal Length(s) (mm)	80	150, 305, 460	460	52
Field-of View	48° x 143°	20°, 10°, 7°	14°8' x 14°8'	58°36' x 58°36'
Exposure time (sec)	1/100 - 1/2000	1/60 - 1/3000	1/50, 1/200, 1/1000	1/60 - 1/500
Type	focal plane	focal plane	focal plane	Graflex
Weight (kg)	10.3	33-40	30	2.7
Exposure Control	auto	auto, internal	manual	auto

<sup>a</sup>AWAR (Area Weighted Average Resolution) is determined by dividing the picture format into concentric annular zones and using the ratio of the area of a zone to the total format area as a weighting factor for the resolution of that area. AWAR is calculated by the formula

$$AWAR = \sum_i \frac{A_i}{A} \sqrt{R_i T_i}$$

where

A = total area of the picture format over which the summation is made

A<sub>i</sub> = area of a particular zone

R<sub>i</sub> = average radial resolving power in zone A (or the radial resolving power at the midpoint of a zone)

T<sub>i</sub> = average tangential resolving power in zone A [(or tangential resolving power in zone A (or tangential resolving power at the midpoint of the zone)] (ref. 3.1-8)

narrow slit immediately in front of the film. This small field-of-view allows the panoramic camera to obtain resolutions on the order of 100 lines per mm over the entire picture format. The film surface is cylindrical with the width of the film parallel to the axis of the cylinder. Table 3.1-5 is a list of panoramic cameras for consideration.

The horizon-to-horizon scan of the panoramic camera is achieved by the relative motions of the lens, slit, and film. There are three types of panoramic cameras divided according to scan type:

1. Direct Scan - The lens and slit rotate while the film remains constant.
2. Rotating prism - A prism between a stationary lens and stationary slit can rotate at half the rate of the moving film.
3. Split Scan and Optical Bar - The relative motion is divided between the film and the lens/slit combination.

Panoramic photography contains distortions not present in frame photography:

1. Panoramic Distortion - Because of the cylindrical film plane and method of scanning, the projection between the ground and the film plane is not orthogonal but shows a characteristic trapezoidal grid pattern.
2. Scan Positional Distortion - Images are displaced in the cross track direction because of the forward motion of the aircraft. In addition; forward motion compensation and tilt complicate distortion.

#### 3.1.3.3 Strip Cameras

Although the first strip camera was operational in 1932 (the KA-18A) outside of text book references (3.1-9, 3.1-10, 3.1-11) there is no mention made in the literature of current application. The strip camera relies on the forward motion of the

TABLE 3.1-5. - PANORAMIC CAMERAS FOR EVALUATION

Camera	KA-91A	KS-116	CA-144	KA-59	KA-79A	KA-81A	KA-82C	KA-92	KA-55	KA-80A	KA-83A
Manufacturer	Chicago Aerial	Chicago Aerial	Chicago Aerial	Fairchild	Fairchild	Fairchild	Fairchild	Fairchild	Hycon	Itek	Itek
Format (cm)	11.4x48	11.4x25	11.4x102	11.4x96	11.4x64	11.4x21.3	11.4x74	11.4x72	11.4x48	11.4x128	11.4x128
Film Length	305, 610	150, 305	150, 305	1, 070	610	610	610	150	150, 305	1067	610
Thickness (µm)	64, 100, 130	64, 100, 130	64	64	64	64	64	64	130, 64	.1	.1
Frames/Roll Magazine	265, 530 cassette	290, 580 cassette	280-1150 cassette	1,100 integral	890 cassette	2,400-685 cassette	740 cassette	2,000 cassette	315, 630 cassette	N/A integral	N/A integral
Cycle Time	.75	.5	.5	1.0-60.0	1.7-20	.9-5.9	1.7-20	.53-1.5	2.0	3.5 +	1.74 +
FMC Type	moving lens	moving lens	moving lens	moving lens	moving lens	moving lens	moving lens	moving lens & moving mirror	moving lens	rocking mount	rocking mount
FMC Rate (mm/sec)	3,3-67	3,3-101	2,54-100.6	2,3-46	5,1-58	159 (max)	5,1-58	8-400	5,1-51	5-25 mrad/sec	20-100 mrad/sec
FMC Error	5%	5%	N/A	N/A	N/A	N/A	N/A	N/A	20%	N/A	N/A
AWAR(1:1000) 1/mm Film	70 PAN-X	70 PAN-X	60 PAN-X	60 Plus-X	85 PAN-X	N/A N/A	85 PAN-X	95 3400	74 Plus-X	N/A N/A	70 PAN-X
Focal Length	460	305	610	305	305	1,220	305	230, 610	305	610	610
F1 No Range	4,0	4,0	5,6	3,8	3,8-22	4	3,8-22	4	5,6-16	3,5	3,5
Wavelength	.4-.9	.4-.9	.55-.66	.4-.7	.4-.7	.4-.7	.4-.7	.4-.7	.5-.7	.55-.7	.55-.7
Angular Coverage	14°5'x60°	21°12'x 40°-140°	10°x20°-95°	21°x180°	21°x120°	5°22'x 10°-40°	21°x140°	N/A	21°14'x 90°	12°x120°	12°x120°
Shutter Speed	1/100-1/1500	1/100-1/1500	1/100-1/1500	1/100-1/1500	1/30-1/12,000	1/50-1/16,800	1/30-1/12,000	1/1600-1/11,000	1/100-1/300	1/35-1/300-4	1/90-1/550
Shutter Type	Scanning slit & capping shutter	Scanning slit & capping shutter	Scanning slit & capping shutter	focal plane	focal plane, scanning slit	scanning slit	scanning slit				
Weight (kg)	73	55	N/A	137	85	95	90	N/A	50	110	104
Data Annotation	CRT, fixed data counter	CRT, fixed data counter	CRT, fixed data counter	counter, clock card	counter, clock card	counter, clock card	counter, clock card	MIL-STD-782C	binary, A DAS	clock card counter	clock, card counter
Intervalometer	external	external	internal	N/A	N/A	N/A	N/A	N/A	external	yes	yes
Exposure Control	auto, internal	auto, internal	auto, internal	auto	auto	auto	auto	auto	auto	auto	auto

3.1-15

vehicle to provide scanning in the track direction as the film is moved past the stationary focal plane slit at a rate equal to the image motion. Because there are fewer moving parts, the camera is more reliable than others (ref. 3.1-11). The strip camera has a potential application in multiband photography since an array of them can be synchronized by driving them from a single shaft. According to ref. 3.1-11, the strip camera has the advantage over an equivalent frame camera in higher resolution, lower distortion, and more uniform film plane irradiance.

#### 3.1.4 RECOMMENDATIONS

Of all the requirements placed on the system by users, the most critical is resolution. For most disciplines, 5 m resolution is desirable. At projected altitudes of 100-300 n.mi., the dynamic resolution performance of the S-190A multispectral camera is given in figure 3.1-3. It can be seen that it is not possible to satisfy resolutions requirements with a 6-inch focal length lens and current films. By doubling the focal length of the lens, the ground resolved distance would be decreased and 5-m resolution attainable. This presents problems in that a 12-inch focal length multispectral camera is not an off-the-shelf item. In addition to increased size, there are problems with the increased weight and power requirements. The solution to the problem of resolution might be to have a high resolution large format camera bore-sighted to the multispectral camera system.

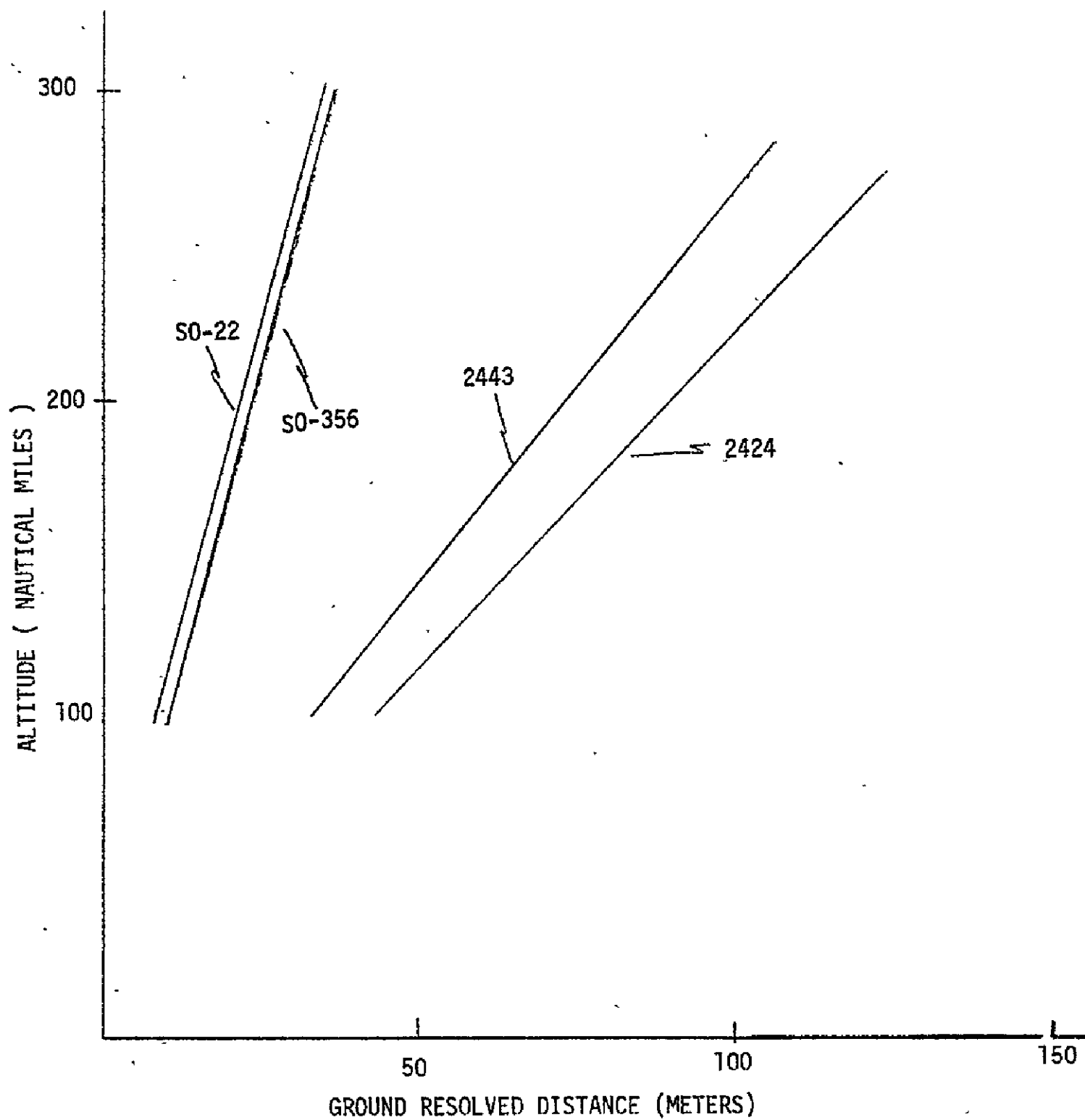


Figure 3.1-3.— Dynamic resolution of S-190A camera system, high contrast target 6.3:1.

## REFERENCES

- 3.1-1 SL/2 Sensitometric Data Package, JLL2-502, 20 July, 1973; SL/3 Sensitometric Data Package, JLL2-503, 23 Nov., 1973; SL/4 Sensitometric Data Package, JLL2-505, 10 June, 1974; and Film Handling Procedures, JLL2-202, 10 Nov. 1972.
- 3.1-2 Pilonero, Joseph T.: Photomapping of the United States, Skylab Experiment No. 498. October 1975.
- 3.1-3 Yost, Edward F.: In Situ Spectro-Radiometric Calibration of EREP Imagery and Estuarian and Coastal Oceanography of Black Island and Adjacent New York Coastal Waters. NAS 9-13308.
- 3.1-4 Colvocoresses, Alden P.: "Overall Evaluation of Skylab (EREP) Images for Cartographic Application." Paper presented at the American Society of Photogrammetry and American Congress of Surveying and Mapping, Fall meeting, Phoenix, Arizona, Oct. 26-31, 1975.
- 3.1-5 Hargis, William: Southern Chesapeake Bay Water Color and Circulation Analysis. EPN #517.
- 3.1-6 Yarger, Harold L.; and McCauley, James R.: Skylab Study of Water Quality. NAS-13271
- 3.1-7 Brooke, Robert K.: "A Single Multiband Camera." Optical Engineering, Vol. 14, No. 4, pp. 347-350.
- 3.1-8 U.S. Gov't Printing Office, 1963 Military Standard 150A (revised): "Military Standard Photographic Lenses." Washington, D.C.
- 3.1-9 Brock, G. C.: "The Physical Aspects of Aerial Photography," New York, 1952.
- 3.1-10 Wolf, Paul R.: "Elements of Photogrammetry," New York, 1974.
- 3.1-11 American Society of Photogrammetry, "Manual of Remote Sensing," 1975. Section 6.

## 3.2 MULTISPECTRAL SCANNERS

### 3.2.1 MSS INTRODUCTION AND BACKGROUND

This section is concerned with past and current multispectral scanner (MSS) sensors for remote sensing from space. This introduction gives an overview of MSS sensors discussing their evolution and development from aircraft MSS's to Landsat-2.

Subsection 3.2.2 discusses current plans for future MSS systems. Subsection 3.2.3 covers MSS design characteristics such as spectral band selection, pixel size, dynamic range, sensitivity and scan geometry.

#### 3.2.1.1 Aircraft Multispectral Scanners

The University of Michigan 12-band and the Bendix 24-band aircraft MSS's were the first such sensors built to obtain digital multispectral earth resources data in large quantities for research purposes. Each MSS was of the object plane scanning type and utilized a rotating, tilted mirror to scan the ground in one direction and at right angles to the aircraft's line of flight. The Michigan 12-band MSS covered the spectrum from the UV to the near IR (.32  $\mu\text{m}$ -1.00  $\mu\text{m}$ ). The Bendix 24-band spectral coverage was much greater, with additional bands in the 0.34-1.3, 1.5-1.7, 2.1-2.36, 3.5-4.75 and 6.13  $\mu\text{m}$  regions. These bands were chosen in order to cover with appropriate spectral bandwidths the visible, near (reflective) infrared, and thermal infrared 'windows' of the atmosphere, i.e., the bands were chosen in order to avoid the strong water, ozone, and carbon dioxide absorption regions. However, two of the Bendix MSS bands (1.05-1.09, 1.12-1.16  $\mu\text{m}$ ) were positioned at a water absorption band with the expectation that their ratio would be useful in calculating the amount of precipitable water vapor, and therefore enabling some atmospheric corrections to be made (see section 2.2.2 for more details).

Since the much more complex 24-band MSS was not available until 1971 and experienced many operational problems, the older, more reliable 12-band MSS was used to provide the multispectral agricultural data used by the Purdue University's Laboratory for the Application of Remote Sensing (LARS) in its rapidly expanding investigation (in the late 1960's) of the use of digital multispectral data for crop classification. This is indicated in figure 3.2-1 which diagrammatically shows the development of and relationships between earth resources MSS's over the 1965-1980 time frame.

### 3.2.1.2 SO-65 Experiment

About the same time that the Michigan 12-band MSS data were being used by LARS to develop agricultural computer classification techniques, the Apollo 9 multiband camera experiment, SO-65, was carried out in early 1969. The SO-65 experiment used four 70 mm Hasselblad cameras mounted together. Three cameras had film-filter combinations which produced green, red, and near infrared (0.68-0.89  $\mu\text{m}$ ) bands. The fourth camera used color infrared film. As the Apollo astronauts took photographs over an agricultural test area in the Imperial Valley of California, ground truth data obtained by workers in the test area and aircraft underflights were made using the Michigan 12-band MSS. Although the SO-65 data were limited in spectral coverage by the nature of the film and in the number of bands by the physical size and complexity of mounting cameras together, they were nonetheless unique in being the first such multispectral data taken from orbital altitude (over 100 n.mi. in this case) and in an experimental setup with emphasis on agricultural classification. One of the SO-65 objectives was to compare the classification performance of the color infrared film with that obtained using the three corresponding black and white film bands. The results obtained by LARS indicated that the digital data from the three separate black and white bands outperformed the data obtained from the color infrared film (ref. 3.2-1). This had been

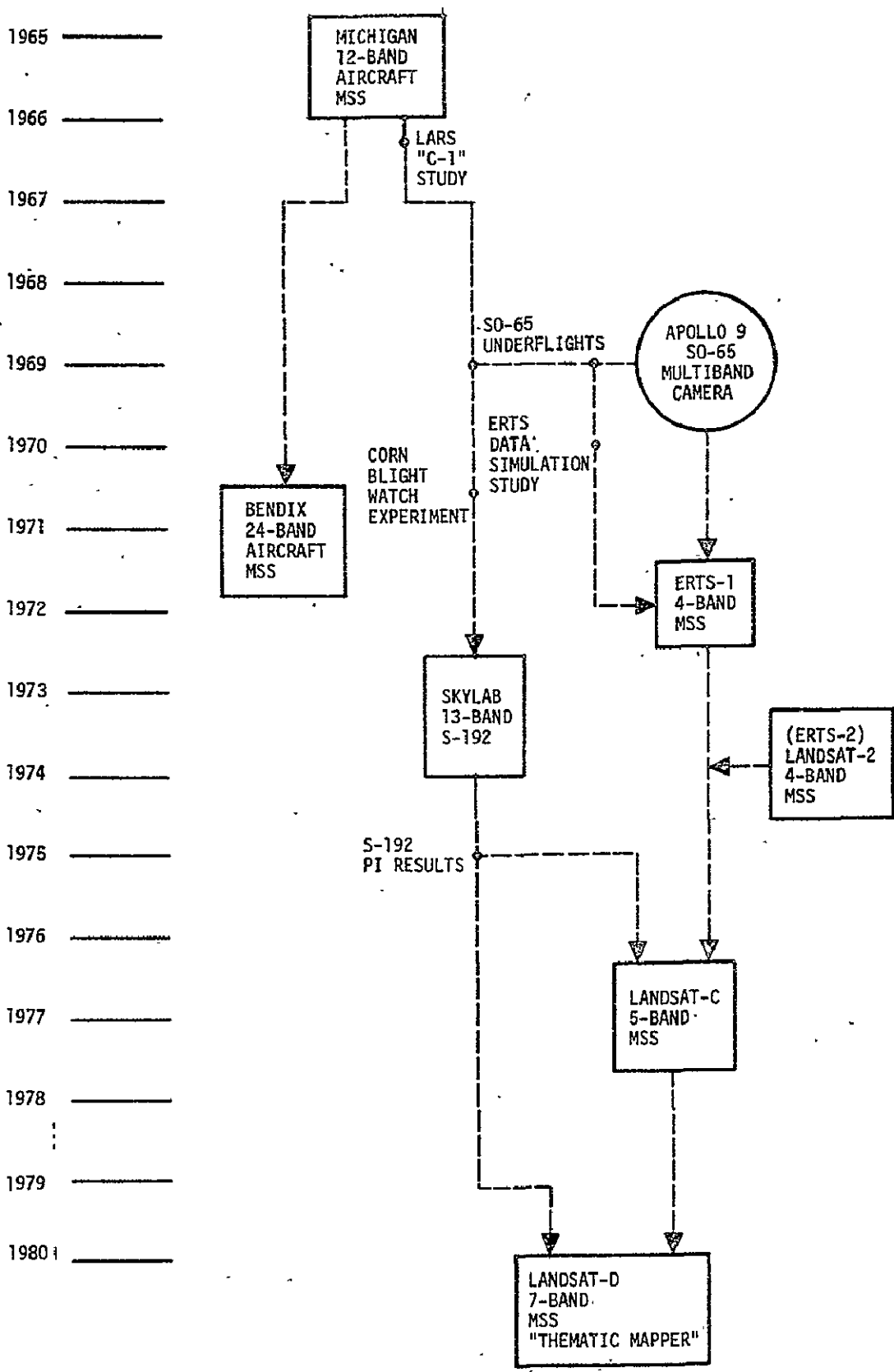


Figure 3.2-1. - Earth Resources MSS development, 1965-1980.

anticipated because of the spectral overlap in the multi-emulsion color film and the consequent difficulty in trying to adequately separate the individual spectral band data. It should be noted, however, that this experiment failed to take advantage of the inherent band-to-band spatial registration of the color film since it was scanned with a microdensitometer three separate times in order to obtain the spectral data. This, compiled with the fact that the classification results by individual crops were mixed, prevented any final conclusions in the comparison of multi-emulsion film versus multiple camera approaches.

The SO-65 underflight data taken with the Michigan 12-band MSS were also used in a simulation of the Earth Resources Technology Satellite (ERTS) 4-band MSS data (ref. 3.2-2). At the time this study was made, the ERTS-1 launching was close at hand and therefore, the primary objective was to obtain 'ERTS like' data with which to develop appropriate data processing techniques and to evaluate the usefulness of the proposed ERTS bands and spatial resolution. In addition, microdensitometer data from the SO-65 frames were also available for ERTS simulation studies. A secondary objective was to evaluate alternative procedures and techniques for correlating the SO-65 photographic data with the underflight MSS and field team ground truth data. The simulated ERTS data were used primarily in checking out the software that was being developed in the limited amount of time prior to the ERTS-1 launch. This software enabled the anticipated flood of ERTS-1 data to be screened and edited on JSC's Data Analysis Stations (DAS's). In addition, the simulated ERTS data were used to aid the establishment of Purdue University's LARS System (LARSYS) multispectral data processing software routines on JSC's computer systems. However, no real attempt was made to evaluate the potential usefulness of the upcoming ERTS data, mostly because of the limited time frame.

### 3.2.1.3 ERTS-1 to Landsat-2

The ERTS-1 with its 4-band MSS was launched July 23, 1972 and became the first earth resources satellite system designed to enable nearly worldwide coverage on a regular basis. The ERTS-1 (now referred to as Landsat-1) was placed in a sun-synchronous orbit at 907 km altitude, designed so that it passed southward, repeating its coverage over any given location every 18 days.

The ERTS-1 MSS's first three spectral bands approximated the green (0.5-0.6  $\mu\text{m}$ ), red (0.6-0.7  $\mu\text{m}$ ), and near infrared (0.7-0.8  $\mu\text{m}$ ) bands which had been used for over 20 years with color infrared photography. The latter had been used extensively for camouflage detection as early as World War II. It later was used in aircraft remote sensing work for spotting diseased trees or crops, since such changes in vegetation vigor were discovered to appear first in the near infrared region. The fourth ERTS-1 band (0.8-1  $\mu\text{m}$ ) went well beyond the long wavelength limit of color infrared film. No attempt was made to shape any of the ERTS-1 bands, especially the fourth one, with respect to avoiding or at least minimizing absorption band effects. In addition, no special consideration was given in the band selection to the spectral reflectance characteristics which were most important to the primary objective, i.e., crop classification. This was probably due both to a lack of a consensus as to which bands, if any, were superior or optimum, and to a lack of sufficient time to implement any changes in the ERTS-1 design.

The ERTS-1 MSS was an objective plane scanner, just as were the previously discussed aircraft MSS's. The main differences are that an oscillating mirror is used instead of a rotating one and six detectors are used for each band such that six scan lines are generated with each mirror scan cycle. Both of these features helped to give the ERTS-1 MSS a scan efficiency of 44 percent, a challenging design task for the 907 km altitude

and relatively small  $11.5^\circ$  scan angle. See table 3.2-1 for a comparison of various sensor system parameters for the MSS's covered in this and the following subsection.

The ERTS-2 or Landsat-2 was originally planned to have five bands; the same ERTS-1 bands plus a thermal infrared band (10.4-12.6  $\mu\text{m}$ ) to obtain relative temperature data. However, the Landsat-2, put into orbit on Jan. 22, 1975, was in effect a copy of ERTS-1 and the fifth or thermal IR band was left off, to be added to the MSS system on Landsat-C, the next satellite in the series. In addition to replacing the 'aging' ERTS-1, the Landsat-2 system also gave investigators increased temporal coverage in combination with the still functioning ERTS-1, i.e., twice as many passes and data for a given time frame. Further details on the Landsat-1 and Landsat-2 scanners are in reference 3.2-4.

#### 3.2.1.4 Skylab S-192

The 13 bands of the Skylab S-192 MSS were chosen in much the same manner that the Bendix aircraft MSS bands were chosen, i.e., they covered the visible, near infrared, and thermal infrared atmospheric windows (see figure 3.2-2) with the exception of the 3-5  $\mu\text{m}$  window. The latter window would have required another type of detector. The number of bands and their spectral coverage were limited by data rates, sensor size and complexity, and detector spectral responsivities. The S-192 pixel size was almost exactly the same as Landsat-1 and -2. The S-192 was, in effect, designed to take orbital multispectral data which could be used to select optimum bands from a wider spectral range and with better spectral resolution and also to allow comparison with the data and performance results from Landsat-1 and -2. However, there was one major difference; the S-192 was a conical or circular scanner. A circular scanner was chosen since the fixed look angle (from nadir) gave it an essentially constant

TABLE 3.2-1. -- AIRCRAFT AND SPACEBORNE MSS DATA COMPARISON

Parameter	Aircraft		Spaceborne			
	Michigan 12-band	Bendix 24-band	Landsat-1,2 (ERTS) 4-band	Skylab 13-band S-192	Landsat-C 5-band	Landsat-D** 7-band
Scanner type	Objective plane, rotating mirror	Objective plane, rotating mirror	Objective plane	Image plane, circular scan	Objective plane	Not yet decided
Altitude	—	(v/h = .02-.18)	~907 km	435 km	~907 km	702.4 km
Coverage cycle	—	—	every 18 days	—	every 18 days	every 9 days
Swath Width (Scan Angle)	1.41 h (90°)	1.29 h (80°)	185 km (11.5°)	68.5 km	185 km	185 km
IFOV	2-3.3 μrad	2 μrad	86 μrad	182 μrad	86 μrad (Th.IR-260 μrad)	33-44 μrad (Th.IR-X3)
Pixel Size	.002-.0033 h	.002 h	79 m	~79 m	79 m (Th.IR-240 m)	30-40 m (Th.IR-X3)
Scan Efficiency	25%	22%	44%	~30%	45%	80%
Dynamic Range/Sensitivity	9 bits	NEΔρ = .001-.0022 NEΔT = .25-2.0°k		NEΔρ = .001-.002		NEΔρ = .005
Calibration			each mirror scan (6 scan lines)	Each scan line	Th.IR views mirror for cold reference	
No. bands/ Detector Type:						
UV	(1)*	1 (PMT)	0	0	0	0
Visible	10 (Si)	5 (Si)	2 (PMT)	5 (HgCdTe)	2 (PMT)	3 (PMT)
Near IR	2 (SI InAs)	11 (SI Ge/InSb)	2 (PMT Si)	7 ( " )	2 (PMT Si)	3 (PMT)
Thermal IR	0 (Ge:Hg)	7 (InSb HgGe)	0	1 ( " )	1 (HgCdTe)	1 (HgCdTe)

\*0.32 - 0.38 μm band was used on early version.

\*\*June, 1975, Final Report, Landsat-D TMTWG.

†Using two satellites.

††Honeywell conical design.

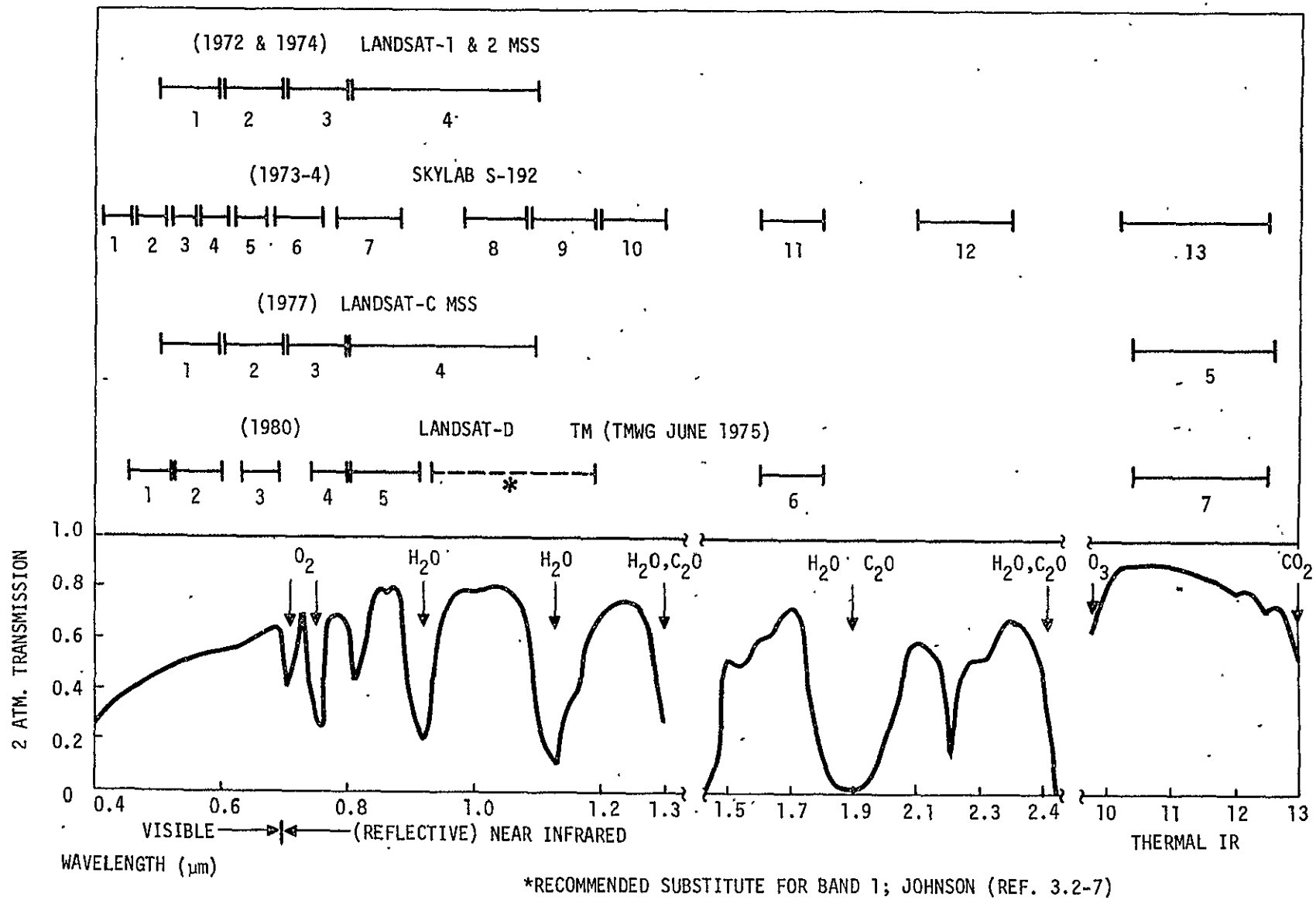


Figure 3.2-2. - Spaceborne MSS spectral bands and atmospheric transmission.

atmospheric path length throughout each scan, unlike the rectilinear object plane scanners of Landsat-1 and -2 and the aircraft MSS's (see section 3.2.5). This constant path length was sought in order to eliminate atmospheric differences due to scanner geometry, and therefore, simplify any atmospheric corrections that might still need to be made. This was an efficient scanning design; however, the circular scan has two major drawbacks:

1. The data displays and computer classification routines were all designed for rectilinear data; therefore, the digital data had to be converted to rectilinear format using very complex geometrical correction routines. (See section 3.2.5 for discussion of other scan geometry effects.)
2. The  $110^\circ$  active portion of the S-192 circular scan created a large variation in look versus sun angle relations, much greater than that experienced with an orbital scanner with a nadir centered scan of  $\pm 5.75^\circ$  such as the Landsat-1 and -2.

It is felt that these two major drawbacks with conical scanners are sufficient to preclude their further use unless continued studies should warrant it.

The S-192 thermal IR band data, though somewhat limited by poor sensitivity ( $NE\Delta T \approx 1^\circ$ ), were nonetheless useful in evaluating the potential for the thermal infrared band to be included on the Landsat-C, to be orbited in 1977. Also, as indicated in figure 3.2-1, the results obtained by S-192 Principal Investigators (PI's) will be very instrumental in determining the optimum spectral bands for the second generation (Landsat-D) in 1980. This could be considered the real payoff from the S-192, i.e., the choice of optimal bands for earth resources satellites of the 1980's. The choice of seven optimal bands for Landsat-D is discussed in section 3.2.2 and the choice of pixel size is covered in section 3.2.3. More general aspects of the

Landsat-D are given in the following subsection and a new two-satellite, two-spectral band set concept is proposed in subsection 3.2.1.6.

### 3.2.2 FUTURE MULTISPECTRAL SCANNERS

#### 3.2.2.1 Landsat-C

The general objective of Landsat C, which is to be launched September, 1977, will be to extend the period of space-data acquisition for earth resources applications initiated by Landsat-1 and continued by Landsat-2 and to improve the spectral observing capability with the addition of a thermal infrared channel providing intercomparisons of thermal data with simultaneous measurements at visible and near infrared wavelengths. In addition to the spectral imagery, an improved Return Beam Vidicon (RBV) system (see section 3.6.1) will provide high-resolution (40 meter) panchromatic imagery. The RBV data may be used independently or in conjunction with the lower resolution spectral data from the MSS to provide increased information content. The capability to relay data from remote land-based sensors will be continued by the Data Collection System (DCS) on Landsat-C.

One of the primary objectives of the Landsat-C mission is the continued acquisition and complete coverage of the United States with (1) multispectral 80-meter resolution images in reflected solar radiation; (2) 240-meter resolution images in emitted terrestrial infrared radiation; and (3) 40-meter resolution panchromatic images.

The sensors selected for this mission are the five-band MSS, the two-camera RBV, and the DCS receiver and transmitter. The MSS images the surface of the earth in several spectral bands simultaneously through the same optical system. The MSS for

Landsat-C has four bands operating in the reflected solar spectral region from 0.5  $\mu\text{m}$  to 1.1  $\mu\text{m}$  wavelength, and a fifth band from 10.4  $\mu\text{m}$  to 12.6  $\mu\text{m}$  in the emitted infrared range. It scans cross-track swaths of 185 kilometers (100 n. mi.) width simultaneously imaging six scan lines across in each of the first four spectral bands and two lines in the fifth band.

The MSS is used on all three missions; for the first two (Landsat-1 and 2), the four spectral bands have been designated bands 4, 5, 6 and 7 (the multispectral RBV bands were designated bands 1, 2 and 3). For the Landsat-C mission, a fifth band (band 8) 10.4  $\mu\text{m}$  to 12.6  $\mu\text{m}$ , is added in the thermal (emissive) spectral region. This band uses mercury-cadmium-telluride, long-wave infrared detectors that are cooled to approximately 100° Kelvin by a passive radiation cooler. The dimensions that can be resolved in this band are about three times larger (240 m) than for bands 4 through 7. Energy is accepted through a slit near the fiber optics matrix and conducted by relay optics onto the detectors which form the field stops. The 5-band MSS has 26 video channels. Table 3.2-2 lists the performance characteristics for the Landsat-C MSS.

#### 3.2.2.2 Landsat-D

Landsat-D, which is planned to be orbited in 1980, represents the first significant "evolutionary" step in the Landsat satellite series. The specifications for its multispectral scanner, referred to as the Thematic Mapper (TM), have not yet been finalized. However, the Thematic Mapper Technical Working Group (TMTWG), composed of a cross section of scientists and engineers from the government, industry and universities, has made the following recommendations for the Landsat-D 7-band TM in its Final Report (June 1975) (ref. 3.2-5).

TABLE 3.2-2. - LANDSAT-C MSS PERFORMANCE CHARACTERISTICS

## BANDS 4, 5, 6, and 7

Spectral Band 4	.5 $\mu\text{m}$ - 6 $\mu\text{m}$
Spectral Band 5	.6 $\mu\text{m}$ - .7 $\mu\text{m}$
Spectral Band 6	.7 $\mu\text{m}$ - .8 $\mu\text{m}$
Spectral Band 7	.8 $\mu\text{m}$ - 1.1 $\mu\text{m}$
Instantaneous Field-of-View	86 x 86 $\mu$ radians
Number and type of detectors	
Band 4, 5, and 6	6 photomultiplier tubes
Band 7	6 silicon photodiodes
Information Bandwidth	42.3 kHz per detector
Sampling Rate (each detector)	100,418 samples per second
Quantization	6 bits
Samples Per Line	3317
Nominal Aperture Diameter	22.8 cm (9 inches)
f/no	3.6
Ground Resolution Element	78 meters (260 feet)
Swath Width	185 km (100 n. mi)
Modulation Transfer Function (MTF), minimum	0.29 for 0.075 mrad sinusoidal bars
Inflight Calibration	(a) internal lamp sources (b) Sun
Gain Steps	(a) commanded to step between x1 and x3 (in bands 4 and 5 only) (b) linear mode or compressed mode (bands 4, 5, and 6 only)

TABLE 3.2-2. — LANDSAT-C MSS PERFORMANCE CHARACTERISTICS (concluded)

(Band 8)

Spectral Band	10.4 $\mu\text{m}$ to 12.6 $\mu\text{m}$
Dynamic Range (Scene Apparent Temperature)	260°K to 340°K
Instantaneous Field-of-View	0.26 x 0.26 $\mu$ radians
Number of Detectors	2
Information Bandwidth	14.1 kHz
Effective Aperture	308 $\text{cm}^2$
f/no	1.9
Ground Resolution Element	238 meters (780 feet)
Lines/Scan	2
Swath Width	185 km (100 n. mi.)
Detector Material	Mercury Cadmium Telluride (Hg Cd Te)
Noise Equivalent Power (NEP)	$2.5 \times 10^{-10}$ watts
Responsivity	3100 Volt/Watt (nom)
Cooler Field-of-View	72° x 100°
Cooler	Passive Radiator
Detector Operation Tem.	100 $\pm$ 10°K
NEAT (Noise Equivalent Temperature Difference)	1.52°K for 300°K scene
Modulation Transfer Function (MTF), minimum	0.29 for 238 meter sinusoidal bars
In-flight Calibration	(a) Ambient blackbody (b) Reflected detector
Gain Steps	Commandable in eight (8) gain levels in increments of 1.22 (i.e., 1.0, 1.22, 1.22 <sup>2</sup> ... 1.22 <sup>7</sup> )

Spectral Bands (see section 3.2.2 for more details):

7 bands - 3 in the visible (see fig. 3.2-2)

3 in the near infrared

1 in the thermal infrared.

2. Sensitivity:

Noise Equivalent Reflectance,  $NE\Delta\rho = 0.005$  at 13 percent reflectance for all visible and near-IR bands.

Noise Equivalent Temperature,  $NE\Delta T = 0.5^\circ K$  at  $300^\circ K$ .

3. Spatial Resolution (see section 3.2.3):

Visible and near infrared 30-40 meters (compared to 78 m for Landsat-1, 2 and C)

Thermal IR = 3 times above resolution, i.e., ~90-120 meters

4. Dynamic Range:

Practically unchanged from Landsat-1 and -2. However, the sensitivity recommendation will require an equivalent 10-bit range overall (8 bits per scene) and two possible ways for achieving this were given:

- Use 10 bits
- Use 8 bits with different gain levels at the high and low ends of the radiance level.

5. Geometric Accuracy:

Registration of pixels from two separate passes to within 0.5 pixel (rms).

6. Temporal Resolution:

A nine-day repeat cycle obtained with two identical satellites having 18-day repeat coverages.

7. Scanning Method:

Rectilinear scanning was chosen over circular scanning because of the reasons discussed in subsection 3.2.1.4,

complexity in data format and scan-look angles, and larger geometric error resulting from greater relief displacement effects (see section 3.2.5).

The TMTWG relied heavily upon their own knowledge and experience and the findings in the NASA funded Multispectral Scanner Data Applications Evaluation study. This report, released in December 1974, was in two volumes. The first volume (ref. 3.2-6), "User Applications Study," was generated by the Environmental Research Institute of Michigan (ERIM). It covered most of the sensor characteristics listed above. The second volume (ref. 3.2-3), "Sensor Systems Study," was generated by Honeywell Radiation Center (HRC) and was primarily concerned with engineering aspects, such as data transmission rate limitations, various systems tradeoffs, and the prospects for system improvements due to advances in electronics and sensor technology. While the bulk of these studies and the conclusions drawn from them remain quite valid, it is felt that the spectral band selection should be reconsidered. This is because the S-192 principal investigator (PI) final reports were not available until very late 1975 and early 1976; over a half a year after the TMTWG met in May 1975 and a full year after the ERIM study. Section 3.2.2 presents the results and adds support to a recent study (ref. 3.2-7) of S-192 PI results which recommends replacing at least one visible band with an additional near-infrared band.

#### 3.2.2.2.1 A Two-Satellite, Two-Band Set Landsat-D

In concluding this section, a "two-band set" concept (ref. 3.2-12) is proposed for Landsat-D. Agricultural classification performance has been found to show little, if any, gain when more than four or five bands are used (ref. 3.2-6). Agricultural classification is not only the primary objective for Landsat-D, it also has the clearest need for closer temporal coverage (i.e., nine days between passes with Landsat-D as opposed to 18 days with

Landsat-1 and -2). Other application areas such as geology, land-use mapping, and forestry do not in general need the same close temporal coverage. However, as it is shown in section 3.2.2, the major application areas could be better served with additional spectral bands in the near-infrared and ultraviolet ends of the optical region. Therefore, it is interesting to consider two Landsat-D satellites giving nine-day temporal resolutions as recommended, but having only four or five bands in common that are optimal for agriculture or any combination of primary applications (ref. 3.2-6). The remaining two or three bands (still seven bands on each TM) would be different, chosen to optimize results in the secondary applications areas. The two-satellite Landsat-D system would thus have an overall nine or ten spectral bands. The only difference would be in the temporal coverage among the bands. Of course, some of the "18-day bands" could be chosen to be less "temporally sensitive" bands which would also be useful for crop classification.

The data presented in section 3.2.2 have been used to generate the following example illustrating the two-band set approach:

Band No.	Landsat-D(1)	Landsat-D(2)	
1	.52 $\mu\text{m}$ -.60 $\mu\text{m}$	.52 $\mu\text{m}$ -.60 $\mu\text{m}$	} Agriculture Bands
2	.63 $\mu\text{m}$ -.69 $\mu\text{m}$	.63 $\mu\text{m}$ -.69 $\mu\text{m}$	
3	.98 $\mu\text{m}$ -1.03 $\mu\text{m}$	.98 $\mu\text{m}$ -1.03 $\mu\text{m}$	
4	1.55 $\mu\text{m}$ -1.75 $\mu\text{m}$	1.55 $\mu\text{m}$ -1.75 $\mu\text{m}$	
5	.46 $\mu\text{m}$ -.51 $\mu\text{m}$	1.2 $\mu\text{m}$ -1.3 $\mu\text{m}$	} Geology Bands
6	.68 $\mu\text{m}$ -.76 $\mu\text{m}$	2.1 $\mu\text{m}$ -.2.35 $\mu\text{m}$	
7	.78 $\mu\text{m}$ -.88 $\mu\text{m}$	10.4 $\mu\text{m}$ -12.6 $\mu\text{m}$	

### 3.2.2.3 Synchronous Earth Observatory Satellite (SEOS)

The SEOS (refs. 3.2-8, 3.2-9) due to be launched in 1981 will be the first earth resources satellite to be placed into a geosynchronous orbit. It will serve applications in the areas of earth resources, weather phenomena and warnings. Its sensors will be pointable, allowing it an unprecedented ability to gather earth resources related data of transient events, primarily within the continental U.S. and its coastal regions, on a target of opportunity basis. These events include disasters, such as floods, earthquakes, forest fires, hurricanes, etc., for which a means of monitoring their development (where possible) issuing warnings, and assessing the extent of damage are needed. In addition, SEOS will also provide valuable agricultural data of relatively transient growth phenomena. These data can be obtained from agricultural areas under intensive study and can also be used to supplement studies using Landsat data where greater temporal coverage is required or cloud cover has coincided with a Landsat pass, preventing a data take.

The prime sensor on the SEOS will be the Large Earth Survey Telescope (LEST), a multispectral sensor with a 1.5 meter diameter aperture. It will have 18 or more bands in the visible, near infrared, and thermal infrared regions of the spectrum. Some of these bands will be non-imaging and used primarily for atmospheric sounding data. The imaging bands of the LEST will utilize a pushbroom scanner design whereby large linear detector arrays are used to "sweep out" continuous scan lines across an entire swath width. This not only simplifies the scan geometry, but also enables a much slower scan rate. The latter is desirable in maximizing the signal-to-noise ratio and resolution so critical at geosynchronous altitude. The visible and near infrared imaging bands will have a resolution of 100 meters, while the thermal infrared imaging bands will have a resolution of 800 meters. This compares with the corresponding Landsat-C

bands which will have resolutions of 80 meters and 240 meters, respectively. The LEST will have a ground swath width of about 200 km which is very close to the Landsat swath width of 185 km.

Other sensors under consideration for the SEOS are: (1) the Advanced Atmospheric Sounder and Imaging Radiometer (AASIR), (2) the Microwave Sounder and (3) the Framing Camera. More data on the LEST and other potential SEOS sensors are given in the SEOS table in appendix A at the end of this report. The AASIR will have two imaging bands, one covering the visible-near infrared (0.55  $\mu\text{m}$ -1.1  $\mu\text{m}$ ) and the other in the thermal infrared (11.11  $\mu\text{m}$ ). The other non-imaging atmospheric sounding bands (about 15) will be in the mid-thermal infrared spectral region. The Microwave Sounder under consideration will cover the 50 GHz to 220 GHz region in five bands with the ground resolution ranging from 200 km to 50 km, respectively. The Framing Camera presently under study would be a television-type sensor providing a color imaging capability over the visible and near infrared regions of the spectrum.

In 1973-74 ERIM conducted two detailed studies (refs. 3.2-10, 3.2-11) for Goddard Space Flight Center of the applications and sensor requirements for a geosynchronous earth resources satellite such as the SEOS. The first of these studies (ref. 3.2-10) defined earth resources applications that require the unique temporal coverage provided by a geosynchronous sensor. This study ranked 31 such applications according to their importance, uniqueness, and the corresponding utility of the SEOS sensors.

The second study used the top twenty of these applications (see table 3.2-3) for examining in more detail the sensor and data requirements, e.g., spectral bands, resolution, etc., for such a system. As indicated in the table, these applications can

TABLE 3.2-3. - TOP 20 SEOS APPLICATIONS (from ref. 3.2.2-4)

Rank	Application	General Group
1	Water Pollution Detection and Monitoring	W
2	Estuarine Dynamics	W
3	Snow Cover Monitoring	M
4	Volcanic Region Monitoring	G
5	Plankton Monitoring	W
6	Fish Location and Movement	W
7	Ocean Dynamics	W
8	Forest Disease and Insect Damage	V
9	Forest Inventory and Management	V
10	Rangeland Evaluation	V
11	Irrigation Management	V
12	Oil Pollution Detection and Monitoring	W
13	Lithologic Survey	G
14	Lake Dynamics	W
15	Wildfire Monitoring	M
16	Flood Survey and Damage Assessment	V
17	Water Erosion	V
18	Thematic Mapping	G,V
19	Aeolian Soil Erosion	V
20	Agricultural Disease and Insect Damage Monitoring	V

Legend:

- W = Water-oriented
- V = Vegetation-oriented
- G = Geology-oriented
- M = Miscellaneous

be divided into four general categories: water, vegetation, geology, and miscellaneous. The optimum spectral bands were then determined for each of these categories using prior investigation results, spectral reflectance data, atmospheric transmission data, etc. The total number of such optimal bands would be prohibitive if those for each category were simply added together. Therefore, through various compromises, the number of bands was reduced while maintaining good overall performance in each applications category. A total of 18 bands were chosen in the .4  $\mu\text{m}$  to 13  $\mu\text{m}$  region and 3 microwave bands in the 1 cm to 30 cm region. These are listed in table 3.2-4 along with the corresponding applications categories best served by each. Note from this table that there are seven visible, five near infrared, two mid-infrared and four thermal infrared bands. Those bands which correspond closely to the Skylab S-192 bands (see sec. 3.2.1.4) are designated with an (S). The thermal infrared region from 10  $\mu\text{m}$ -13  $\mu\text{m}$  is divided into three bands where there had been only one on the S-192. This was necessary in order to enable corrections for atmospheric effects; allowing greater accuracy in temperature measurements. Figure 3.2-3 shows in bar chart form the applications for which each band was given the top priority by earth resources investigators. The numbers within each bar refer to the specific application areas listed in table 3.2-3. For example, this figure indicates that there are seven water-oriented, six vegetation-oriented and two geology-oriented applications for which the 0.65  $\mu\text{m}$  to 0.69  $\mu\text{m}$  band is considered absolutely necessary. Note that the ERIM study (ref. 3.2.2-11) from which these data were taken also listed application-band combinations having second "very necessary", third "helpful" and fourth "backup" priorities. Thus, although the 0.85  $\mu\text{m}$  to 0.89  $\mu\text{m}$  and the 0.95  $\mu\text{m}$  to 1.10  $\mu\text{m}$  bands are not first priority for any applications, there are applications (#13 & 18) which require them on a second priority level. Several other observations can be made from this figure. The

TABLE 3.2-4. — SEOS BANDS AND GENERAL APPLICATIONS AREAS  
(from table 3, ref. 3.2.2-4)

Band ( $\mu\text{m}$ )	Water	Geology	Vegetation	Wildfire
0.42-0.46 (S)	X	X		
0.45-0.50 (S)	X	X		
0.47-0.52	X	X		
0.53-0.57 (S)	X	X	X	
0.56-0.60 (S)	X			
0.60-0.65 (S)	X	X		
0.65-0.69	X	X	X	X
0.70-0.73 (S)	X	X		
0.78-0.82		X	X	
0.85-0.89 (S)		X		
0.89-0.95 (S)		X		
0.95-1.10 (S)		X		
2.05-2.35 (S)		X	X	
3.6-4.1		X	X	X
8.3-9.4		X		
10.3-11.3 (S)	X	X	X	X
11.3-12.0 (S)	X	X	X	X
12.0-12.9 (S)	X	X	X	X
1 cm			X	
30 cm	X			
10 cm (radar)	X		X	

(S) = Indicated bands closely approximated by the Skylab S-192 bands.

WAVE-LENGTH	MISCELLANEOUS							GEOLOGY							VEGETATION							WATER																											
	1	2	3	4	5	6	7	1	2	3	4	5	6	7	1	2	3	4	5	6	7	1	2	3	4	5	6	7	1	2	3	4	5	6	7														
.42 -.46															17														2 6 14																				
.45 -.50															17																																		
.47 -.52															17																					12 14													
.53 -.57															16																					1 2 6 7 12 14													
.56 -.60															18																					1 2 7 12 14													
.60 -.65															13 18																					1 2 5 6 7 12 14													
.65 -.69															13																					1 2 5 6 7 12 14													
.70 -.73																																				1 5 7													
.78 -.82																																																	
.85 -.89																																																	
.89 -.95																																																	
.95 -1.10																																																	
2.05 -2.35																																																	
3.6 -4.1																																																	
8.3 -9.4																																																	
10.3 -11.3																																				2 6 7 14													
11.3 -12.0																																				2 6 7 14													
12.0 -12.9																																				2 6 7 14													
1cm																																																	
30cm																																																	
10cm																																																	
	VISIBLE							NEAR INFRARED							MID INFRARED							THERMAL INFRARED							MICROWAVE																				

Figure 3.2-3.- SEOS first priority applications versus spectral bands (derived from table 4, ref. D).

water-oriented applications appear to rely heavily on the visible and thermal infrared bands. The vegetation-oriented applications have the broadest first priority spectral band requirements, from the visible through the near, mid- and thermal infrared. The geology-oriented applications have spectral band priorities almost as broad, but with a noticeable emphasis on the thermal infrared bands. The latter bands were rated high in each of the general categories.

The data handling and processing for SEOS will present unique problems due to the quantity of the data and the near real-time use which will be required when monitoring disasters and issuing timely warnings. This will require the development of a new and much more efficient approach to the data processing and dissemination processes.

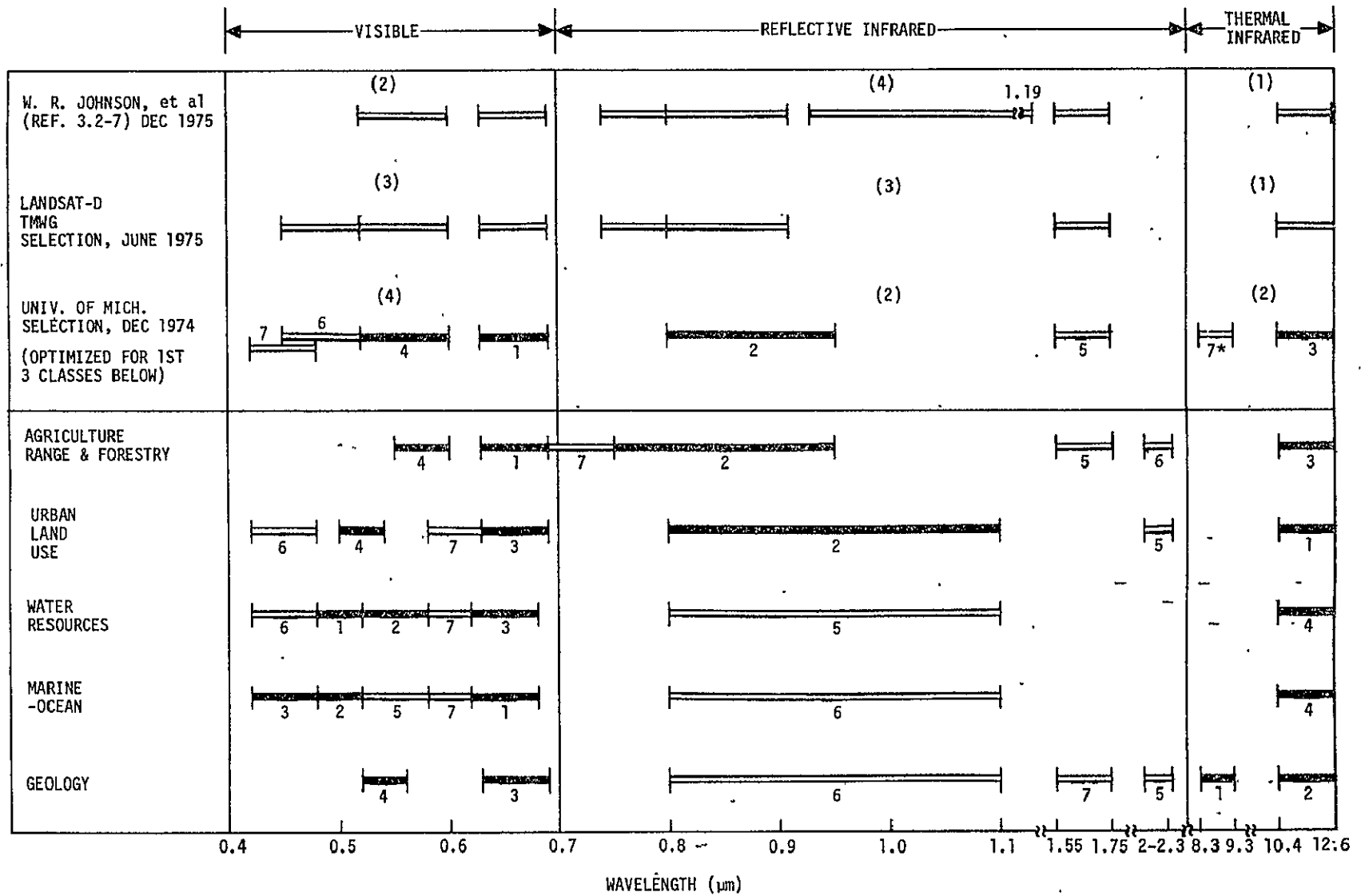
### 3.2.3 MULTISPECTRAL SCANNER DESIGN CHARACTERISTICS

#### 3.2.3.1 Spectral Bands

The choice of the spectral bands to be used on any future earth resources satellite is perhaps the most difficult task of all. First, the primary application areas have to be determined and scoped. Then, for a given application, the number of spectral bands, by necessity, has to be narrowed down to those that are most useful. The findings of a number of separate investigations must be examined in the process. Each investigation varies in scope and objectives, experimental quality, and data preprocessing and classification techniques.

The TMTWG members made their choice of seven spectral bands (see second line, fig. 3.2-4) for the Landsat-D TM using a combination of their direct and indirect experiences. They also relied heavily on the results of the JSC/University of Michigan MSS study (ref. 3.2-6). This study, published in December, 1974,

3.2-24



\*2ND CHOICE FOR 7TH BAND

Figure 3.2-4. — Landsat-D bands and Michigan study results.

half a year before the TMTWG Final Report (ref. 3.2-5), used aircraft and spacecraft MSS data including early S-192 results to determine the required characteristics of future MSS systems. Spectral band rankings were determined in each of the following five applications areas:

- (1) agriculture, range and forestry.
- (2) urban land use
- (3) water resources
- (4) marine - ocean
- (5) geology.

The top seven bands chosen for each of these areas are indicated in the bottom five lines in figure 3.2-4. The top four bands for each area are shown with dark bars to place emphasis on the better bands. The figure also shows the final University of Michigan selection of seven bands for the TM. The choice was a compromise. The "top" four bands (note the numbers indicating the rankings) corresponded to the best bands for the agriculture and urban land use categories, in keeping with the primary goal of scene classification or thematic mapping. The remaining three bands were chosen such that the seven bands satisfied the widest range of applications.

The TMTWG band selection differed from the Michigan selection by one band as can be seen in figure 3.2-4. The 0.42  $\mu\text{m}$  to 0.48  $\mu\text{m}$  visible band was dropped in favor of a 0.74  $\mu\text{m}$  to 0.80  $\mu\text{m}$  near infrared band. Also, the 0.80  $\mu\text{m}$  to 0.95  $\mu\text{m}$  Michigan band was shortened to 0.80  $\mu\text{m}$  to 0.91  $\mu\text{m}$  to avoid the water absorption band near 0.92  $\mu\text{m}$ .

The TMTWG spectral band selections were made before final S-192 PI results were available. In December, 1975, a study (ref. 3.2-7) was conducted at JSC of just received S-192 PI final reports in

a wide range of applications areas. The PI spectral band preferences or rankings within each area were combined using a weighted ranking system. An overall spectral band ranking was then determined and the TMTWG band selection was assessed. The TMTWG 0.45  $\mu\text{m}$  to 0.52  $\mu\text{m}$  band was rejected and a 0.93  $\mu\text{m}$  to 1.19  $\mu\text{m}$  near infrared band was recommended to replace it (see top line of figure 3.2-4. Note in this figure that the original University of Michigan recommendation was for four visible, two near infrared, and one thermal infrared band. The TMTWG Final Report later modified this to three visible, three near infrared, and one thermal infrared band, and most recently, in the light of final S-192 PI reports, even further emphasis is placed on the near infrared bands with a choice (ref. 3.2-7) of two visible, four near infrared, and one thermal infrared band.

Yet another spectral band selection was made for this report, primarily using the S-192 PI spectral band rankings and preferences given in the JSC study (ref. 3.2-7). Two additional studies were used in ranking the bands for agriculture and an additional study was used for geology. The spectral band preferences expressed in the applications writeups in section 2 of this report were not included here simply because they were not available. The S-192 spectral rankings within each application area were obtained using an objective, but nonquantative evaluation whereby only the top seven bands were noted in any one study.

The band rankings by application area and study are given in table 3.2-5 and summarized in table 3.2-6. The top four bands within each area are indicated with a P for "primary", the remaining by an S for "secondary" and ties are indicated with parentheses. The Landsat-1, and -2 bands, the TMTWG Landsat-D band selection, and the latest JSC band selection (ref. 3.2-7) are indicated at the bottom of the table. Note that the S-192

TABLE 3.2-5. -- APPLICATIONS PERFORMANCE RANKINGS OF S-192 BANDS

AGRICULTURE (NOTE: Only top 7 ranked bands shown)

PI	Spectral Bands												
	1	2	3	4	5	6	7	8	9	10	11	12	13
Nalepka*			3			6	4	2	7	5	1		
Chang (Ref. 3.2-9)		4					7		3	6	1	2	5
Morgenstern (Ref. 3.2-10)			3			4	5	1	7	6	2		
Lee* (veg. cover)						X		X	X		X	X	
Thompson* (veg. mapping)									X		X		
OVERALL			3			6	5	2	4	(7)	1	(7)	

WETLANDS\*

PI	Spectral Bands												
	1	2	3	4	5	6	7	8	9	10	11	12	13
Thompson			6	4		3	1	5					2
Higer			7	6			3	2	5		1	4	
OVERALL			9	7		4	1	6	8		2	5	3

LAND USE\*

PI	Spectral Bands												
	1	2	3	4	5	6	7	8	9	10	11	12	13
Silva						6	5	3	4	2	1	7	
		X	X	X			X	X	X		X		
Simonett	X		X		X	X	X	X			X		
Sattinger			5		7	4	1	3			2	6	
OVERALL			7		9	6	2	4	5	3	1	8	

\*From W. R. Johnson (Ref. 3.2-7)  
 NOTE: X designates optimum but unranked bands.

TABLE 3.2-5. - APPLICATIONS PERFORMANCE RANKINGS OF  
S-192 BANDS (Continued)

FORESTRY

PI	Spectral Bands												
	1	2	3	4	5	6	7	8	9	10	11	12	13
Hoffer*		X					X		1				
Higer* (pines)								1					
Simonett* (conifer/deciduous)									1				
OVERALL								2	1				

GEOLOGY

PI	Spectral Bands												
	1	2	3	4	5	6	7	8	9	10	11	12	13
G. Petzel* (geol. map./petroleum)									2		1		
F. Thompson* (geol. mapping)				X	X	X			X		X	X	
K. Lee* (lithology)									X	X	X		
R. Morrison* (geomor. map.)							1	2	(3)	(3)			
R. Houston* (geol. map.)							X	X	X		X	X	
R. Vincent (Ref. 3.2-11) (geol. map.)								2				1	
OVERALL							3	4	2	5	(1)	(1)	

\*From W. R. Johnson (Ref. 3.2-7)

NOTE: X designates optimum but unranked bands.

TABLE 3.2-5. - APPLICATIONS PERFORMANCE RANKINGS OF  
S-192 BANDS (Concluded)

OCEANOGRAPHY & HYDROLOGY\*

PI	Spectral Bands													Landsat-1, 2				
	1	2	3	4	5	6	7	8	9	10	11	12	13	1	2	3	4	
Polcyn (water quality)		1																
Trumbull (turbidity)			X	X	X													
Trumbull (oil spills)			1	X	2	X	3											1
Watarabe (Chlor., Phytopl.)														X		X		
OVERALL		2	1	5	3	6	4											

\*From W. R. Johnson (Ref. 3.2-7)

NOTE: X designates optimum but unranked bands.

TABLE 3.2-6. -- EARTH RESOURCES APPLICATIONS AND VISIBLE -- IR MSS REQUIREMENTS --  
GENERAL SUMMARY

Application	S-192 Bands; No. & Center Wavelength (μm)													LANDSAT-1,2				Pixel Size (meters)
	P-Primary (Strong Preference-Top 4 bands)				s-Secondary (Useful-Rank 5-7)									1	2	3	4	
	1	2	3	4	5	6	7	8	9	10	11	12	13	55	.65	.75	.95	
AGRICULTURE			P			s	s	P	P	(s)	P	(s)						30-78 m
FORESTRY								P	P						P	(P)	(P)	-30 m
GEOLOGY							P	P	P	s	P	P						
LAND-USE			s			s	P	P	s	P	P							
WETLANDS				s		P	P	s			P	s	P					
OCEANOGRAPHY		P	P	s	P	s	P							x		x		10-30 m
Center Wavelengths, S-192 Bands (μm)	.44	.48	.54	.59	.64	.72	.83	1.0	1.14	1.25	1.65	2.2	11.4					
Landsat-D Bands (TMWG Selection)		<u>1</u>	<u>2</u>		<u>3</u>	<u>4</u>	<u>5</u>				<u>6</u>	<u>7</u>						30-39 m
Landsat-D Bands (W. R. Johnson, Ref. 3.2-7)			<u>2</u>		<u>3</u>	<u>4</u>	<u>5</u>		<u>1</u>		<u>6</u>	<u>7</u>						
Landsat-1,2 Bands			<u>1</u>		<u>2</u>	<u>3</u>		<u>4</u>										

3.2-30

applications band rankings support the replacement of the 0.45  $\mu\text{m}$  to 0.50  $\mu\text{m}$  band with a 0.93  $\mu\text{m}$  to 1.19  $\mu\text{m}$  band on Landsat-D.

The spectral band rankings and selections presented in this subsection represent fairly recent evaluations. The Landsat-D TMTWG's final report represents an especially thorough study utilizing the talents of several dozen of the top people in the earth resources field. However, the TMTWG report nonetheless represents a joint effort conducted with a very limited amount of time prior to the availability of all S-192 PI final reports. Therefore, a strong need exists for a re-evaluation of the present Landsat-D spectral band selection. Such an effort will also be very useful to other future earth resources satellite systems as well, e.g., SEOS.

#### 3.2.3.2 Pixel Size and Sampling

The determination of pixel size represents a tradeoff or compromise between the data that users need for fine enough spectral resolution and the engineering limitations, i.e., detector sensitivity and size, and the data transmission rates. While data users seemingly always want ever smaller pixels, they also desire to keep the computer processing time within reasonable bounds when working with digital data. For the resolution requirements in the various earth resources applications areas see section 2.

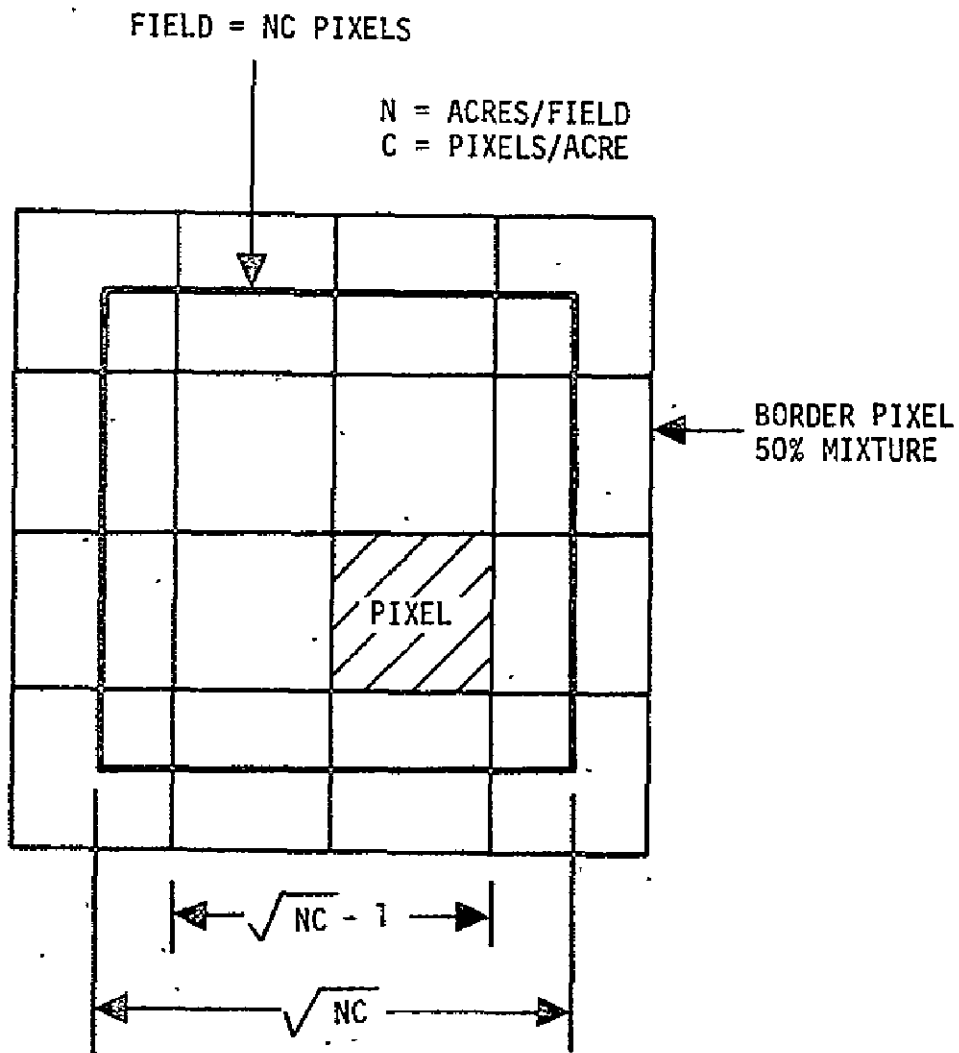
The TMTWG on Landsat-D recommended a pixel size of 30 meters to 40 meters based on the assumption that in the primary application area of agriculture, fields of 20 acres or larger would include most of the crop acreage of interest. For fields as small as 20 acres and assuming that at least 30 non-boundary or "center" pixels are needed for good classification (ref. 3.2-5), it can be shown that a pixel size of around 40 meters or smaller is required. Consider a square field of  $n^2$  pixels where  $n$  is

the number of acres/field and  $c$  is the number of pixels/acre. If the case where all border pixels are 50 percent mixture pixels (see fig. 3.2-5) and is taken as average, then pixel size can be calculated as a function of field size in acres for a required number,  $N$ , of center pixels using the equations given in the figure. Figure 3.2-6 shows such plots for  $N = 10, 20$  and  $30$ . Note the design point for Landsat-D of  $N = 30$  center pixels and  $n = 20$  acres, which indicates a pixel size requirement of  $\leq 44$  meters. The percentages given in parentheses with each curve indicate the fraction of borderless or center pixels in each case, e.g., for  $N = 30$ , approximately 54 percent of a square field's pixels are, on the average, mixture pixels. Obviously, for rectangular fields the situation worsens. However, for aspect ratios of 2:1 or less, there is no significant difference.

The engineering considerations and tradeoffs in determining the pixel size for Landsat-D were reported in reference 3.2-3. This study concluded that the smallest pixel size which could be utilized with the 120 megabit multiplexer planned for the TM would be 30 meters, using 10-bit words.

### 3.2.3.3 Dynamic Range and Sensitivity

The Landsat-D TMTWG recommended a noise equivalent reflectance difference,  $NE\Delta\rho$  of 0.005, for all visible and near infrared bands, in keeping with the University of Michigan study's empirical results (ref. 3.2-6). A noise equivalent temperature difference of  $0.5^\circ\text{K}$  was recommended for the thermal IR band. Classification performance was examined as a function of the number of bits and also for various simulated small percentage changes in gain. Both simulation studies indicated the need for approximately 0.5 percent  $NE\Delta\rho$  to avoid degrading performance by more than 5 percent in agriculture and land use classification



N = NO. OF BORDERLESS OR 'PURE' PIXELS

$$N = (\sqrt{NC} - 1)^2 = NC - 2\sqrt{NC} + 1$$

$$NC - 2\sqrt{NC} + 1 - N = 0$$

Figure 3.2-5. — Pixel size determination.

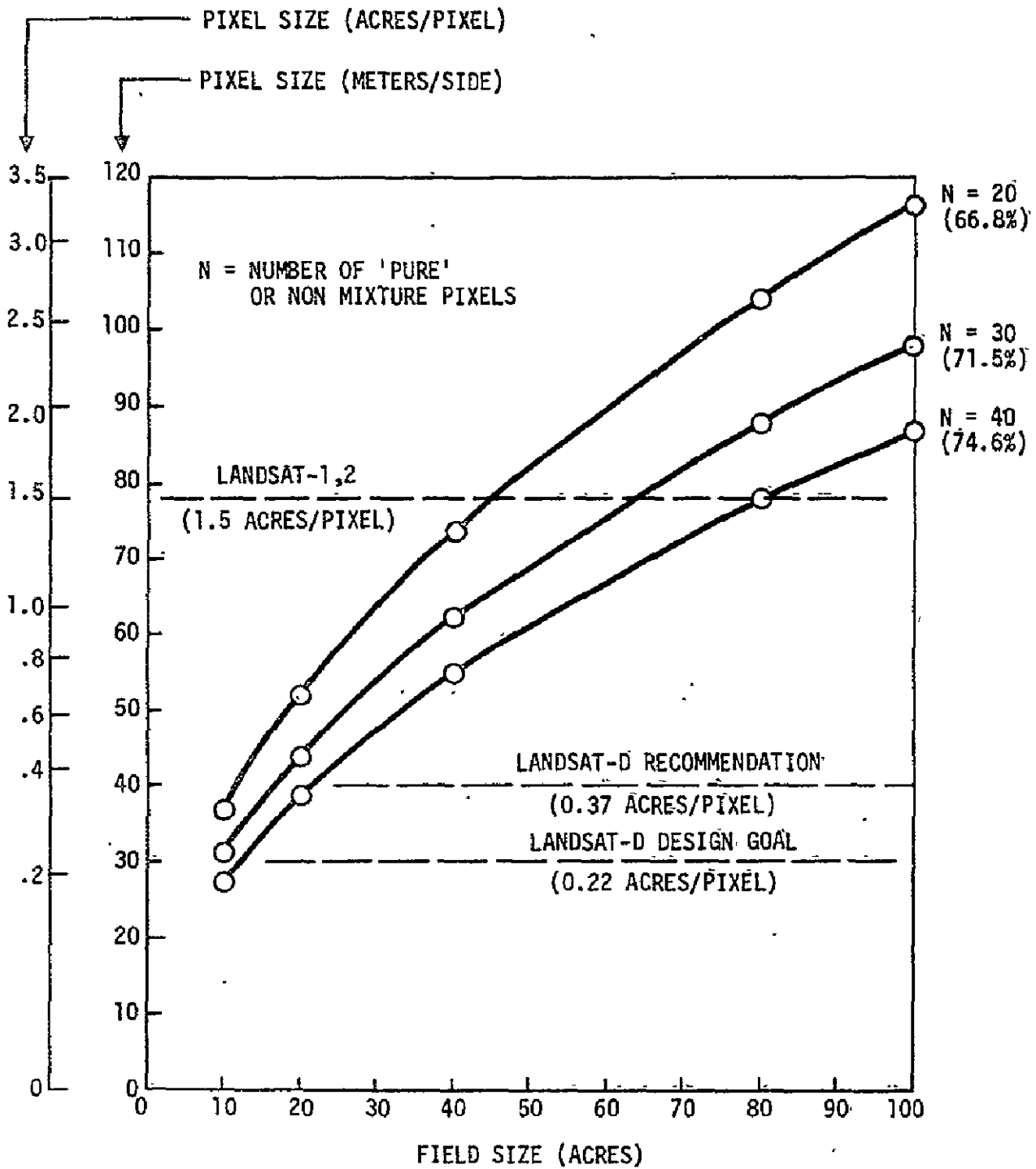


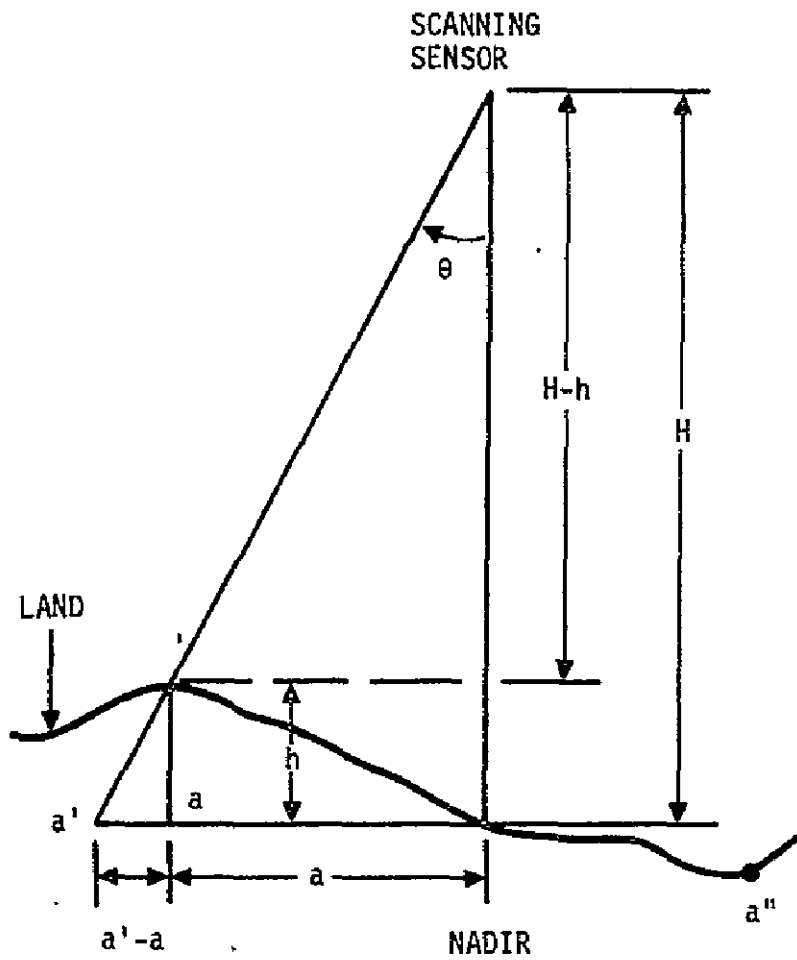
Figure 3.2-6. - Pixel size as a function of field size and number of non-boundary pixels.

The TMTWG suggested that a study be conducted to evaluate the potential feasibility and usefulness of breaking the radiance signal versus reflectance plot into 2 or 3 regions of differing gain to effectively stretch the 8 bits dynamic range.

#### 3.2.3.4 Relief Displacement and Scan Geometry

Relief displacement errors occur when elevation differences exist between the subsatellite or nadir point and other points along a sensor's scan. Figure 3.2-7 shows the geometry involved. At scan angle  $\theta$ , the height  $h$  of point  $a$  makes it appear to be at point  $a'$ . The horizontal distance ( $a' - a$ ) is the error resulting from relief displacement and it is easily calculated to be  $ah/(H - h)$  where  $H$  is the altitude of the sensor. This was incorrectly given as  $ah/H$  in ref. 3.2-5. Note that the relief displacement error can also be negative if  $h$  is negative, e.g., point  $a''$  in figure 3.2-7. Also note that for rectilinear scanners such as Landsat the relief displacement is a function of both elevation difference ( $h$ ) and the distance ( $a$ ) from the nadir point. On the other hand, conical scanners such as the S-192 have a fixed scan angle  $\theta$  and relief displacement is only a function of elevation difference. However, this also means that relief displacement error for conical scanners is always greater than that for rectilinear scanners, especially near the nadir point. Figure 3.2-8 shows plots of relief displacement error in meters versus distance from the nadir point in kilometers for rectilinear and conical scanners with the same altitude and swath width. Note that this can significantly affect the problems of geometric accuracy within a single frame and the spatial registration problem with temporally separated frames.

Another scan geometry problem that occurs with rectilinear scanners is the so called "bow tie" effect. As a fixed IFOV scanner scans outward from the nadir point, the pixel size on the ground increases simply because of the increasing distance



$$a' - a = h \tan \theta$$

$$\theta = \tan^{-1} \frac{a}{H-h}$$

$$\therefore a' - a = \frac{ah}{H-h}$$

Figure 3.2-7. - Relief displacement geometry.

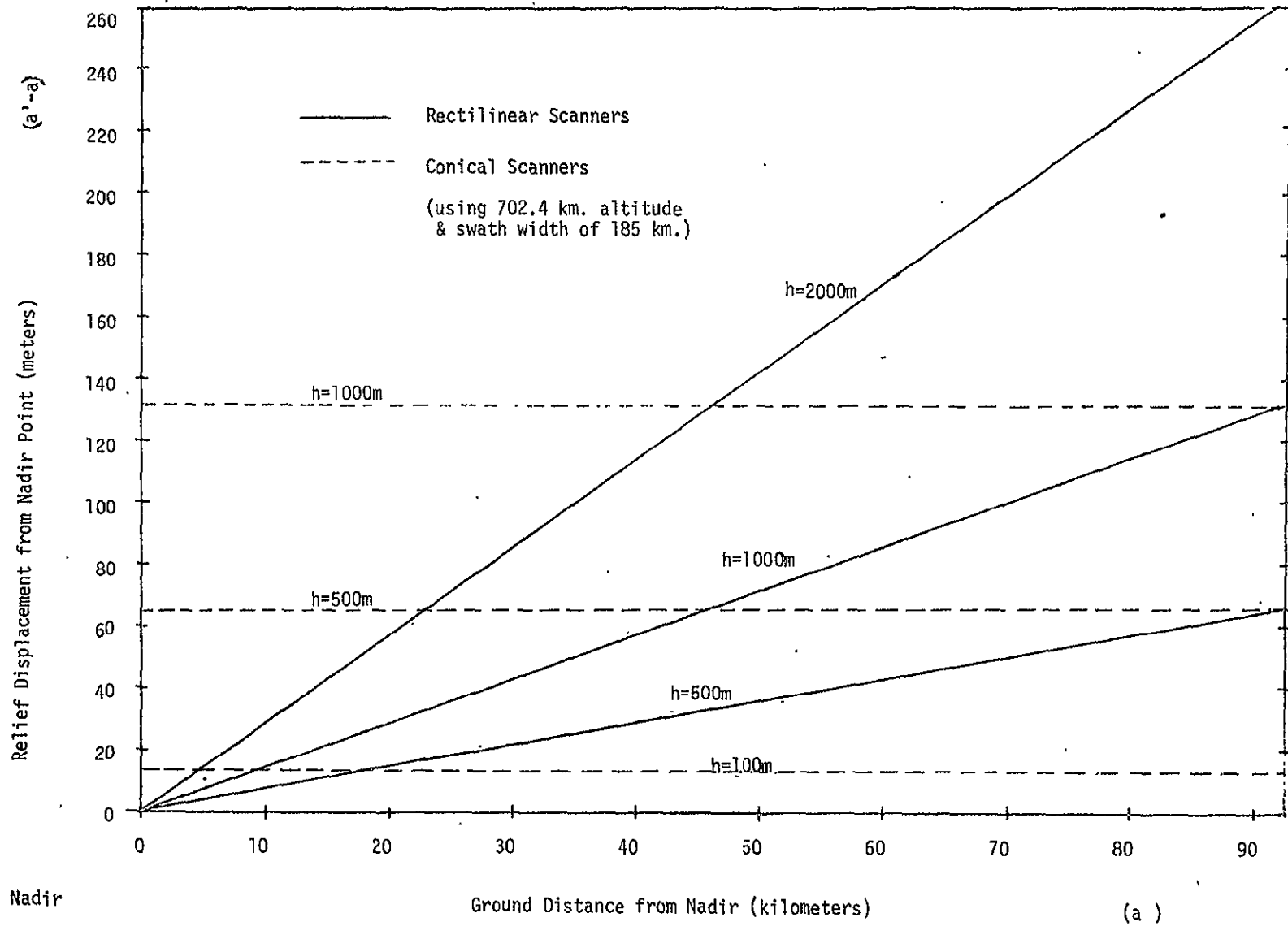
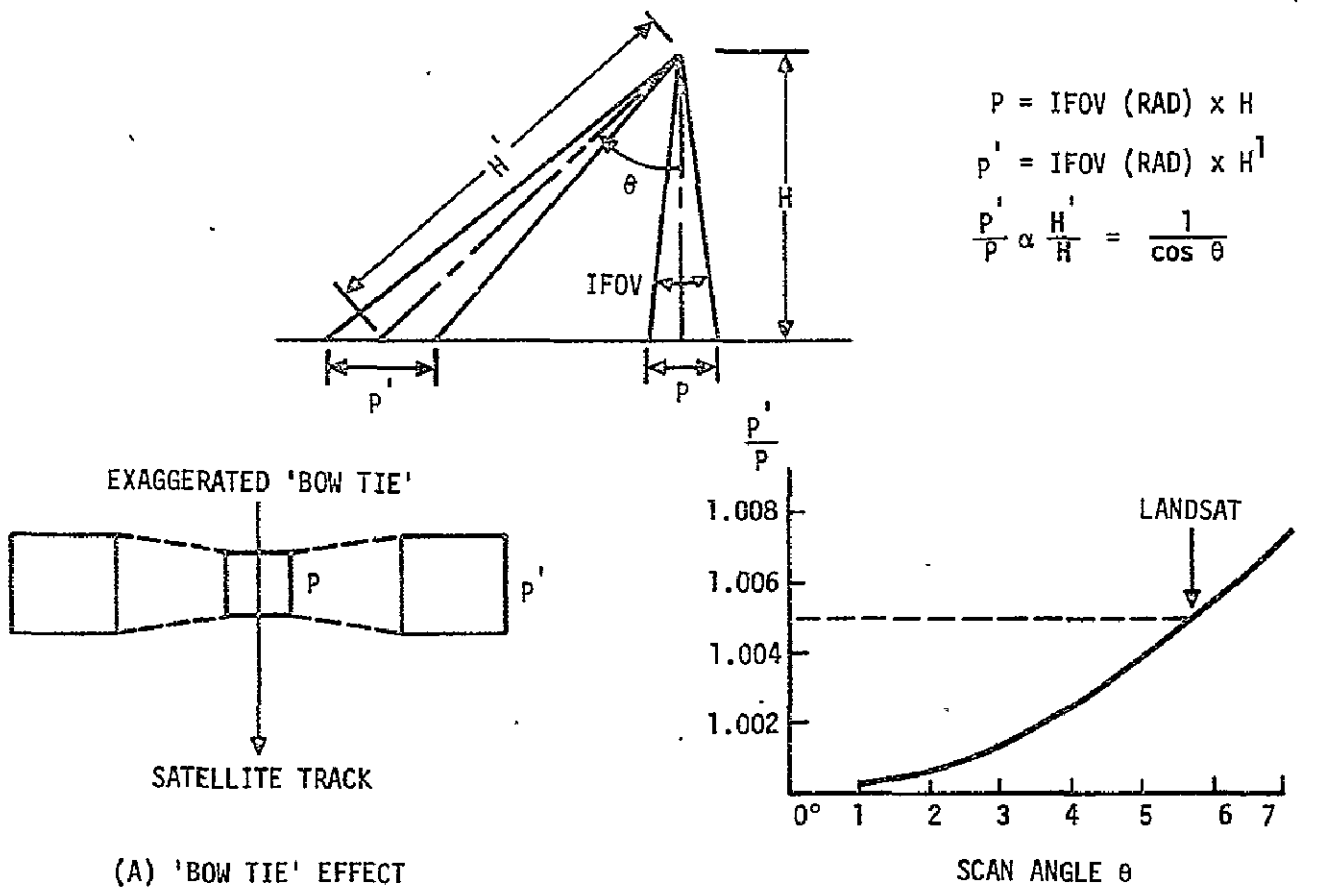


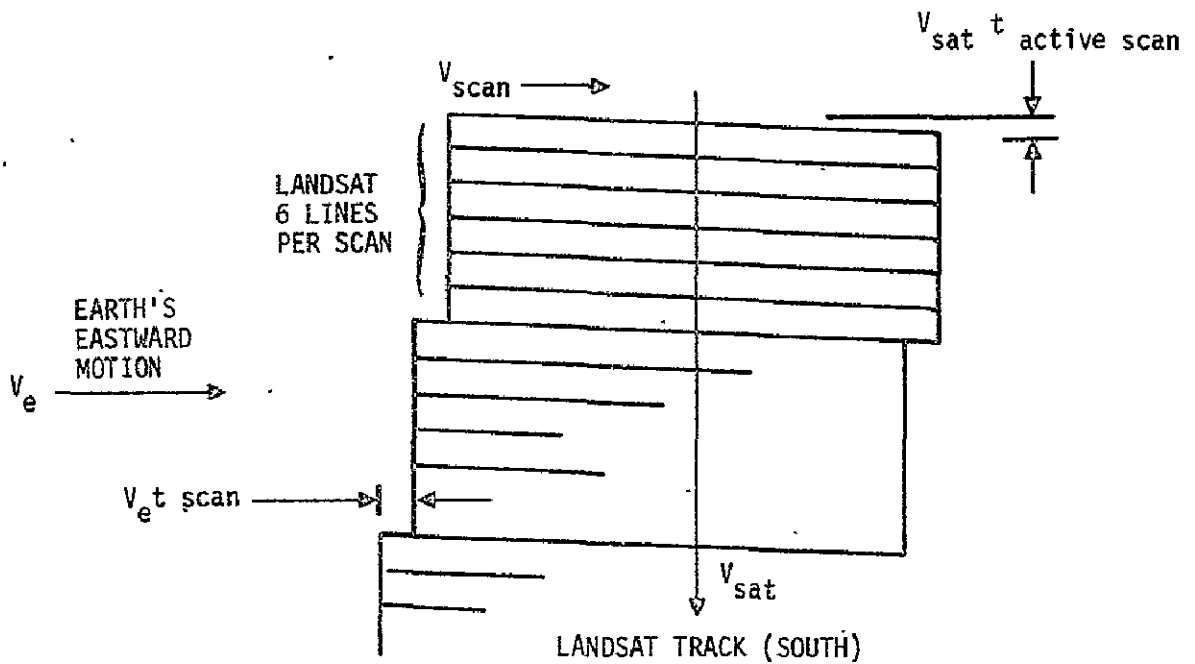
Figure 3.2-8. - Relief displacement plots.

to the ground. This is illustrated in figure 3.2-9(a). The effects of the motion of the earth and the sensor platform are shown in figure 3.2-9(b) for the southward moving Landsat MSS which sweeps out six scan lines with each mirror scan.

The scan geometry problems are much more complex with a conical scanner. There is no "bow tie" effect since the scan angle is fixed. However, the circular scan has many more complex scan geometry problems. The most serious one, as has been discussed, is the very difficult problem of "line-straightening" the data, i.e., reformatting the data to approximate a rectilinear ground sampling geometry. The study reported in reference 3.2-13 concluded that the initial scan line straightened data had much greater band-to-band pixel misregistration (up to 2 pixels!) and accordingly gave much poorer classification results. It was not determined whether this was due to a poor line straightening procedure or a problem inherent in the conical scan data. Besides the obvious geometric difficulty of reformatting sampled data from circular to rectilinear, the more subtle scan geometry effects illustrated in figure 3.2-10 must also be considered. Note that the along-the-track scan line spacing,  $t$  is identical to the radial scan spacing  $r$ , i.e.,  $t = r_c$ . As the scan moves from the center point,  $t$  remains the same but  $r$  decreases to about  $t \cos \theta$  (see point E). The pixel sizes remain the same along the scan. Therefore, there is increasing pixel overlap between adjacent scans toward either scan end. Another effect is caused by the fact that at the beginning of a scan, the scan direction is mostly with the satellite track direction and at the end of a scan it is mostly against the satellite track direction. The general result is roughly as indicated in the lower portion of figure 3.2-10.



(A) 'BOW TIE' EFFECT



(B) EARTH AND SATELLITE MOTION EFFECTS

Figure 3.2-9. - Scan geometry effects for rectilinear scanner.



## REFERENCES

- 3.2-1 Anuta, P. E.; and MacDonald, R. B.: Crop Surveys from Multiband Satellite Photography Using Digital Techniques. Remote Sensing of the Environment, Vol. 2, pp. 53-67, 1971.
- 3.2-2 Hughes, C. L.: Screening and Data Handling Plan for SO-65 Data Used in ERTS Simulation. Lockheed Electronics Technical Report 640-TR-135, NASA/JSC EOD2874, Aug. 1972.
- 3.2-3 Multispectral Scanner Data Applications Evaluation, Vol. II - Sensor Systems Study. Honeywell Radiation Center, NASA JSC-09241, ERIM 102800-40-F, Dec. 1974.
- 3.2-4 Lansing, J. C., Jr.; and Cline, R. W.: The Four- and Five-Band Multispectral Scanners for Landsat. Optical Engineering, Vol. 14, July-Aug. 1975; pp. 312-322.
- 3.2-5 Hovis, W.; Nichols, J.; Potter, A.; and Thomson, F.: Landsat-D Thematic Mapper Technical Working Group, Final Report, JSC-09797, June 1975.
- 3.2-6 Thomson, F. J., et al.: Multispectral Scanner Data Applications Evaluation. Vol. I, User Applications Study, NASA-JSC 09241, ERIM Report 102800-40-F, Dec. 1974.
- 3.2-7 Johnson, W. R.: Evaluation of Thematic Mapper Bandwidth Selection Using Skylab S-192 Principal Investigator Results. Technical Memorandum, Dec. 1975 (to be published).
- 3.2-8 Lowe, D. S.: Requirements for a Synchronous Earth Observation Satellite (SEOS). Proceedings of SPIE, Vol. 51, Scanners & Imagery Systems for Earth Observation, San Diego, Calif., pp. 115-123, Aug. 19-20, 1974.
- 3.2-9 Walter, L. S.: Synchronous Earth Observatory Satellite (SEOS). IEEE Electronics and Aerospace Systems Conference (EASCON), Washington, D. C., pp. 631-636, Oct. 1974.
- 3.2-10 Lowe, D. S.; and Cook, J. J., et al.: Earth Resources Applications of the Synchronous Earth Observatory Satellite (SEOS). ERIM 103500-1-F, 309 pp., Dec. 1973.

- 3.2-11 Goldman, G. C.; et al.: Investigation of Transient Earth Resources Phenomena: Continuation Study. Final Report, ERIM 107400-2-F, 125 pp, Nov, 1974.
- 
- 3.2-12 Chism, S. B., Jr.: Two Spectral Band Set Concept for the Landsat-D Thematic Mapper. LEC Technical Memorandum, LEC-8238, Mar. 1976.
- 3.2-13 Chang, C. Y.: Skylab S-192 Data Evaluation: Comparisons with ERTS-1 Results. Lockheed Electronics Co., Inc., LEC-1711, Jan. 1974 (JSC).
- 3.2-14 Morgenstern, J.; et al.: S-192 Analysis: Conventional and Special Data Processing Techniques. ERIM, Sept. 1975, Final Report 101900-61-F.
- 3.2-15 Vincent, R. K.; and Pillars, W. W.: Skylab S-192 Ratio Codes of Soil, Mineral, and Rock Spectra for Ratio Image Selection and Interpretation. Proc. of 9th Int'l Symposium on Remote Sensing of Environment, Vol. III, pp. 875-895, Apr. 1974.

### 3.3 MICROWAVE SCATTEROMETERS

#### 3.3.1 USES OF FUTURE SCATTEROMETERS

The need for and future use of active microwave sensors (scatterometers) for remote sensing has been established. Past and present scatterometers are given in table 3.3-1 (ref. 3.3-1). These uses include studies in the following areas: ocean studies and wind measurements, ice studies, soil moisture studies, agriculture and vegetation studies, geoscience, and weather. Primarily, the first four areas have received the most attention. Scatterometers are used to measure the reflection or scattering coefficient of various objects. The scattering coefficient of a particular object is dependent upon the frequency, polarization, and incident angle of the impinging electromagnetic energy upon the object. The scattering coefficient of an object is expressed as the backscattering radar cross section ( $\sigma^{\circ}$ ) which is the backscattered power-per-unit area normalized for antenna gain, range loss, and transmitted power.

The Joint Soil Moisture Experiment (JSME) being conducted by JSC, University of Kansas (KU), Texas A&M University (TAMU), and others is an effort to determine the relationship between soil moisture and radar cross section ( $\sigma^{\circ}$ ) or backscatter. One end objective of this study is to evaluate the usefulness of scatterometer data to measure soil moisture as an aid in predicting crop yields. Agricultural and vegetation studies are being performed by the University of Kansas to relate  $\sigma^{\circ}$  to vegetation types and vegetation condition with crop classification, maturity assignment, and health assignment as the end goal. The relationship between  $\sigma^{\circ}$  and sea state is being studied to aid forecasting wave heights and wind direction in order to assist shipping, locate storms, locate oil slicks, etc. Ice and snow studies can be used to differentiate between polar ice and new snow in helping to ascertain estimated water runoff. Geoscience applications include

TABLE 3.3-1. — PAST AND PRESENT SCATTEROMETERS

Type of measurement and organization	Frequency (GHz)	Type	Polarization combinations	Applications	Instrument dynamic range (dB)	Instrument angle of incidence capability, degrees	Resolution
<u>Spaceborne Experiments:</u>							
NASA/JSC	13.9	Pulse CW	All	1,2,3,4,5,6	52	0° to ±53°	6 n. mi.
<u>Airborne Experiments:</u>							
NASA/JSC	13.3	CW	VV	1,2,3,4,5,6	55	0 to 60°	50' **
NASA/JSC	1.6	CW	} All (VV, VH, HV, HH)	1	~55	±5° to ±60°	150' **
NASA/JSC	.4	Pulse/CW		1,3	~55	0° to ±60°	200' **
NRL	.428	CW		3,4,6	~50	0° to 89°	
NRL	1.228	CW		3,4,6	~50	0° to 89°	
NRL	1.25	CW		3,4,6	~50	0° to 89°	
NRL	4.425	CW		3,4,6	~50	0° to 89°	
NRL	8.95	CW	3,4,6	~50	0° to 89°		
<u>Ground Experiments:</u>							
KU	2-8*	FM/CW	VV, VH, HH	1,2	~80	0° to 80°*	
KU	8-18*	FM/CW	All	1,2	~82	0° to 80°*	
NRL	34.88	CW	VV	3,4,6	~50		
NRL	24	CW	VV	3,4,6	~50		
NRL	9.375	CW	VV	3,4,6	~50		

\*Not continuous

\*\*@ 1000 ft altitude, cross track

- 1) Joint Soil Moisture Experiment
- 2) Agriculture and Vegetation Studies
- 3) Ocean Studies
- 4) Ice and Snow Studies
- 5) Geoscience
- 6) Weather

3.3-2

geophysical exploration. Scatterometer data can be used to assist in weather forecasting. Table 3.3-1 lists scatterometers that have been used in the past and includes many that are being used presently in various investigations and applications.

Analysis of the data obtained from using the scatterometers given in table 3.3-1 has started to establish a set of guidelines for future scatterometers, both in terms of their application and actual design.

#### 3.3.1.1 Sea State Studies

In terms of measuring sea state, the remote sensor selected for this surface wind measurement is the microwave scatterometer, (refs. 3.3-1 and 3.3-2). Aircraft and satellite scatterometer data show that for windspeeds less than 20 m/sec and incidence angles beyond 25°, the ocean radar scattering coefficient ( $\sigma^0$ ) changes about one-half dB per 10 log m/sec change in wind speed. The sensitivity of  $\sigma^0$  to wind speed is still sufficient (even to gale-force winds) to make the scatterometer a viable remote sensor of wind speed and direction if proper attention is given to instrument accuracy.

Figure 3.3-1 shows representative backscatter ( $\sigma^0$ ) return versus wind speed (ref. 3.3-3).

The capillary waves develop with increasing wind speed above approximately 3 m/sec. Below 3 m/sec, the capillary waves die away very rapidly. Thus, for wind speeds lower than 3 m/sec, it is believed that scatterometer measurements will be invalid. This is so because small gusts of wind will create patches of capillary waves which will dominate the radar return (ref. 3.3-2).

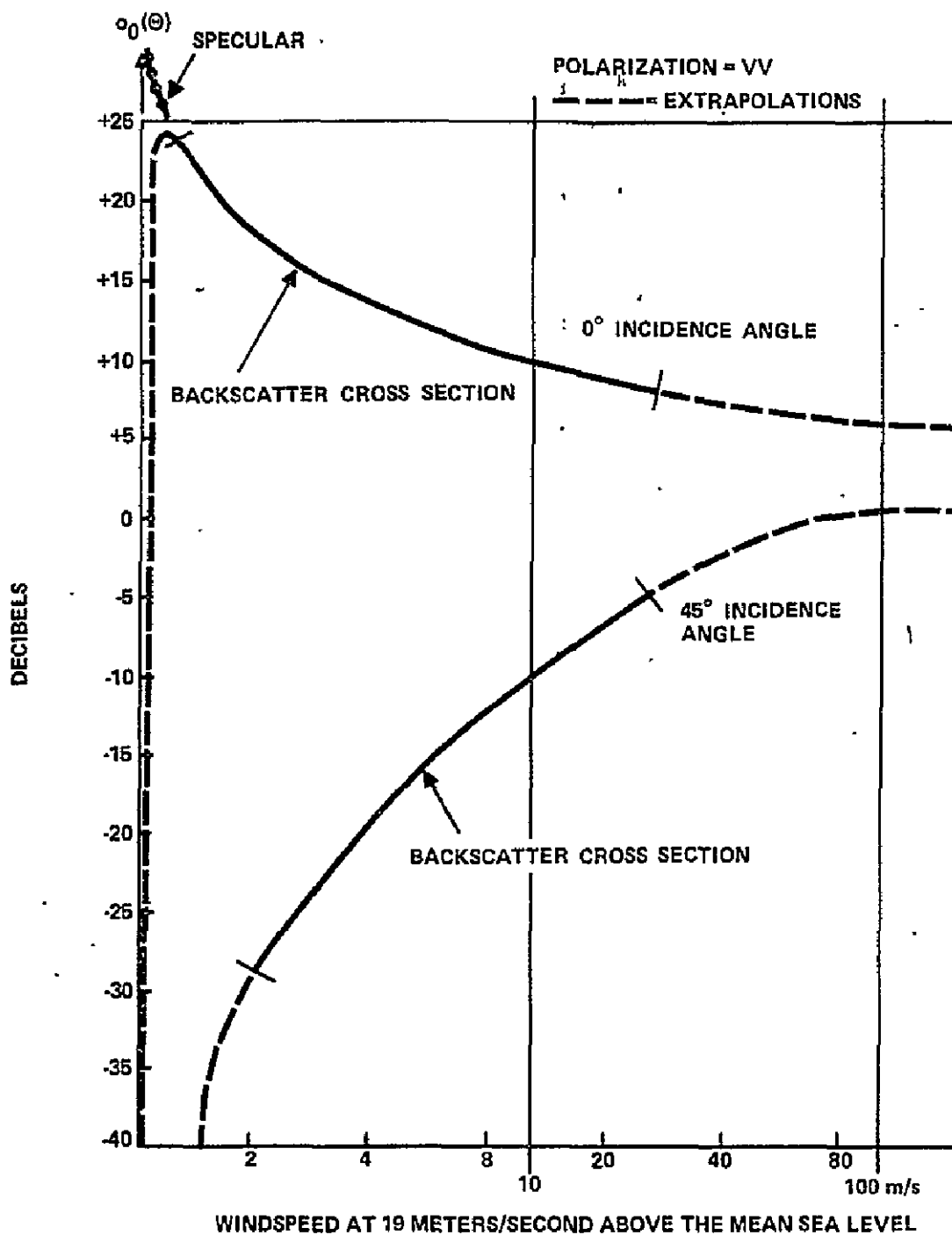


Figure 3.3-1.— Representation of approximate magnitude of backscatter cross sections from ocean at 2- to 3-cm radar wavelengths (ref. 3.3-3).

Good  $\sigma^\circ$  data has been reported up to between 20 m/sec and 25 m/sec wind speeds [refs. 3.3-1, 3.3-2, and 3.3-3].

Of interest are the curves shown in figure 3.3-2, (ref. 3.3-2). Shown are the  $\sigma^\circ$  curves for upwind, downwind, and crosswind conditions for various wind speeds. It should be noted that  $\sigma^\circ$  for upwind conditions is greater than for downwind conditions. This implies that a 'multilook' scatterometer is required for wind direction determination.

In summary, for incident angles of  $0^\circ$  to  $20^\circ$ , scatterometer data provides sea state information through the detection of the slope statistics of ocean waves. For higher incident angles ( $20^\circ$  to  $60^\circ$ ), local wind fields can be determined.

No effort has been made here to discuss the mechanism of scattering from the ocean and considering the ocean waves as a composite surface. Adequate reference as to this can be found elsewhere (refs. 3.3-2, 3.3-4, and 3.3-5).

### 3.3.1.2 Ice Studies

Polar ice includes three distinct forms of ice which have widely divergent properties:

1. Sea ice, which is several meters thick, has an age of several hours to many years, and is brackish.
2. Ice caps and glaciers, up to several kilometers in thickness; thousands of years old, and fresh water in content.
3. Lake ice, fresh or brackish water, and a few hours old to months old.

The important aspect of radar (imaging or scatterometers) for polar studies is that for many months the polar regions are in the dark and when sunlit, they are cloud covered. Thus, microwave instruments are required in terms of remote sensing of

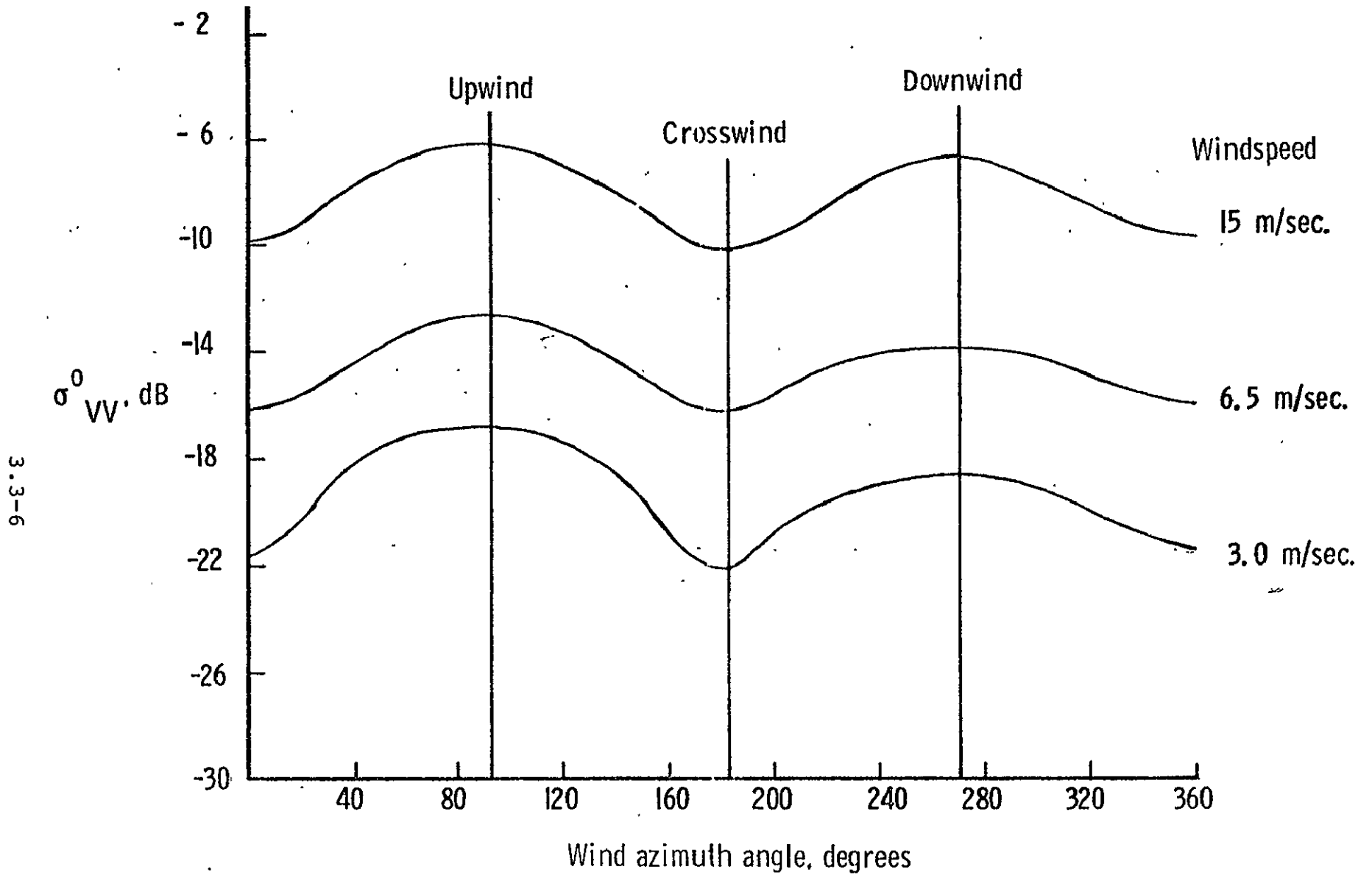


Figure 3.3-2. - AAFE Radscat Scatterometer wind direction sensitivity (ref 3.3-2).

polar ice fields. Figure 3.3-3, (ref. 3.3-6) shows average backscatter data versus ice thickness for varying incident angles. These data were taken with a 13.3 GHz scatterometer. It was shown that the 13.3 GHz scatterometer data exhibited an ambiguity where, with the use of a 0.4 GHz scatterometer, this ambiguity could be resolved (ref. 3.3-6). The ambiguity was between ice <5 cm thick and ice approximately 1 m thick. The 13.3 GHz scatterometer could distinguish thin (new) ice and thicker (old) ice. The 0.4 GHz could not distinguish between 0.5 m thick ice and thicker multi-year ice. These studies were for sea ice. It was reported that not enough is known to date with respect to frequency or polarization to ascertain the optimum for monitoring sea ice or lake ice (ref. 3.3-6). In concluding this section, it has been established that multi-angle scatterometer observations can be correlated with ice type (refs. 3.3-6 and 3.3-7).

#### 3.3.1.3 Soil Moisture Studies

Soil moisture content is an important parameter in crop yield prediction, runoff prediction, and other applications in hydrology, agriculture, and meteorology. Remote sensing offers a potential means for the determination of the spatial distribution of moisture content over large areas, within a short time and at a reasonable cost. Among the various electromagnetic sensors, radar is the least affected by atmospheric conditions. It is also time-of-day independent and has the capability of mapping terrain surfaces from satellite altitudes with a spatial resolution compatible with the requirements of the above applications.

Moisture content of soils influences the dielectric properties of the soils and this in turn affects the magnitude of the back-scattered energy from the soil, particularly at angles of incidence close to nadir. Both the real and imaginary parts of

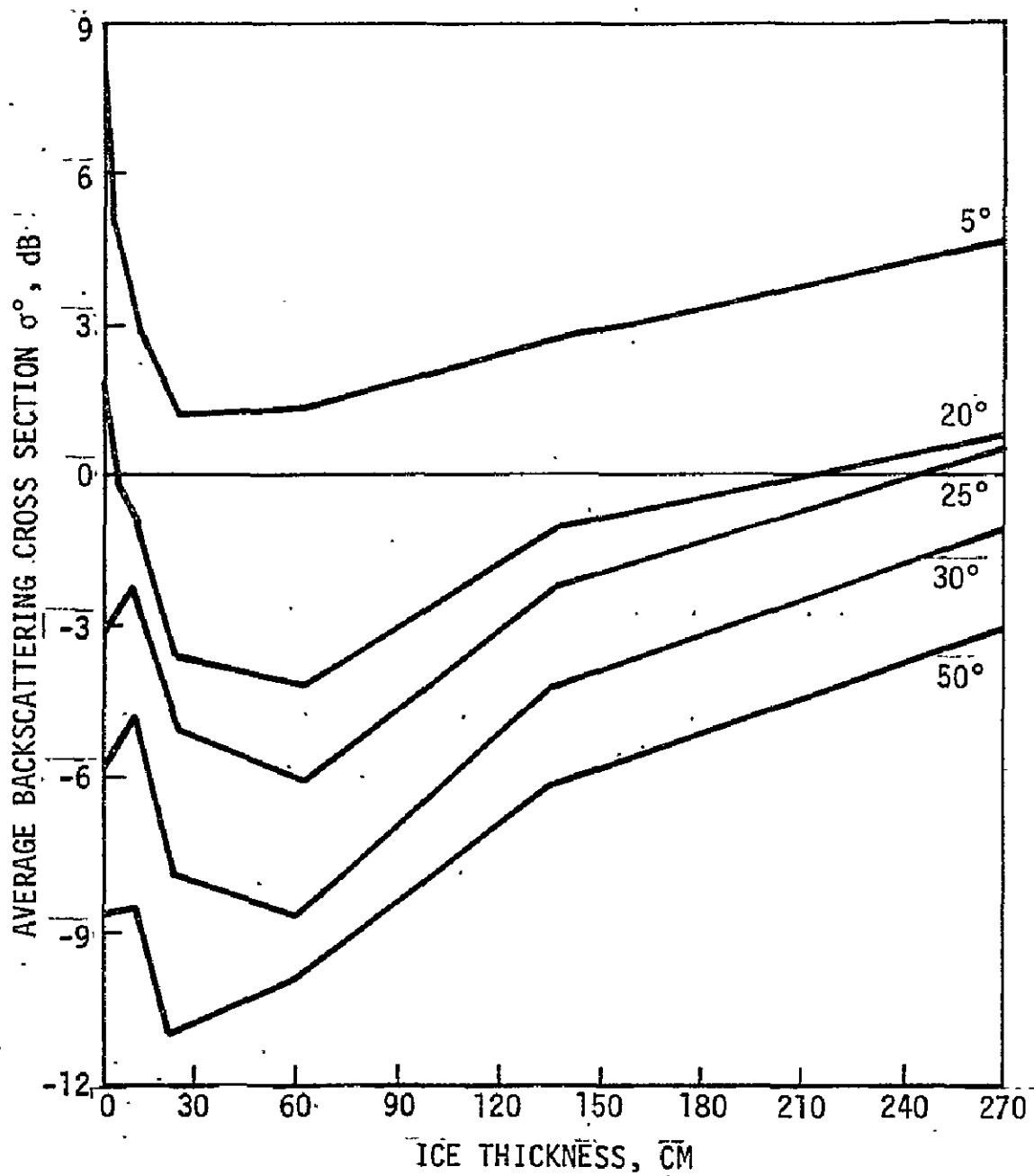


Figure 3.3-3.— Experimental  $\sigma^0$  compared to ice thickness for different incident angles (frequency of 13.3 GHz, vertical transmit/vertical receive polarization) (ref. 3.3-6).

the dielectric constant of the soil are affected by variation in soil moisture. Bare fields have shown more sensitivity to variations in soil moisture than have vegetated fields. Not only does vegetation affect the absolute value of  $\sigma^\circ$  and sensitivity of  $\sigma^\circ$  to soil moisture variations, but so does the soil surface roughness.

Data taken from .400 GHz and 13.3 GHz scatterometers (NASA/JSC) aboard a P3A aircraft in 1970 was analyzed (ref. 3.3-8). Using the 13.3 GHz scatterometer, it was found that a definite increase in backscatter ( $\sigma^\circ$ ) occurred for fields under irrigation. This increase was on the order of 5 to 7 dB and occurred where the angle of incidence of the incident energy was less than 40 degrees. On June 26, 1970 (Mission 130), the data obtained by the NASA flight was for eleven totally irrigated fields and eight partially irrigated fields. These fields were vegetated. The terrain was flat. Also, data was taken from two bare fields. One field was plowed and the other drilled. The plowed field was very rough with rows and had clods and thus fit the description of a composite rough surface. The drilled field had no rows and very fine clods and fit the classification of a small perturbation surface (ref. 3.3-8). Both fields were partially irrigated. The backscatter from the wet areas was about 5 dB above backscatter from the dry areas for both fields. The conclusion to be drawn from this data (ref. 3.3-8) is that for vegetated fields (corn, alfalfa, sorghum, wheat stubble, wheat, weeds) and bare fields (rough and smooth), the wet fields were from 5 to 7 dB greater in backscatter value than for dry fields.

Data taken from the .4 GHz scatterometer exhibited a difference in backscatter between wet and dry fields but the magnitude of the difference and range of incidence angles over which the

differences were significant varies much more from field to field than with data taken by the 13.3 GHz scatterometer. The 13.3 GHz data is shown in figure 3.3-4, (ref. 3.3-8).

More recent data taken by the University of Kansas, using two multiple frequency scatterometer systems, has shown more trends regarding soil moisture and vegetation measurements. These trends have indicated a more optimum frequency range and set of incidence angles for which to make soil moisture and vegetation measurements. The indication is to use an S or C-band scatterometer and smaller incidence angles (<25 degrees).

Radar backscatter data were acquired from three bare fields with a considerable variation in surface roughness between each of them. This data was taken using a 2-8 GHz scatterometer mounted on a truck. This particular system is termed a Microwave Active Spectrometer (MAS). In addition to measuring soil moisture, effects of surface roughness, angle of incidence, polarization, and frequency on backscatter characteristics were investigated. In terms of roughness, the three fields were designated as smooth (S), medium rough (M), and rough (R).

The surface features of the three fields were measured and the three surface roughness classifications were identified as follows:

	rms height (cm)	peak to peak variation (cm)
Smooth	0.88	2.0
Medium Rough	2.6	7.5
Rough	4.3	15.0

The medium rough and rough fields are typical of plowed-then-disked and plowed fields. The surface of the smooth field is representative of only a very few of the cultivated farm lands.

MISSION 130

SITE GARDEN CITY, KANSAS

FREQUENCY 13.3 GHz

DATE MAY 27, 1970

POLARIZATION VV



Figure 3.3-4. - Average of all the wet and dry fields in the entire test site, Ku-Band, Mission 130.

After acquiring one scatterometer data set per field with the fields dry, the fields were sprinkler irrigated for 12 hours. Scatterometer data sets were then acquired from the three fields on a rotating basis for a period of 13 days. Each radar data set consisted of measurements of the backscattered return at five angles of incidence ( $0^\circ$  (nadir) through  $40^\circ$  in  $10^\circ$  steps) for HH and VV polarizations at each of eight frequencies (2.75, 3.25, 4.75, 5.25, 5.75, 6.25, 6.75, 7.25 GHz) in the 2-8 GHz band. A combination of frequency and spatial averaging were used to reduce signal fading.

For each scatterometer data set, soil samples were taken. The three fields were side by side. There were eight soil sampling locations per field. At each location samples were collected from five depths: 0-1 cm, 1-2 cm, 2-5 cm, 5-9 cm, and 9-15 cm. These samples were later processed in the laboratory to determine their moisture contents by weight and their bulk densities. Using these results along with backscatter response allows for optimizing scatterometer operation.

From the scatterometer data that was taken from the smooth, medium rough, and rough bare fields, considerable effort was expended to relate surface roughness to soil moisture measurements. Results showed that the effect of surface roughness was minimized at incidence angles of  $4^\circ$  and 2.75 GHz,  $10^\circ$  incidence angle and 5.25 GHz, and  $20^\circ$  incidence angle and 7.25 GHz.

Soil moisture responses were studied for all three roughnesses as a function of the various system parameters. It has been demonstrated that the effects of roughness can be reduced by proper choice of frequency and angle of incidence, while at the same time retaining good sensitivity to soil moisture.

A parameter chosen to represent roughness is rms height,  $h$ . As the radar responds to both large scale and small scale roughness, this representation is undoubtedly not optimal. Linear regression lines of  $\sigma^\circ$  as a function of soil moisture content were calculated for each individual surface roughness (rms height of 0.88 cm, 2.6 and 4.3 cm) at each angle of incidence, polarization and frequency combination (ref. 3.3-9).

Based on optimum correlation coefficient and optimum sensitivity considerations, studies indicate that the angular range extending between about  $7^\circ$  and  $15^\circ$  is optimum. The corresponding optimum frequency is around 4 GHz. Over the  $7^\circ$ - $15^\circ$  angular range, HH and VV polarizations appear to have approximately the same soil moisture response.

In summary, from analyzing this data, the recommended scatterometer operating parameters for soil moisture detection are:

Angle of Incidence Range:  $7^\circ$ - $15^\circ$

Frequency: Around 4 GHz

Polarization: HH or VV.

#### 3.3.1.4 Vegetation Studies

Critical to the successful application of radar remote sensing techniques to agricultural land use mapping is the understanding of the dependence of the backscattering coefficient  $\sigma^\circ$  of a vegetated scene on the geometrical and electrical properties of the remotely sensed scene. Establishing these relationships requires (a) the acquisition of backscatter data over a wide range of the measurable target parameters and (b) the construction of theoretical and/or empirical models (based on the measured data) from which in-depth inferences can be made on the target-signal interaction process. Moreover, since the desired

relationships are often a function of the signal parameters (frequency, polarization, and incidence angle), it is important that the data collection and modeling be made over as wide a range of the signal parameters as is practically feasible with present day sensors.

From scatterometer data taken in 1974 by the University of Kansas, the following quoted conclusions are given (ref. 3.3-22). (This information became available in January 1976. The scatterometers used covered the frequency range of 1 to 8 and 8 to 18 GHz.)

An analysis of the scattering data collected from fields of wheat, alfalfa, and corn during the summer of 1974 has led to a number of observations:

- a. In general,  $\sigma^\circ$  of wheat as measured during its final 30 days of maturity is an increasing function of plant development. The scattering coefficient is most sensitive to plant development at nadir incident angle where a significant linear trend between the passage of time is observed to exist. Although less sensitive to plant growth,  $\sigma^\circ$  at  $50^\circ$  incident angle also indicates a positive correlation with the passage of time.
- b. By monitoring the rate of change of  $\sigma^\circ$  of wheat, it may be possible to estimate the time for harvest and to follow the progress of harvest.
- c. Like  $\sigma^\circ$  of wheat,  $\sigma^\circ$  of alfalfa shows the greatest response to plant development when monitored at nadir incident angle. In contrast to wheat, however, the scattering coefficient of alfalfa is in general a decreasing function of plant maturity (height). Furthermore, it was possible to account for the variations observed in  $\sigma^\circ$  of alfalfa with a nonlinear regression equation incorporating plant height, plant moisture, and soil moisture.

- d. To effectively monitor the growth of corn with radar, incidence angles of  $40^\circ$  or larger are imperative to increase the ratio of canopy scatter to soil scatter. Furthermore, this ratio can be improved by operating at higher signal frequencies.

Measurements taken using a multiple frequency scatterometer to map crop types have given some distinct results (ref. 3.3-10). The frequency range of the scatterometer used was 4 to 8 GHz. The scatterometer antenna was mounted on a boom with the scatterometer housed on a truck. The data results were grouped in such a way that three center frequency points were used as reference in analyzing the data. These three center frequency points were 4.7 GHz, 5.96 GHz, and 7.1 GHz. Four crops were studied (corn, milo, alfalfa, soybeans). The results have been summarized as follows (refs. 3.3-9, 3.3-11):

1. To lessen the effects of soil moisture, use angles of incidence outside the range of 5 to 15 degrees.
2. Vertical transmit, vertical receive, and cross polarization yield the best results.
3. For crop identification, larger angles of incidence should be used ( $\geq 30^\circ$ ) to lessen the effect of soil moisture on the backscatter measurements.
4. The spread in backscatter values ( $\sigma^\circ$ ) for the four crops is largest using frequencies around 4 GHz. However, corn and milo can be better distinguished from backscatter measurements using frequencies around 7 GHz and angles of incidence between 30 and 40 degrees.
5. Alfalfa is the easiest to distinguish.
6. Comparing healthy and blighted corn can best be done for incidence angles between 40 and 60 degrees.

7. Soybeans can be distinguished from milo and corn using any polarization combination and any incidence angle greater than  $30^\circ$ .

The preceding conclusions were reached from examining scatterometer data taken before 1974.

The study presented here gives the results of an investigation conducted to determine the microwave backscattering properties of a continuous vegetation canopy over the 8-18 GHz frequency region. Using a truck-mounted scatterometer, measurements were acquired from an alfalfa field at angles of incidence ranging from nadir ( $0^\circ$ ) to  $70^\circ$  for horizontal transmit-horizontal receive (HH) and vertical transmit-vertical receive (VV) polarization configurations. As a perennial crop, alfalfa is usually harvested three, or often four times per year. Upon reaching a height of 50-70 cm, it is cut, dried and baled, and then allowed to grow again. During the 1974 summer season, scatterometer observations were made over two complete growing cycles of alfalfa (ref. 3.3-12).

The scatterometer employed in collecting the data used in this study is the 8-18 GHz Microwave Active Spectrometer (MAS 8-18) (ref. 3.3-13). This is a truck-mounted system capable of making scattering measurements at 11 frequencies in its 8-18 GHz range. It employs a dual antenna system configured to allow both horizontal-transmit horizontal-receive (HH) and vertical-transmit vertical-receive (VV) modes of operation. Measurements can be made at angles of incidence between  $0^\circ$  (nadir) and  $70^\circ$ . Being a wide band scatterometer, the MAS 8-18 provided fading reduction by averaging samples of the return signal energy over its

800 MHz bandwidth. Because of the limited extent of the resolution cell area, frequency averaging would not provide the fading reduction necessary for the data precision and accuracy desired. Thus, spatial-averaging was also employed.

Reiterating, soil moisture played the overwhelming role in determining the complex dielectric constant of soil. In turn, the dielectric properties of the soil are reflected in  $\sigma^\circ$ . To aid in determining the relationship between  $\sigma^\circ$  and soil moisture content, soil samples were collected at the time of each scattering measurement. The location of each pair of sampling points was chosen so that they approximately corresponded to scattering measurements made within the angular ranges of  $0^\circ$ - $20^\circ$ ,  $30^\circ$ - $50^\circ$ , and  $60^\circ$ - $70^\circ$ , respectively. After recording the sample weight, they were dried in an oven and again weighed so that the gravimetric soil moisture content could be determined. The measured values of the soil moisture content were then averaged in a pair-wise manner and converted to volumetric soil moisture content using the soil bulk density as the conversion factor. Thus, all soil moisture contents reported herein, designated as  $m_s$ , are expressed in units of  $g/cm^3$ . Only the top 2 cm samples were used in this analysis. Subsequent analyses involving  $m_s$  will make use of the soil sample location and incidence angle correspondence. There were six data points at the perimeter of the field, three on each side.

As with soil moisture, plant moisture has been shown to significantly influence the dielectric properties of vegetation (ref. 3.3-14). Thus, as part of the scattering experiment, a number of alfalfa plant samples were collected at the time a scattering measurement was made. These samples were processed so that the plant moisture content as measured on a wet weight basis was obtained.

In addition to the previous parameters, the time history of the average height of the vegetation canopy was also recorded. It should be noted that the alfalfa completed two growth cycles during the observation period. While plant height is certainly one indicator of plant maturity, there are a variety of physiological phenomena occurring during the maturation process.

By observing the data, it was found that the dynamic range of  $\sigma^0$  (at 8.6 GHz,  $0^\circ$  incident angle) during the observation period was nearly 18 dB, implying that indeed the scatterometer responded to the physical variations of the alfalfa as it completed two growth cycles. Two distinct maxima and minima are also noted. The maxima occur on May 22 and July 10 and the minima, while not quite as pronounced, occur near June 28 and August 1. From figure 3.3-5 it is found that the maxima coincide exactly with the days on which the harvested alfalfa was observed. Furthermore, the minima correspond to those time periods during which the alfalfa reached maximum height. In fact, it is noted that throughout the observation period,  $\sigma_V^0$  and  $\sigma_H^0$  are roughly inversely related to plant height.

The promising aspect of these and other studies is that the response of  $\sigma^0$ , near nadir, to variations in the height of alfalfa appears to be rather consistent. It is this sort of consistency that is needed for studying the various agricultural targets of interest on an operational basis.

Among the parameters affecting the signal strength of the scatterometer return from row crops is the look direction relative to the crop row direction. Using a truck-mounted 2-8 GHz scatterometer, backscatter measurements were acquired from a field of sorghum with look directions parallel and orthogonal to the row direction at six incidence angles (nadir to  $50^\circ$  in  $10^\circ$  steps) for both HH and VV polarizations over the 2-8 GHz frequency band.

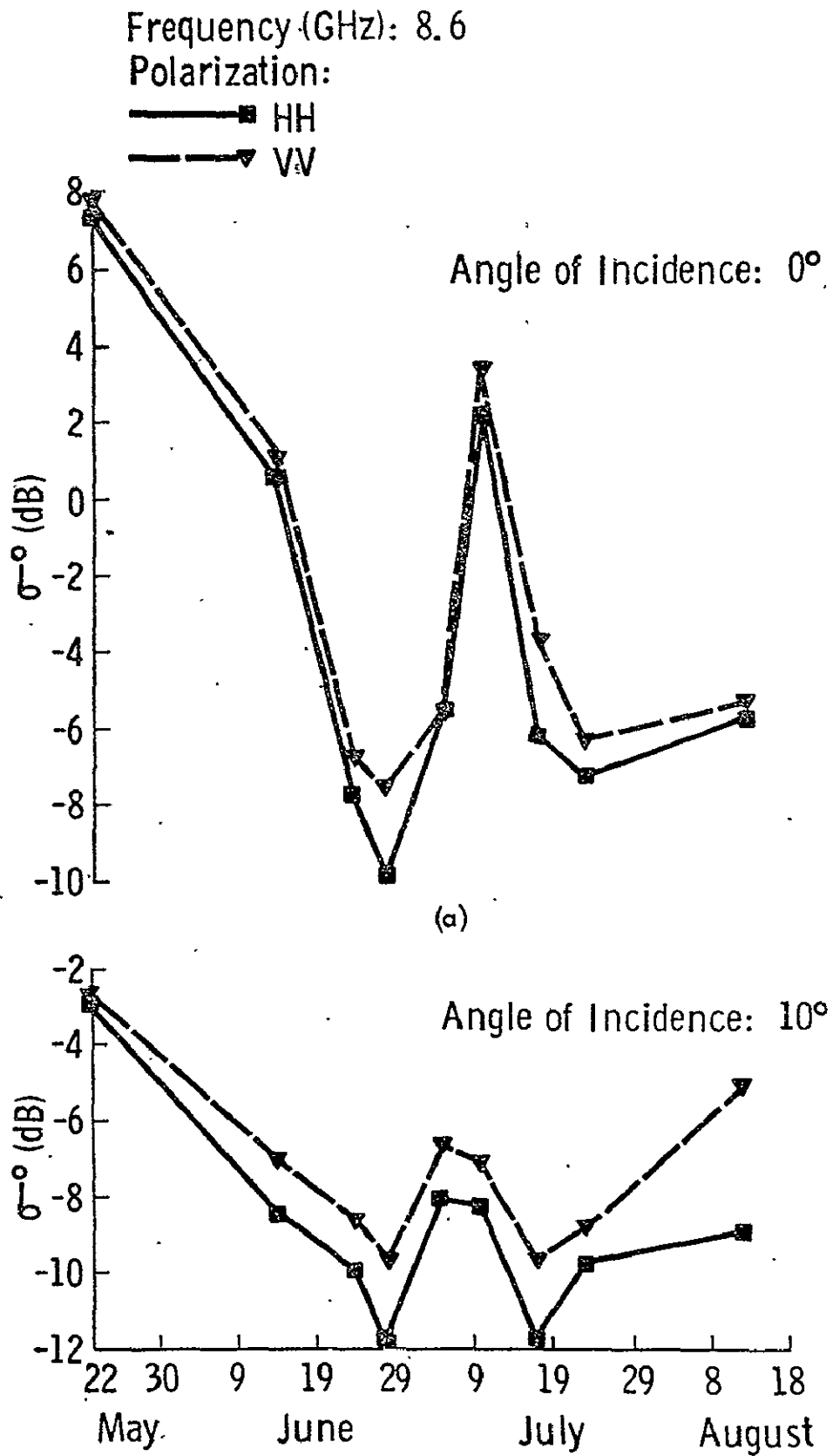


Figure 3.3-5.— Temporal variations of  $\sigma^0$  measured at 8.6 GHz for angles of incidence of (a) 0°, (b) 10°, (c) 40°, and (d) 70°, (ref 3.3-12).

Frequency (GHz): 8.6

Polarization:

—■— HH

- - - ▾ - - - VV

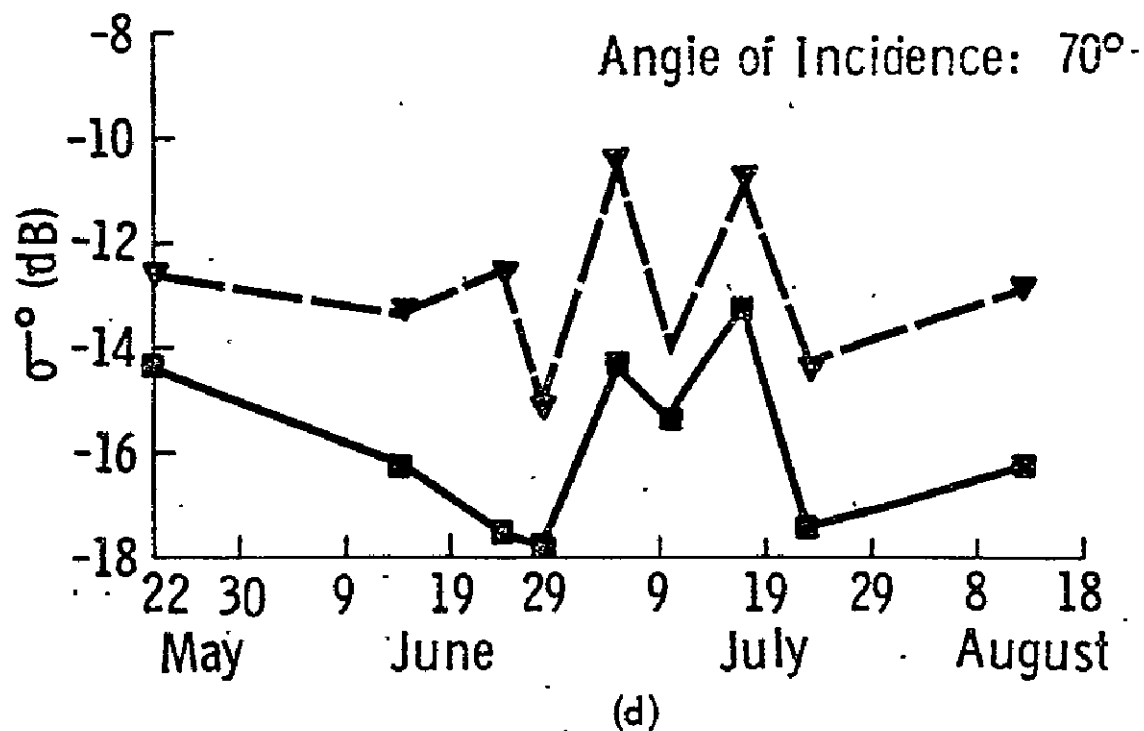
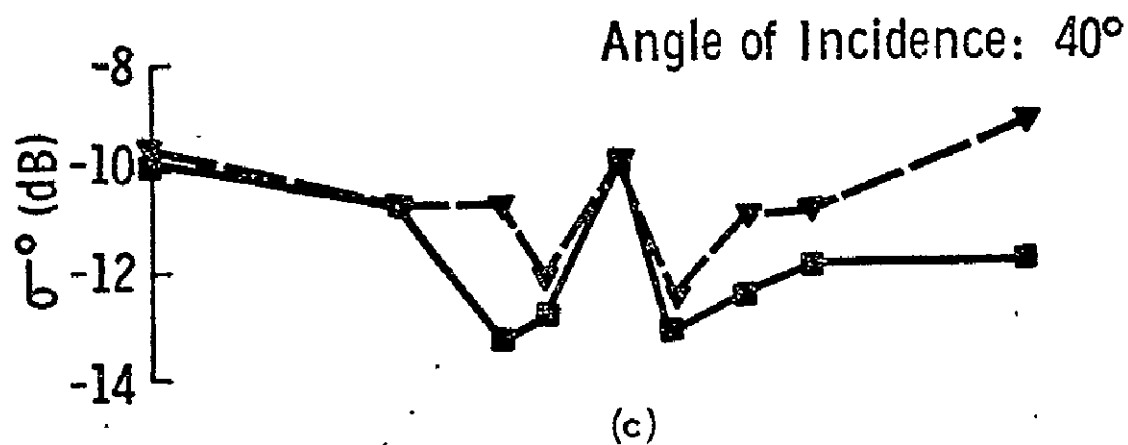


Figure 3.3-5.— Temporal variations of  $\sigma^0$  measured at 8.6 GHz for angles of incidence of (a) 0°, (b) 10°, (c) 40° and (d) 70°, (ref 3.3-12) — (Concluded).

The results confirm observations made from radar imagery indicating that the difference in return between the two look directions increases with wavelength and is larger for HH polarization than for VV polarization (ref. 3.3-15).

The scattering coefficient data reported herein was acquired by the University of Kansas MAS 2-8 system (ref. 3.3-16) which is a FM-CW scatterometer capable of operating over the 2-8 GHz band. The system is mounted atop a 20 m truck-mounted boom.

Several weeks prior to the experiment, a field at the Texas A&M University Agricultural Experiment Station was planted with sorghum with a row spacing of 1 m. At the time of the experiment, the sorghum plants had reached a height of about 2.5 m. This investigation was part of a joint effort with Texas A&M University to determine the active (MAS 2-8) and passive (NASA X- and L-band radiometer system) microwave responses to soil moisture. The row sorghum field was one of several types of targets interrogated at the Texas A&M site. Although initially it was planned to conduct the row sorghum part of the experiment for different plant heights, system and logistic problems delayed the start of the microwave part of the experiment. By then, the sorghum was fully grown.

Data acquired with the look direction parallel to the row direction will be designated by "//" and those acquired with the antenna beam pointing orthogonal to the row direction will be designated by "⊥". Each data set consisted of backscatter measurements at incidence angles of 0° (nadir) to 50° in 10° steps, VV (vertical transmit-vertical receive) and HH (horizontal transmit-horizontal receive) polarizations and 8 frequencies between 2 and 8 GHz. To reduce the effects of signal fading and to insure proper target "representation", spatial averaging was employed by moving the truck alongside the field and repeating

the data taking procedure. Hence, for each frequency-incidence angle-polarization-look direction combination, data points represent an average of several spatially independent measurements. Three frequencies have been chosen to discuss results in this section; these are 2.75 GHz, 5.25 GHz, and 7.25 GHz representing, respectively, the lower end, the middle, and the upper end of the 2-8 GHz band. The angular response of the scattering coefficient,  $\sigma^\circ$ , is presented in figure 3.3-6 for // and  $\perp$  look directions at the three frequencies. In general, the difference between the two curves is most pronounced in the  $10^\circ$ - $30^\circ$  range at the lowest frequency. At  $20^\circ$ , for example,  $\sigma^\circ_{\perp} - \sigma^\circ_{//}$  is about 9.0 dB at 2.75 GHz compared to 4.0 dB at 7.25 GHz. The frequency response of the scattering coefficient,  $\sigma^\circ$ , is presented in figure 3.3-7 for // and  $\perp$  look directions for  $20^\circ$  and  $50^\circ$  incidence angles.

These results show definite trends in terms of backscatter response when viewing a row crop. This is further supporting material that an operational sensor must be adequately 'designed' both in terms of hardware characteristics (scatterometer type, components, specifications), and operating requirements (i.e., look angle, polarization, frequency, angle of incidence and distance from the object to be viewed).

Measurements of radar backscattering coefficient of densely planted fields of sorghum were conducted using a scatterometer placed on a 20 meter truck-mounted boom, (ref. 3.3-17). Data was collected at 8 frequencies between 2 and 8 GHz, using 2 polarizations (HH, VV) and 6 angles of incidence ( $0^\circ$  to  $50^\circ$  from nadir in  $10^\circ$  steps). The objective was to determine the backscatter response to soil moisture variations beneath a continuous vegetation cover with soil surface roughness and plant height as parameters. Four fields were prepared having different surface roughness and plant height combinations. The four fields were

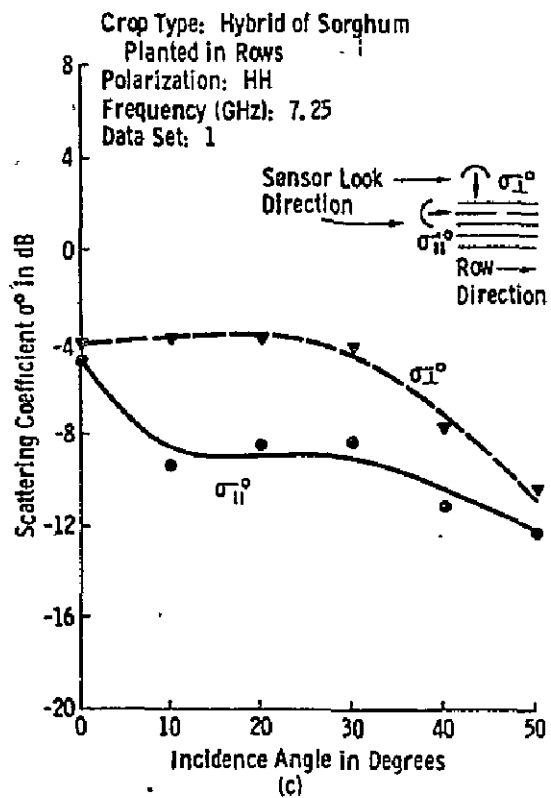
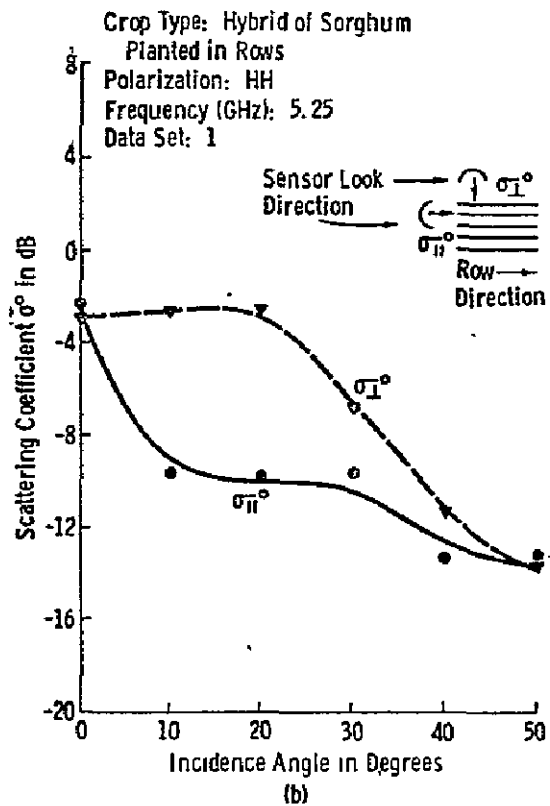
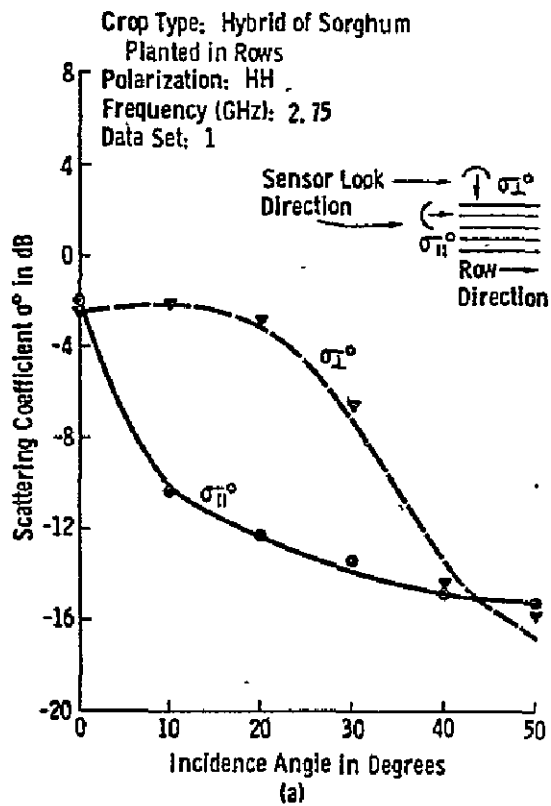


Figure 3.3-6.— Scattering coefficient  $\sigma^0$  as a function of incidence angle at (a) 2.75 GHz, (b) 5.25 GHz, and (c) 7.25 GHz. Data set #1, July 16, 1974, (ref. 3.3-15).

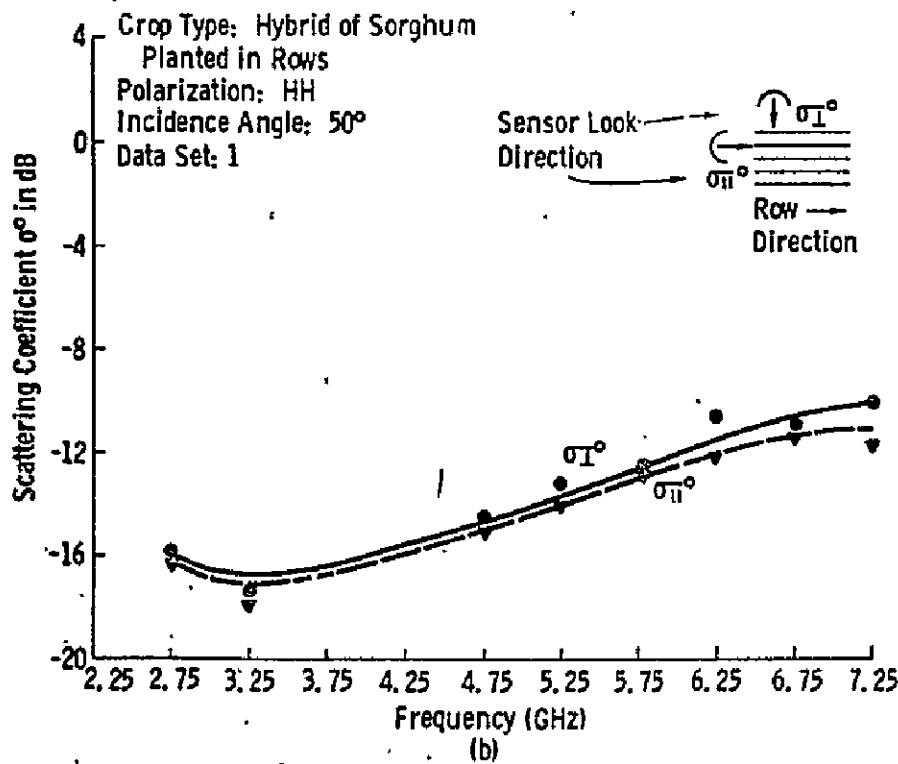
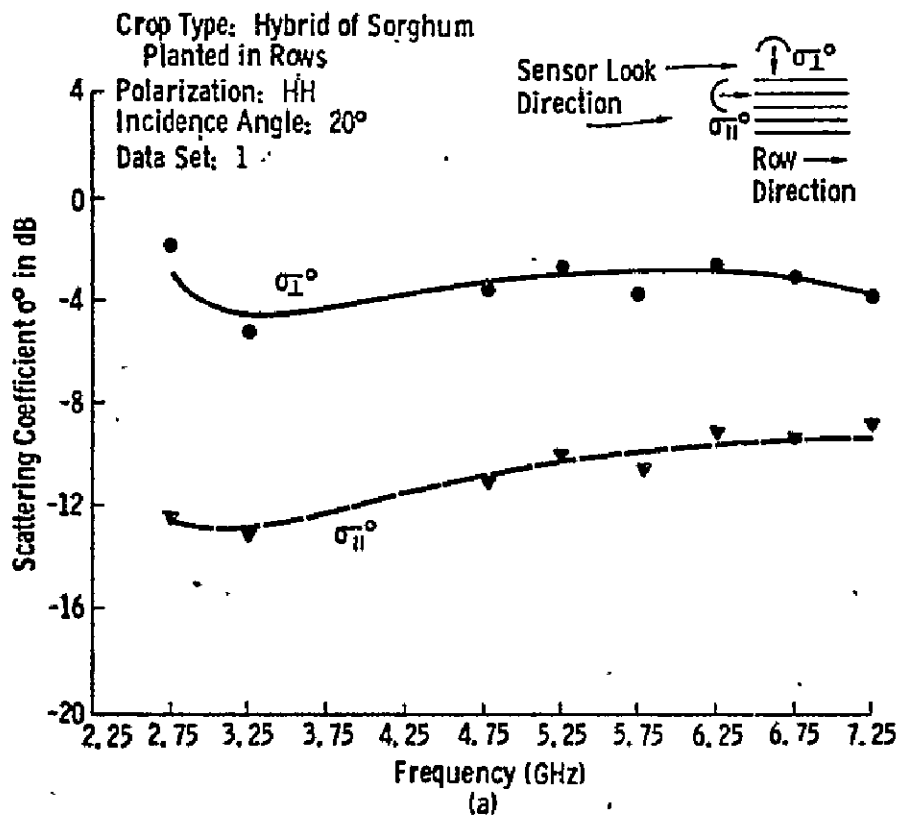


Figure 3.3-7.— Spectral response of  $\sigma^o$  at incidence angles of (a) 20° and (b) 50° for data set #1, July 16, 1974, (ref. 3.3-15).

watered for 12 hours. Then adequate time was allowed for the water droplets on the leaves to evaporate. Backscatter measurements were made on the four fields on a rotating basis for several days. A resulting analysis of the backscatter data indicated no discernible sensitivity to soil moisture variation. This is attributed to the 100 percent plant cover. The shortest plant height was 90 cm. The backscatter measurements appeared sensitive to frequency and angle of incidence but not polarization. The backscattering showed a definite discernible variation pattern.

Ground-based experimental measurements of the backscattering coefficient  $\sigma^{\circ}$  of bare ground over the 4-8 GHz region indicated a high degree of sensitivity to soil moisture variations. Similar measurements conducted for vegetation-covered surfaces show that  $\sigma^{\circ}$  responds to soil moisture variations at angles near nadir provided the vegetation cover is in the form of row crops (with adequate spacing between rows) or a short canopy. As would be expected, the presence of the vegetation reduces the  $\sigma^{\circ}$  sensitivity to soil moisture and causes it to decrease rapidly with frequency. Increase in the magnitude of the radar return caused by soil moisture variations has also been observed by airborne (refs. 3.3-18, 3.3-19) and spaceborne (refs. 3.3-20, 3.3-21) scatterometers.

Preliminary analysis of the sorghum fields data revealed that the contribution to the radar return by the underlying soil (attenuated by the vegetation) must be much smaller than the contribution by the vegetation as evidenced by the lack of consistent correlation between  $\sigma^{\circ}$  and soil moisture content. Hence, in terms of the experiment objective, the conclusion is that lower frequencies have to be used in order to successfully penetrate the canopy. For a given incidence angle-frequency-polarization combination, the variation of  $\sigma^{\circ}$  over the total number of data

sets acquired (from each of the four fields of sorghum) was observed to be considerably larger than the expected fluctuations due to system measurement accuracy or signal fading. A closer look at the data revealed that these variations are associated with a diurnal pattern. Although diurnal variations of the scattering characteristics of plants in the optical part of the spectrum have been extensively reported in the literature, no such note has been reported at microwave frequencies. The existence of this phenomenon is not surprising since it is well known that plant leaves change their orientation as a function of time of day, but the magnitude of this diurnal variation as a function of the scatterometer parameters is significant for vegetation remote sensing applications.

The scattering coefficient data reported here was acquired by the University of Kansas MAS 2-8 system which consists of a FM-CW scatterometer on a truck-mounted boom. The following observations were made:

- a. Off-nadir,  $\sigma^\circ$  of all fields exhibits a diurnal pattern having a peak close to dawn and a minimum around 6 p.m.
- b. The magnitude of this variation is most pronounced at the lowest frequency with HH polarization.

The effect of the diurnal variation on the angular and frequency responses of  $\sigma^\circ$  will be discussed next by comparing data sets acquired close to dawn with data sets acquired during the day for each of the four fields. The day data set chosen was the one acquired closest in time to the early morning data set of the same field. This choice provided a minimization of any variations due to plant height or soil moisture changes.

The angular response curves of the scattering coefficient  $\sigma^\circ$  of data sets taken at 6 a.m. and (6 p.m.) are compared at three

different frequencies for both, HH and VV, polarizations. The general shape of the angular response indicates that as the frequency is increased, the vegetation appears electromagnetically rougher. Also the difference in the magnitude of  $\sigma^0$  between the two cases shown decreases significantly between 2.75 GHz and 7.25 GHz; whereas, the difference at  $30^\circ$ , for example, is about 5.5 dB at 2.75 GHz, and the corresponding difference at 7.25 GHz is less than 0.5 dB. From the data, diurnal variation is most apparent at the lower end of the frequency band (S and L).

The significance of the experimental results reported here depends on the intended application. In terms of soil moisture mapping, the recommendation is to operate at frequencies lower than 2.75 GHz in order to better penetrate through the vegetation cover. While conducting such experiments, special attention should be given to the diurnal variation of the vegetation return to avoid erroneous results. Since the diurnal variation effect appears to decrease with frequency, the recommendation for vegetation mapping investigations using scatterometer remote sensing is to operate at frequencies about 8 GHz.

### 3.3.2 MEASUREMENT REQUIREMENTS OF FUTURE SCATTEROMETERS

The design and final operating characteristics of a scatterometer depend upon its ultimate use. The principal recognized use of scatterometers to date is measuring surface winds over the ocean and ocean waves. The scatterometer has become recognized as the remote sensing tool to do this (refs. 3.3-1, 3.3-2). Technology and data regarding other areas of usage for the scatterometer are not as well developed as is that for the scatterometer as a remote oceanic sensing tool.

The orbiting of an active microwave sensor aboard a satellite has the potential for revolutionizing the methods by which global

ocean wind and wave information are obtained and for improving the quality of presently obtained information. For both meteorologists and oceanographers, this could represent a large increase in the amount of global ocean wind and wave information to become available on a regular basis for both short- and long-range weather and wave prediction. The knowledge of sea-surface conditions in the Southern hemisphere would increase because little information is presently available from the Southern hemisphere oceans by conventional means. Large-scale air/sea interactions between the northern and southern hemispheres could be monitored and studied. Predictions of upper-air meteorological parameters would improve as a result of more reliable lower boundary (surface) input parameters. The total impact of an active microwave system orbiting the Earth cannot now be determined; however, the process of monitoring and forecasting the marine environment could be revolutionized by having such a system in orbit.

To provide the most meaningful information about global-scale ocean winds and waves, certain minimum specifications are required for parametric values (table 3.3-2).

Information on global sea-surface conditions has many applications. Accurate sea-surface conditions are important to commercial fishing, both near shore and in the open ocean; naval operations; optimum-time ship routing; search-and-rescue operations; deep-sea and near-shore drilling operations; long-range weather prediction; hurricane detection, tracking, and prediction; near-shore recreational activities; and further scientific research. Within these major categories are numerous smaller categories. Essentially, a satellite system providing global wind and wave information on an operational basis will be immediately cost effective. Such a global ocean system has long been awaited by meteorologists and oceanographers.

TABLE 3.3-2.— SENSOR MEASUREMENT REQUIREMENTS FOR REMOTE SENSING OF SURFACE WINDS AND WAVES (ref. 3.3-2)

Deep Water (global)	
Surface Winds:	
Velocity, m/sec	2 to 50 ( $\pm 2$ or 10 percent)
Direction, deg.	0 to 360 ( $\pm 20$ )
Field-of-view, km.	20 by 20
Sample intervals, km.	250
Waves	
Length, m	50 to 500 ( $\pm 25$ )
Direction, deg.	0 to 360 ( $\pm 10$ )
Height, m	0.5 to 30 ( $\pm 0.5$ or 10 percent)
Field-of-view, km.	20 by 20
Sample intervals	250
Shallow water (local)	
Surface winds:	
Velocity, m/sec	2 to 50 ( $\pm 2$ or 10 percent)
Direction, deg.	0 to 360 ( $\pm 5$ )
Field-of-view, km.	3 by 3
Sample intervals, km.	50
Waves	
Length, m.	50 to 500 ( $\pm 25$ )
Direction, deg.	0 to 360 ( $\pm 5$ )
Height, m.	0.5 to 30 ( $\pm 0.5$ or 10 percent)
Field-of-view, km.	3 by 3
Sample intervals, km.	50

The design of a particular scatterometer for oceanic measurements is dependent upon the type of measurement requirements given in table 3.3-2. A brief but basic design procedure will be given in this section, followed by the design goal criteria for one specific application, Seasat-A.

The radar scatterometer is a special-purpose instrument that measures the relative value of the radar-backscatter coefficient at a range of angles. Because no spatial resolution is required other than the area illuminated by the antenna, this system is less complex than other systems that require a high degree of spatial resolution. The data rate generated by a scatterometer is also much lower than imaging systems because the coarse resolution does not require close spatial sampling of the surface. Measurements of the relative radar-backscatter coefficient of the surface at various angles, polarizations, and wavelengths are used to infer characteristics regarding the surface (such as wind velocity and direction for the ocean and surface roughness for the land).

The scatterometer measures the microwave backscatter cross section of a surface for various angles of incidence. During flight over an area of interest, radar backscatter as a function of incident angle is generated from which some physical attributes of the surface can be inferred. These measurements may be taken at different polarizations or wavelengths to enhance interpretation of the surface characteristics. These measurements are taken by illuminating the surface with microwave energy and measuring the portion of this energy that is reflected back to the transmitting/receiving antenna. The output of the scatterometer system is a set of data points corresponding to radar backscatter as a function of angle for each data cell on the surface.

System noise is a primary source of error in the measurement of radar backscatter. Radar scatterometers have been built that measure a minimum backscatter coefficient of  $-30$  dB. However, this does not in any way mean that microwave scatterometers capable of measuring smaller backscatter cannot be built. Most observed phenomena have backscatter coefficients exceeding this value. Because of the simplicity of the radar scatterometer, its weight, excluding the antenna system, may be in the tens of kilograms and power consumption is in tens of watts. Thus, the scatterometer is suitable for spacecraft use from the standpoint of its vehicular requirements.

The scatterometer consists of (1) a microwave transmitter, (2) an antenna, (3) a microwave receiver, and (4) a data integrator. Variation of these four basic components results in the two basic scatterometer types: the beamwidth-limited scatterometer and the pulse-width-limited scatterometer.

The beamwidth-limited scatterometer consists of a long-pulse-width transmitter, a pencil-beam antenna, a microwave receiver and downconverter, and a detector with an integrator. The transmitter pulse is sufficiently long to simultaneously illuminate the area of the antenna footprint. The return energy from the illuminated area is down-converted, amplified, narrow-bandpass-filtered, then square-law-detected and integrated.

Because all of the energy entering the antenna illuminates the surface, the sensitivity of backscatter coefficient varies as the square of the range to the surface. To obtain a backscatter function from which to infer surface characteristics, the pencil-beam antenna will be scanned in elevation while measurements are taken. In addition, the antenna may radiate and receive energy at different polarizations as an aid in inferring surface characteristics.

Beam limited (long-pulse) scatterometers have been used to measure the scattering signatures of rough surfaces such as terrain or the ocean. The quantity of interest is the normalized radar cross section  $\sigma^\circ$ , which is the backscattered power per unit area normalized for antenna gain, range loss, and the transmitted power. In the beam-limited mode, the return in a given range cell comes simultaneously from many scatterers over the entire antenna footprint; therefore, the radar return can be interpreted by using the methods of statistical analysis. To assure antenna-beam-filled conditions, the pulse length  $\tau$  must satisfy the criterion :

$$\tau > \frac{2H\beta}{c \cos(\theta_i)}$$

where  $H$  is altitude,  $\beta$  is antenna half-power beamwidth (total angle),  $c$  is speed of light, and  $\theta_i$  is surface angle of incidence.

Pencil antenna beam scatterometer. - A simplified block diagram of a microwave scatterometer that uses a narrow-beam antenna is given in Figure 3.3-8. This type of instrument typically operates in a long-pulse or ICW mode (i.e., the receiver is cut off only during the pulse transmission period). The received pulses are shifted in center frequency by the Doppler effect of target and instrument platform motion and have a continuous power spectrum over a finite bandwidth because of the Doppler frequency spread across the antenna footprint. The received signals are down-converted, amplified, narrow-bandpass-filtered, square-law-detected, and integrated.

The normalized radar cross section of the surface can be found from the conventional radar range equation

$$\sigma^\circ = \frac{P_r (4\pi)^3 R_s^4}{P_t G^2 \lambda^2 A}$$

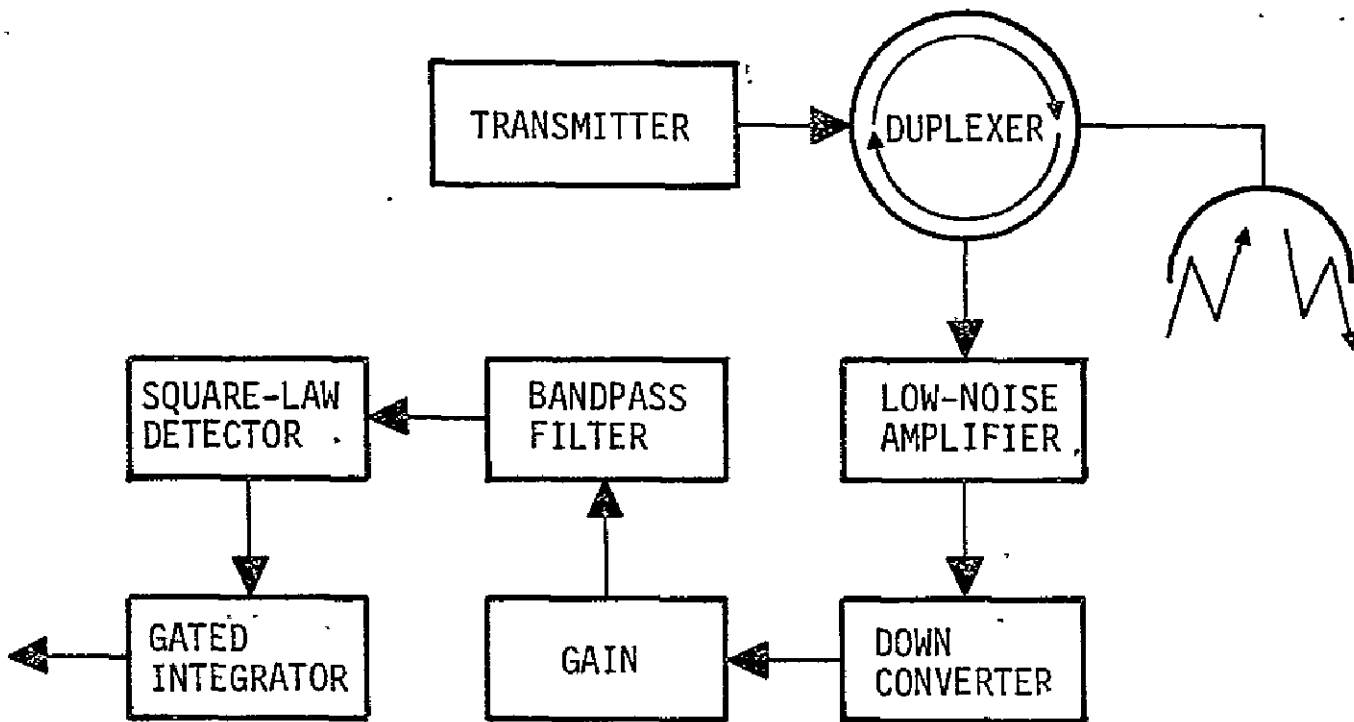


Figure 3.3-8. — Simplified block diagram of a microwave scatterometer that uses a narrow-beam antenna (ref. 3.3-2).

where  $P_r$  is power in return pulse,  $P_t$  is power in transmitted pulse,  $R_s$  is slant range to illuminated area,  $\lambda$  is free space wavelength,  $A$  is effective illuminated area (antenna footprint), and  $G$  is antenna gain. For the case of a beam-limited scatterometer at satellite altitudes (where curved Earth effects are important), the normalized radar cross section is

$$\sigma^{\circ} = \frac{P_r (A\pi)^2 H^2 L_{atm}^2 \cos^2 \theta_i}{P_t G \lambda^2 (1-K)^2 \cos^2 \phi \eta}$$

where  $H$  is satellite altitude,  $L_{atm}$  is one-way atmospheric power loss factor,  $\theta_i$  is Earth incident angle,  $k$  is  $H (\tan^2 \phi) / 2R_E$ ,  $R_E$  is Earth radius,  $\phi$  is nadir angle, and  $\eta$  is antenna efficiency =  $(G\beta^2) / (A\pi)$ . Because of the antenna-beam-filled conditions, the antenna gain appears as the first power, and the altitude (range) is squared; whereas, in the generalized radar range equation, the gain is squared, and range is to the fourth power.

Unfortunately, the output voltage from the square-law detector is corrupted by rectified received antenna noise. A gated ideal integrator is used to average the detector output for several return pulses, yielding a measurement of signal plus noise. This measurement is followed by an integration of noise alone (square-law detector output in the absence of return pulses). The subtraction of these measurements yields an estimate of the received power.

The form of the radar equation appropriate to the design of a scatterometer is

$$(S/N)_{in} = \frac{P_t G \lambda^2 \sigma^{\circ} \cos^2 \phi \eta}{(4\pi)^2 H^2 \cos^2 \theta_i L_{atm}^2 L_s^2 K T_s B_{lf}}$$

where  $(S/N)_{in}$  is input signal-to-noise ratio,  $L_s$  is predetection intermediate frequency bandwidth. The precision of the scatterometer measurement is

$$\frac{\Delta\sigma^\circ}{\sigma^\circ} \approx \left[ \frac{1}{B_{if}\tau_{s+n}} \left( 1 + \frac{1}{(S/N)_{in}} \right)^2 + \frac{1}{B_{if}\tau_n} \left( \frac{1}{(S/N)_{in}} \right)^2 \right]^{1/2}$$

where  $\Delta\sigma^\circ/\sigma^\circ$  is normalized standard deviation in measuring  $\sigma^\circ$ ,  $\tau_{s+n}$  is total integration time of noise-contaminated signal, and  $\tau_n$  is total integration time for noise alone.

Figure 3.3-9 is a plot of  $\Delta\sigma^\circ/\sigma^\circ$  as a function of  $(S/N)_{in}$  for various integration times, where  $\tau_{s+n}$  is assumed equal to  $\tau_n$ . The intermediate frequency bandwidth  $B_{if}$  is 11 kHz and is assumed to be approximately the Doppler spread and equal for the "signal-plus-noise" and "noise-alone" measurements. A sufficient integration yields good measurement standard deviations for negative  $(S/N)_{in}$ .

For applications in which large ground coverage is required, the maximum allowable measurement (integration) time is based on the antenna slew rate and the allowable smear (caused by platform motion) of the antenna footprint.

The pulse-width-limited scatterometer differs from the beamwidth-limited scatterometer in that a shorter pulse is transmitted to the surface by a fan-shaped antenna beam. The return echo is then time-gated to obtain elevation angle resolution. The received energy processing is the same as that for the beamwidth-limited scatterometer, except that a number of channels are required for the measurements. Each of these channels is time-gated for a slightly different delay from the transmitted pulse, and, consequently, each of these channels processes energy corresponding to a different range of elevation angles from the

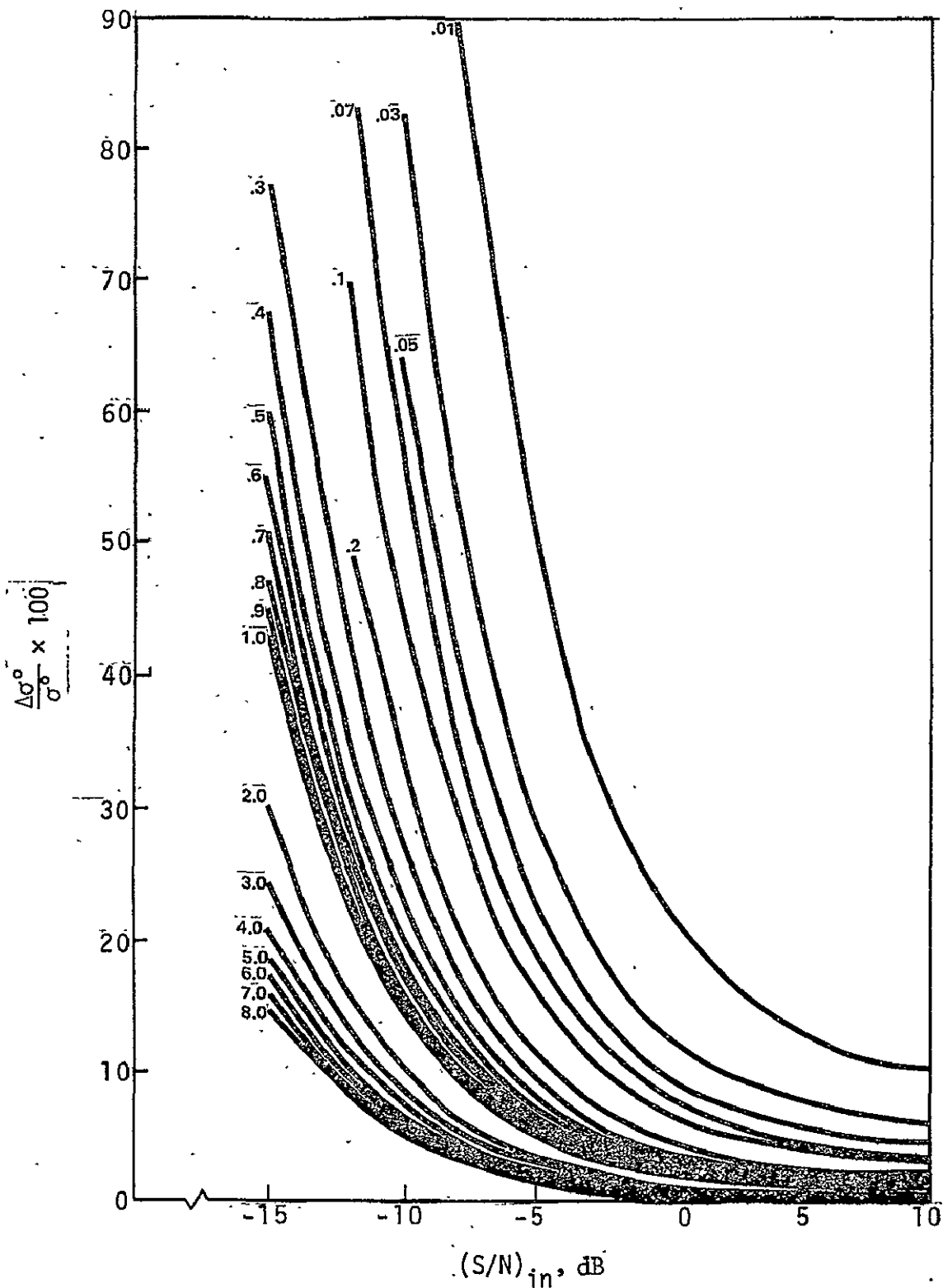


Figure 3.3-9.— Plot of  $\Delta\sigma^\circ/\sigma^\circ$  as a function of  $(S/N)_{in}$  for integration times indicated;  $\tau_{S-N}$  is assumed equal to  $\tau_n$ ; the intermediate frequency bandwidth  $B_{if}$  equals 11 kHz and is assumed to be approximately the Doppler spread (ref. 3.3-6).

spacecraft. Scanning of the antenna angle in elevation is not needed to generate a backscatter function. As with the beamwidth-limited scatterometer, different polarizations can be used as an aid to data interpretation. The operation of a fan-beam antenna microwave scatterometer is equivalent to several simultaneous pencil-beam systems. The effective multiple pencil-beam operation is achieved by filtering the Doppler-shifted radar return to subdivide the broad beam into an arbitrary number of resolution cells. A simplified block diagram is shown in figure 3.3-10. The system is beam limited in each Doppler cell, although it may not be beam limited simultaneously over the entire fan beam.

Because of differences in slant range across the antenna footprint, separate range gates are required for each channel.

The parameter to be measured by the scatterometer is  $\sigma^0$ . Although the  $\sigma^0$  sensitivity to wind speed variation is about the same for upwind, downwind, or crosswind conditions, the magnitude of  $\sigma^0$  for crosswind is less; hence, the crosswind design used is a worst case design. In addition, since the instrument design is controlled by the expected  $\sigma^0$  levels for low wind speeds, its performance as a wind sensor will generally exceed requirements for moderate and high wind speeds.

The scatterometer's ability to measure wind speed does not cut off sharply at low wind values but simply becomes less accurate. This is in keeping with user requirements since interest in wind speed begins to wane in the 3 to 5 m/sec zone; the scatterometer is specified to measure wind speeds at least as accurate as  $\pm 2$  m/sec down to 4 m/sec with decreased accuracy below that.

From figure 3.3-1 (ref. 3.3-3), it can be seen that very accurate backscatter measurements are required in order to detect small

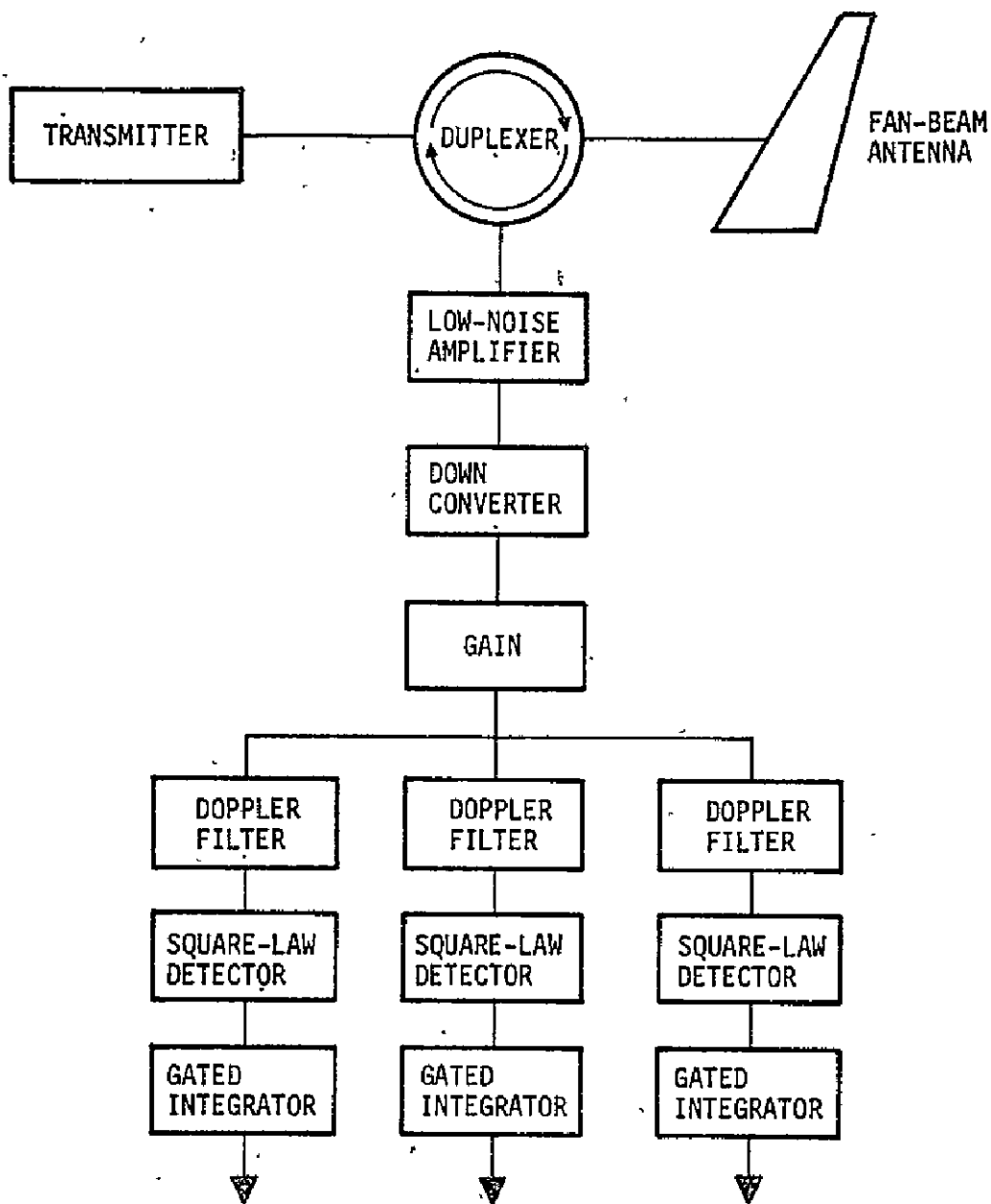


Figure 3.3-10.— Simplified block diagram of a fan-beam microwave scatterometer (ref. 3.3-2).

changes in wind speed for high wind speeds, whereas for low wind speeds, less accurate backscatter measurements are needed to detect large changes in wind speed.

In the design of a scatterometer, the first selection to be made is frequency. With respect to oceanic measurements, frequency selection for the scatterometer has two conflicting directives. To minimize weather effects, X-band frequencies are best while the higher Ku-band frequencies are preferred for maximum sensitivity to local wind speed. Skylab data taken at 13.9 GHz shows favorable wind speed sensitivity which compares well with aircraft data also taken at 13.9 GHz, (ref. 3.3-2). Less wind speed sensitivity is generally shown by NRL data taken at 8.9 GHz. In addition to frequency selection, potential RFI from other on-board microwave sources must be kept in mind.

For narrow pencil beam antennas, the following constraints must be established in order to determine the desired antenna gain and antenna half power points: satellites or aircraft altitude, antenna footprint or cell size, scan rate, range of incidence angles to be sampled, polarization, frequency, and size and weight considerations.

To establish a particular fan beam scatterometer instrument design, certain parameters and constraints must be established. The parameters that are fixed include satellite altitude, resolution ( $H$ ), spacing between successive scans of the same antenna beam ( $S_s$ ), number of antennas and polarizations to be sampled per scan, approximate range of incidence angles ( $\theta_i$ ) to be sampled, transmitter frequency ( $F$ ), antenna half power beamwidths ( $\beta, \phi$ ), minimum and maximum  $\sigma^\circ$  to be measured, and the maximum error allowable on the radar scattering coefficient ( $\sigma^\circ$ ) measurement. In addition, the center of each resolution cell of the

aft antenna must overlap the data from the center of the corresponding resolution cell of the forward antenna if both forward and aft viewing is done. Using these parameters, the remaining parameters which establish the resolution data cell geometry and the instrument characteristics can be determined.

Once the antenna beamwidth is established, the choice of Doppler offset frequency of the IF and the corresponding bandwidths must be determined. For the fan beam antenna, these IF frequencies along with the data sample period ( $T_p$ ) establish the resolution of the Doppler cells on the surface of the Earth. For the pencil beam antenna system, different Doppler filters are selected according to the different viewing areas, and the strongest Doppler filter output signal is selected. The other Doppler filter output represent unwanted noise or sidelobe return. Doppler cell separation and Doppler cell base length in the case of the fan beam antenna determine the remaining geometric parameters. Doppler frequencies and Doppler cell bandwidths for each resolution data cell can be determined (ref. 3.3-2).

Two different timing sequences must be accounted for. They are: the measurement to measurement timing and the transmit/receive/processing timing during each measurement.

Measurement to measurement timing for the pencil beam system is determined by the radar signal path travel time and number of pulses to be integrated. For the fan beam system, the timing is determined by the beam scan spacing ( $S_s$ ) and the vehicle ground speed ( $V_g$ ), i.e., ( $S_s/V_g$ ), (ref. 3.3-2).

The following are the parameters of intrameasurement timing which must be determined for each Doppler cell in the fan beam pattern.

1. Transmit pulse length,  $T_p$
2. Range gate "ON" time

3. Range gate "OFF" time
4. Noise gate "ON" time
5. Noise gate "OFF" time
6. Time between successive transmit pulses, T.

The range gates are the periods when the signal plus noise from a particular Doppler cell is filtered, square law detected, and integrated. The range gate time for each Doppler cell is adjusted to match the two-way propagation time for each Doppler cell. The noise gate is the period for filtering, detecting, and integrating the mean noise level component with no signal present. The mean noise level is subtracted from the signal plus noise level measurement. This could be done by using a bi-polar integrator whose polarity is reversed during the noise integration period or by storing the noise level measurement for subtraction at a later time. To maximize the integration time, the transmit pulse length,  $\tau_p$ , should be picked as long as possible. However, the sum of  $\tau_p$  plus the transmit fall time, plus the i.f., relaxation time must be less than the two-way propagation time of the nearest point of the closest Doppler cell.

Once  $\tau_p$  has been chosen, the range gate on and off times can be determined. The range gate on time is determined by the two-way range to the nearest point of a particular Doppler cell. The range gate off time is determined by the sum of the two-way propagation time to the farthest point of that same Doppler cell and the transmit pulse length  $\tau_p$ . The noise gate period is chosen to minimize the required signal-to-noise ratio needed to obtain a specified measurement accuracy. The noise on-and-off gate times are chosen to occur after all signal from a particular Doppler cell has been received.

The time,  $T$ , between successive transmit pulses is determined by the transmit pulse length, the two-way range to the farthest point of the outer Doppler cell, the length of the noise integration period, and an additional small period of time to allow for data readout and pulse rise and fall times. The transmit pulses are repeated every  $T$  seconds throughout the measurement period,  $t_p$ . The total effective integration period,  $\tau_{SN}$ , is equal to the duty factor  $(\frac{\gamma_P}{T})$  times the measurement period,  $t_p$ .

The minimum resolution of a measurement for a fan beam system is generally the standard deviation of  $\sigma^\circ$  of the measurement (ref. 3.3-2).

To account for relative motion of the Earth (tangential motion of the Earth at the equator is 0.465 km/s) with respect to an orbiting vehicle, a vehicle can be rotated ( $\pm$ ) about the yaw axis.

In concluding this section, the design criteria and the particular system selected depend upon the object whose backscattering cross section is to be measured.

### 3.3.3 TENTATIVELY ESTABLISHED SCATTEROMETER DESIGN GOALS FOR ONE PARTICULAR APPLICATION

A scatterometer is scheduled to operate aboard the Seasat-A satellite. Two principal modes of operation are planned for this fan-beam type scatterometer. In the first mode, the antenna pattern is to view two parallel swaths on either side of the subsatellite track but separated by 400 km. In the second mode, the area along the subsatellite track is viewed (ref. 3.3-2). For more details see figure 3.3-11. The basic operating specifications are given in table 3.3-3 (ref. 3.3-2).

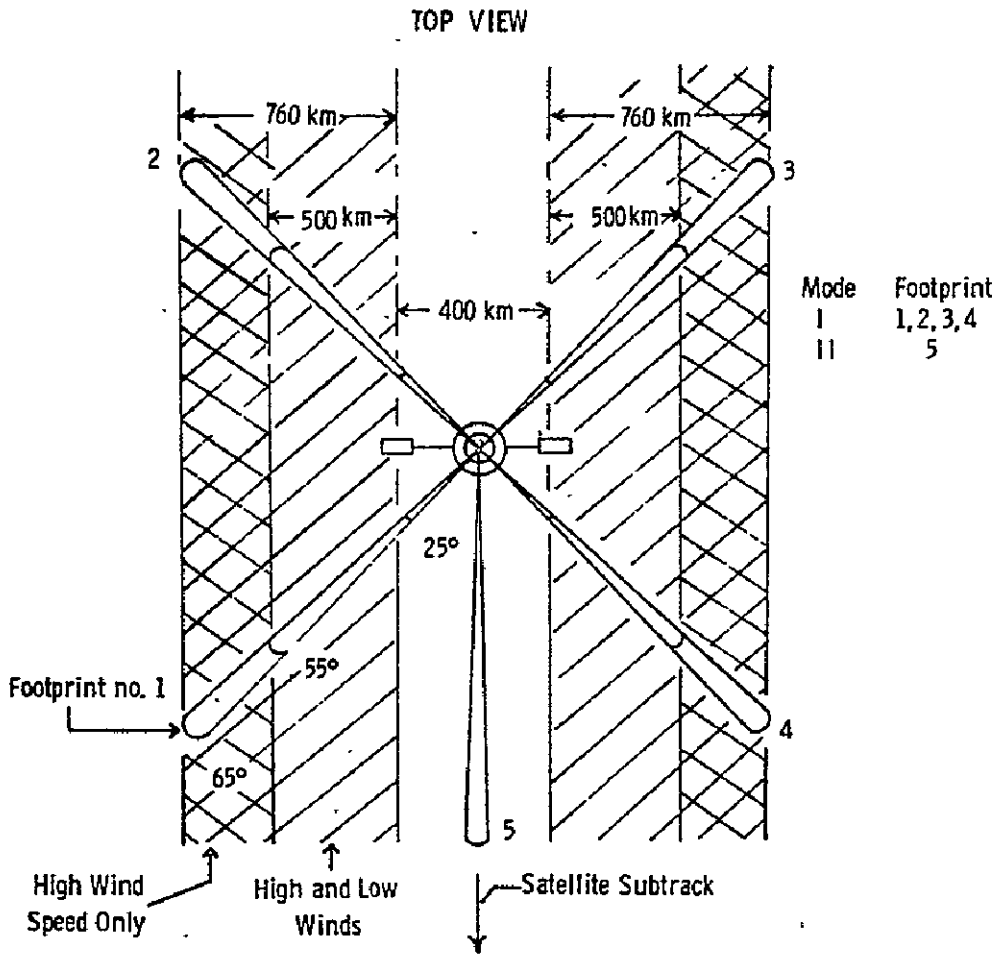
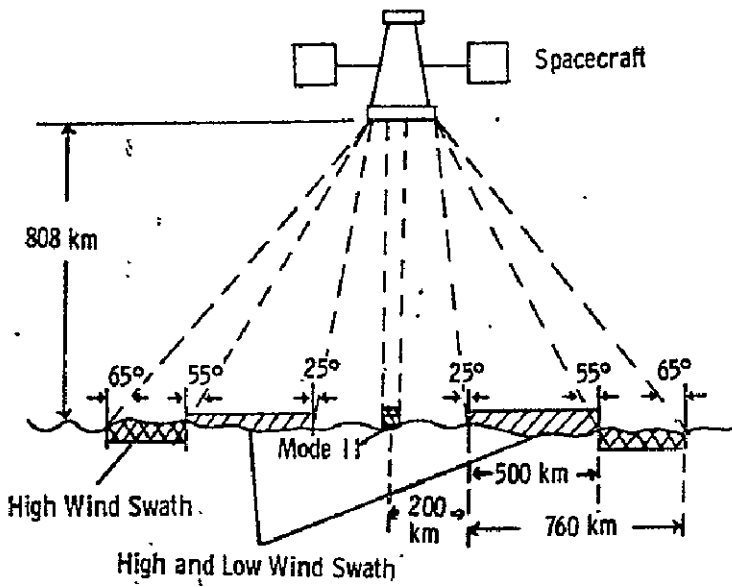


Figure 3.3-11.— Scatterometer fan beam geometry for SEASAT-A.

TABLE 3.3-3.-- SCATTEROMETER PARAMETERS AND CONSTANTS  
FOR SEASAT-A (ref. 3.3-2)

$\sigma^\circ = -10.6$  dB for  $\theta_i = 25^\circ$ , and  $-25.5$  dB for  $\theta_i = 55^\circ$

Altitude = 808 km

Measurement accuracy,  $\sigma_m^\circ/\sigma^\circ = .5$ , where  $\sigma_m^\circ$  is the backscatter deviation for a given measurement.

Transmit pulse width,  $\tau_p = 5.5$  msec.

Pulse repetition period,  $T = 26.7$  msec.

Integration period for signal plus noise,  $\tau_{SN} = 195$  msec. for 50 km spacing and 389 msec for 100 km spacing

Integration period for noise only,  $\tau_N = 2\tau_{SN}$

Transmitted frequency,  $F_o = 13.9$  GHz ( $\lambda = 2.157 \times 10^{-5}$  km)

Antenna efficiency,  $\epsilon = .5$

Antenna beamwidth,  $\beta = 25^\circ$

Antenna beamwidth,  $\phi = .35^\circ, .5^\circ$  and  $1.0^\circ$

#### 3.3.4 SUMMARY

The usage of scatterometers as a remote sensing tool is gaining increased importance as more and more experimental results become available. The basic trend of the experimental results for the four basic application areas (sea state, ice, vegetation, soil moisture) is given in section 3.1. These results show definite advances in the science of scatterometry. As more experimental results for particular applications become available, the design criteria for future scatterometers will be better specified. In short, by being able to better understand the object to be viewed by a scatterometer in terms of its back-scattering characteristics, a more optimum scatterometer design can be employed. The design steps, described in section 3.2, (ref. 3.3-2), can be used as a guideline for designing new scatterometer sensors. This includes both space oriented and aircraft based sensors. Section 3.3 gives design goals for a satellite based sensor to be used to measure sea state.

## REFERENCES

- 3.3-1. Veziroglu, T. Nejat: "Remote Sensing, Energy-Related-Studies", Hemisphere Publishing Corporation, 1975.
- 3.3-2. Grantham, W. L.; Bracalente, E. M.; Jones, W. L.; Schrader, J. H.; Schoreder, L. C.; Mitchell, J. L.: "An Operational Satellite Scatterometer for Wind Vector Measurements Over the Ocean," NASA Technical Memorandum 72672, 1975.
- 3.3-3. Krishen, K.: "Remote Sensing of Oceans Using Microwave Sensors," LEC-4522, November 1974.
- 3.3-4. Kaufman D. E.: "RF Link Equation for the Skylab S-193 Radiometer/Scatterometer," LEC-4119, 1974.
- 3.3-5. Barrick, D. E.: "Radar Cross Section Handbook," Plenum Press, New York, 1970.
- 3.3-6. Matthews, R. E., et al.: "Active Microwave Workshop Report," NASA SP-376, 1975.
- 3.3-7. Rouse, John W., Jr.: "Arctic Ice Type Identification by Radar." Proc. IEEE, vol. 57, no. 4, April 1969, pp. 605-611.
- 3.3-8. King, C.: "Agricultural Terrain Scatterometer Observations with Emphasis on Soil Moisture Variations." CRES Technical Report 177-44, 1973.
- 3.3-9. Batlivala, P. P.; Ulaby, F. T.: "Effects of Roughness on the Radar Response to Soil Moisture of Bare Ground." CRES Technical Report 264-5.
- 3.3-10. Ulaby, F. T.: "Radar Response to Vegetation." CRES Technical Report 177-42, 1973.
- 3.3-11. Ulaby, F. T.; More, R. K.: "Radar Spectral Measurements of Vegetation." CRES Technical Report 177-40, 1973.
- 3.3-12. Bush, T. F.; Ulaby, F. T.: "Radar Return from a Continuous Vegetation Canopy." Remote Sensing Laboratory Technical Report 177-56, University of Kansas for Research, Inc., August 1975.
- 3.3-13. Bush, T. F.; and Ulaby, F. T.: "8-18 GHz Radar Spectrometer," RSL Technical Report 177-43, University of Kansas Center for Research, Inc., Lawrence, Kansas, September 1973.

- 3.3-14. Carlson, N. L.: "Dielectric Constant of Vegetation at 8.5 GHz," Ohio State University, Electro Science Lab., Technical Report 1903-5, 1967.
- 3.3-15. Batlivala, P. P.; Ulaby, F. T.: "The Effect of Look Direction on the Radar Return from a Row Crop." Remote Sensing Laboratory Technical Report 264-3, University of Kansas Center for Research, Inc., Lawrence, Kansas, May 1975.
- 3.3-16. Oberg, J. M.; Ulaby, F. T.: "MAS2-8 Radar and Digital Control Unit," RSL Technical Report 177-37, University of Kansas Center for Research, Inc., Lawrence Kansas, October 1974.
- 3.3-17. Ulaby, F. T.; Batlivala, P. P.: "Measurements of Radar Backscatter from a Hybrid of Sorghum," Remote Sensing Laboratory Technical Report 264-2.
- 3.3-18. Dickey, F. M.; King, C.; Holtzman, J. C.; Moore, R. K.: "Moisture Dependency of Radar Backscatter from Irrigated and Non-Irrigated Fields at 400 MHz and 13.3 GHz," IEEE Transactions on Geoscience Electronics, vol. GE-12, no. 1, 1974, pp. 19-22.
- 3.3-19. Ulaby, F. T.; Moore, R. K.; "Radar Sensing of Soil Moisture," Proceedings 1973 International IEEE-GAP & USNC/URSI Meeting, Boulder, Colorado, August 1973.
- 3.3-20. Eagleman, J.; Ulaby, F. T.: "Radiometer-Scatterometer Soil Moisture Detection," Proceedings of the American Astronomical Society Meeting, Los Angeles, California, August 1974.
- 3.3-21. Ulaby, F. T.: "Soil Moisture Detection by Skylab's Microwave Sensors," Proceedings of the URSI Specialist Meeting, Bern, Switzerland, September 1974.
- 3.3-22. Ulaby, F. T.; Bush, T. F.: On the Feasibility of Monitoring Croplands with Radar. To be presented at the Michigan Symposium, January 22, 1976.

### 3.4 SYNTHETIC APERTURE RADAR (SAR)

Synthetic Aperture Radar (SAR) has been used in earth resources investigations since 1971 when Litton's Aero Service flew the Goodyear APQ-102 X-band Side-Looking Airborne Radar (SLAR) (Ref. 3.4-1). At this time, however, no satellite versions of this type radar have been used in an earth resources effort.\*

At least three satellite or orbital altitude SAR systems are presently under study. After final definition and development, these systems will be aboard the (1) Seasat-A which is due to be launched in 1978, (2) the Shuttle Imaging Radar (SIR) to be flown on the Space Shuttle in 1982, and (3) SARSAT, a European entry, due to be launched in 1981. The SARSAT is the least defined system at this time (ref. 3.4-3) because not enough information is available to determine its system characteristics or earth resources applications.

#### 3.4.1 SEASAT-A SAR

The Seasat-A satellite to be launched early 1978 will represent a significant step forward in the study and monitoring of the oceans. Surface wind, water temperature, and sea state data among other data will be obtainable regularly on a global scope. The 36-hour coverage to be provided by the first satellite in this series will be reduced as other satellites are added, forming a Seasat network, e.g., six satellites would reduce the coverage interval to 6 hours (ref. 3.4-4).

The Seasat-A will have five sensors: three active and one passive microwave, and a passive visible-IR radiometer. See the table on Seasat-A in appendix A for details on each of

---

\*A side-looking radar was utilized on the Apollo 17 lunar mission to map parts of the moon (see ref. 3.4-2).

these sensor systems. The Seasat-A SAR, one of the active microwave sensors, will be the first such sensor to be operated from earth orbit. (See table 3.4-1.) It will operate at 1.275 GHz (L-band, wavelength = 23.5 cm) and provide a resolution of 25 m. Its field-of-view (FOV) will range 17° to 23° from nadir to the right of ground track providing a 100 km wide swath. Data takes will normally be 10 minutes long, corresponding to 4000 km swath lengths. Figure 3.4-1 shows the angular and ground coverage of the Seasat-A SAR and for comparison purposes shows the corresponding coverage of the five band microwave radiometer (SMMR) and the scatterometer (SCAT). The surface coverage of the SAR will be much less than the other sensors because of its much smaller FOV and its extremely high data rate which prevents onboard storage, i.e., its data must be transmitted in real time when it is in range of a limited number of receiving stations.

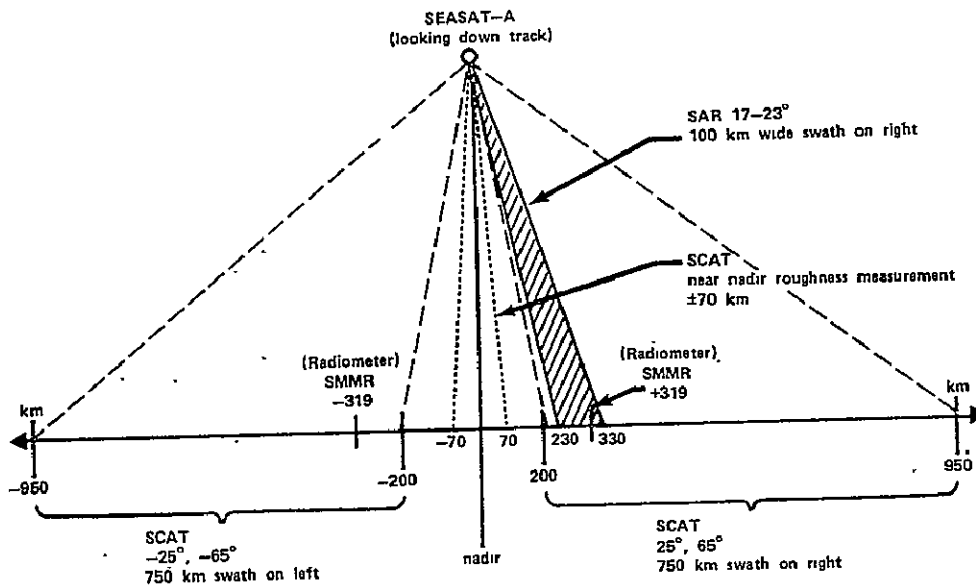


Figure 3.4-1.- Seasat-A sensor coverage.

TABLE 3.4-1. — FUTURE SPACEBORNE EARTH RESOURCES IMAGING RADARS

	Seasat-A SAR	Shuttle Imaging Radar (SIR)	SARSAT
Launch/First Use	May 1978	1982	1981
Altitude	790 km	nominally 185 km	—
Orbit	circular, near polar & non-sunsynchronous		—
Frequency	1.275 GHz	1.3 GHz & 8.33 GHz	X- & L-bands
Polarization	H	HH, HV, VH, VV	HH, HV
Spatial Resolution	25 m	25 m-50 m	50 m
Coverage	100 km (230 km-330 km from nadir; 17°-23°)	100 km (max) -40 km (min)	—
Primary Applications (no order)	oceanography: currents storms sea ice etc.	flood monitoring soil moisture agriculture sea & lake ice geology & mapping	oceanography cartography ice & snow monitoring sea state soil moisture
Other Applications (no order)	oil spill monitoring soil moisture forestry geology	forestry hydrology land use	

3.4-3

According to J. Apel (ref. 3.4-5), the Seasat-A SAR will be primarily used in obtaining and analyzing images of ocean waves. Waves of greater than 50 m near shorelines and in storms can be detected; images of ice, oil spills, current patterns, and similar features will also be monitored. The method utilized in analyzing ocean waves is quite interesting and will consist of computations on the radar data to obtain the wave directional spectrum. This method will allow one to ascertain the relative distribution of wave energy among different wavelengths traveling in various directions. This information along with surface wind velocity will give the fundamental information needed in forecasting wave conditions on the ocean.

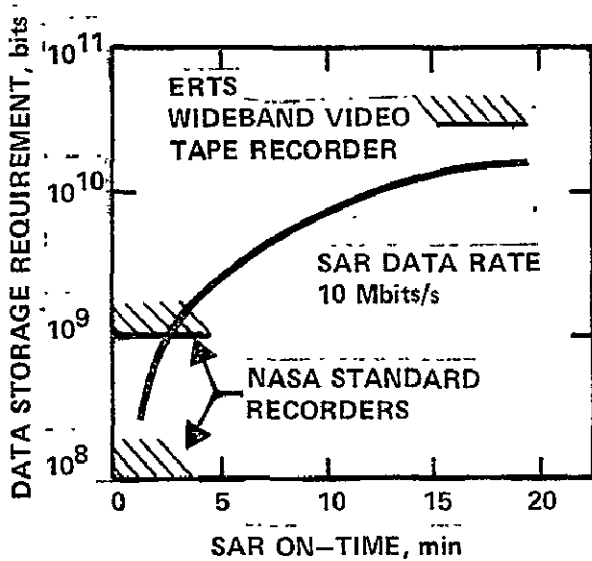
Due to high data rates, the Seasat-A SAR will be used in view of tracking stations and data will be retrieved in real time. U.S. coastal sites will have good coverage, and studies of storm wave patterns near potential offshore nuclear power plant sites, deep water oil ports, harbors, and breakwaters will be accomplished. Navigation aid will be accomplished through ice mapping over the Northwest Passage and the Great Lakes.

The capability of the Seasat-A SAR to meet user requirements is shown in table 3.4-2 (from ref. 3.4-5).

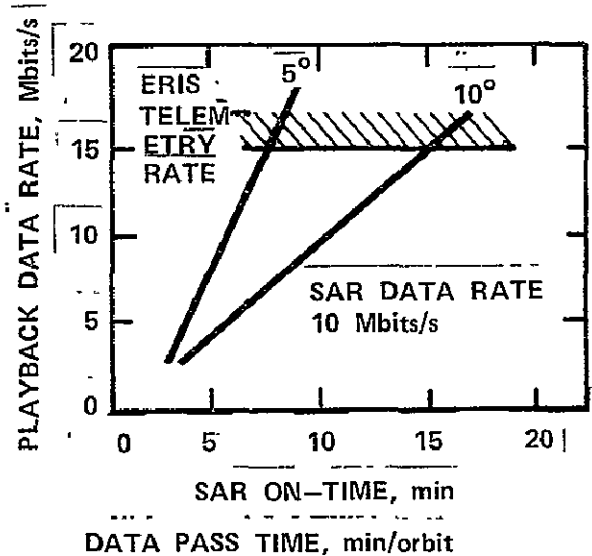
TABLE 3.4-2. - CAPABILITY OF SEASAT-A SAR IN MEETING USER REQUIREMENTS

Physical Parameter	Instruments	Range	Precision	Resolution or IFOV	Total FOV	Comments
Directional Wave Spectrum $S(\lambda, \theta, x, y)$	Imaging radar (2-D transform)	S: unknown $\lambda$ : 50-1000 m O: 0-360°	S: --- $\lambda$ : $\pm 10\%$ O: $\pm 10^\circ$	50-m resolution	20x20 km squares	Global samples at 250-km intervals
Oceanic, Coastal, & Atmospheric Features (Patterns of waves, temp., currents, ice, oil, land clouds, atmospheric water content)	Imaging radar	High resolution	All weather	25 or 100m	100 or 200 km	Sampled direct or stored images

The SAR data rate is estimated at  $\approx 10$  to 20 megabits per second and is incompatible with data storage when the satellite is out of range of receiving stations (ref. 3.4-6). Only three such receiving stations are capable of receiving at this rate according to J. R. Rose and S. Walter McCandless (ref. 3.4-6), and real time reception must be limited to these stations. If ERTS high density recording and storage techniques had been employed, then greater open ocean coverage could have been obtained. However, this capability is outside the desired Seasat-A capabilities. Some of these Seasat data management problems encountered during the study phase are illustrated in figure 3.4-2 (from ref. 3.4-6).



(a) Data storage requirements



(b) Playback data rate.

Figure 3.4-2.— Seasat SAR data management considerations.

The primary emphasis in the selection and design of sensors for Seasat-A has been on oceanographic applications. However, the data from these instruments can be very useful in studying land applications, e.g., geology, soil moisture, etc. The Seasat system, from orbital design to receiving station coverage, can readily be used to provide such data as may be required by land applications investigators. In addition, such efforts could provide valuable experience for those planning to use the Shuttle Imaging Radar (SIR) in the early 1980's (see subsection 3.4.2).

### 3.4.2 SHUTTLE IMAGING RADAR (SIR)

The Shuttle Imaging Radar (SIR) is a SAR system under consideration for tentative use in 1982 on the Space Shuttle. The SIR will have two frequencies, one in the L-band and one in the X-band. The baseline resolution is 25 m  $\times$  25 m, at a design altitude of 200 km. A swath width up to 85 km will be obtainable over a range of 35 km to 365 km from the ground track, covering a 10° to 60° angle range from nadir.

The SIR will be dual polarized with either vertical or horizontal polarization selected for transmission at each frequency. The received signals vertical and horizontal polarization components will be recorded separately, resulting in four signals at any one time as indicated in the basic data flow diagram in figure 3.4-3. As indicated in this figure, the chosen data may be viewed with an onboard display and either recorded on magnetic tape or transmitted to the Ground System at the GSFC. The main purpose of the Ground Processing System (GPS) is to process the raw SAR data from the SIR into digital data types, photographs, and CRT displays useful to investigators.

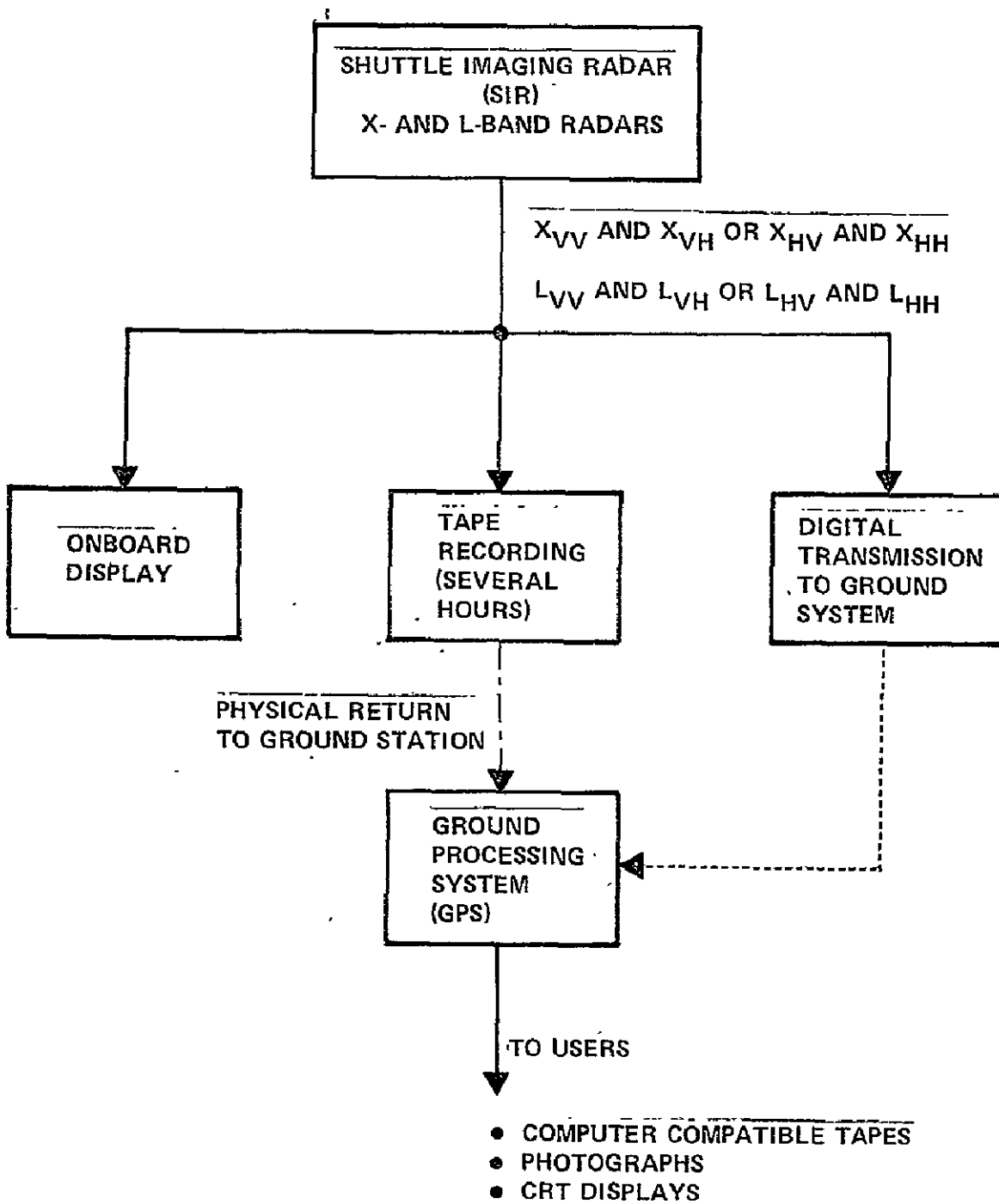


Figure 3.4-3.— Basic data flow diagram for the Shuttle Imaging Radar (SIR).

The processing of the raw SAR data, which is either digitally transmitted or recorded on tape and transported to the ground, will be accomplished with a completely electronic processor. Until recent dramatic results in electronic integrated circuits, such processing was done with relatively simple yet elegant coherent optical processors utilizing lasers and lens systems. The SAR electronic processor made feasible with electronic micro-miniaturization is extremely complex. However it offers the following advantages:

1. Greater flexibility - parameters are more easily selected or changed and a wider range of techniques is available.
2. Digital data compatibility - the digital data is more readily usable by investigators (i.e., compared to the film output from optical processors).

These factors weighed heavily in the choice of digital processing since optical processing offers the following important advantages:

1. Much greater simplicity - resulting in greater reliability.
2. Lower cost.

An optical processor is being considered for use as a backup system should problems develop with the digital processor.

A recent report edited by Simonett (ref. 3.4-7) presents the analyses and conclusions of the Active Microwave Study Group on the Space Program Imaging Radar (SPIR). This report was funded by NASA/JSC and examined the potential applications of spaceborne imaging radar, specifically the SAR to be flown on the Space Shuttle. The general application areas studied were:

- Water resources: soil moisture, flood, snow, watersheds
- Mineral and petroleum exploration
- Vegetation: crops, pastures, forests

- Oceans: waves, sea state, ice packs, oil spills
- Cartography: small scale mapping, mosaicing
- State and regional; e.g., water in California
- Federal; e.g., Department of the Interior

Simonett's report compares the state of imaging radar and other radar sensors today with that of visible and near infrared sensors before Landsat-1. The theoretical basis for the use of microwaves in remote sensing is strong and growing. However, microwave sensors have yet to be tested thoroughly in orbit. With the advent of Seasat-A (1978) and the SIR (approx. 1982) microwave sensors, active and passive, will be undergoing the stages of investigation and techniques development that visible and near infrared sensors have already begun. The Seasat-A SAR will help prepare the way for the use of the Space Shuttle SIR data.

Radar sensors offer unique advantages such as the ability to penetrate clouds, vegetation, and measure soil moisture. Shorter wavelengths (14 GHz to 18 GHz) may be useful in vegetation discrimination and biomass measurements. It is because of complementary advantages such as these that it is expected that the SIR data will be used jointly with and in support of Landsat data. Specifically, the SIR and the Landsat-D Thematic Mapper (TM) (see section 3.2.2.2) will have similar resolutions, making both optical and digital merging of their data all the more attractive. The spatial details (e.g., hills, man-made features, etc.) detected with the SIR when registered with the TM data will aid in the interpretation of the latter. The addition of two radar frequency images to the seven TM bands (visible to thermal infrared) will in some applications enable greater classification accuracies. Furthermore, the all-weather capability of the SIR will provide at least partial application of investigations to

areas frequently clouded over, and, similarly, extension of a study temporally by providing at least partial data in those cases where Landsat-D passes over a site are "clouded out." Another possibility, mentioned in the SPIR report, is that of using joint TM and SIR data to provide for "bridging cloudy areas." For example, crop classification perhaps could be extended in a partly cloudy scene into the cloudy areas using the radar data alone and knowledge of its use in clear areas.

### 3.4.3 SARSAT

The Synthetic Aperture Radar Satellite (SARSAT) is being developed by the European Space Research Organization (ESRO) and will be flown either on a THOR Delta 2910 (ref. 3.4-3) or the Space Shuttle. Some of the intended uses of the satellite will be:

- Polar ice study in the Arctic Sea
- Ice pack monitoring in the Baltic Sea
- Snow limit monitoring in the Alps
- Surface wind measurement and sea state forecast in the Northern Atlantic and in the Northern Sea
- Oil slick detection in the same areas
- Soil moisture study in the Mediterranean areas
- Mapping of geological features
- Global cartography at small scale

An optimal set of technical features, desired in the parametric study of the instrument were as follows:

- Width of ground strip                    50 km - 100 km
- Sensitivity of receiver                1 dB
- Frequencies                                X- and L-bands

- Polarization two simultaneous modes (HH and HV)
- Spatial resolution 50 m × 50 m
- Depression angle of sight to the horizon adjustment within the range 20° - 80°.

The preferred solution of the radar system characteristics frequency was 10 GHz, and several of the features, such as dual polarization and number of wavelengths, were under consideration for change and/or elimination because of the large data rate requirements.

Several onboard storage and processing or preprocessing techniques were also under consideration because of the maximum anticipated data rate of 100 megabits per second, with 4 meter resolution (50 m required). A final configuration had not been "firmed up" at the time of this preliminary study in reference 3.4-3.

## REFERENCES

- 3.4-1 Lyon, R. J. P.: Exploration Applications of Remote Sensing Technology (Image Forming Systems). Mining Congress Journal, June 1972, pp. 20-26.
- 3.4-2 Leberl, F.: Lunar Radargrammetry with ALSE-VHF Imagery. Proceedings of the American Society of Photogrammetry, October 28-31, 1975, Phoenix, Arizona, pp. 266-285.
- 3.4-3 Skenderoff, C.; Guignard, J. P.; Coldrick, J. R.; Mooney, H.; and Noel, J.: A Preliminary Feasibility Study on a Synthetic Aperture Radar (SARSAT) for Earth Resources Surveys. Proceedings of the Ninth International Symposium on Remote Sensing of Environment, April 15-19, 1974, pp. 1517-1540.
- 3.4-4 Elson, B. M.: Seasat Faces Multiple Sensor Challenges. Aviation Week & Space Technology, Dec. 8, 1975.
- 3.4-5 Apel, J. F.: SEASAT: A Spacecraft Views the Marine Environment with Microwave Sensors. Remote Sensing Applied to Energy Related Problems Symposium, Miami, Florida, 1974.
- 3.4-6 Rose, J. R.; McCandless, S. W.: System Definition of Seasat-A, An Ocean Observation Satellite. American Institute of Aeronautics and Astronautics, 13th Aerospace Sciences Meeting, Pasadena, California, January 20-22, 1975.
- 3.4-7 Simonett, D. S.; editor: Applications Review for a Space Program Imaging Radar (SPIR). Univ. of Calif. at Santa Barbara, JSC/NASA Contract NAS 9-14816, July 1976.

## 3.5 MICROWAVE RADIOMETERS

### 3.5.1 INTRODUCTION

Microwave radiometers are one of the more recent additions to the growing list of remote sensing tools used in earth observations work. Consequently, the development of passive microwave sensor technology, the technology itself, and development of applications have not reached the maturity of the older optically based systems. Since the sensors are new and the phenomena they respond to are in a spectral region far removed from that observed by the human eye, microwave radiometers have not been well understood or employed to their full capability as sensors. Section 3.5.2 will be devoted to a brief description of microwave radiometers, the target characterization to which they respond, and some of the advantages and disadvantages of passive microwave sensors.

Research and development of applications is still in progress utilizing ground based passive microwave systems. These systems are performing important basic work in measuring the radiometric characteristics of terrestrial targets and are discussed in section 3.5.3. Finally, in section 3.5.4 recommendations for future sensors and future work will be discussed.

### 3.5.2 INSTRUMENT CHARACTERISTICS, ADVANTAGES, DISADVANTAGES, AND APPLICATIONS

All material objects are capable of absorbing, emitting, reflecting, and scattering electromagnetic energy. The absorption, emission, reflection, and scattering properties of a material object are determined by the dielectric properties of its materials, geometry (size, shape, surface roughness),

orientation, temperature, and the frequency (or wavelength) of radiation under consideration. These electromagnetic properties of objects form the basis of most remote sensing.

To aid in understanding passive microwave remote sensing, some of its characteristics will be compared with human vision. Both are passive sensors responding to direct emission, reflection, and scattering of electromagnetic energy from the objects to be viewed. The human eye responds to a continuous spectrum that is almost one octave wide (approximately .4 micrometers to .7 micrometers). Individual microwave radiometers generally respond to narrow frequency bands selected from wavelengths of about 1 millimeter to about 30 centimeters (about 8 octaves).

While the eye depends on the sun or artificial light, which are relatively high level sources of electromagnetic energy, the microwave radiometer depends on the low temperature microwave emission from deep space, gray body microwave emission in the atmosphere, and the interaction of these radiations with terrestrial targets supplemented by the emission from the target itself.

According to Planck's law, the brightness of a black body is

$$B = \frac{2hf^3}{c^2} \frac{1}{e^{\frac{hf}{kT}} - 1}$$

where

h = Planck's constant

k = Boltzmann's constant

f = frequency in Hertz

c = velocity of light

T = temperature

In the microwave frequency range,  $e^{\frac{hf}{kT}} - 1$  can be approximated by  $\frac{hf}{kT}$ . If one utilizes this simplification, then the brightness,  $B$ , at wavelength,  $\lambda$ , can be approximated by the Rayleigh-Jean formulae.

$$B = \frac{2kT}{\lambda^2}$$

This approximation introduces less than 1 percent error in brightness,  $B$ , provided that  $\lambda T > 0.77$  meters-degrees Kelvin. This approximate equation gives satisfactory results for most targets throughout the microwave region. However, errors will be apparent for cold targets at millimeter wavelengths.

This equation suggests immediately why most microwave radiometric measurements are stated in terms of brightness temperature. The brightness temperature of a target is simply the absolute temperature of a perfect black body emitting the same power as the power which is actually emitted by the real target. The observed brightness temperature at the sensor consists of the power emitted by the object plus the power reflected and scattered by the object as modified by the intervening atmosphere. In addition, corrections must generally be made to the sensor output to correct for hardware imperfections.

Microwave radiometers possess a number of advantages over other sensors:

1. The sensor power and electronics size and weight requirements are lower.
2. Since the sensor is passive, there are no transmit/receive isolation problems.
3. Range dependence is  $1/R^2$  instead of  $1/R^4$ .

4. Microwave radiometers in many frequency ranges can be considered all weather sensors.
5. Microwave radiometers can function without solar illumination.
6. Sensor data rates are generally low.
7. Microwave radiometers appear to have some capability of penetration through vegetation and into soil.

On the other hand microwave radiometers have the following disadvantages:

1. The detected signals are very weak.
2. Antennas with large real apertures are required to obtain acceptable sizes of ground cell resolution.
3. Required observation time per ground cell is longer than for active sensors.
4. Microwave radiometers are subject to in-band interference and strong out-of-band interference.

### 3.5.3 GROUND BASED RADIOMETER SYSTEMS

Two ground based radiometer systems have been used to gather earth resources data. The Aerojet Ground Based Remote Sensing Laboratory constructed and owned by Aerojet Electrosystems of Azusa, California, is presently inactive. This system is mounted on a single truck. It has the capability of recording data but does not provide real-time data reduction. The Microwave Signature Acquisition System is owned by the NASA Johnson Space Center and operated by Texas A&M University. Its real-time data reduction capability is now being upgraded by the Texas A&M University remote sensing center. The system as presently configured requires a "cherry picker" truck to hold the antennas and a data van to carry the data reduction and

recording equipment. At the present time, plans are being made to add a capability at C band (4.99 GHz).

### 3.5.4 FUTURE SENSORS AND FUTURE WORK

#### 3.5.4.1 Background and Current Trends

The tasks posed for remote sensing in the future are very challenging. To meet these challenges a new generation of sensor systems must be developed. While no one can accurately forecast the future, certain trends appear to be developing:

1. Demands for data on a real time basis or short turnaround time are increasing.
2. Demands for repetitive data over the same sites are also increasing.
3. Quality and accuracy requirements are increasing.
4. The community of data users is becoming larger with more and more users who do not have a detailed understanding of remote sensing entering the community.
5. Requirements are for lower costs to achieve comparable results.
6. The larger community of users will require dissemination to more users of a given data set.
7. Data is accumulating rapidly. Soon it will be impossible to store it all, if that point has not already passed.
8. As remote sensing proves itself in one task, requirements for its use in more sophisticated tasks will develop.

In short these trends mean that a requirement is growing for more sophistication and fuller development in sensor systems to make useful results available quickly to persons who do not have a background in remote sensing. Fortunately, trends in

the following technological developments support these objectives:

1. Lower noise and higher power microwave devices are appearing at a rapid pace; the cost of low noise microwave amplification is coming down along with size and weight; and the power output available from solid state sources continues to increase.
2. New generations of microprocessors of greater speed and computational abilities are appearing at a rapid pace at ever decreasing costs for a given capability.
3. The costs, power, and volume requirements of data memory are also coming down; new technologies are being developed which offer the potential of significant breakthroughs in this area.
4. The miniaturization of all types of electronics offers promise of packing more capability into a given size package as more and more functions are being produced on integrated circuit chips.

#### 3.5.4.2 Anticipated Trends

Combining these developing requirements and technological trends, some reasonable predictions about future sensors can be made. Future microwave sensors will become more sophisticated than those presently available. Anticipated trends are as follows:

1. Dual polarization - Both horizontal and vertical polarization are required for many tasks, and simultaneous reception of two polarizations will become more common. Developments in solid-state devices and circuits are cutting size and costs while increasing performance.
2. Multifrequency - In certain tasks, a number of variables must be separated out, making these variables respond

differently to changes in frequency. For example, to measure soil moisture vegetation effects, soil roughness effects and soil type must be separated out. Therefore, new sensors will require more parallel channels of information at different frequencies. For passive sensors, these channels will be chosen, in general, to correspond with the quiet radio astronomy bands.

3. Larger Antennas - Passive microwave sensors in space have been hampered in the past by using only small antennas, resulting in large to very large ground footprints. Antennas in space will become much larger. L-band antennas on the order of 100 feet to 300 feet across will permit data to be gathered by satellite from areas on the ground which are one nautical mile across or less.
4. Imaging - Most applications will require evaluation of parameters over an area on the earth. Therefore, the sensors will be of an imaging type to permit displays of data which are capable of being overlaid on a map.
5. Multi-applications - In order to be more cost effective a single microwave sensor will be used for a number of purposes.
6. Repairability - Experience gained during an attempted repair of the S-193 during Skylab indicates that sensors can be repaired in space. During the Shuttle era, repair of sensors in space will become more cost effective. The options to repair or replace a system in space, or bring it back to earth to repair it and return it to space will influence the design of units for use in space.
7. Scanning Mechanisms - Experience with previous sensors in space including those on Skylab suggest that antenna scanning methods will be simple mechanical scans and electronic scanning.

8. Low Cost Microwave Amplifiers - The construction of reliable gain and phase stable microwave amplifiers at a low cost will open new possibilities and potential performance. Then a number of simultaneous channels can be operated in parallel, making possible the reduction or elimination of scanning mechanisms. By allowing more time to be spent on a given data cell, the precision of measurements will be significantly improved.
9. Absolute accuracy - As more sensors are flown, the need for comparison of data gathered by different microwave sensors will increase significantly. Consequently, more attention will be given to assuring the absolute accuracy of sensors so that data from different sensors will be comparable.
10. On board real-time data processing - Improved ground resolution will result in more data points for a given area covered and higher sensor data rates. As more experience is gained with sensors, confidence in their measurements will increase, decreasing the requirements for maintaining complete raw data and housekeeping data files. Passive microwave sensors operate at relatively low data rates, so the addition of onboard processing to the system appears to be technically feasible even now. Onboard processing will reduce the amount of data to be recorded or preserved and will allow quick analysis. Onboard real-time processing will be a step toward making perishable data available immediately.
11. Combined active-passive microwave sensors - Experience with the S-193 has shown that a combination of active and passive microwave sensors can be more effective than either alone, therefore, more combination active and passive microwave sensors may be expected in the future.
12. Reference Loads - A comparison of the S-193 and S-194 radiometer performance indicates that radiation-cooled

reference loads for radiometers can be used in space instead of, or in addition to, a hot load to improve instrument calibration. Care must be taken to insure sufficient range and accuracy in the temperature sensors employed to monitor the reference loads. Consequently, we can expect that future sensors will use radiation-cooled loads or antennas observing cold sky to improve the absolute accuracy of radiometric temperature measurements.

#### 3.5.4.3 Potential Problems

Experience with past and present remote sensing projects indicates that certain problems as follows may occur which can be minimized by prior planning:

1. Location of field-of-view - Past experience with the S-193 and other sensors indicates that vehicle position and attitude must be known very accurately in order to calculate accurately the instrument's field-of-view on the ground. The requirements for accuracy in vehicle position and attitude will become more stringent as the sensor's field-of-view shrinks.
2. Multiple integration times - If different integration times are used in a radiometer, they may have different effective gains. This makes averaging the calibrations and baselines taken with the different times difficult. The fact that the data processing may not have a "look ahead" capability combined with other factors can make data processing difficult. Consequently, a single radiometer integration time is recommended for future systems.
3. Polarization Purity - In the dual polarized sensors built to date, software correction for cross polarization has been necessary to obtain good quality data. It may not be possible to completely eliminate the need for such correc-

tions. However, if careful attention is paid to keep cross polarization effects to a minimum in the design and construction of the sensor, and if the sensors cross polarization characteristics are carefully measured, errors from cross polarization can be substantially reduced.

4. Data Processing - Experience with the S-193 and other sensors indicates that it is of primary importance to begin consideration of data handling at the time of specifications and instrument design.

Close cooperation between design engineers, scientists, and computer programmers throughout the design, development, construction, and testing of the instrument will minimize the problems and delays encountered after scientific data collection begins. The data processing algorithms should be developed before system testing begins and used in conjunction with raw system test data to finalize the algorithm and evaluate the system's performance.

The nature of microwave sensors, particularly passive sensors, is such that multipass data processing may be necessary to obtain best results. Since noise sources are required to calibrate radiometers, the calibration and baseline data, by its very nature, is noisy. To provide the test calibration, the noisy calibration and calibration data should be integrated for 5 to 25 times the length of the measurement time. A single calibration time of this length would be wasteful of observation time. Therefore, a number of short calibrations centered about the observation time should be averaged together in some manner. This could be done either by a "look ahead" capability in the data processing system, which requires keeping large volumes of data in core storage, or by using a more efficient two-pass data processing system.

5. Promptness of Data Reduction - For many sensors to date, there have been significant time lags between data acquisition and data dissemination to the users. For principal investigators working in a research and development environment, these delays have proven to be a hindrance. However, for an operational system in certain applications, such delays may render the data worthless. Therefore, care should be taken to have data reduction software systems checked out before data acquisition begins.

Ideally, the data processing system should be able to operate on a run ratio of 1 to 1 or better, i.e., it should take no more time to process data than it takes to acquire it. This run ratio could be relaxed somewhat if the sensor system is not in continuous operation.

6. Data archiving and destruction - As microwave sensors grow in number and accumulated data increase, the data base will grow larger and larger until it can no longer be contained. At that time or before, decisions must be made as to which data are kept and which are discarded. Central facilities will be limited in size, and the responsibility for maintaining needed data will eventually fall to the user. The volume of data will be such that almost all unessential data will have to be discarded. Consequently, rapid and thorough analysis of data will be a necessity.

#### 3.5.4.4 Recommendations for Future Work

In the past, passive microwave sensors have been built and flown on aircraft and spacecraft before sufficient ground measurements were available to adequately predict or analyze the flight data. This tends to limit the usefulness of the flight data gathered by leaving many unresolved questions. For various reasons, this fly-first-ask-questions-later approach will continue. In order to minimize the detrimental impact

of such an approach, the ground measurements program should be expanded.

One of the available ground systems, the Microwave Signature Acquisition System (MSAS) was designed for field use with a great deal of flexibility and near real-time data reduction. It is a key system in providing the data necessary for supporting present applications and in developing future applications. Comments and recommendations concerning this system are as follows:

1. The MSAS system has not been utilized fully because the boom truck and data van have been unavailable most of the time. A boom truck capable of carrying the sensors and a data van should be made available as soon as possible.
2. Other difficulties which became evident during field usage have been encountered in system hardware and software. Texas A&M University is now in the process of improving the system's software and repairing system hardware. These efforts should be completed as soon as possible.
3. The proposed addition of another radiometer head at C-band should be expedited. The frequency proposed (4.99 GHz) is fairly close to those which are expected to fly on the Shuttle system and Nimbus G (6.6 GHz). It is also in a frequency range which the University of Kansas investigators believe shows considerable promise in measuring soil moisture using active systems.
4. Work should begin immediately on adding other frequencies which are now being flown or are planned to be flown in the future.
5. Primary emphasis should be placed on achieving the best accuracy that is attainable from this sensor in order to make as meaningful as possible data comparisons between sensors. This system has not been fully utilized. It has

the potential capability of supporting two or more intensive investigations in the same general time frame provided care is taken to prevent critical schedule conflicts.

## 3.6 VIDICONS

### 3.6.1 LANDSAT-C RETURN BEAM VIDICON (RBV)

The return beam vidicon combines the elements of both the vidicon and image orthicon. As shown in figure 3.6-1, this sensor uses the photoconductive surface of the vidicon and the return beam principle of the image orthicon. It is configured in order to obtain the best possible resolution of the two sensor elements.

The photoconductive surface of antimony sulfide-oxysulfide (ASOS) has been employed in visual sensors because of its high sensitivity and its ability to perform over a broad range of spacecraft environmental conditions. The multiplier and electron gun, both image orthicon elements, provide a high gain low noise amplifier. When coupled to the vidicon surface (ASOS), it produces a sensor with wide dynamic range (40 dB) and excellent resolving power (5000 elements) for the 2.5 inch RBV. (See reference 3.6-1 for more details)

The return beam vidicon (RBV) system for Landsat-C will provide panchromatic earth images with nominally a factor of two improvement in ground resolution compared to the Landsat-1 and Landsat-2 multispectral RBV systems. Table 3.6-1 gives the parameters for the Landsat-C RBV system.

The ground resolution of the Landsat-1 and 2 RBV systems is nominally 80 meters. The increase in ground resolution to 40 meters is achieved by doubling the focal length of the lens system, halving the exposure time to reduce the effect of ground smearing, and removing the spectral filters (see plots in figure

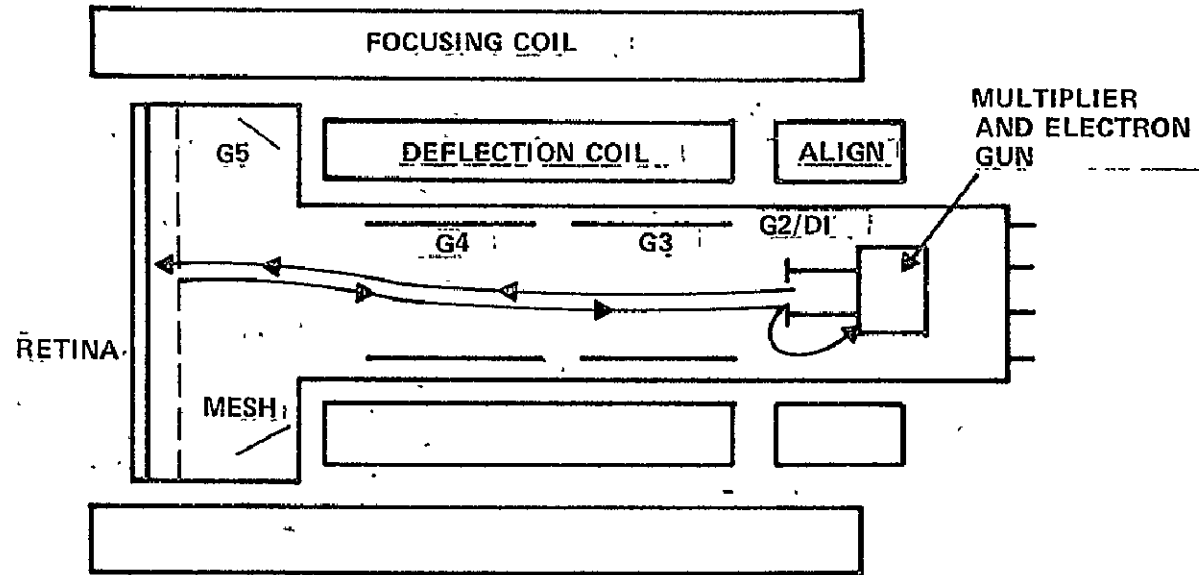


Figure 3.6-1.- Landsat return beam vidicon.

TABLE 3.6-1. - LANDSAT-C RBV: FUNCTIONAL CONSTANTS SUMMARY

Landsat-C Orbit Altitude	911.8 km (492 n.mi.)
Imaging Tube	2" RBV
Deflection Focus	Electromagnetic
Imaging Size, on Target	25.4 mm x 25.4 mm
Number of Cameras	2
Ground Coverage/Camera	98 km x 98 km
Highlight Irradiance	2,013 - mw/cm <sup>2</sup> - sr
Spectral Coverage	.505 μm - .750 μm
Lens Effective Focal Length	236 mm
Horizontal Limiting Resolution (CNTR)	4500 TV lines (90 lines per mm)
Edge Resolution	80% of center
Read Horizontal Line Rate	1250 lines per sec
Active Horizontal Lines	4125 per image
Video Bandwidth	3.2 MHz
Shading	± 15% within 25.4 mm DIA circle ± 25% elsewhere
Residual Image	< 1%
Image Distortion	± 1%
Aspect Ratio	1:1 at set-up
Skew	≤ ± 0.5°
Size and Centering	≤ ± 2%
Peak Signal/rms Noise	33 dB
Erase/Prepare/Expose/Read Out	Staggered for 2 cameras
Two Camera Cycle Rate	12.5 sec
Erase Time	0.5 sec
Prepare Time	8.5 sec
Total Read Out Time Per Exposure	3.5 sec
Available (By Command) Exposure Time	2.4, 4, 5.6, 8, or 12 ms
Nominal Exposure Time	5.6 ms

TABLE 3.6-1. -- LANDSAT-C RBV: FUNCTIONAL CONSTANTS SUMMARY  
(concluded)

<u>DCS PERFORMANCE CHARACTERISTICS</u>	
Transmitter Power Output	5 watts
Nominal Transmitter Frequency	401.9 MHz
Maximum Number of Sensor Inputs	8
Number of Quantization Levels Per Sensor	256 (8 bits)
Total Sensor Data Capacity Per Platform	64 bits

3.6-2), thus doubling the incoming energy to compensate for the faster exposure times.

The RBV system for Landsat-C contains two identical cameras that operate in the spectral band from .50  $\mu\text{m}$  to .75  $\mu\text{m}$ . The two cameras are aligned to view adjacent nominal 98 km (53 n.mi.) square ground scenes with a 14-km slidelap yielding a 183 km x 98 km scene pair. Two successive scene pairs will nominally overlap each MSS frame. The four RBV scenes which nominally fill each MSS frame will be designated A, B, C and D. (See fig. 3.6-3).

3.6-5

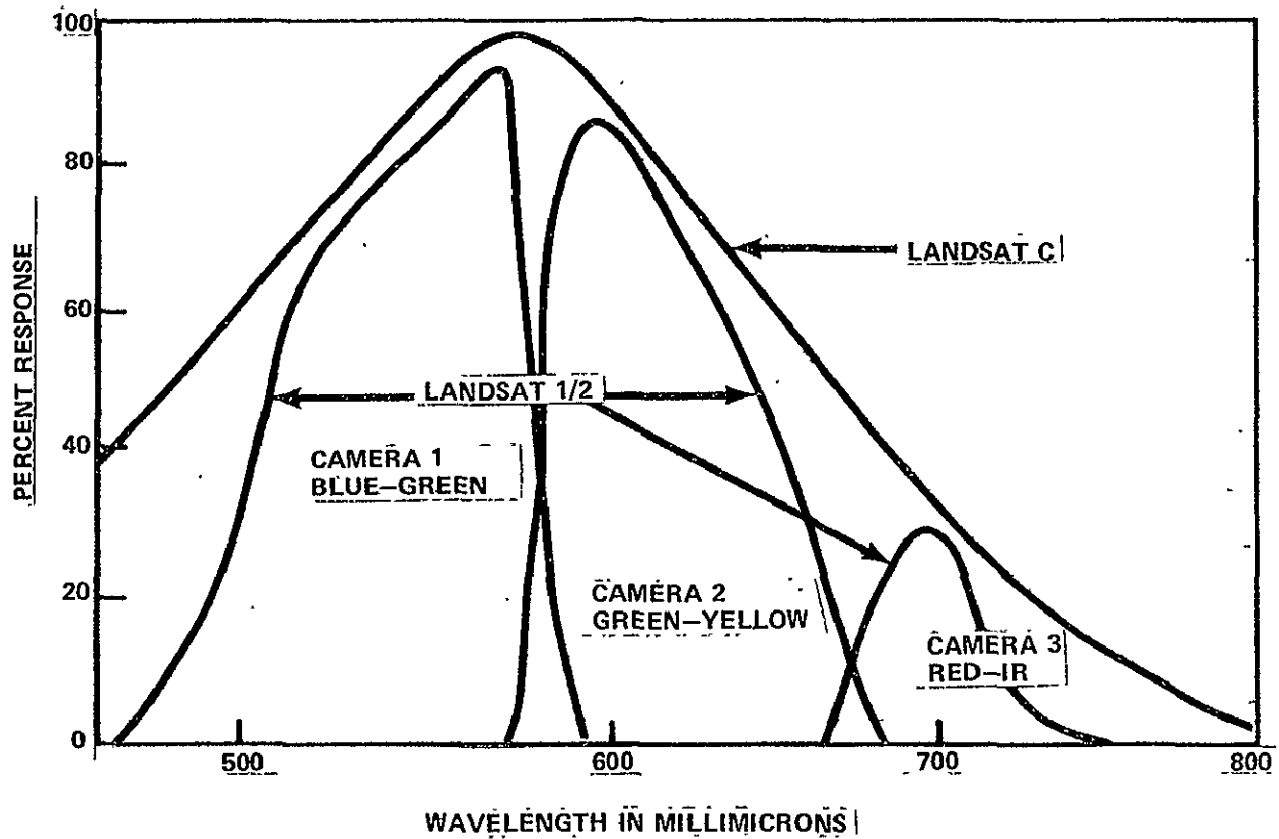


Figure 3.6-2.- Landsat RBV spectral sensitivity.

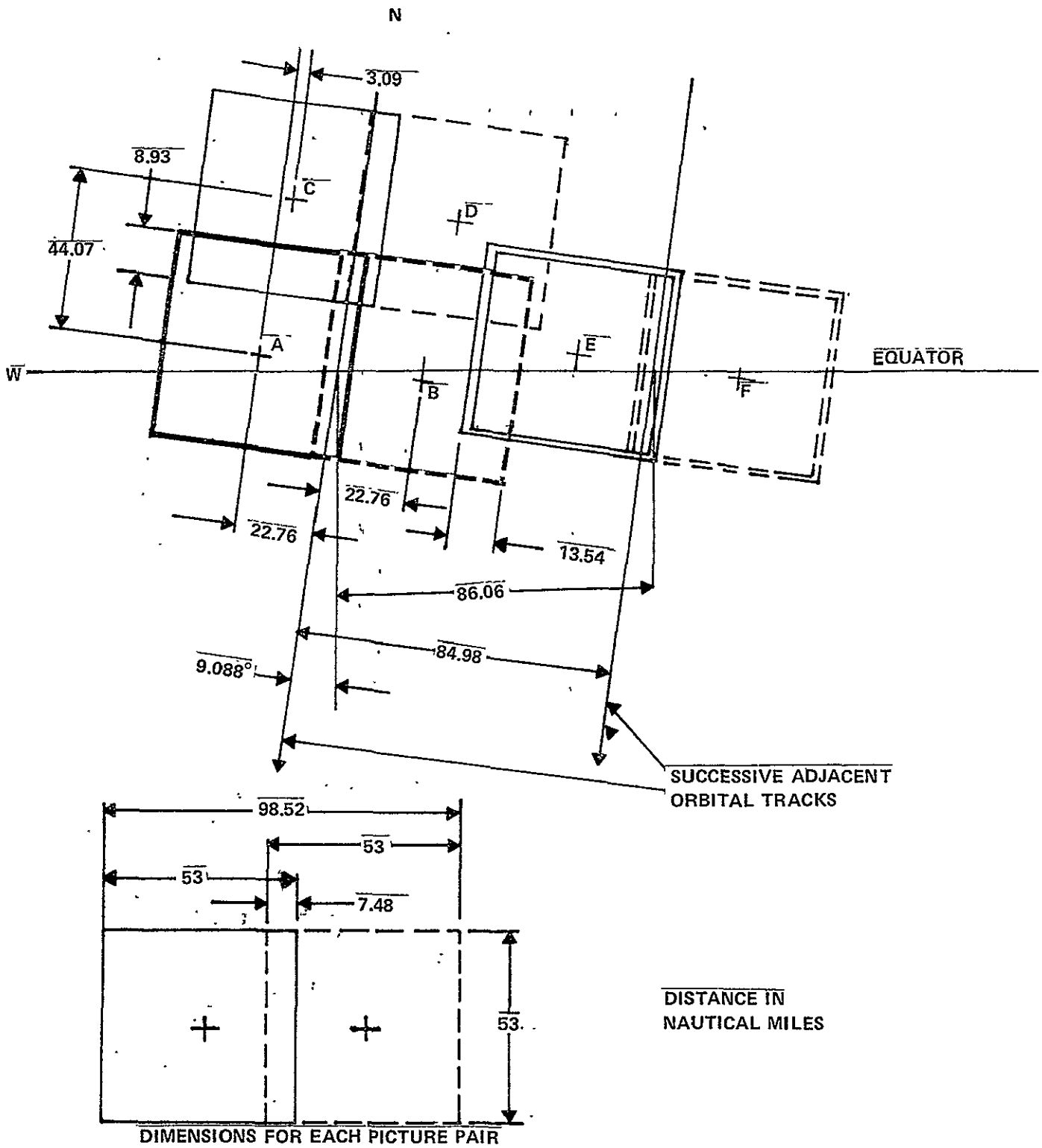


Figure 3.6-3.— Picture coverage at the Equator with all parameters at nominal values.

## REFERENCES

- 3.6-1 Dishler, J. J.: Visual Sensor Systems in Space. IEEE Convention, Mar. 1967.
- 3.6-2 Landsat Users Handbook

APPENDIX A

REMOTE SENSING SYSTEMS  
RECENT, CURRENT AND FUTURE

SYSTEM	AIRCRAFT MULTISPECTRAL SCANNERS (page 1 of 2)				
SENSOR SUBSYSTEMS	Michigan 12-band M-7	Bendix 24-band	Modular MMS (M <sup>2</sup> S)	RS-14	RS-18 MS**
Type	objective plane scanner	objective plane scanner	45° mirror objective plane scan	4-sided mirror objective scan	45° single mirror
Manufacturer	ERIM	Bendix Corp.	Bendix Corp.	Texas Instr.	Texas Instr.
Ground Coverage Aircraft	swath = 2.0 h* C-47	swath = 1.68 h* C-130	swath = 2.38 h* P3	swath = 1.68 h* -	swath = 1.68 h* RB-57
IFOV	2-3.3 mrad	2 mrad	2.5 mrad	1 or 3 mrad	1 mrad
Resolution	2-3.3 x 10 <sup>-3</sup> h*	2 x 10 <sup>-3</sup> h*	2.5 x 10 <sup>-3</sup> h*	1 or 3 x 10 <sup>-3</sup> h*	1 x 10 <sup>-3</sup> h*
Scan Efficiency	25%	22%			
Total Weight	225 kg (500 lbs)	273 kg (2800 lbs)	118 kg (261 lbs)	120 kg (264 lbs)	≈300 lbs
Status	operational	in storage	operational	operational, probably to be surplused	Mounted on pallet, requires aircraft modification**
Bands	Any 12 at one time: 0.32-0.38 μm 0.40-0.44 μm 0.44-0.46 μm 0.46-0.48 μm 0.48-0.50 μm 0.50-0.52 μm 0.52-0.55 μm 0.55-0.58 μm 0.58-0.62 μm 0.62-0.66 μm 0.66-0.72 μm 0.72-0.82 μm 0.82-0.96 μm 1.0-1.4 μm 1.5-1.8 μm 2.0-2.6 μm 8.0-13.5 μm	0.34-0.40 μm 0.40-0.44 μm 0.46-0.50 μm 0.53-0.57 μm 0.57-0.63 μm 0.64-0.68 μm 0.71-0.75 μm 0.77-0.81 μm 0.82-0.87 μm 0.97-1.06 μm 1.06-1.095 μm 1.13-1.17 μm 1.18-1.3 μm 1.52-1.73 μm 2.1-2.4 μm 3.54-4.0 μm 6.0-7.0 μm 8.3-8.8 μm 8.8-9.3 μm 9.3-9.8 μm 10.1-11.0 μm 11.0-12.0 μm 12.0-13.0 μm	0.38-0.44 μm 0.44-0.49 μm 0.49-0.54 μm 0.54-0.58 μm 0.58-0.62 μm 0.62-0.66 μm 0.66-0.70 μm 0.70-0.74 μm 0.76-0.86 μm 0.97-1.05 μm 8.0-12.0 μm	Any 2 modes at one time: 0.3-0.55 μm 0.7-0.9 μm 1.0-1.5 μm 1.5-1.8 μm 2.0-2.5 μm 3.0-3.5 μm 8.0-14.0 μm	10-12 μm Ch 1 0.5-0.6 μm Ch 2 0.6-0.7 μm Ch 3 0.7-0.8 μm Ch 4 0.8-1.1 μm Ch 5  HgCdTe - thermal detector  Si (blue enhanced) visible-NIR detectors

\*h = altitude of aircraft

\*\*Aircraft modification will be complete sometime in 1977

SYSTEM	AIRCRAFT MULTISPECTRAL SCANNERS (page 2 of 2)			
SENSOR SUBSYSTEMS	RS-18B	NS001**	Active/Passive multispectral scanner	SAS (Solid State Array Spectroradiometer)
Type	45° single mirror cassegrain reflector	45° single mirror Newtonian reflector	Boresighted laser and passive scanner	Pushbroom CCD detectors
Manufacturer	Texas Instr.	JSC	ERIM	JSC
Ground Coverage	2.38 h*	2.38 h*	2 h*	0.263 h*
Aircraft	RB-57	C-130		C-130 and RB-57
IFOV	1 mrad	2.5 mrad	2 mrad	0.76 mrad
Resolution	1. x 10 <sup>-3</sup> h*	2.5 x 10 <sup>-3</sup> h*	2.0 x 10 <sup>-3</sup> h*	.76 x 10 <sup>-3</sup> h*
Scan Efficiency				
Weight	≈110 lbs		2600 lbs.	
Status	operational	operational in one channel, others under construction	operational January 1977	operational March 1977
Bands	10-12 μm HgCdTe	0.45-0.52 μm 0.52-0.60 0.63-0.69 0.76-0.90 1.00-1.30 1.55-1.75 2.08-2.35 10-12	Active (laser) 1.06 μm (IMAGE) .4 - .64 μm (Profiler, tunable) Passive (band center) 0.45 μm 0.48 0.50 0.52 0.54 0.57 0.61 0.65 0.75 1.7 or 2.3 or 11.0 μm	20 bands .4 to .8 μm equally distributed

\*h = altitude of aircraft  
\*\* = New Scanners

SYSTEM	LANDSAT 1 & 2				
Agency	NASA				
Launch Date	Landsat-1, July 1972; Landsat-2, January 1975				
Altitude/ Orbit	907 km; near polar, sun-synchronous orbit				
SENSOR SUBSYSTEMS	Multispectral Scanner (MSS)	Return Beam Vidicon (RBV)			
Type	objective mirror scanner	3 RBV camera			
Manufacturer	Hughes	RCA			
Ground Coverage	swath = 185 km	185 x 185 km			
Repeat Coverage	every 18 days	every 18 days			
IFOV	.86 $\mu$ rad				
Resolution	79 m	80 m			
Scan Efficiency	45%				
f/Number	3.6				
Bands	0.5-0.6 $\mu$ m 0.6-0.7 $\mu$ m 0.7-0.8 $\mu$ m 0.8-1.1 $\mu$ m	0.475-0.575 $\mu$ m 0.580-0.680 $\mu$ m 0.698-0.830 $\mu$ m			

SYSTEM	LANDSAT-C				
Agency	NASA				
Launch Date	1977				
Altitude/ Orbit	911.8 km; circular, near polar, sun-synchronous orbit				
SENSOR SUBSYSTEMS	Multispectral Scanner (MSS)	Return Beam Vidicon (RBV)			
Type	objective mirror scanner	2 RBV camera (side-by-side coverage)			
Manufacturer	Hughes	RCA			
Ground Coverage	swath = 185 km	93 x 93 km			
Repeat Coverage	every 18 days	every 18 days			
IFOV	86 $\mu$ rad				
Resolution	visible/NIR 79m	40 m			
	Th.Ir 240 m				
		4500 TV lines			
		90 lines/mm			
Bands	0.5-0.6 $\mu$ m 0.6-0.7 $\mu$ m 0.7-0.8 $\mu$ m 0.8-1.1 $\mu$ m	0.50-0.75 $\mu$ m (both RBV's)			
	10.4-12.6 $\mu$ m  1-3 bands PMT 4th Si Photo- diode 5th HgCdTe				

SYSTEM	Landsat-D				
Agency	NASA				
Launch Date	1980				
Altitude/ Orbit	702.4 km; circular, near polar, sun-synchronous orbit				
SENSOR SUBSYSTEMS	Thematic Mapper (TM)				
Type	6-band MSS (type-TBD)				
Manufacturer	TBD				
Ground Coverage	swath - 185 km				
Repeat Coverage	every 9 days *				
IFOV	43 and 250 urad				
Resolution	30 m visible/near IR, 120 m thermal				
Scan Efficiency	~80%				
Bands	0.45-0.52 $\mu\text{m}^{**}$ 0.52-0.60 0.63-0.69 0.76-0.90 1.55-1.75 10.4-12.5				

\*with 2 satellite system

\*\*According to O Weinstein, NASA Technical Officer,  
GSFC, 19 October 1976.

SYSTEM	AEM-A (Applications Explorer Mission)				
Agency	NASA/GSFC				
Launch Date	1978, second quarter				
Altitude/ Orbit	600 km, polar orbiting, sun synchronous				
SENSOR SUBSYSTEMS	Heat Capacity Mapping Radiometer (HMR)				
Type	Visible/in- frared imager				
Manufacturer	ITT				
Ground Coverage	693 km				
Repeat Coverage	every 12 hrs 2:00 am, 2:00 pm local time				
IFOV	.83 mrad				
Resolution	0.518 km				
Scan Efficiency					
Bands	.55-1.1 $\mu\text{m}$ 10.5-12.5 $\mu\text{m}$				

SYSTEM	ITOS - Improved TIROS Operational Satellite				
Agency	NOAA				
Launch Date	NOAA-2, Oct. 1972; NOAA-3, Nov. 6, 1973; NOAA-4, Nov. 15, 1974				
Altitude/ Orbit	NOAA-5, July 29, 1976. 1464 ± 46 km; polar, sun-synchronous orbit				
SENSOR SUBSYSTEMS	Scanning Radiometer (SR)	Very High Reso- lution Radiometer (VHRR)	Vertical Temp. Profile Radiometer (VTPR)	Solar Proton Monitor (SPM)	
Type	line-scanning visible-IR radiometer	line scanning radiometer	visible - IR spectroradi- ometer		
Manufacturer	Santa Barbara Research Center	RCA	Barnes Engineering		
Ground Coverage	Global*	±75°	± 31.45°		
Repeat Coverage (Imagers only)	every 12 hrs, 0900/2100 local time		N/A	N/A	
IFOV	5.3 mrad	0.6 mrad	38 mrad		
Resolution	7.5 km at nadir	0.9 km at nadir	55.6 km		
Scan Efficiency					
Bands	0.5-0.7 μm 10.5-12.5 μm  Si Photo- voltaic for visible  Thermistor bolometer for IR	0.6-07. μm 10.5-12.5 μm  Si Photodiode for visible  HgCdTe for IR	6 channels in CO <sub>2</sub> band (~15 μm) 1 channel in H <sub>2</sub> O band (18.7 μm) 1 channel in 'window' (8-12 μm)	Protons: 10 <sup>+</sup> , 30 <sup>+</sup> , 60 <sup>+</sup> MeV  Electrons: 100-750 KeV	

\*horizon to horizon

SYSTEM	Nimbus 5 (page 1 of 2)				
Agency	NASA/GSFC				
Launch Date	December 11, 1972				
Altitude/Orbit	600 n. mi.; circular sun-synchronous orbit				
SENSOR SUBSYSTEMS	Electrically Scanning Microwave Radiometer (ESMR)	Temperature Humidity Infrared Radiometer (THIR)	Surface Composition Mapping Radiometer (SCMR)	Infrared Temperature Profile Radiometer (ITPR)	Selective Chopper Radiometer (SCR)
Type	imaging microwave system	thermal mapper	thermal and near infrared mapper	atmospheric sounder	atmospheric sounder
Manufacturer					
Ground Coverage	swath = 3200 km	Global	swath = 800 km	swath = 1050 km	nadir only
Repeat Coverage (Imagers only)	every 12 hours-local noon/midnight			N/A	N/A
IFOV					
Resolution (Nadir)	25x25 km	22 km (6.5-7.0 $\mu\text{m}$ ) 8 km (10.5-12.5 $\mu\text{m}$ )	660x660 m	31.8 km	42 km (15 $\mu\text{m}$ ) 29 km (all others)
Bands	19.225-19.475 GHz	6.5-7.0 $\mu\text{m}$ 10.5-12.5 $\mu\text{m}$	0.8-1.1 $\mu\text{m}$ 8.3-9.3 $\mu\text{m}$ 10.2-11.2 $\mu\text{m}$	3.8 $\mu\text{m}$ 11.0 $\mu\text{m}$ 13-15.0 $\mu\text{m}$ (4 bands) 19.8 $\mu\text{m}$	2-100 $\mu\text{m}$ (16 bands)

SYSTEM	Nimbus 5 (page 2 of 2)				
Agency	NASA/GSFC				
Launch Date	December 11, 1972				
Altitude/Orbit	600 n. mi.; circular sun-synchronous orbit				
SENSOR SUBSYSTEMS	Nimbus-E Microwave Spectrometer (NEMS)				
Type	atmospheric sounder				
Manufacturer					
Ground Coverage	continuously along nadir				
Repeat Coverage	N/A				
IFOV					
Resolution	100 n. mi.				
Bands	27.23 GHz 31.40 53.65 54.90 58.80 				

SYSTEM	Nimbus-6 (page 1 of 2)				
Agency	NASA/GSFC				
Launch Date	June 12, 1975				
Altitude/Orbit	1100 km; polar sun-synchronous orbit				
SENSOR SUBSYSTEMS	Temperature Humidity Infrared Radiometer (THIR)	High Resolution Infrared Radiation Sounder (HIRS)	Scanning Microwave Spec-trometer (SCAMS)	Electrically Scanning Microwave Radiometer (ESMR)	Earth Radiation Budget (ERB)
Type	thermal imager	atmospheric sounder	atmospheric sounder	atmospheric sounder (conical scan)	spec-trometer
Manufacturer					
Ground Coverage	swath = 3000 km	swath = 1650 km	2060 km	1200 km	500x500 km
Repeat Coverage (Imagers only)	every 12 hrs. local noon/midnight	N/A	12 hrs. local noon/midnight	12 hrs. local/noon midnight	N/A
IFOV					
Resolution (Nadir)	22.5 km (6.5-7.1 $\mu$ m) 8.2 km (10.3-12.5)	25 km	145 km	18-22 km cross track 35-54 km down track	
Bands	6.5-7.1 $\mu$ m 10.3-12.5 $\mu$ m	.69 $\mu$ m 3.71 $\mu$ m 4.24-4.57 $\mu$ m (5 bands) 6.7 $\mu$ m 8.2 $\mu$ m 11.0 $\mu$ m 13.4-15 $\mu$ m (7 bands)	22.235 GHz 31.650 52.850 53.850 55.450	37.0 GHz	.2-50 $\mu$ m (22 channels)

SYSTEM	Nimbus-6		(page 2 of 2)		
Agency	NASA/GSFC				
Launch Date	June 12, 1975				
Altitude/Orbit	1100 km; polar sun-synchronous orbit				
SENSOR SUBSYSTEMS	Limb Radiance Inversion Radiometer (LRIR)	Pressure Modulator Radiometer (PMR)			
Type	IR MS scanning radiometer	atmospheric sounder			
Manufacturer					
Ground Coverage	N/A scans earth limb	Steerable to $\pm 15^\circ$ FWD & AFT			
Repeat Coverage	N/A	N/A			
IFOV					
Resolution at Tangent Height (in order of bands)	2x11.7 km	77 km along track			
	2x20.7 km	383 km across track			
	2x20.7 km 2.5x25.4 km				
Bands	14.9-15.5 $\mu\text{m}$ (Narrow CO <sub>2</sub> band)  14.4-16.9 (Broad CO <sub>2</sub> band) 8.6-10.2 (O <sub>3</sub> ) 23.0-27.0 $\mu\text{m}$ (H <sub>2</sub> O)	CO <sub>2</sub> pressure comparison in several bands around 15 $\mu\text{m}$			

SYSTEM	Nimbus-G				(page 1 of 3)
Agency	NASA/GSFC				
Launch Date	1978				
Altitude/Orbit	955 km; polar sun-synchronous orbit				
SENSOR SUBSYSTEMS	Stratospheric and Mesospheric Sounder (SAMS)	Temperature Humidity Infrared Radiometer (THIR)	Coastal Zone Color Scanner (CZCS)	Solar Backscatter Ultraviolet Spectrometer and Total Ozone Mapping (SBUV/TOM)	
Type	atmospheric sounder	2-channel scanning radiometer	scanning radiometer		
Manufacturer					
Ground Coverage			+ 0.7 rad scan + 0.35 rad view angle		
Repeat Coverage (Imagers only)	N/A	every 12 hrs.	every 12 hrs.	Unknown	
IFOV	28x2.8 mrad	21 mrad (6.5-7.0 μm) 7 mrad (12.5 μm)	.865 mrad sq.	.052 rad sq.	
Resolution					
Bands	15 μm (CO <sub>2</sub> ) 4.1-5.4 μm (CO <sub>2</sub> , CO, NO) 2.7, 2.5-100 μm (H <sub>2</sub> O) 7.6-7.8 μm (N <sub>2</sub> O, CH <sub>4</sub> ) Detectors: 4 TGS 1 InSb 1 PbS	6.5-7.0 μm 12.5 μm	0.433-0.453 μm 0.510-0.530 0.540-0.560 0.660-0.680 0.700-0.800 10.5-12.5 Detectors: Th. IR = HgCdTe Others = SiPD	160-400 μm continuous scan (PMT)	

SYSTEM	Nimbus-G (page 2 of 3)			
Agency Launch Date Altitude/Orbit	NASA/GSFC 1978 955 km; polar sun-synchronous orbit			
SENSOR SUBSYSTEMS	Limb Infrared Monitoring of Stratosphere (LIMS)	Earth Radiation Budget	Stratospheric Aerosol Measurement II	Scanning Multichannel Microwave Radiometer (SMMR)
Type	infrared radiometer -modified Nimbus-6 LRIR	22 channel radiometer		5 wavelength dual polarized
Manufacturer				
Ground Coverage			altitude range 10 km to space	
Repeat Coverage	N/A	N/A	N/A	12 hrs.
IFOV	0.5 mrad sq. (1x8 mrad-H <sub>2</sub> O, NO <sub>2</sub> )	4.4x89.4 mrad (scan) 2.32 rad cone (earth) 0.46 rad (solar)	0.145 mrad	
Bands	6.08-6.39 μm (NO <sub>2</sub> ) 6.41-7.25 (N <sub>2</sub> O) 8.64-10.64 (O <sub>3</sub> ) 10.87-11.76 (HNO <sub>3</sub> ) 13.16-17.24 (CO <sub>2</sub> (wb)) 14.71-15.75 (CO <sub>2</sub> (nb)) Detectors: HgCdTe	'Solar' channels: 0.2-4.0 μm (2ch.) 0.4-0.5 0.35-0.45 0.2-0.5 0.53-3.0 0.7-3.0 0.3-0.4 0.28-0.35 0.25-0.30 (this column cont. on next page)	0.06 μm band at 1.0 μm	37 GHz (0.8 cm) 21 GHz (1.4 cm) 18 GHz (1.7 cm) 10.7 GHz (2.8 cm) 6.6 GHz (4.0 cm)

SYSTEM	Nimbus-G (page 3 of 3)		
SENSOR SUBSYSTEMS		Earth Radiation Budget	
Bands (cont. from previous page)		'Earth' channels: 0.2-0.5 $\mu\text{m}$ (2 ch.) ↓ 0.2-4.0 ↓ 0.7-3.0 ↓ 'Scanning' channels: 0.2-5.0 $\mu\text{m}$ (4 ch.) ↓ 4.5-5.0 (4 ch.) ↓	

SYSTEM	Seasat-A (page 1 of 2)				
Agency	NASA/JPL				
Launch Date	May 1978				
Altitude/Orbit	790 km; circular, non sun-synchronous, near polar orbit				
SENSOR SUBSYSTEMS	Synthetic Aperture Radar (SAR)	Radar Scatterometer	Scanning Multi-frequency Microwave Radiometer (SMMR)	Radar Altimeter	Visible-Infrared Radiometer (VIRR)
Type	imaging system, single polarization	fan beam	bidirectional scan	precision pulse	scanning 2-band
Manufacturer	Hughes/JPL	GE	JPL	APL, Johns Hopkins	Santa Barbara Research Center
Ground Coverage	100 km on one side from 17°-23°	750 km ea. side ± 25°-65° around nadir ± 70 km	638 ± 70 km	12 km circle*	2127 km
Repeat Coverage	within receiving station range, real time only	N/A	36 hours	N/A	36 hours
IFOV					visible: 2.8 mrad IR: 5.3 mrad
Resolution	25 m	50 km ± 5%	(see following page)	1.6 km*	visible: 2.2 km IR: 4.2 km
Polarization	H	sequenced HH, VV	dual linear		
Bands - (see following page)					

\*due to integration

SYSTEM	Seasat-A (page 2 of 2)				
Agency Launch Date Altitude/Orbit	NASA/JPL May 1978 <sup>t</sup> 790 km; circular, non sun-synchronous, near polar orbit				
SENSOR SUBSYSTEMS	Synthetic Aperture Radar (SAR)	Radar Scatterometer	Scanning Multi-frequency Microwave Radiometer (SMMR)	Radar Altimeter	Visible-Infrared Radiometer (VIRR)
Bands	1.275 GHz	14.6 GHz	6.6 GHz 10.69 GHz  18.0 GHz 21.0 GHz 37.0 GHz  *footprint sizes in order: 121x79 km 74x49 km 44x29 km 38x25 km 21x14 km	13.5 GHz	0.47-0.94 μm  10.5-12.5 μm

SYSTEM	SMS/GOES (Synchronous Meteorological Satellite/Geostationary Operational Environmental Satellite)			
Agency	SMS*, NASA/GFSC; GOES*, NOAA			
Launch Date	SMS-1, May 1974; SMS-2, Feb. 1975; GOES-1, Oct. 1975;			
Altitude/ Orbit	GOES-B, May 1977; GOES-C, January 1978 34,781 km, earth synchronous			
SENSOR SUBSYSTEMS	Visible/Infrared Spin Scan Radiometer (VISSR)			
Type	Visible/Infrared Imager			
Manufacturer	Hughes Aircraft			
Ground Coverage	Earth Disc			
Repeat Coverage	Earth Disc every 20 min.			
IFOV	.026 mrad (visible) 0.20 mrad (infrared)			
Resolution	.9 km (visible) 7 km (infrared)			
Scan Efficiency				
Bands	.55 to .75 $\mu\text{m}$ . 10.5-12.5 $\mu\text{m}$ (advanced versions also include bands centered at 3.94; 4.44, 4.52, and 13.3 $\mu\text{m}$ )			

\*SMS-Developed and experimentally flown by NASA; GOES-operationally flown by NOAA.

SYSTEM	SEOS-A				(page 1 of 2)
Agency	NASA/GSFC				
Launch Date	1981				
Altitude/Orbit	~35,700 km; geosynchronous; equatorial orbit				
SENSOR SUBSYSTEMS	Large Earth Survey Telescope (LEST)	Advanced Atmospheric* Sounder and Imaging Radiometer (AASIR)	Microwave Sounder*	Framing Camera*	
Type	multispectral scanner with pushbroom scan	imaging radiometer		television	
Manufacturer	TBD	Santa Barbara Research Center			
Ground Coverage	Pointable to $\pm 1$ km			1000x1000 km & 200x200 km	
Repeat Coverage	nearly continuous on earth disc	N/A	N/A	frame every 15 sec. of earth disc	
IFOV	imaging: vis. 2.8 $\mu$ rad IR 22.4 $\mu$ rad				
Resolution	imaging: vis. 100m IR 800m IR sounding: 18-30 km		200 km at 50 GHz 50 km at 220 GHz	216m for 1000 km 45m for 200 km	
FOV	0.6x1.2°				
Bands -  (see following following page)					

\*potential candidates; L.S.Walter, EASCON 1974, pp. 631-636.

SYSTEM	SEOS-A (page 2 of 2)			
SENSOR SUBSYSTEMS	Large Earth Survey Telescope (LEST)	Advanced Atmospheric* Sounder and Imaging Radiometer (AASIR)	Microwave Sounder*	Framing Camera
Bands	series of bands in the following spectral regions: .45-1.1 $\mu\text{m}^{**}$ 2.3 3.5 4.3 6.5-7.0 10.5-12.5** 14-15 23-24	.55 - 1.1 $\mu\text{m}^{**}$ 3.7 $\mu\text{m}$ 4.24-4.57 $\mu\text{m}$ (5 chs.) 6.71 $\mu\text{m}$ 7.25 $\mu\text{m}$ 11.11 $\mu\text{m}^{**}$ 12.66-15 $\mu\text{m}$ (7 chs.)	5 bands in the 50-220 GHz region	0.4-0.9 $\mu\text{m}$

\*potential candidates; L.S. Walter, EASCON 1974, pp. 631-636.  
 \*\*imaging bands

SYSTEM	SKYLAB Earth Resources Experiment Package (EREP) (page 1 of 3)				
Agency	NASA				
Launch Date	Operated: May 1973 - February 1974				
Altitude/Orbit	435 km				
SENSOR SUBSYSTEMS	S-190A	S-190B	S-191	S-192	S-193
Type	6 multiband cameras	earth terrain camera	pointable filter wheel spectrometer	13 band conical scanner	Ku band, 3 modes: 1) radiometer 2) scatterometer 3) altimeter
Manufacturer	Itek	Actron	Block Engineering/Martin	Honeywell	General Electric
Ground Covering	163 x 163	109 x 109	non-imaging	swath = 68.5 km	total scan of 22.7°
Repeat Coverage	N/A	N/A	N/A	N/A	N/A
IFOV	(FOV = 21.23° sq)	(FOV = 14.24° sq)	1 mrad	0.182 mrad sq.	1.6° half power beam width
Resolution	78-223 ft.**	35-99 ft*	0.435 km dia.	79.2 m	11.0 km dia. circle at nadir
Format (cameras)	5.7x5.7 cm	11.5x11.5 cm			
Focal Length	152 mm	457 mm			
f/Number	2.8	4			
Forward Motion Compensation	0-30 mrad/sec	0-25 mrad/sec			

\*35 ft for S0-242 aerial color film, 99 ft. for EK 3443 color IR film  
 \*\*78 ft for S0-356 color film, 223 ft. for EK 2424 B&W IR film

SYSTEM	SKYLAB Earth Resources Experiment Package (EREP) (page 2 of 3)				
SENSOR SUBSYSTEMS	S-190A	S-190B	S-191	S-192	S-193
Bands	6 bands 0.4-0.9 $\mu\text{m}$ bands selected with filters .7-.8 $\mu\text{m}$ BW IR .8-.9 BW IR .5-.88 $\mu\text{m}$ Color IR .4-.7 $\mu\text{m}$ Color .6-.7 BW Red .5-.6 $\mu\text{m}$ BW Green	0.40-0.90 $\mu\text{m}$ film selected from following: aerial color .4-.7 $\mu\text{m}$ aerial B&W .5-.7 $\mu\text{m}$ color IR .5-.88 $\mu\text{m}$	continuous 0.39-2.5 $\mu\text{m}$ (Si and PbS) 5.82-15.99 $\mu\text{m}$ (HgCdTe)	0.41-0.46 $\mu\text{m}$ 0.46-0.51 0.52-0.56 0.56-0.61 0.62-0.67 0.68-0.76 0.78-0.88 0.98-1.08 1.09-1.19 1.20-1.30 1.55-1.75 2.10-2.35 10.2-12.5 $\mu\text{m}$	13.9 GHz
Remarks	Grid reseau  0-30 frames/min.	varying overlap between frames  0-25 frames/min.			

SYSTEM	SKYLAB Earth Resources Experiment Package (EREP) (page 3 of 3)			
Agency	NASA			
Launch Date	Operated: May 1973 - February 1974			
Altitude/Orbit	435 km			
SENSOR SUBSYSTEMS	S-194			
Type	Non-imaging L-band radiometer			
Manufacturer	ALL			
Ground Coverage				
Repeat Coverage	N/A			
IFOV				
Resolution	half power pts: 124 km dia.			
Bands	1.414 GHz			

SYSTEM	Space Shuttle Earth Resources Sensors*			
Agency	NASA			
Launch Date	1980's			
Altitude/Orbit	- - -			
SENSOR SUBSYSTEMS	Shuttle Imaging Radar (SIR)*	Mark II Interferometer*	Spaceborne Meteorological Radar*	Shuttle Imaging Microwave System* (SIMS)
Type	synthetic aperture radar	non-imaging	synthetic aperture radar; afocal	passive scanning, imaging radar
Manufacturer	JPL/Hughes**	JPL	Hughes**	JPL
Ground Coverage				FOV = 106°
Repeat Coverage	Unknown	N/A	N/A	Unknown
I FOV	1-17 mrad	fixed nadir FOV		26 mrad
Resolution				
Launch Date	1982			
Bands	1.4 GHz 9.8 GHz	1-9 μm	~10 GHz	0.61 GHz 1.4 2.7 6.6 10.7 20 22.2 37 53 94 118.7 GHz

\*definition stage  
\*\*under study

SYSTEM	TIROS-N* (page 1 of 2)				
Agency	NASA/NOAA				
Launch Date	1978				
Altitude/Orbit	833 ± 90 km polar orbit				
SENSOR SUBSYSTEMS	Basic Sounding Unit (BSU)	Stratospheric Sounding Unit (SSU)	Microwave Sounding Unit (MSU)	Advanced Very High Resolution Radiometer (AVHRR)	Space Environment Monitor (SEM)
Type	rotating mirror, cross track scan	selective absorption pressure cells	4-channel Dicke radiometer	4-channel visible-IR radiometer	four detector arrays
Manufacturer	Ball Brothers Research Corp.	Provided by United Kingdom	JPL	ITT	NOAA/ERL Boulder, Colo.
Ground Coverage	+ 1127 km (± 49.5°)	+ 737 km (± 40°)	± 47.35°		
Repeat Coverage	N/A	N/A	N/A	12 hrs.	N/A
IFOV					
Resolution	21.8 km dia. -nadir 75.2x37.3 km -scan end	147 km dia. -nadir 244x186 km -scan end	7.5°	1.1 & 4 km	
No. Steps/Angle per step	56/1.8°	8/10°	11/9.47°		
Bands (see following page)					

\*2nd generation of TIROS/NOAA

SYSTEM	TIROS-N* (page 2 of 2)				
SENSOR SUBSYSTEMS	Basic Sounding Unit (BSU)	Stratospheric Sounding Unit (SSU)	Microwave Sounding Unit (MSU)	Advanced Very High Resolution Radiometer (AVHRR)	Space Environment Monitor (SEM)
Bands	3.70 $\mu\text{m}$ 4.26 9.71 11.12 13.33 13.61 13.99 14.29 14.49 14.75 14.95 18.80 23.15 29.41	3 channels each at $668\text{cm}^{-1}$ central wave number cell pressures: 100 mb 35 10	50.3 GHz 53.74GHz 54.96GHz 57.95GHz	0.55-0.9 $\mu\text{m}$ 0.725-1.0+ 3.55-3.93 10.5-11.5 (11.5-12-5)**	Detector arrays: 1) High Energy Proton-Alpha Telescope (HEPAT) protons = 100,400,600 MeV alpha = 2400, 4000, MeV 2) Low Energy Proton-Alpha Telescope (LEPAT) protons = 150 KeV - 40 MeV alpha = 0.6-100 MeV 3) Proton Omni-directional detector (POD) protons = .75,10,30, 60 MeV alpha = 75, 40,120,140 MeV 4) Total Energy Detector (TED)

\*2nd generation of TIROS/NOAA

\*\*not on first, but considered on later TIROS-N/NOAA satellites as AVHRR-II

SYSTEM	Defense Meteorological Satellite Program (page 1 of 2) (DMSP 1 & 2; Block B/C)			
Agency	Air Force			
Launch Date	Unknown; now in orbit			
Altitude/ Orbit	450 n. mi. polar, sun-synchronous orbit			
SENSOR SUBSYSTEMS	Scanning Radiometer* (SR)	Special Meteoro- logical Sensor (SSE)	Precipitating Electron Spectrometer	
Type	Visible/ infrared imager	atmos- pheric sounder	unknown	
Manufacturer			unknown	
Ground Coverage	swath = 1600 n.mi.		unknown	
Repeat Coverage (imagers only)	DMSP-1 sunset, sunrise DMSP-2 midnight, noon	N/A	N/A	
IFOV			unknown	
Resolution	Visible: VHR-.34 n.mi. HR-2.0 n.mi.  Infrared: WHR-.36 n.mi. IR-2.4 n.mi.		unknown  unknown	
Bands (see following page)				

\*includes Very High Resolution (VHR) and High Resolution (HR) for visible  
Very High Resolution (WHR) and High Resolution (IR) for infrared

SYSTEM	Defense Meteorological Satellite Program (page 2 of 2) (MDSP 1 & 2; Block B/C)		
SENSOR SUBSYSTEMS	SR*	SSE	
Bands	0.4-1.1 $\mu\text{m}$ 8-13 $\mu\text{m}$  Detectors: <ul style="list-style-type: none"> <li>● Visible:                VHR-back                biased                Si diode                 HR-photo-                conductive                mode-Si diode</li> <li>● Infrared:                VHR-HgCdTe                IR-thermister                bolometer</li> </ul>	<ul style="list-style-type: none"> <li>● 5 CO<sub>2</sub> bands                around 15 <math>\mu\text{m}</math></li> <li>● atmospheric                window                at 12 <math>\mu\text{m}</math></li> <li>● 1 H<sub>2</sub>O band                at 20 <math>\mu\text{m}</math></li> </ul>	

\*includes Very High Resolution (VHR) and High Resolution (HR) for visible  
 Very High Resolution (VHR) and High Resolution (IR) for infrared

SYSTEM	Defense Meteorological Satellite Program (DMSP - Block D)		
Agency	Air Force		
Launch Date	to be launched		
Altitude/ Orbit	450 n. mi., polar, sun-synchronous orbit		
SENSOR SUBSYSTEMS	Operational Linescan System (OLS)	Special Meteorological Sensor H (SSH)	
	Type	imager	atmospheric sounder
Manufacturer	Westinghouse	Barnes Engineering	
Ground Coverage	1655 n. mi.	± 551.1 n. mi. 25 steps across track	
Repeat Coverage (IMAGERS only)	every 12 hrs.	N/A	
IFOV		2.7°	
Resolution	0.3 n. mi. 1.5 n. mi.		
FOV		± 48°	
Bands	0.41-1.1 μm 8-13 μm  Detectors: PMT Si photo- diode HgCdTe	9.8 μm - O <sub>3</sub> 12.0 - window 13.4 CO <sub>2</sub> 13.8 14.1 14.4 14.8 15.0 18.7 22.7 23.9 24.5 25.2 26.7 28.2 28.3	